

Electronic Theses and Dissertations, 2004-2019

2015

Multi-Row Film Cooling Boundary Layers

Greg Natsui
University of Central Florida

 Part of the [Mechanical Engineering Commons](#)
Find similar works at: <https://stars.library.ucf.edu/etd>
University of Central Florida Libraries <http://library.ucf.edu>

This Doctoral Dissertation (Open Access) is brought to you for free and open access by STARS. It has been accepted for inclusion in Electronic Theses and Dissertations, 2004-2019 by an authorized administrator of STARS. For more information, please contact STARS@ucf.edu.

STARS Citation

Natsui, Greg, "Multi-Row Film Cooling Boundary Layers" (2015). *Electronic Theses and Dissertations, 2004-2019*. 1464.
<https://stars.library.ucf.edu/etd/1464>

MULTI-ROW FILM COOLING BOUNDARY LAYERS

by

GREG NATSUI

B.S. Aerospace Engineering, University of Central Florida, 2010

M.S. Aerospace Engineering, University of Central Florida, 2012

A dissertation submitted in partial fulfillment of the requirements
for the degree of Doctor of Philosophy
in the Department of Mechanical and Aerospace Engineering
in the College of Engineering and Computer Science
at the University of Central Florida
Orlando, Florida

Fall Term
2015

Major Professor: Jayanta S. Kapat

© 2015 by Greg Natsui

ABSTRACT

High fidelity measurements are necessary to validate existing and future turbulence models for the purpose of producing the next generation of more efficient gas turbines. The objective of the present study is to conduct several different measurements of multi-row film cooling arrays in order to better understand the physics involved with injection of coolant through multiple rows of discrete holes into a flat plate turbulent boundary layer.

Adiabatic effectiveness distributions are measured for several multi-row film cooling geometries. The geometries are designed with two different hole spacings and two different hole types to yield four total geometries. One of the four geometries tested for adiabatic effectiveness was selected for flowfield measurements. The wall and flowfield are studied with several testing techniques.

Pressure sensitive paint and discrete gas sampling taps are simultaneously used to measure adiabatic film cooling effectiveness by taking advantage of the heat and mass transfer analogy. All cooling regimes documented by Goldstein [1] for a single row are seen in the multi-row geometries studied. As the blowing ratio increases from 0, the laterally averaged effectiveness increases everywhere, until a point is reached at which upstream rows begin to drop in performance while the downstream rows increase in performance. Finally, a point is reached at which the cooling performance drops everywhere as the blowing ratio is increased.

Detailed boundary layer measurements are obtained with hot wire anemometry. The boundary layer is measured at two upstream locations to characterize the approaching flow and provide boundary conditions for computational predictions. The hot wire technique is then applied to the array at up to 15 streamwise locations to obtain measurements of mean velocity, RMS of the fluctuations and integral length scale, in the presence of film cooling. It was seen that injection thickens the boundary layer significantly. Due to the low turbulence mainstream and jets, turbulence production takes place primarily at regions of high shear between mainflow and coolant or in wakes for the lifted case.

Finally, particle image velocimetry measurements are taken to provide streamwise and wall normal velocity measurements at two streamwise aligned planes in the flow; an array centerline and $d/2$ plane corresponding to the edge of the jets. These measurements show how an increase in blowing ratio decreases turbulence levels throughout the array. The entire structure of the boundary layer changes from shearing at the top to a wall-bounded jet flow as the blowing ratio increases. Despite lower turbulence levels, the high blowing ratio case is seen to perform worse than the low blowing case from the effectiveness measurements. The particle image velocimetry measurements corroborate the hot wire measurements in that the turbulence production occurs where the mainflow and coolant jets meet and interact.

For my Family

ACKNOWLEDGMENTS

I have met countless people throughout my infinitesimal existence.

Each one has influenced who I am today.

Thank you Family – past, present and future. You inspire me.

Thank you UCF. You showed me the real world is not the ideal world.

Thank you Committee. Without you, I would have an empty form.

Thank you Lab. You were the perfect place to grow.

Thank you Siemens. You built me up.

Thank you GE. You polished me down.

Thank you Friends. You're the greatest.

Thank you Miami. I wouldn't have had it any other way.

Thank you Orlando. It has been legen – wait for it – dary. Truly a pleasure.

Thank you

TABLE OF CONTENTS

LIST OF FIGURES	xv
LIST OF TABLES	xxiv
CHAPTER 1 INTRODUCTION	1
1.1 Film Cooling	4
1.1.1 Progression from Transpiration to Modern Day Film Cooling	6
1.1.2 Heat Transfer to a Film Cooled Boundary Layer	7
1.1.3 Control Volume Analysis of a Film Cooled Boundary Layer	9
1.1.4 Film Cooling Parameters	13
1.1.5 Slot Cooling	21
1.1.6 Discrete Film Cooling	23
1.2 Full-Coverage Film Cooling	30

1.2.1	Literature	31
1.3	Motivation and Objectives of the Present Study	45
1.3.1	Novelty	46
1.4	Outline	47
CHAPTER 2 EXPERIMENTAL SETUP		50
2.1	Test Geometries	50
2.1.1	Shaped Film Cooling Geometry	52
2.2	Wind Tunnel	55
2.2.1	Pressure Gradient at the Test Section	59
2.2.2	Inlet Boundary Layer	61
2.2.3	Coolant Supply	65
CHAPTER 3 TIME RESOLVED FLOWFIELD		67
3.1	Thermal Anemometry Background	68
3.1.1	Heat Transfer to a Heated Wire	69

3.1.2	Wheatstone Bridge	71
3.2	Measurements with a Single Wire	72
3.2.1	Probe, Stem, Flow Coordinate Systems	73
3.2.2	Velocity Analysis	74
3.3	Turbulent Boundary Layers	75
3.3.1	Linear Sublayer	79
3.3.2	Logarithmic Layer	79
3.3.3	van Driest Damping Function	80
3.3.4	Cole's Wake Function	81
3.3.5	Modified Wake Function	81
3.3.6	Clauser Fit	82
3.3.7	Length Scales	84
3.4	Data Reduction	87
3.5	Experimental Methodology	90

3.5.1	Hotwire Calibration	90
3.5.2	Hardware	91
3.5.3	Sampling Convergence	93
3.6	Results	97
3.6.1	Measurement Locations	97
3.6.2	Mean Velocity	99
3.6.3	$\sqrt{\langle u'^2 \rangle}$ Results	101
3.6.4	Length-Scale Calculations	103
3.6.5	Derived Quantities	105
3.7	Summary of Hot Wire Findings	110
CHAPTER 4 SPATIALLY RESOLVED FLOWFIELD		112
4.1	Flowfield Measurements of Film Cooling	113
4.2	Particle Image Velocimetry	114
4.3	PIV Experimental Setup	115

4.4	Testing Methodology	119
4.5	PIV Processing	120
4.5.1	Image Calibration	122
4.5.2	File Formats and Timing Attributes	123
4.5.3	Pre-Processing	123
4.5.4	Geometric Mask	123
4.5.5	Interrogation Algorithms	124
4.5.6	Vector Validation	124
4.5.7	Extraction of Scalar and Vector Fields	125
4.6	Results	127
4.7	Summary of PIV Findings	134
CHAPTER 5 ADIABATIC FILM COOLING EFFECTIVENESS		142
5.1	The Heat and Mass Transfer Analogy	143
5.2	Pressure Sensitive Paint	144

5.2.1	PSP Photophysics	144
5.2.2	Effectiveness from Pressure Ratio	146
5.3	PSP Experimental Setup	148
5.3.1	PSP Preparation and Test Methodology	148
5.3.2	CCD camera	149
5.3.3	Paint	150
5.4	PSP Calibration	150
5.4.1	Calibration Setup	152
5.4.2	Calibration Procedure	155
5.5	Processing	158
5.6	Uncertainty Estimation	159
5.6.1	Propagation of Error Sensitivity Coefficients	160
5.6.2	CCD System Considerations	166
5.6.3	Sampling Convergence	168

5.6.4	Temporal Degradation of Intensity	169
5.6.5	Temperature Dependence of PSP	172
5.7	Single Row Results	177
5.7.1	Repeatability	181
5.7.2	Validation	187
5.8	Evaluation of Test Uncertainty	189
5.8.1	$\eta = 0$ Statistics	193
5.9	Multi-Row Results	193
5.9.1	Spatially Resolved Film Cooling Effectiveness, $\eta(x_i/d, z_j/d)$	196
5.9.2	Spatially Resolved Uncertainty Estimates, $u_\eta(x_i/d, z_j/d)$	216
5.9.3	Laterally Averaged Effectiveness for Multi-Row Geometries	226
5.9.4	Testing of Stereolithography Manufactured Hardware	230
5.9.5	Auto-Illumination	236
5.9.6	Gas Sampling	238

5.9.7 Superposition Predictions of Multi-Row Performance	242
5.10 Summary of Effectiveness Findings	244
CHAPTER 6 FINDINGS	247
APPENDIX A DESIGN CALCULATIONS	251
APPENDIX B MEASUREMENTS OF TEST GEOMETRIES	255
APPENDIX C HOTWIRE MEAN PROCESSING ALGORITHM	261
APPENDIX D HOTWIRE CLAUSER FIT PROCESSING ALGORITHM	266
APPENDIX E HOTWIRE LENGTH SCALE PROCESSING ALGORITHM	278
APPENDIX F PSP PROCESSING ALGORITHM	282
APPENDIX G PSP UNCERTAINTY PROCESSING ALGORITHM	306
LIST OF REFERENCES	314

LIST OF FIGURES

Figure 1.1	$P - v$ and $T - S$ diagrams of the Ideal Brayton Cycle.	2
Figure 1.2	John Barber’s original heat engine operating on the Brayton Cycle.	2
Figure 1.3	Diagram defining orientation angles α and β	16
Figure 1.4	Diagram of geometric parameters	17
Figure 1.5	Effect of momentum flux ratio I	19
Figure 1.6	Diagram of full-coverage film cooling.	30
Figure 2.1	Parameter space for multi-row film; literature and present study	53
Figure 2.2	Diffuser shaped hole studied by Gritsch et al. [2]	54
Figure 2.3	New diffuser modeled after the fan shaped hole studied by Gritsch et al.	55
Figure 2.4	Isometric view of wind tunnel showing main components	56
Figure 2.5	Cross-sectional view of wind tunnel test section	56
Figure 2.6	Physical test section dimensions	57
Figure 2.7	Streamwise pressure gradient in wind tunnel primary flow	59
Figure 2.8	$K(x)$, acceleration parameter throughout the test section	60
Figure 2.9	Inner scaled boundary layer upstream of film cooling array	62

Figure 2.10	Outer scaled boundary layer upstream of film cooling array	63
Figure 2.11	Measurements to determine boundary layer uniformity	64
Figure 2.12	CO ₂ microbulk tank with electric and ambient vaporizers	65
Figure 2.13	Measurements of various ΔT 's in coolant loop	66
Figure 3.1	Bridge circuit	71
Figure 3.2	Probe coordinate system	73
Figure 3.3	The different laws and functions describing a turbulent boundary layer	78
Figure 3.4	Clouser fit to obtain $\tau_{y=0}$ and y_{offset}	83
Figure 3.5	Estimation of Λ_I and λ_r	88
Figure 3.6	Sample hot wire calibration relating bridge voltage with flow velocity	90
Figure 3.7	Hotwire probe used in experiment	92
Figure 3.8	Hotwire probe in tunnel at the lowest wall normal position	92
Figure 3.9	Relation between physical wall normal coordinate and y^+ location	92
Figure 3.10	Convergence of $\langle u \rangle$	94
Figure 3.11	Convergence of $\langle u'^2 \rangle$	95
Figure 3.12	Convergence of Λ_I	96
Figure 3.13	$\langle u \rangle$ measurements	100
Figure 3.14	$\langle u' \rangle$ measurements	102
Figure 3.15	Λ_I measurements upstream of the film array	104

Figure 3.16	Integral length-scale, Λ_I , measurements throughout Geometries 1 and 5	106
Figure 3.17	Particle density flow visualization for $M = 0.45$ showing rows 1 and 3	107
Figure 3.18	Particle density flow visualization for $M = 1.05$ showing rows 1 and 3	108
Figure 3.19	Boundary layer thickness development throughout the multi-row arrays	109
Figure 3.20	Streamwise development of wall shear stress	109
Figure 4.1	Experimental setup for PIV testing	116
Figure 4.2	Reference image used for determining spatial resolution	122
Figure 4.3	Nomenclature for mean and instantaneous velocities	126
Figure 4.4	$u(x, y)$, $v(x, y)$, $\omega_z(x, y)$ and $k(x, y)$ for $M = 0.45$ at $z/d = 0$	129
Figure 4.5	$u(x, y)$, $v(x, y)$, $\omega_z(x, y)$ and $k(x, y)$ for $M = 0.75$ at $z/d = 0$	130
Figure 4.6	$u(x, y)$, $v(x, y)$, $\omega_z(x, y)$ and $k(x, y)$ for $M = 1.05$ at $z/d = 0$	130
Figure 4.7	$k(x, y)$, $R_{xy}(x, y)$, $R_{xx}(x, y)$ and $R_{yy}(x, y)$ for $M = 0.45$ at $z/d = 0$	132
Figure 4.8	$k(x, y)$, $R_{xy}(x, y)$, $R_{xx}(x, y)$ and $R_{yy}(x, y)$ for $M = 0.75$ at $z/d = 0$	133
Figure 4.9	$k(x, y)$, $R_{xy}(x, y)$, $R_{xx}(x, y)$ and $R_{yy}(x, y)$ for $M = 1.05$ at $z/d = 0$	133
Figure 4.10	$u(x, y)$, $v(x, y)$, $\omega_z(x, y)$ and $k(x, y)$ for $M = 0.45$ at the $d/2$ plane	134
Figure 4.11	$u(x, y)$, $v(x, y)$, $\omega_z(x, y)$ and $k(x, y)$ for $M = 0.75$ at the $d/2$ plane	135
Figure 4.12	$u(x, y)$, $v(x, y)$, $\omega_z(x, y)$ and $k(x, y)$ for $M = 1.05$ at the $d/2$ plane	135
Figure 4.13	$k(x, y)$, $R_{xy}(x, y)$, $R_{xx}(x, y)$ and $R_{yy}(x, y)$ for $M = 0.45$ at the $d/2$ plane	136
Figure 4.14	$k(x, y)$, $R_{xy}(x, y)$, $R_{xx}(x, y)$ and $R_{yy}(x, y)$ for $M = 0.75$ at the $d/2$ plane	136

Figure 4.15	$k(x, y)$, $R_{xy}(x, y)$, $R_{xx}(x, y)$ and $R_{yy}(x, y)$ for $M = 1.05$ at the $d/2$ plane	137
Figure 4.16	$\langle u \rangle(y/d; z/d = 0)$	138
Figure 4.17	$\langle u' \rangle(y/d; z/d = 0)$	139
Figure 4.18	$\langle \omega_z \rangle(y/d; z/d = 0)$	140
Figure 4.19	$u'v'(y/d; z/d = 0)$	141
Figure 5.1	Relation between pressure ratio and adiabatic film cooling effectiveness	147
Figure 5.2	PSP calibration facility	153
Figure 5.3	PSP calibration	157
Figure 5.4	Diagram showing locations from which results were calculated	159
Figure 5.5	Propagation of error estimate, using Equation 5.8	161
Figure 5.6	$u_\eta(\eta)$	161
Figure 5.7	η propagation of error uncertainty tree	167
Figure 5.8	Convergence of estimator over 100 images	169
Figure 5.9	PSP emission over time	171
Figure 5.10	Calibration of PSP for different dT relative to reference temperature	174
Figure 5.11	Collapse of different temperature curves	176
Figure 5.12	Estimation of PSP error due to temperature	176
Figure 5.13	Spatially resolved effectiveness for single row case	178
Figure 5.14	Centerline effectiveness for single row	179

Figure 5.15	Single row area averages	180
Figure 5.16	Day-to-day repeatability of $\bar{\eta}$ for $M = 0.3$	182
Figure 5.17	Day-to-day repeatability of $\bar{\eta}$ for $M = 0.5$	183
Figure 5.18	Day-to-day repeatability of $\bar{\eta}$ for $M = 0.6$	183
Figure 5.19	Day-to-day repeatability of $\bar{\eta}$ for $M = 0.8$	184
Figure 5.20	Day-to-day repeatability of $\bar{\eta}$ for $M = 0.9$	184
Figure 5.21	Day-to-day repeatability of $\bar{\eta}$ for $M = 1.2$	185
Figure 5.22	Day to day repeatability of centerline film effectiveness, η_{cl}	185
Figure 5.23	Lateral uniformity of η_{cl}	186
Figure 5.24	Single row validation for $M \approx 0.5$	188
Figure 5.25	Single row validation for $M \approx 0.9$	189
Figure 5.26	$\eta(x/d = 0, z/d)$ compared with ideal distribution	190
Figure 5.27	Maps of uncertainty, calculated according to [81], for $M = 0.3$ and 1.2	192
Figure 5.28	PSP system response to step input	193
Figure 5.29	Region sampled for $\eta = 0$ statistics	194
Figure 5.30	Probability density functions of a nominally $\eta = 0$ sample	194
Figure 5.31	Measurements of upstream systematic error	195
Figure 5.32	Measurements of upstream random error	195
Figure 5.33	Geometry 1, $M = 0.30$; spatially resolved η	198

Figure 5.34	Geometry 1, $M = 0.44$; spatially resolved η	198
Figure 5.35	Geometry 1, $M = 0.60$; spatially resolved η	199
Figure 5.36	Geometry 1, $M = 0.79$; spatially resolved η	199
Figure 5.37	Geometry 1, $M = 0.97$; spatially resolved η	200
Figure 5.38	Geometry 1, $M = 1.08$; spatially resolved η	200
Figure 5.39	Geometry 1, $M = 1.23$; spatially resolved η	201
Figure 5.40	Geometry 1b, $M = 0.30$; spatially resolved η	203
Figure 5.41	Geometry 1b, $M = 0.48$; spatially resolved η	203
Figure 5.42	Geometry 1b, $M = 0.63$; spatially resolved η	204
Figure 5.43	Geometry 1b, $M = 0.81$; spatially resolved η	204
Figure 5.44	Geometry 1b, $M = 0.94$; spatially resolved η	205
Figure 5.45	Geometry 1b, $M = 1.11$; spatially resolved η	205
Figure 5.46	Geometry 1b, $M = 1.34$; spatially resolved η	206
Figure 5.47	Geometry 2, $M = 0.31$; spatially resolved η	207
Figure 5.48	Geometry 2, $M = 0.45$; spatially resolved η	208
Figure 5.49	Geometry 2, $M = 0.63$; spatially resolved η	209
Figure 5.50	Geometry 2, $M = 0.75$; spatially resolved η	210
Figure 5.51	Geometry 2, $M = 0.90$; spatially resolved η	211
Figure 5.52	Geometry 2, $M = 1.20$; spatially resolved η	212

Figure 5.53	Geometry 5, $M = 0.549$; spatially resolved η	214
Figure 5.54	Geometry 5, $M = 1.06$; spatially resolved η	214
Figure 5.55	Geometry 5, $M = 1.56$; spatially resolved η	215
Figure 5.56	Geometry 5, $M = 2.20$; spatially resolved η	215
Figure 5.57	Geometry 6, $M = 0.53$; spatially resolved η	217
Figure 5.58	Geometry 6, $M = 1.05$; spatially resolved η	218
Figure 5.59	Geometry 6, $M = 1.59$; spatially resolved η	219
Figure 5.60	Geometry 6, $M = 2.20$; spatially resolved η	220
Figure 5.61	Geometry 1: $u_\eta(x_i/d, z_i/d; M = 0.30)$	221
Figure 5.62	Geometry 1: $u_\eta(x_i/d, z_i/d; M = 0.44)$	221
Figure 5.63	Geometry 1: $u_\eta(x_i/d, z_i/d; M = 0.60)$	222
Figure 5.64	Geometry 1: $u_\eta(x_i/d, z_i/d; M = 0.79)$	222
Figure 5.65	Geometry 1: $u_\eta(x_i/d, z_i/d; M = 0.97)$	223
Figure 5.66	Geometry 1: $u_\eta(x_i/d, z_i/d; M = 1.08)$	223
Figure 5.67	Geometry 1: $u_\eta(x_i/d, z_i/d; M = 1.23)$	224
Figure 5.68	$u_\eta(\eta; M = 0.30)$	225
Figure 5.69	$\bar{\eta}(x_i/d; M)$ for Geometry 1	228
Figure 5.70	$\bar{\eta}(x_i/d; M)$ for Geometry 1b	228
Figure 5.71	$\bar{\eta}(x_i/d; M)$ for Geometry 2	229

Figure 5.72 $\bar{\eta}(x_i/d; M)$ for Geometry 5	229
Figure 5.73 $\bar{\eta}(x_i/d; M)$ for Geometry 6	230
Figure 5.74 SLA Transmission	231
Figure 5.75 LED shining through SLA test hardware	232
Figure 5.76 SLA Transmission	233
Figure 5.77 Primers investigated for SLA testing	233
Figure 5.78 Different primer combinations tested	234
Figure 5.79 Aluminum hardware compared with SLA hardware	235
Figure 5.80 Evidence of reflections within the wind tunnel	236
Figure 5.81 Schematic of how reflections can influence results	237
Figure 5.82 Siemens Ultramat 23 gas analyzer used for gas sampling measurements .	238
Figure 5.83 Gas sampling tap locations, shown on Geometry 5	239
Figure 5.84 $\eta(x/d, P_z/4; M = 0.3)$ comparison to gas sampling results	239
Figure 5.85 $\eta(x/d, P_z/4; M = 0.45)$ comparison to gas sampling results	240
Figure 5.86 $\eta(x/d, P_z/4; M = 0.6)$ comparison to gas sampling results	240
Figure 5.87 $\eta(x/d, P_z/4; M = 0.75)$ comparison to gas sampling results	240
Figure 5.88 $\eta(x/d, P_z/4; M = 0.9)$ comparison to gas sampling results	241
Figure 5.89 $\eta(x/d, P_z/4; M = 1.05)$ comparison to gas sampling results	241
Figure 5.90 $\eta(x/d, P_z/4; M = 1.2)$ comparison to gas sampling results	241

Figure 5.91	Repeatability of gas sampling results	242
Figure 5.92	Superposition predictions for $M = 0.3, 0.5$ and 0.9	243
Figure B.1	Measurements of Geometry 1	256
Figure B.2	Measurements of Geometry 1b, hot side	256
Figure B.3	Measurements of Geometry 1b, cold side	257
Figure B.4	Inlet vs outlet difference in hole diameter	257
Figure B.5	Measurements of Geometry 2	258
Figure B.6	Measurements of Geometry 5	259
Figure B.7	Measurements of Geometry 6	260

LIST OF TABLES

Table 1.1	Full-coverage film cooling literature	32
Table 2.1	Test matrix with nominal parameters	51
Table 2.2	Test matrix with actual measured parameters	51
Table 2.3	Diffuser hole parameters	54
Table 2.4	Measured boundary layer parameters	61
Table 2.5	Parameters describing equation to recover boundary layer	62
Table 2.6	Hot wire details	63
Table 3.1	Hotwire specifications	91
Table 3.2	Hotwire test matrix	97
Table 3.3	Streamwise locations for hot wire traverses	98
Table 3.4	Hotwire parameters compared with guidelines from [3]	111
Table 4.1	Conditions and measurement plane locations tested with PIV	127
Table 5.1	pco.1600 camera characteristics	150
Table 5.2	Sources of PSP error	160
Table 5.3	Single row geometry	177

Table 5.4	Single row flow conditions	177
Table 5.5	Literature for comparison with single row results	188

CHAPTER 1

INTRODUCTION

Gas turbines are enablers for power generation and propulsion of all types. Sizes range from micro turbines used to propel snowboarders and skydivers all the way to massive gas turbines used for power generation with many variants in between. Gas turbines use a gas, typically air, as the working fluid. The fluid is first compressed through a compressor. Fuel is added and burnt with the compressed air in the combustor. Then this mixture passes through the turbine which extracts the usable power from the flow. The turbine drives the compressor and can be connected to a generator for power generation, a propeller or fan for low speed propulsion or in the case of jet engines the exhaust gas is nozzled to produce thrust directly. Gas turbines operate on the Brayton Cycle which is characterized by four ideal steps:

- 1 – 2: Isentropic Compression
- 2 – 3: Isobaric Heat Addition
- 3 – 4: Isentropic Expansion
- 4 – 1: Isobaric Heat Extraction

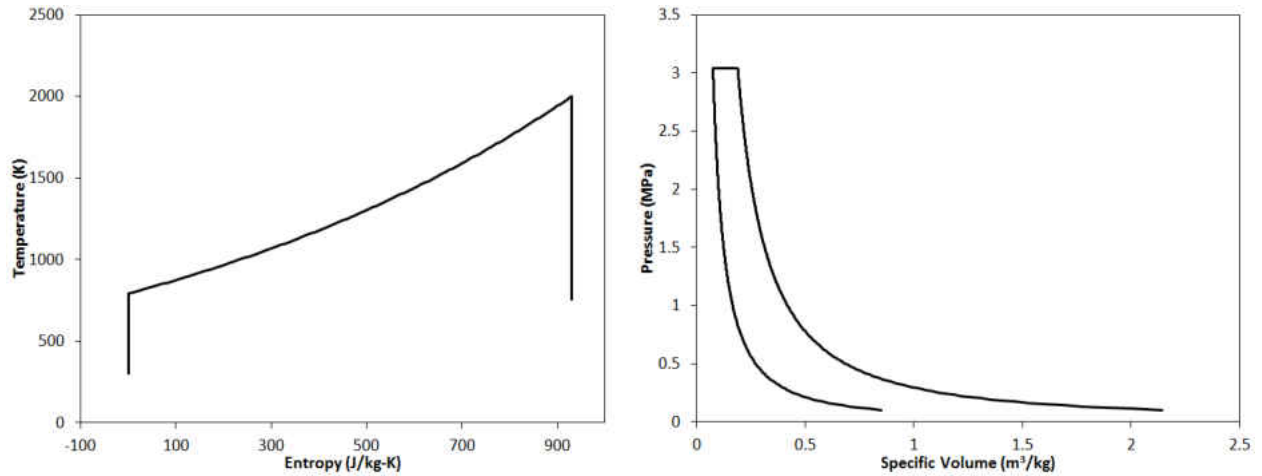


Figure 1.1: $P - v$ and $T - S$ diagrams of the Ideal Brayton Cycle.

These processes are plotted on $P-v$ and $T-s$ diagrams in Figure 1.1. The first patent incorporating the Brayton Cycle was a reciprocating style closed loop engine, patented by John Barber in 1791. The intent was for this engine to power a “horseless carriage”; however, due to limitations in technology at that time the engine was unable to produce successful work. A picture of his invention from his patent can be seen in Figure 1.2.

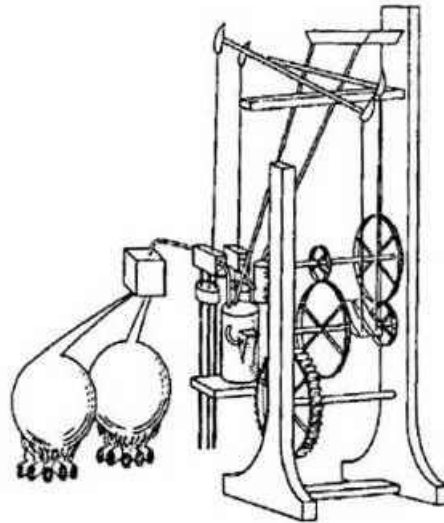


Figure 1.2: John Barber’s original heat engine operating on the Brayton Cycle.

$$\eta_{Brayton} = 1 - \frac{T_1}{T_3} = 1 - \left(\frac{P_1}{P_3}\right)^{\frac{\gamma-1}{\gamma}} \quad (1.1)$$

Equation 1.1, shows the thermal efficiency of the Brayton cycle increases as the firing temperature increases. This is the ultimate motivation for raising current firing temperatures, which already cause heat fluxes on the order of $2MW/m^2$ and temperatures exceeding $1900K$ in the first stage of gas turbines, even higher [4]. With temperatures far past the allowable metal temperature of engine components, gas turbines survive by advanced materials and coating along with several different advanced cooling schemes working in tandem to prevent engine failure. However, cooling does come at a cost. Coolant is extracted from mid to late stages in the compressor. Work is used to compress this coolant which would otherwise represent power generated.

The use of 20 to 30% of this compressed air to cool the high-pressure turbine presents a severe penalty on the thermodynamic efficiency unless the firing temperature is sufficiently high for the gains to outweigh the losses. — R. S. Bunker [5]

Modern cooling technologies require complete understanding in order to design a component with a high level of confidence which is cooled better and with less flow than previous generations. In the 1950's turbines were uncooled implying that the hot gas path was maintained at a level in which the components can survive. The desire to increase turbine efficiency forced engineers to find ways to increase the hot gas temperature. This was accomplished by passing compressor air through the blades, which is appreciably cooler than the hot gas path, effectively lowering the metal temperatures, this scheme is known as convection cooling. This technology advanced from simply passing cold air through the blade to utilizing serpentine internal passages, turbulators, and impingement-cooling. This was good yet left much to be desired and film-cooling was introduced. Film cooling allowed for a quantum leap in hot gas path temperatures as it very effectively cuts the source temperature to the blade by several hundreds of Kelvin. Modern turbines utilize a combination of film, impingement and sophisticated internal cooling schemes to realize temperatures of the working fluid exceedingly hotter than the allowable metal temperature of the components.

1.1 Film Cooling

Film cooling is the introduction of a secondary fluid (coolant or injected fluid) at one or more discrete locations along a surface exposed to a high temperature environment to protect that surface not only in the immediate region of injection but also in the downstream region. — R. J. Goldstein [6]

Due to the large rewards and even greater complexity related to film cooling, there has been a startling amount of research over several decades in the area focusing on every imaginable aspect of the technology. Studies have been conducted on the effects on cooling due to turbulence intensity of the main-flow, hole roughness, hole blockage, hole manufacturing technique, freestream boundary layer thickness, density ratio between the two stream, momentum flux ratio, mass flux ratio, hole inclination angle, hole compound angle, hole length, hole spacing, hole inlet conditions, adverse and favorable pressure gradients, downstream of a rotating wake, hole exit shaping, hole embedded in trenches, film jet Mach number, several Reynolds numbers based on different scales, the list goes on and on. There are literally thousands of academic and industry studies in the single area of film cooling; hence, not every paper can be summarized below and focus will be placed only upon studies of immediate importance to the present work.

Film cooling has been studied extensively for many years. Eckert (1950) first studied film cooling analytically as an extension of the fundamental transpiration problem.

The primary difference between traditional forms of film cooling and transpiration is that film cooling is focused on providing a film downstream of the injection location. Transpiration traditionally focuses on the region which is transpiring and would neglect the film generated as it flows downstream.

Transpiration brought about slot cooling which brought about discrete injection through cylindrical holes and then eventually on to shaped holes in order to attempt to recover some of the performance lost by discrete injection.

Early on Eckert showed some fundamental parameters in characterizing film cooling include the adiabatic effectiveness and the mass flux ratio or blowing ratio.

Film cooling is a cooling method used in virtually all of today's aircraft turbine engines and in many power-generation turbine engines and yet is a very difficult phenomena to predict [7].

1.1.1 Progression from Transpiration to Modern Day Film Cooling

In slot cooling the manner in which the slot is injecting (e.g. normal or tangential, lip thicknesses, ...) affects the performance. In discrete film cooling the pitch to diameter ratio, normalized lateral distance between adjacent holes and the inclination angle are prime geometric parameters influencing performance. A discrete injection through cylindrical holes can be compared to a slot by calculating the equivalent slot width defined as $s = \frac{\pi d}{4p_z/d}$. Traditional hole shaping is termed "diffuser". In a diffuser hole, the metering length and overall length dictate the amount the hole expands. There are 4 expansion angles which must be defined; upstream, downstream and both lateral angles. Then there are the radii of curvature for all edges within the hole. In recent years there have been many novel variations on a traditional hole in an effort to generate even better protection with as little coolant as possible. Examples include (anti-vortex, neko-mimi, etc).

1.1.2 Heat Transfer to a Film Cooled Boundary Layer

In general, a heat flux can be calculated from Newton's Law of Cooling, Equation 1.2,

$$q'' = h(T_{hot} - T_{cold}) \quad (1.2)$$

Because h is a function of the coolant temperature T_c , it is necessary to define a datum temperature. In the hypothetical situation in which the wall is adiabatic, i.e. $q''_{film} = 0$, the wall would reach a certain temperature distribution. Let us define this temperature as T_{aw} , the adiabatic wall temperature. The heat flux into the wall can now be defined as

$$q''_f = h_f(T_w - T_{aw}) \quad (1.3)$$

This new temperature T_{aw} is still dependent upon the injection temperature of the coolant. In order to circumvent this dependency let us define yet another new parameter, adiabatic film cooling effectiveness, η ;

$$\eta \equiv \frac{T_\infty - T_{aw}}{T_\infty - T_c} \neq f(T_\infty, T_c) \quad (1.4)$$

This new parameter η successfully removes the dependence of injection temperatures and is now only a function of the parameters influencing film cooling performance. Now, the film temperature, or adiabatic wall temperature T_{aw} , can be obtained from the definition for film cooling effectiveness, η . η , is zero when $T_{aw} = T_\infty$ and equal to unity when $T_{aw} = T_c$.

The same issue for T_{aw} arises when considering h_f , in that it is a function of some very specific parameters, specifically T_c and T_{aw} . In order to remove this dependency an augmentation factor, h/h_0 , is defined as;

$$\frac{h}{h_0} \equiv \frac{h_f}{h_0} \quad (1.5)$$

where h_0 is the heat transfer coefficient in the absence of a coolant film.

Heat transfer augmentation, h/h_0 , is the factor indicating the added mixing that film cooling promotes near the wall. Typically the augmentation is greater than unity, however, has been known to drop below unity in the recovery region. More times than not, however, the effect of injection is to increase the heat transfer conductance of the boundary layer.

All parameters have now been defined in order to investigate the main parameter of interest, the net heat flux reduction ($\Delta q''$), which is a measure of how much the film has reduced heat transfer into the wall. Equation 1.6 defines $\Delta q''$ as,

$$\Delta q'' \equiv 1 - \frac{q_f''}{q_0''} \quad (1.6)$$

which reduces to

$$\Delta q'' = 1 - \frac{h}{h_0} \left(1 - \frac{\eta}{\phi} \right) \quad \text{where} \quad \phi = \frac{T_\infty - T_w}{T_\infty - T_c} \quad (1.7)$$

Upon examination of Equation 1.7 it can be shown that it is of interest to minimize the heat transfer augmentation h/h_0 and to maximize film cooling effectiveness η . The parameter ϕ represents a goal dictated by design requirements, but is dependent upon the cooling performance.

In practice it is not straight forward to measure the heat transfer coefficient in the presence of film defined by rearranging Equation 1.3. It is easier to compute Equation 1.2 and convert to the desired heat transfer coefficient. This relation can be derived by equating Equations 1.2 and 1.3 then solving for q_f'' . The result is shown as Equation 1.8,

$$h_f = h_u (1 - \eta\theta)^{-1} \quad (1.8)$$

in which the uncorrected heat transfer coefficient h_u is the h from Equation 1.2 because it has yet to be “corrected” properly for film temperature.

1.1.3 Control Volume Analysis of a Film Cooled Boundary Layer

In order to gain some insight into the physics of a film cooled boundary layer, a very simplistic analysis is repeated here from Goldstein [6].

Assumption 1 Constant property ideal gases

Assumption 2 Flow over the wall is adiabatic

Assumption 3 \bar{T} is equal to the adiabatic wall temperature T_{aw}

Assumption 4 A 1/7th power turbulent profile

Assumption 5 The boundary layer thickness grows as a typical turbulent profile over a flat plate with no injection

Assumption 6 Hydrodynamic boundary layer starts at the point of injection ($x' = x$), noting at the injection location $x = 0$

Assumption 7 $C_{p\infty} = C_{pc}$

First, a mass and energy balance on the control volume around a simplified film flow is performed. From continuity,

$$\dot{m} = \dot{m}_c + \dot{m}_\infty = \int_0^\delta \rho u dy \quad (1.9)$$

Equation 1.9 will be used in conjunction with an assumed velocity profile once the energy equation is reduced. Let us define the average temperature in the boundary layer, \bar{T} , as,

$$\bar{T} - T_\infty = \frac{\int_0^\delta \rho u C_p (T - T_\infty) dy}{\int_0^\delta \rho u C_p dy} \quad (1.10)$$

Following Assumption 1, the average specific heat at constant pressure is then,

$$\bar{C}_p = \frac{\dot{m}_c C_{p2} + \dot{m}_\infty C_{p\infty}}{\dot{m}_c + \dot{m}_\infty} \quad (1.11)$$

Following Assumption 2, the energy balance can be written as,

$$\left(\dot{m}_c + \dot{m}_\infty \right) \bar{C}_p \bar{T} = \dot{m}_c C_{p2} T_c + \dot{m}_\infty C_{p\infty} T_\infty \quad (1.12)$$

After a significant amount of algebra, and using Assumption 3, this can be written in the form,

$$\frac{T_{aw} - T_\infty}{T_c - T_\infty} = \eta = \frac{1}{1 + \frac{\dot{m}_\infty C_{p\infty}}{\dot{m}_c C_{p2}}} \quad (1.13)$$

Now continuity, Equation 1.9 is used to determine \dot{m}_∞/\dot{m}_c . Assumption 4 implies,

$$\frac{u}{U_\infty} = \left(\frac{y}{\delta} \right)^{1/7} \quad (1.14)$$

From Equations 1.9 and 1.14,

$$\dot{m}_\infty = \int_0^\delta \rho_\infty U_\infty \left(\frac{y}{\delta} \right)^{1/7} dy = \frac{7}{8} \rho_\infty U_\infty \delta \quad (1.15)$$

Assumption 5 implies,

$$\frac{\delta}{x'} \approx 0.376 Re_{x'}^{-1/5} \quad (1.16)$$

Combining Equations 1.15 and 1.16 and incorporating Assumption 6 leads to the following expression for \dot{m}_∞ ,

$$\dot{m}_\infty = 0.329\rho_\infty U_\infty x Re_x^{-1/5} \quad (1.17)$$

Dividing by $\dot{m}_c = \rho_c u_c s$, where s is the length of the slot in the streamwise direction, yields an expression for \dot{m}_∞/\dot{m}_c ,

$$\frac{\dot{m}_\infty}{\dot{m}_c} = \frac{0.329\rho_\infty U_\infty x \left(\frac{U_\infty x \rho_\infty}{\mu_\infty} \right)^{-1/5}}{\rho_c u_c s} \quad (1.18)$$

This expression leads to the notion that the ratio between coolant mass flux and mainstream mass flux is an important parameter. Defining the mass flux ratio, or blowing ratio, M as,

$$M \equiv \frac{\rho_c u_c}{\rho_\infty u_\infty} \quad (1.19)$$

and re-arranging, Equation 1.18 can be written as

$$\frac{\dot{m}_\infty}{\dot{m}_c} = 0.329 \left(\frac{x}{Ms} \right)^{4/5} \left[Re_c \left(\frac{\mu_c}{\mu_\infty} \right) \right]^{-1/5} \quad (1.20)$$

In order to simplify this equation, define the parameter ξ as,

$$\xi = \left(\frac{x}{Ms} \right) \left[Re_c \left(\frac{\mu_c}{\mu_\infty} \right) \right]^{-1/4} \quad (1.21)$$

Finally, using Assumption 7, Equation 1.13 can be written as,

$$\eta = \frac{1}{1 + 0.329\xi^{4/5}} \quad (1.22)$$

1.1.4 Film Cooling Parameters

Some parameters driving film cooling performance will be reviewed. Independent geometry parameters and fluid mechanic parameters are described in sections §1.1.4.1 and §1.1.4.2 respectively. The dependent parameters which described film cooling performance are reviewed in section §1.1.4.3.

1.1.4.1 Geometric Independent Parameters

Hole Diameter, d – The length-scale used for film cooling studies is generally the hole diameter, d .

Hole Length, L – measured from inlet breakout to exit breakout. The length of the hole, L , is typically fixed by the application, however, the hole length does have a significant impact on the dynamics of the exiting film jet. The non-dimensional hole length is L/d . A short hole ($L/d < 4$) will not allow the flow to develop from the vena-contracta generated as the flow enters the hole, this will increase the ability of the coolant flow to jet into the mainstream because of a locally high momentum flux. A long hole ($L/d > 6$) allows the entrance effects to diminish as well as more time for the wall to affect the velocity profile; the net effect is to reduce the jets ability to penetrate into the main flow.

Inclination Angle (Surface Angle), α – measured from surface to hole axis, in the plane of the hole axis. α is typically between $20-90^\circ$ for film cooling applications. The effect of α is to adjust the wall normal component of momentum of the coolant jet as it leaves the wall.

Compound Angle (Flow Angle), β – measured from axis projected onto wall relative to flow. β can vary anywhere between $\pm 90^\circ$. Any deviation from 0° will cause an asymmetric vortex pair exiting the film hole. This is beneficial because it disrupts the induced wall normal velocity, and instead promotes spreading of the jet. Once $\beta = 90^\circ$, the film jet is characterized by a single dominant vortex, with z -vorticity opposite the sign of β .

Lateral Pitch, P_z – the lateral distance between two adjacent holes, measured from hole exit breakout to adjacent hole exit breakout. The pitch is non-dimensionalized by the hole diameter to create a non-dimensional spacing, P_z/d .

Streamwise Pitch, P_x – the streamwise distance between two adjacent rows and is normalized to P_x/d . Both P_z/d and P_x/d impact the amount of interaction between the neighboring jets and overall affect the solidity of the film array.

Equivalent Slot Width, s – relates the cross-sectional area of a discrete film row with an equivalent 2D slot. Typically used to non-dimensionalize the streamwise coordinate (x/Ms) in classic film cooling correlations.

Coverage, t – the physical projected area of the hole array normalized by the pitch. For a cylindrical row of holes spaced a distance P_z apart with no compound angle the coverage is given by, $t = d/P_z$.

Lateral Expansion Angles, $\Phi_{1,2}$ – define the expansion angles of side walls of a diffuser hole. $\Phi_1 + \Phi_2$ is the full expansion angle of a shaped hole. These angles dictate how much diffusion will take place within the shaped hole. If these angles are too large there is potential for separation off the lateral walls.

Layback Angle, Φ_3 – defines the expansion angle of the downstream surface of a diffuser hole.

Plunge Depth, L' – diffuser holes have a metering length and a shaped length. The plunge depth defines the length of the hole which shaping is applied to.

Area Ratio, AR – for shaped holes the exit cross sectional area is larger than the metering area. The ratio of these two areas is known as the area ratio, AR . This represents the idea velocity reduction which can be imposed on the coolant flowing through a diffuser. This is why shaped holes can operate at much higher blowing ratios than cylindrical holes, the area increase acts to provide a lower effective M .

These parameters are sketched in Figures 1.3 and 1.4.

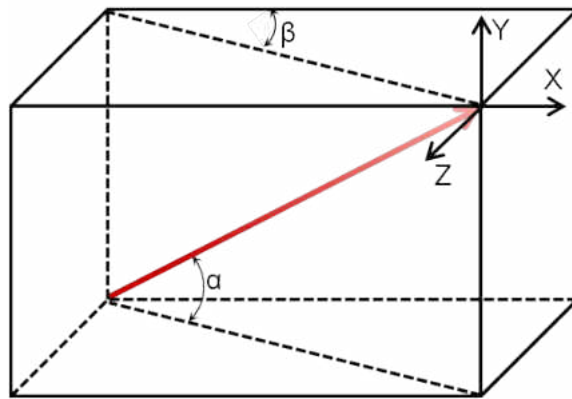


Figure 1.3: Diagram defining orientation angles α and β

1.1.4.2 Fluid Mechanics Independent Parameters

Other than the film source geometry, the fluid mechanic parameters of the flow are also hugely influential to the performance. Shown in Equation 1.23, the blowing ratio (M)

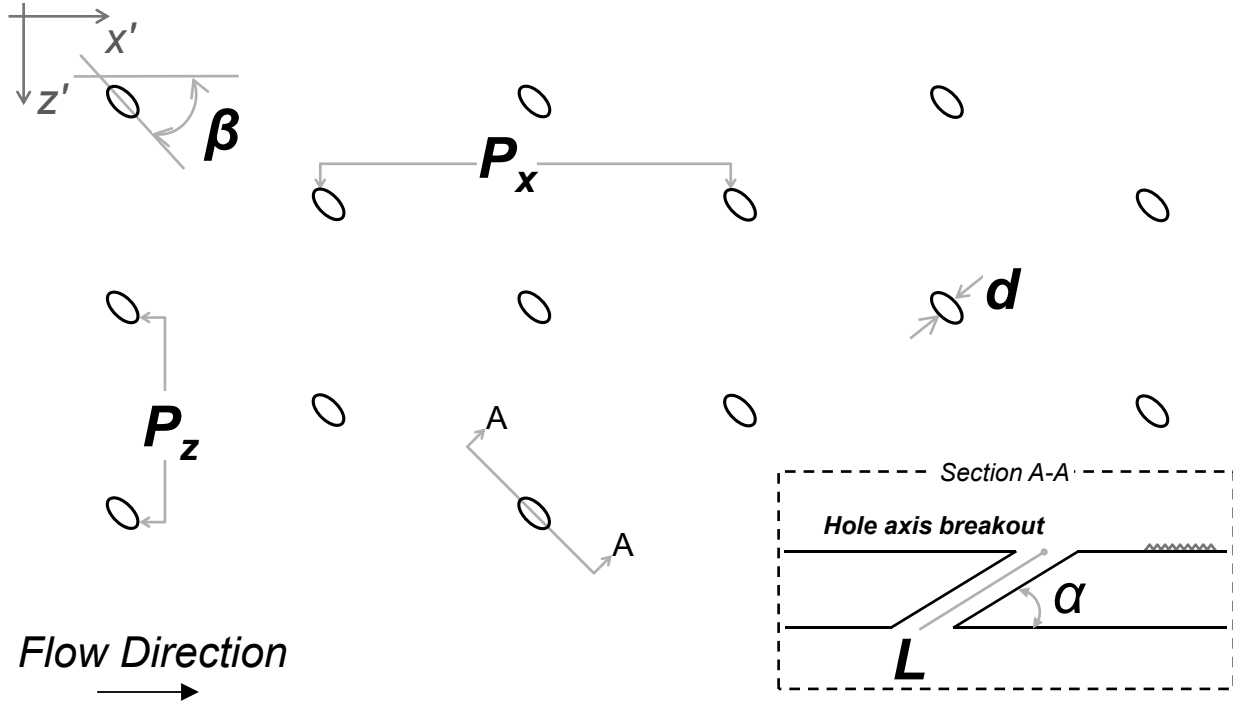


Figure 1.4: Diagram of geometric parameters

describes the ratio of coolant mass flux to mainstream hot gas mass flux. This ratio indicates the amount of mass injected into the boundary layer. The mainstream and coolant density (ρ), average coolant velocity magnitude (U_c) and freestream velocity (U_∞) are used.

$$M = \frac{(\rho U)_c}{(\rho U)_\infty} \quad (1.23)$$

Other parameters often used to describe film cooling performance are the density ratio (DR) and the momentum flux ratio (I). These are calculated using Equation 1.24 and Equation 1.27 respectively. The effect of density ratio is to influence the momentum flux ratio for a given blowing ratio. That is, once a blowing ratio is fixed, the momentum ratio

is determined based on the density ratio. A density ratio less than unity is commonly used in laboratory testing; however, the density ratio of an engine is much greater than unity. A value of $DR < 1$ will raise the momentum flux ratio. A very large DR would be ideal ($DR \gg 1$) however, designers have little control of this parameter.

$$DR = \frac{\rho_c}{\rho_\infty} \quad (1.24)$$

For the thermal problem (e.g. air into air but $T_c \neq T_\infty$) this can be reduced to

$$DR = \frac{T_\infty}{T_c} \quad (1.25)$$

For the mass transfer problem (e.g. CO₂ into air and $T_c = T_\infty$) this can be reduced to

$$DR = \frac{R_\infty}{R_c} \quad (1.26)$$

$$I = \frac{(\rho U^2)_c}{(\rho U^2)_\infty} = \frac{M^2}{DR} \quad (1.27)$$

$$VR = \frac{U_c}{U_\infty} = \frac{M}{DR} \quad (1.28)$$

The influence of momentum flux ratio on the dynamics of the jet is shown in Figure 1.5. The limits are vague due to several other factors impacting the behavior, hence, only a qualitative explanation is possible without being more specific elsewhere.

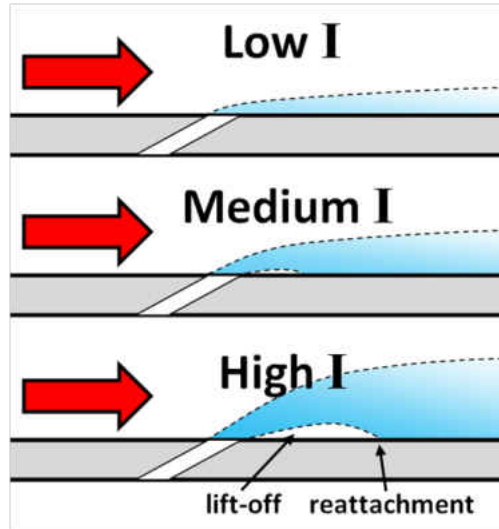


Figure 1.5: Effect of momentum flux ratio I .

These three momentum flux ratio regimes have been described previously, quoted from Goldstein [6]:

- *Mass addition regime* — Effectiveness increases with M due to increased thermal capacity of the coolant, but the effectiveness is independent of the density ratio and velocity ratio parameters.
- *Mixing regime* — Effectiveness distribution depends on M , DR due to opposing influence of increased thermal capacity and increased coolant/free-stream mixing and penetration.

- *Penetration Regime* — Effectiveness distribution is completely dominated by a complex interaction of excessive coolant penetration and augmented turbulent diffusivity and turbulent diffusion of the coolants' thermal effect toward the surface.

Other important flow parameters include;

Velocity Ratio VR – The velocity ratio dictates the amount of shearing at the leading edge of the hole where the jet meets the primary flow. The shear layer generates turbulence and dictates the amount of TKE production. A rearrangement of M , DR and I , VR is a more common parameter in fluid mechanics studies of a jet-in-crossflow in which the two streams are typically the same temperature. Once two of these four parameters are specified, the remaining two are fixed.

Reynolds Number Based on Hole Diameter and Freestream Velocity, $Re_{d,\infty}$ – A Reynolds number which is similar to a cylinder in crossflow. Simply a convenient definition which gives some insight into the significance of the film jet interacting with the mainflow.

Momentum Thickness to Hole Diameter Ratio δ_2/d – A measure of the relative thickness of the incoming boundary layer. Typically a low value of this parameter, < 0.2 is representative of engine conditions.

1.1.4.3 Dependent Parameters of Film Cooling

The main parameter of interest is the net heat flux reduction, $\Delta q''$. The reduction in heat flux is affected by each parameter described above as well as some parameters not mentioned, e.g.,

$$\Delta q'' = f(x, z, d, L, \alpha, \beta, P_x, P_z, M, I, Re_{d,\infty}, \delta_2/d,$$

Surface Roughness, Hole Geometry, Surface Curvature,

Freestream Turbulence, Pressure Gradient, ...) (1.29)

1.1.5 Slot Cooling

The most fundamental approach to film cooling is that of a film introduced through a 2-D slot.

1.1.5.1 Goldstein, Shavit and Chen (1965)

Goldstein et al. [1] study the coolant film generated by a strip of porous material embedded in a wall. The group experimentally investigates the effects of varying coolant temperature, blowing ratio and freestream velocity. The temperature and velocity boundary layers due to the presence of film are measured and indicate that normal injection through a porous strip is akin to tangential injection through a slot. This is also confirmed in the similarity between downstream effectiveness and the authors further go on to show that for the same the mass injection per unit width of the strip (Ms), the two geometries provide the same coverage.

The adiabatic film-cooling effectiveness downstream of the injection point can be correlated against (X/Ms), very similar to other film cooling correlations. It was also shown that existing correlations for slot cooling can be readily applied to strip transpiration scenarios.

1.1.5.2 Hartnett, Birkebak and Eckert (1961)

Hartnett et al. [8] fully characterize the external aerodynamics and heat transfer downstream of a tangential slot for one slot geometry and one blowing ratio. While this study does not address trends that designers would be interested in, it does lay the groundwork for a comprehensive understanding of the given film scenario. It is noted that for some cases of slot injection there is no heat transfer augmentation due to the presence of film; however, this is not the case for all films.

1.1.6 Discrete Film Cooling

In practice a film cannot readily be introduced through a slot due to the significant impact on part strength resulting from removing material. Hence, successful designs incorporate discrete holes through which the coolant is introduced to the boundary layer.

1.1.6.1 Pedersen et al. (1977)

Pedersen et al. [9] experimentally investigate the effects of density ratio in film cooling. The injection sources investigated are a porous strip and and inclines holes with $\alpha = 35^\circ$ and $P/D = 3$. Several different secondary gases are used (such as CO_2 and He) to yield density ratios ranging from 0.75-4.17.

Measurements are taken by the gas sampling technique which involves drawing a small amount of gas from the near-wall region into a gas analyzer which measures concentration. From the results presented it can be seen that the density ratio augments the momentum flux ratio for a given blowing ratio, thereby influencing the dynamics of the jet

1.1.6.2 Sinha et al. (1991)

Sinha et al. [10] study an inclined row of holes ($\alpha = 25^\circ$, $P/D = 3$, $L/D = 1.75$) to investigate the effect of density ratio in film cooling. Cryogenically cooled air allows the density ratio to vary from 1.2-2.0. The test surface is constructed out of expanded polystyrene foam with a thermal conductivity of 0.027 W/m-K. These ribbon thermocouples are used to obtain temperatures which results in negligible thermocouple conduction error. It is concluded that film cooling performance cannot be predicted with either M or I alone. There are distinct ranges over which each parameter is of leading importance.

1.1.6.3 Aga (2009)

Particle image velocimetry data was provided for a single row of film cooling holes spaced four diameters apart with α and β being 20° and 45° respectively by Aga [11]. Blowing ratio, density ratio and, therefore, momentum flux ratios were varied. The results show a skewed vortex structure of the film jet as compared to the CVP found in its $\beta = 0^\circ$ counterpart. Important to notice is that no liftoff off the coolant jet is seen even at the highest blowing ratio ($M = 3.0, I = 9.0$). The jet entrains the boundary layer on the upstream side, while thinning it on the downstream side, leading to higher heat transfer coefficients which then decrease the overall effectiveness of the coolant. Other subtle variations in the jet are seen with changing density ratio and momentum flux ratio.

1.1.6.4 Goldstein, Eckert, Eriksen and Ramsey (1969)

In a fundamental study on discrete hole film cooling by Goldstein et al. [12] the film cooling effectiveness downstream of single holes and rows of holes is obtained experimentally. The main focus is to study the effect of inclination and compound angles for single holes and rows of holes. The authors take the temperature data from a single hole and tried to superpose the temperature distribution to replicate that which one would expect from a row of holes. This approach is most applicable to a row in which the adjacent holes do not interact with one another.

For low blowing ratio cases this method is very good for centerline values however in the area between holes this superposition approach tends to over-predict. This is most likely due to the interaction of the jets enhancing mixing and thereby lowering cooling effectiveness. However, the authors do manage to show that by superposing data from a single hole, one can get an idea of the effectiveness they would expect from a row of similar holes.

1.1.6.5 Baldauf et al. (2002)

Baldauf et al. [13] use IR thermography to investigate a single row of film cooling holes. The holes are inclined and spaced at differing values. The effect of density ratio, inclination angle, hole spacing, and mainstream turbulence are investigated. A comparison to values obtained in literature is made; the current study matches very well with the values in literature. A correlation is made using the current data and data available in open literature.

Two different flow patterns are seen in the laterally averaged downstream effectiveness. A single jet in crossflow mixing and adjacent jet interaction are recognized to affect downstream effectiveness with differing attenuations. Single jet mixing has a greater effect at short downstream distances at lower blowing ratios. Additionally single jet in crossflow mixing can govern whether the jet lifts off. At higher blowing ratios and further downstream, jet spreading allows for adjacent jet interaction to occur. The included correlation predicts downstream film cooling effectiveness in the presence of film cooling from a single, inclined row of holes.

1.1.6.6 Baldauf et al. (2002)

A companion paper to Baldauf et al. [13], Baldauf et al. [14] detail a correlation for heat transfer augmentation. This correlation is applicable to the entire downstream surface and various ejection parameters. This correlation can be combined with the effectiveness correlation presented in the companion paper to analyze wall temperatures.

A net heat flux reduction model is given which does not depend on an arbitrarily chosen wall surface temperature. The actual heat flux reduction is found by combining heat transfer coefficients and adiabatic wall effectiveness values from the same flow conditions. Moderate blowing ratios and ejection angle show the best potential cooling. An optimal velocity ratio is found to be approximately 0.5 for the moderate hole spacing. Very high blowing rates are studied and shown to be useful only in certain circumstances, where a steep blowing angle and wide pitch are required.

1.1.6.7 Natsui, Claretti, Wolski, Ricklick and Kapat (2012)

Natsui et al. [15] assessed the performance of a film cooling source, composed of a segment of permeable wall installed near a row of cylindrical film holes. Coolant is introduced through both the permeable wall and the film holes resulting in a downstream film composed of both transpired and discretely injected coolant. The aerodynamic performance and cooling downstream of this coupled source are studied analytically, experimentally and numerically.

The sensitivity of transpiration blowing ratio, discrete hole blowing ratio, discrete hole pitch, transpiration slot width, and the relative positioning of the two sources on these global parameters of interest is the end result. The analytical results are used to get a basic understanding of the issue and design the test matrix for the numerical study. A range of design parameters are studied numerically in a Box-Behnken test matrix to yield global results which are then combined into one parameter, β . A second order response surface of the parameter β allows for a more complete understanding of the coupled source. This numerical analysis is compared with experimental results from two different coupled sources in order to assess the predictions.

The results indicate that coupling of the two sources allows a more efficient use of coolant by generating a more uniform initial film. One coupled case in particular shows a 170% increase in cooling over the baseline cylindrical row, a 22% reduction in aerodynamic losses over the baseline transpiration source, all with a 51% reduction in mass flow as compared with the same cylindrical row baseline.

1.2 Full-Coverage Film Cooling

Multi-row film cooling causes a buildup of film in the boundary layer; characterized by increasing values of adiabatic effectiveness and a heat transfer augmentation factor which levels off. This interaction of successive rows of film cooling has been studied less extensively than single row film cooling but there are many notable works. This can be seen schematically in Figure 1.6.

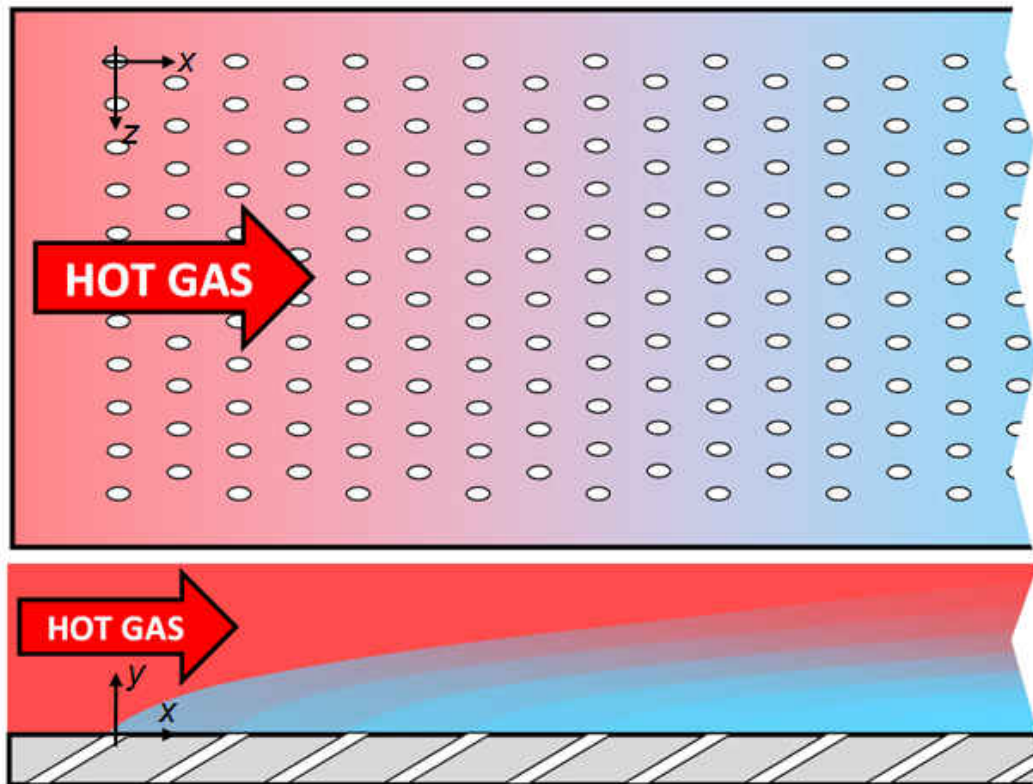


Figure 1.6: Diagram of full-coverage film cooling.

There is an extensive amount of literature on film cooling, yet there is a much less complete look at the field of full-coverage film cooling. Generally full-coverage film cooling is characterized by increasing values of effectiveness and a heat transfer augmentation factor which levels off in the streamwise direction. Adiabatic film cooling effectiveness has been measured for many configurations [16][17][18][19][20][21]. The heat transfer augmentation due to the presence of film has been measured for many different arrays [22][23][24][25][26]. Some researchers measured both effectiveness and heat transfer augmentation [27][28][29][30]. Even overall cooling effectiveness has been measured [31][32]. Less common are flowfield measurements but some studies have been done on that as well [33][34][19][35]. There have even been some analytical developments for multi-row film predictions [36][37].

1.2.1 Literature

One of the earliest studies on multi-row film cooling was by Papell [16]. He experimentally studied film effectiveness throughout four rows of normal holes and compared them with slots of various inclination angles.

Sellers [36] developed a model to predict the performance throughout multiple rows with only the knowledge of a single row. This is called the additive film method. The concept is simple but this method persists even 50 years later.

Table 1.1: Full-coverage film cooling literature

Year	Data	Rows	α	β	P_z/d	P_x/d	Citation
1960	η	4	90°	-	?		Papell [16]
1973	η, h	10	90°	-	4.8	4.8	Metzger [27]
1975	η, h	15	30°	45°	8, 10, 14	6.9, 8.7, 12.1	Mayle [28]
1976	η, h	4	90°	-	4.8	4.8	Metzger [38]
1979	h	?	90°	-	8	8	Le Grives [22]
1979	η	?	45°	0°	3	5, 10	Sasaki [17]
1980	Flow	11	30°	0°	5	5	Yavuzkurt [33]
1980	Modeling	11	30°	0°	5	5	Yavuzkurt [34]
1980	h	6, 11	90°, 30°	0°, 45°	5	5, 10	Crawford [24]
1980	Modeling	6, 11	90°, 30°	0°, 45°	5	5, 10	Crawford [25]
1981	η, h	?	30°	0°	5, 10	5, 10	Kasagi [18]
1995	η, h	7	90°	-	3	3	Cho [39]
1995	η , Flow	7	17°	0°	4.48	7.46	Martiny [19]
2001	η	10	90°	-	7.14	7.14	Harrington [20]
2002	η, h	12, 18	20°	0°	10, 16	10, 16	Ling [29]
2003	h	10	90°	-	7.14	7.14	Kelly [26]
2009	Flow	9	30°	0°	?		Michel [35]
2011	η, h	5, 15	90°, 30°	0°	3.6 - 14	4 - 12.1	Miller [40]
2012	η	23, 30	30°, 45°	45°	14.5, 19.8	14.5, 19.8	Natsui [41]
2012	h	23, 30	30°, 45°	45°	14.5, 19.8	14.5, 19.8	Claretti [42]
2014	η, η_{ov}	14 - 22	90°, 30°	0°	4.7 - 7.4	5.8 - 9.5	Andreini [32]
2015	η, h	22	45°	45°	23	23	Hodges [43]

Angled cylindrical holes in a multi-row array were first studied by Mayle and Camarata [28]. They measured the effect of spacing and blowing rate on film effectiveness and heat transfer throughout 15 rows of holes spaced up to $X/D = 14$. Interaction and coalescence of individual jets was observed to have a detrimental impact on downstream film effectiveness.

An IR camera was used by Sasaki et al. [17] to quantify effectiveness due to inclined holes of very tight spacing. They tested both single and multiple rows in order to assess the Sellers superposition model [36].

Yavuzkurt et al. [33] [34] studied the three-dimensional flow field, with a 3-wire constant temperature anemometer, throughout a full-coverage array and used this information to predict the recovery region hydrodynamics.

Crawford et al. [24] quantified Stanton number augmentation for three different hole orientations for up to 11 rows of injection.

Kasagi et al. [18] studied the cooling effectiveness throughout a film cooling array of inclined, staggered injection holes, $X/D = 5$ and 10. An increase in blowing ratio is seen to decrease effectiveness in both spacings tested, seemingly due to coolant jets penetrating into the mainflow.

Overall and adiabatic cooling effectiveness of a full-coverage effusion plate with 15 rows of inclined holes was measured by Andrews et al. [31]. This was mainly to assess the impact of inclination angle on multi-row film cooling in an effort to cool a large surface area with as little coolant flow as possible.

Martiny, Schulz and Wittig [19] measured adiabatic wall temperatures with IR photography with thermocouples for a 7 row array of cylindrical holes inclined at 17° . Martiny et al. were also among the first to present flow visualization for full-coverage film cooling with Schlieren photography.

Harrington et al. studied [20] effectiveness of 10 rows of short normal holes, $X/D = 7.14$. Two different turbulence intensities were investigated, 0.5% and 18%. It was found that at the high turbulence intensity, laterally averaged effectiveness dropped by 12%.

Ling et al. [29] studied 20° holes pitch of 16d (12 rows) and 10d (18 rows). They measured adiabatic film cooling effectiveness and heat transfer with TLC and tTLC.

Kelly et al. [26] study the heat transfer of the same experimental setup as Harrington [20] where two turbulence intensities were tested; differences in heat transfer augmentation between the two cases were not significant.

Mhetras et al. [21] used PSP to study multiple rows of Nitrogen film cooling on an airfoil PS and SS surfaces in a linear cascade.

Michel et al. [35] used LIF and LDV to study the flowfield throughout 9 rows of compound angle holes located on the concave section of a circular pipe.

Heat transfer augmentation and film effectiveness were obtained for a multi row geometry in the presence of a favorable pressure gradient by Ligrani et al. [30]. This was a thermal test which measured a featured Perspex wall ($k = 0.14W/m - K$) with an IR camera.

A new method for calculating the additive effects of successive rows was proposed by Kirollos and Povey [37]. They showed with CFD that in cases where Sellers method under-predicts effectiveness this new energy-based method can be advantageous.

Andreini et al. [32] used PSP to measure film cooling effectiveness throughout 7 different multi-row film cooled surfaces. They also measured overall effectiveness with thermocouples and stainless steel test articles. They also study the effect of density ratio and turbulence levels. They noted that increased turbulence can improve film cooling performance if the jets are in the penetration regime.

They concluded that inclined holes at low blowing provide a higher adiabatic effectiveness; however, normal holes at higher blowing provide better overall cooling effectiveness. This is mainly attributed to increased heat transfer as the coolant passes through the film holes.

1.2.1.1 Sellers (1963)

Sellers [36] originates a superposition method that is used in many future works. Described is a method of linearly superimposing cooling features in order to predict effectiveness downstream of a single set of features. The goal is to predict how additional rows of film holes add to the effectiveness obtained experimentally from a single row. Data is presented from outside sources with an added correlation that fits well.

1.2.1.2 Metzger et al. (1973)

Metzger et al. [27] present effectiveness and heat transfer data for a full-coverage film cooling array with $P/D = X/D = 4.8$. The holes are normal, $\alpha = 90^\circ$, with inline and staggered arrays. A calorimeter spanning multiple rows is used to measure heat transfer coefficients. Effectiveness values are calculated using the measured heat transfer coefficients, resulting in a 25% uncertainty. A method of single row superposition from Goldstein [12] is used to compare results.

This superposition method does not take into account jet interaction from downstream rows. Downstream contribution of each row is terminated at either 10 or 20 diameters, with 10 better fitting experimental data. Periodically fully developed film is established by the fourth row for the staggered array and the second row for the inline array. Blowing ratios have to be assumed from the given velocity ratios by using a density ratio of one; the resulting blowing ratios are 0.1 and 0.2. Measured heat transfer coefficients are 20 – 25% higher than no coolant conditions. The resulting staggered array results show greater effectiveness values than the inline arrays as a result of reduced jet interaction.

1.2.1.3 Mayle and Camarata (1975)

Mayle and Camarata [28] investigate the effect of hole pitch-to-diameter ratio and blowing ratio by determining adiabatic effectiveness and heat transfer augmentation. The arrays studied are composed of holes inclined at $\alpha = 30^\circ$ and compounded at $\beta = 45^\circ$. The focus of the study is to provide more information on the influence of hole and row spacing on film cooling array performance. Tests are run at a film-cooling Reynolds number of $Re_{D,\infty} = 3600$. Measurements are taken in a span-averaged manner. Heat transfer testing is conducted at steady state with instrumented copper blocks. The adiabatic film-cooling effectiveness measurements are taken on the adiabatic wall with a radiometer and traversing system. Discrete measurements are taken and averaged for each row of holes. The reported uncertainty in heat transfer coefficient is 8%.

A superposition technique is adopted from a previous report by Goldstein et al. [12] which uses effectiveness data following a single row to predict the downstream development of an array of film holes. The superposition technique is based off a point sink model, superimposed to predict the effect of more than a single jet/row. It is consistently noted, both by Mayle and Camarata [28] as well as Goldstein et al. [12], that this technique's main drawback is in areas where there is a large amount of interaction between coolant jets.

Mayle concludes that the integrity of each individual jet can be seen in the adiabatic film-cooling effectiveness. This is universally agreed upon in the current understanding of film literature. The interaction and coalescence of individual jets is found to have a detrimental impact upon downstream film-cooling effectiveness. Average heat transfer augmentations up to $h/h_0 = 2.5$ are measured, showing that heat transfer augmentation must be considered while designing a film-cooling array.

1.2.1.4 Metzger et al. (1976)

Metzger et al. [38] use the same experimental setup used from the previous paper, Metzger et al. [27], to extend the blowing ratio range tested, $M = 0.1, 0.2, 0.3$ and 0.5 . Superposition of single hole, normal injection data provides a reasonable fit for blowing ratios of 0.1 and 0.2 while greatly over-predicting at the higher blowing ratios. The results show that for this four row array, the optimal blowing ratio is between 0.2 and 0.3 .

1.2.1.5 Crawford, Kays, and Moffat (1976, 1980)

Crawford et al. [24][25][23] experimentally obtains Stanton numbers for several full-coverage arrays composed of various hole orientations and spacings. Heat transfer experiments are run with $\alpha = 90^\circ/\beta = 0^\circ$, $\alpha = 30^\circ/\beta = 0^\circ$, and $\alpha = 30^\circ/\beta = 45^\circ$. Zero degree inclination angle produces the greatest heat transfer augmentation. Increasing the number of rows increases the downstream recovery region affected area. A compound angled, inclined hole at a mass flux ratio of 0.4 to 0.5 provides the lowest heat transfer augmentation. The highest increase in heat transfer augmentation is seen by normal injection of coolant. An increase in heat transfer augmentation for all geometries is seen at mass flux ratios greater than 0.4. Increasing the number of downstream rows keeps an elevated heat transfer coefficient while increasing the area being protected.

1.2.1.6 Sasaki et al. (1979)

Sasaki et al. [17] uses an IR camera to study compound angle holes, $\beta = 45^\circ$, with a small lateral spacing, $P/D = 3$, and compares to a point source model. A superposition method proposed first by Sellers [36] is used to compare to the experimental data. Superposition predicts the low blowing ratio cases well for all seven streamwise rows ($X/D = 5$). Single row testing compares favorably with the point source model. The superposition method becomes less accurate at blowing rates greater than 0.15. The number of accurate row predictions decreases from 7 to 3 as the blowing ratio increases, especially for the cases with larger spaces between rows. Row spacing and blowing ratio affect the superposition method's accuracy in an inverse manner, i.e., increasing row spacing and blowing ratio equate a lower accuracy superposition prediction.

1.2.1.7 Kasagi et al. (1981)

Heat transfer data on two inclined, staggered, full-coverage arrays of $P/D = 5$ and 10 with $X/D = P/D$ is presented by Kasagi et al. [18]. An analysis of the heat transfer mechanisms inside of the adiabatic wall is conducted by utilizing a low thermal conductivity acrylic plate and a high thermal conductivity brass plate. Blowing ratio is varied such that the large spacing plate has the same amount of total mass injected as the smaller spacing plate; the values being $M = 0.3$ to 0.7 for the small spacing and $M = 1.1$ to 2.6 for the large spacing. The mainstream is varied between $U_\infty = 10$ and $20m/s$. Local temperature measurements are made possible with cholestelic liquid crystal and verified by thermocouple. The brass plate eliminates any spanwise variation in surface temperature. The head loss as a function of Reynolds number is given, the large spacing has a 10 times larger head loss than the small spacing at the same total secondary flow rate. The larger spacing does, however, have a lower magnitude head loss coefficient. For both the small and large spacing geometries, the effectiveness decreases as blowing ratio is increased, with a greater effect for the large spacing. The large spacing shows strips of very low effectiveness in between the coolant hole exits. It is conjectured that the coolant jet penetrates completely into the mainstream. The brass plate shows considerably higher effectiveness values than the acrylic plate without the noticeable peaks from the coolant holes.

1.2.1.8 Harrington et al. (2001)

Harrington et al. [20] investigate $L/D = 1$ holes, staggered at $P/D = X/D = 7.14$ in a full-coverage array. The novelty of this experiment is utilizing small and large turbulence intensities, $TI = 0.5\%$ and 18% respectively, with a large density ratio of 1.7. A method of reducing error from not having a true adiabatic surface by correcting by using a one-dimensional conduction correction is tested and implemented. The two cases are also simulated computationally using the *RNG* $k - \varepsilon$ model. At these experimental conditions, the intermediate blowing ratio of $M = 0.65$ performs essentially the same as the high blowing $M = 1.0$ case at low turbulence intensities. The high turbulence laterally averaged effectiveness drops by 12% compared to the low turbulence test at the blowing ratio of $M = 0.65$, the lowest difference between the three blowing ratios tested. Comparisons are made with Seller's superposition method [36] and a linear superposition using *CFD*. The superposition method either over-predicts or under-predicts based on the blowing ratio and streamwise location. The low blowing, low turbulence case shows a fully developed film by the fourth row of holes; the superposition prediction over-predicts after the fully developed section after the fourth row.

1.2.1.9 Kelly and Bogard (2003)

Kelly and Bogard [26] experimentally determine heat transfer augmentation in a full-coverage array for a heated and unheated starting length with varying levels of turbulence intensity. Heat transfer augmentation is affected by turbulence levels; however, this is due to the large increase in turbulence only affecting the uncooled heat transfer coefficient, leaving the heat transfer conductance in the presence of film cooling the unaffected. Net heat flux reduction is calculated using experimentally obtained heat transfer coefficients and adiabatic effectiveness values. No significant difference is seen between the low and high turbulence intensity cases. Single row data is taken to evaluate the predictability of the full-coverage array through the superposition method. Simple superposition fails to accurately predict cooling for the full-coverage arrays. A method using the heat transfer coefficient from the measured row is developed which agrees well with the experimental data.

1.2.1.10 Natsui (2012)

Natsui [44] [41] [42] experimentally investigated four large spacing multi row film cooling arrays composed of compound angle ($\beta = 45^\circ$) cylindrical holes. Both heat transfer augmentation and adiabatic film cooling effectiveness measurements were made. Results for adiabatic effectiveness were very consistent with single row findings. Multi row arrays go through the same operating regimes as single row sources with the exception that in the penetration regime, benefits from penetrating upstream rows can be seen several rows downstream. The effect of hole-to-hole spacing, P_z/d and P_x/d , is to dictate the amount of coolant injected. No effect on physics is seen, i.e. no interaction apparent over the range of hole-to-hole spacings tested (14.5 – 19.8). The inclination angle has local effects in the immediate behavior of coolant-mainstream interaction; however, no significant impact on magnitude of laterally averaged profile is seen.

All heat transfer enhancement factors are seen to level off within 5-6 row and seems to be mostly insensitive to blowing ratio and inclination angle. Hole-to-hole and row-to-row spacings are inversely proportional to h/h_0 .

Numerical predictions of a $\beta = 0$ array were done. The local coolant behavior for all blowing rates and the two models investigated (*RKE*, *SSTKW*) is not properly predicted. For the geometry and flow conditions studied, Realizable $k-\epsilon$ compares with experimental laterally averaged effectiveness results better than SST $k-\omega$.

1.3 Motivation and Objectives of the Present Study

High fidelity measurements are necessary to validate existing and future models for the purpose of producing the next generation of more efficient gas turbines, [45]. The objective of the present study is to conduct several different measurements of multi-row film cooling arrays to provide insight into the physics involved with injection of coolant through multiple rows of discrete holes into a flat plate turbulent boundary layer. Several different measurement techniques are applied to this problem.

- PSP measurements of adiabatic film cooling effectiveness
- Gas sampling measurements of adiabatic film cooling effectiveness
- Hot wire measurements of time resolved streamwise velocity
- Particle image velocimetry measurements of wall normal and streamwise velocity
- Particle density images for flow visualization

High accuracy measurements of adiabatic effectiveness are needed to discern between potential designs. Due to the complex fluid mechanics involved with film cooling, understanding the physical mechanisms causing the trends seen on the surface is non-trivial. The velocity and flow visualization measurements help explain the adiabatic effectiveness distributions seen on the surface.

1.3.1 Novelty

There are several novel aspects to this research which are listed below.

- Length scale calculations throughout multi-row array
- PIV measurements throughout multi-row array
- PIV measurements corresponding to PSP measurements for multi-row array
- 20° inclination angle film cooling holes
- Quantification of PSP error sources in detail
- Back to back PSP and gas sampling measurements for film cooling
- Multi-row shaped film cooling array
- Testing of SLA geometries with procedures for successful tests
- Auto-illumination error quantification method

There are very few hydrodynamic measurements taken in multi-row film cooling arrays. Only two are known to the author and they are taken with hot wire and LDV, [33][46]. Length scale calculations have not been reported throughout a multi-row cooling array. Shaped hole multi-row film arrays are not heavily studied in literature. Also, very shallow injection film holes are uncommon in literature, the present study tests a 20° hole geometry.

1.4 Outline

Chapter 2 describes the test hardware and the wind tunnel used in the experiments. First, the test hardware is described in detail; both design intent and as manufactured dimensions are reported in §2.1. Next, the experimental apparatus and tunnel conditions are described in §2.2.

Chapter 3 describes the time resolved velocity measurements taken of the multi-row film cooling geometries with the hot wire anemometry technique. The benefit of hot wire measurements is the very high temporal resolution, up to 300 kHz in this study. First the fundamentals of thermal anemometry are review in §3.1 and §3.2. Then, some relevant aspects of turbulence and turbulent boundary layers are described in §3.3. The specifics of the processing and testing methodologies used are then described in §3.4 and §3.5. Finally, hot wire measurements, including mean velocity, RMS velocity, integral length scale, boundary layer development and wall shear stress, are presented in §3.6.

Chapter 4 describes describes the spatially resolved velocity measurements taken of the multi-row film cooling geometries with particle image velocimetry (PIV). The strength of PIV is its ability to measure two components, streamwise and wall-normal in this case, of velocity over an entire plane. Previously reported measurements from literature of the hydrodynamics of film cooling are presented in §4.1. Then, the PIV technique is described in §4.2. The experimental setup used in this experiment is detailed in §4.3. Testing methodology for the PIV experiments is described in §4.4. Next, the processing algorithm implemented in this experiment is described in §4.5. The correlation statistics method of uncertainty quantification is described in §???. Finally the test results are presented in §4.6.

Chapter 5 describes the measurements of adiabatic film cooling effectiveness, η . These measurements can be broadly divided into PSP experimental methodology and uncertainty and multi-row testing results. First the heat and mass transfer analogy is reviewed, with historical examples of its use for measuring heat transfer scenarios by analogous mass transfer experiments, §5.1. Then an introduction of the PSP technique is presented in §5.2. The PSP measurement system and some methodologies are described in §5.3. PSP calibration hardware and methodology are described in §5.4. The calibration hardware and coupon preparation procedure are described in §5.4.1. The calibration procedure is given in §5.4.2. The processing procedure for PSP results is documented in §5.5.

Several aspects related to PSP uncertainty are discussed in §5.6. The sensitivity coefficients for the PSP data reduction equations are determined in §5.6.1. CCD parameters and their impact on uncertainty are discussed in §5.6.2. Convergence of the intensity sample means is shown in §5.6.3. Temporal degradation of the PSP emission and thermal effects influencing PSP emission are discussed in §5.6.4 and §5.6.5 respectively. Single row film cooling results are presented in §5.7. Aspects related to uncertainty quantification which incorporate the system values which required experimental data are discussed in §5.8. Next, multi-row results are presented in §5.9. Results for adiabatic film cooling effectiveness measurements are shown in §5.9.1. Local distributions of experimental uncertainty estimates for Geometry 1 are shown in §5.9.2. Next, laterally averaged effectiveness results are presented in §5.9.3.

Some interesting experimental aspects encountered in the multi-row PSP measurements are presented next. Aspects of testing on SLA surfaces which are transmissive are discussed in §5.9.4. Then the topic of auto-illumination due to the increased emission intensity of the multi-row arrays is discussed in §5.9.5. Gas sampling measurements and their comparison with the PSP results are then presented in §5.9.6. Finally superposition predictions of multi-row performance using the single row results from §5.7 are presented in §5.9.7.

Chapter 6 presents the conclusions from the series of measurements conducted on the multi-row film arrays.

CHAPTER 2 EXPERIMENTAL SETUP

This chapter describes the physical aspects of the experiment. First, the test hardware is described in detail; both design intent and as manufactured dimensions are reported in §2.1. Next, the experimental apparatus and tunnel conditions are described in §2.2.

2.1 Test Geometries

Two different hole types at two different spacings yield four unique geometries investigated in the current work. Geometries 1 and 2 are composed of round holes machined into Aluminum. Geometries 5 and 6 are fan shaped diffuser holes printed via stereolithography (SLA). Odd numbered geometries have a nominal P_x/d and P_z/d of 7.5. The even numbered geometries have nominal P_x/d and P_z/d of 14 and 10 respectively. In addition to these four geometries geometry 1 was also printed from SLA and is referenced as Geometry 1b. Geometry 1 and 1b are nominally identical differing only by machining methodology. The machining process did result in different measured values. All plates are of thickness (nominally) $3.84d$ with an inclination angle of 20° . Values for the five geometries described are tabulated in Table 2.1.

Table 2.1: Test matrix with nominal parameters

#	Hole	Hole Diameter	Angle	Total Length	Lat. Pitch	Axial Pitch	Material
		d (mils)	α ($^\circ$)	$(L + L')/d$	P_z/d	P_x/d	
1	Cyl	150	20	11.2	7.5	7.5	Al
2	Cyl	150	20	11.2	14	10	Al
5	Diff	150	20	11.2	7.5	7.5	SLA
6	Diff	150	20	11.2	14	10	SLA
1b	Cyl	150	20	11.2	7.5	7.5	SLA

Geometries were measured with a General UltraTech Stainless Steel caliper and Meyer Z+ Gage Pin gauges which have a $+0.0001''$ accuracy (NIST test #: 821/276543-08 on 4/20/2010). Multiple measurements were taken of streamwise pitch, lateral pitch and plate thickness. Each hole was measured with pin gauge. The raw results are documented in Appendix B. A table which summarizes all non-dimensional spacings as well as the 95% confidence interval for these values is in Table 2.2. The 95% confidence intervals were calculated based off a propagation of error analysis using the standard deviations from the measurements and measured values as the inputs.

The geometries will be referred to by their numbers and nominal parameters, e.g. Geometry 1 and $7.5d \times 7.5d$ spacing; however, the true values are the actual measured parameters from Table 2.2.

Table 2.2: Test matrix with actual measured parameters

#	Hole	Hole Diameter	Angle	Total Length	Lat Pitch	Axial Pitch	Material
		d (mils)	α ($^\circ$)	$(L + L')/d$	P_z/d	P_x/d	
1	Cyl	144.2 ± 1.6	20	11.7 ± 0.2	7.8 ± 0.1	7.8 ± 0.1	Al
2	Cyl	146.1 ± 1.6	20	11.5 ± 0.2	14.3 ± 0.2	10.3 ± 0.2	Al
5	Diff	144.4 ± 2.7	20	11.8 ± 0.2	8.0 ± 0.3	7.8 ± 0.2	SLA
6	Diff	144.7 ± 2.0	20	11.9 ± 0.2	14.6 ± 0.2	10.4 ± 0.2	SLA
1b	Cyl	141.2 ± 1.4	20	12.1 ± 0.2	8.1 ± 0.1	8.0 ± 0.1	SLA

Figure 2.1 shows the parameter space of many other multi-row studies compared with the parameters of the present study. The non-dimensional spacings are within the space studied previously by other researchers; however, there is very little work that has been done to study holes inclined at 20° . Even single row studies have mostly neglected holes inclined at 20° . Furthermore, none of these other studies have investigated multi-row arrays composed of shaped film cooling holes. The current study is geometrically novel in that it studies multi-row arrays composed of shallow angle holes as well as shaped holes.

2.1.1 Shaped Film Cooling Geometry

The parameters describing the diffuser holes are shown in Table 2.3. The hole is modeled after one found in literature (the fan shaped hole studied by Gritsch et al. [2]) but modified to match the plate thickness and inclination angle of the cylindrical geometry. The original hole is shown in Figure 2.2 and the modified version studied in this work is shown in Figure 2.3.

- Natsui 2015
- Metzger et al.
- Cho and Goldstein
- Le Grives et al.
- Andrews et al.
- ◆ Natsui 2012
- Mayle and Camarata
- Kasagi et al.
- ✕ Sasaki et al.
- Ling et al.
- Harrington, Kelly, Bogard
- Zhong and Brown
- ✕ Crawford, Kays, Moffat
- ✕ Martiny et al.

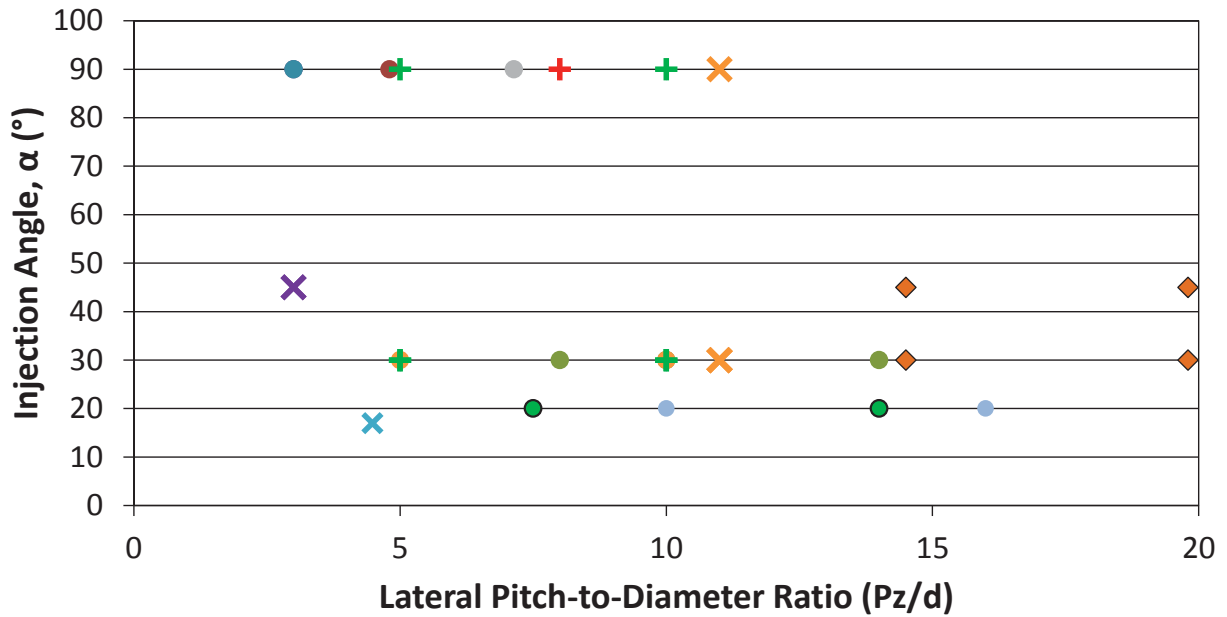
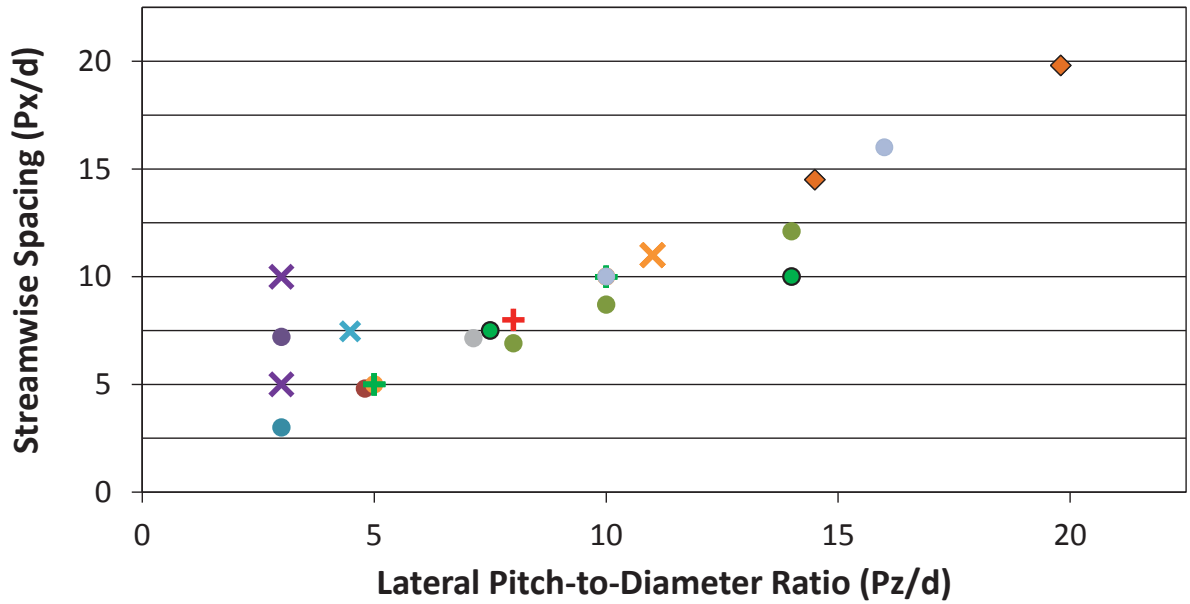


Figure 2.1: Parameter space for multi-row film; literature and present study

Table 2.3: Diffuser hole parameters

Description	Symbol	Gritsch et al.	Present Study
Inclination angle ($^{\circ}$)	α	30	20
Metering hole diameter (mils)	d	400	150
Total length	L_T/d	6	11.2
Metering hole length	L_m/d	2	7.2
Plunge depth	L_p/d	4	4
Lateral expansion angles ($^{\circ}$)	ϕ_1 and ϕ_2	14	14
Layback angle ($^{\circ}$)	ϕ_3	0	0
Area ratio	AR	3	2.66
Coverage	t/d	2.95	3.2
Plate thickness	$thick/d$	3	3.84
Filet radius	r_f/d	-	1
Junction radius	r_i/d	0	0

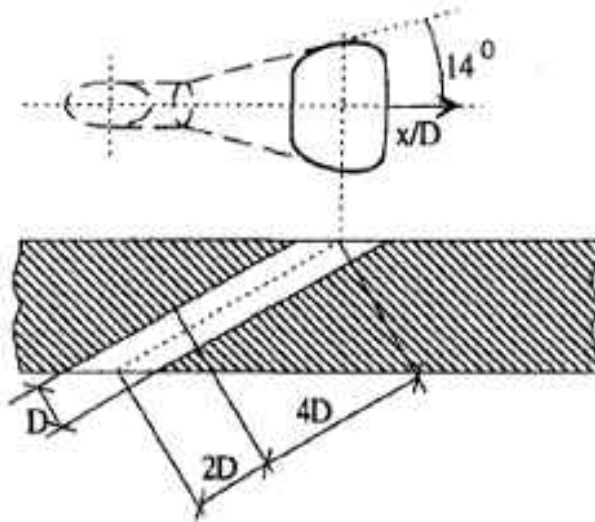


Figure 2.2: Diffuser shaped hole studied by Gritsch et al. [2]

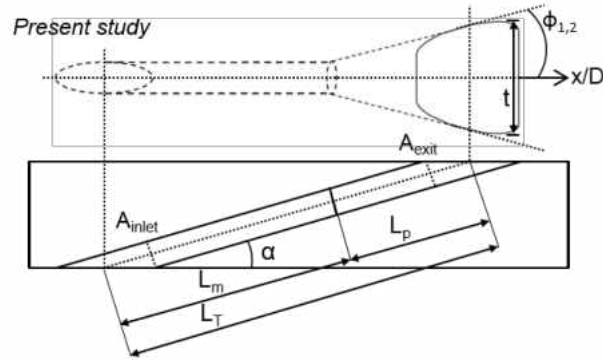


Figure 2.3: New diffuser modeled after the fan shaped hole studied by Gritsch et al.

2.2 Wind Tunnel

The wind tunnel is an external flow wind tunnel with a boundary layer bleed upstream of the test coupon. Isometric and cross-sectional views of the wind tunnel are shown in Figures 2.4 and 2.5. The tunnel was designed by targeting certain non-dimensional film cooling parameters. The critical dimensions were determined by a Matlab code shown in Appendix A. Mainflow is forced with a 3000 l/s, 15 kW blower. There are several screens and honeycombs to condition the flow, which are followed by a 2-D acrylic contraction, contracting the flow only in the direction of the channel height. Air from the boundary layer bleed is then removed by a 2.2 kW suction fan. The suction flowrate is not monitored; however it is maintained consistent and the static pressure in the suction section is recorded as a CFD boundary condition. The film cooling test coupon and the bottom wall are made out of aluminum (the same material as the calibration coupons). All other walls are made out of acrylic, for optical access. The leading edge of the boundary layer bleed is 3 mm thick.

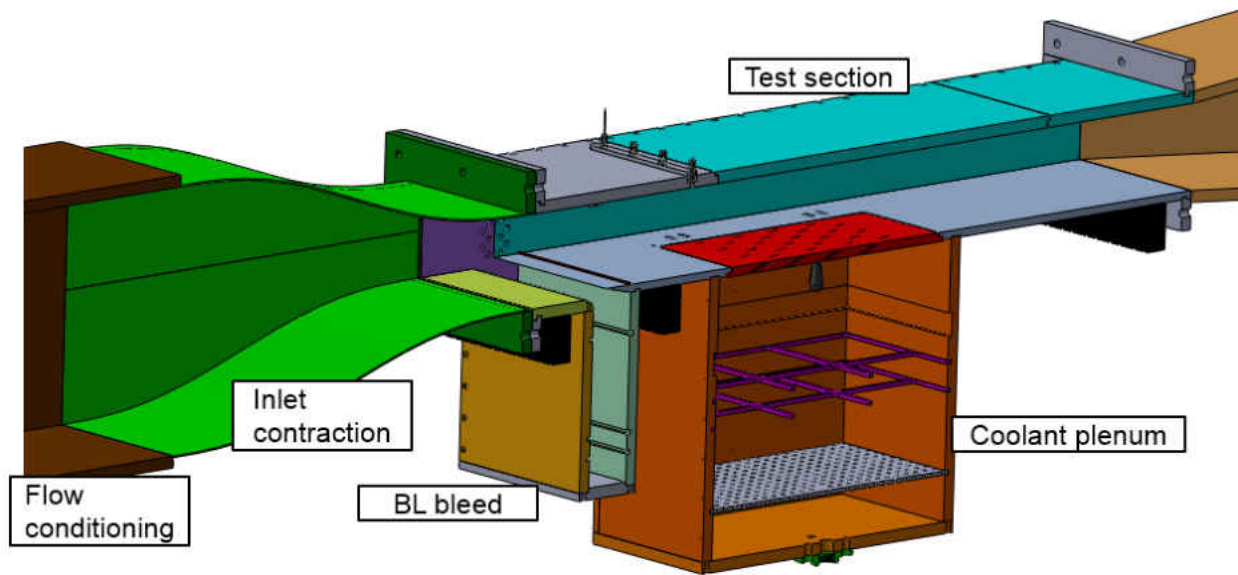


Figure 2.4: Isometric view of wind tunnel showing main components

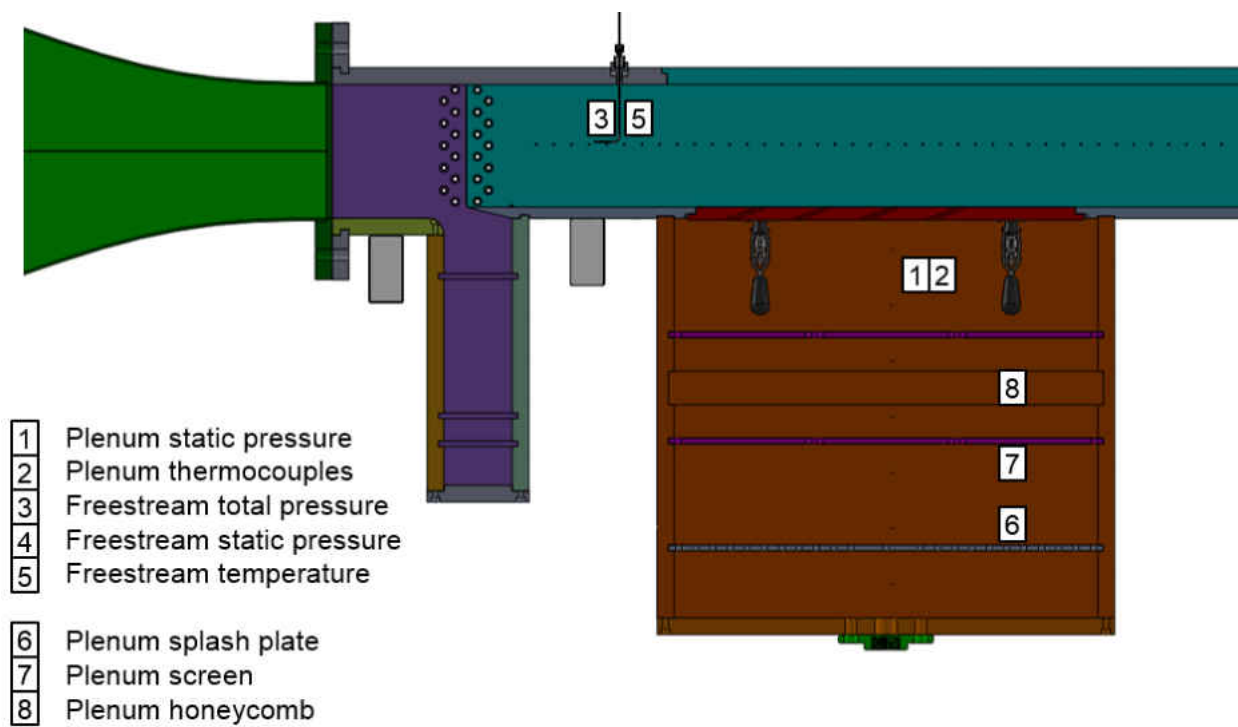


Figure 2.5: Cross-sectional view of wind tunnel showing coolant flow conditioning and measurement locations for pressure and temperature

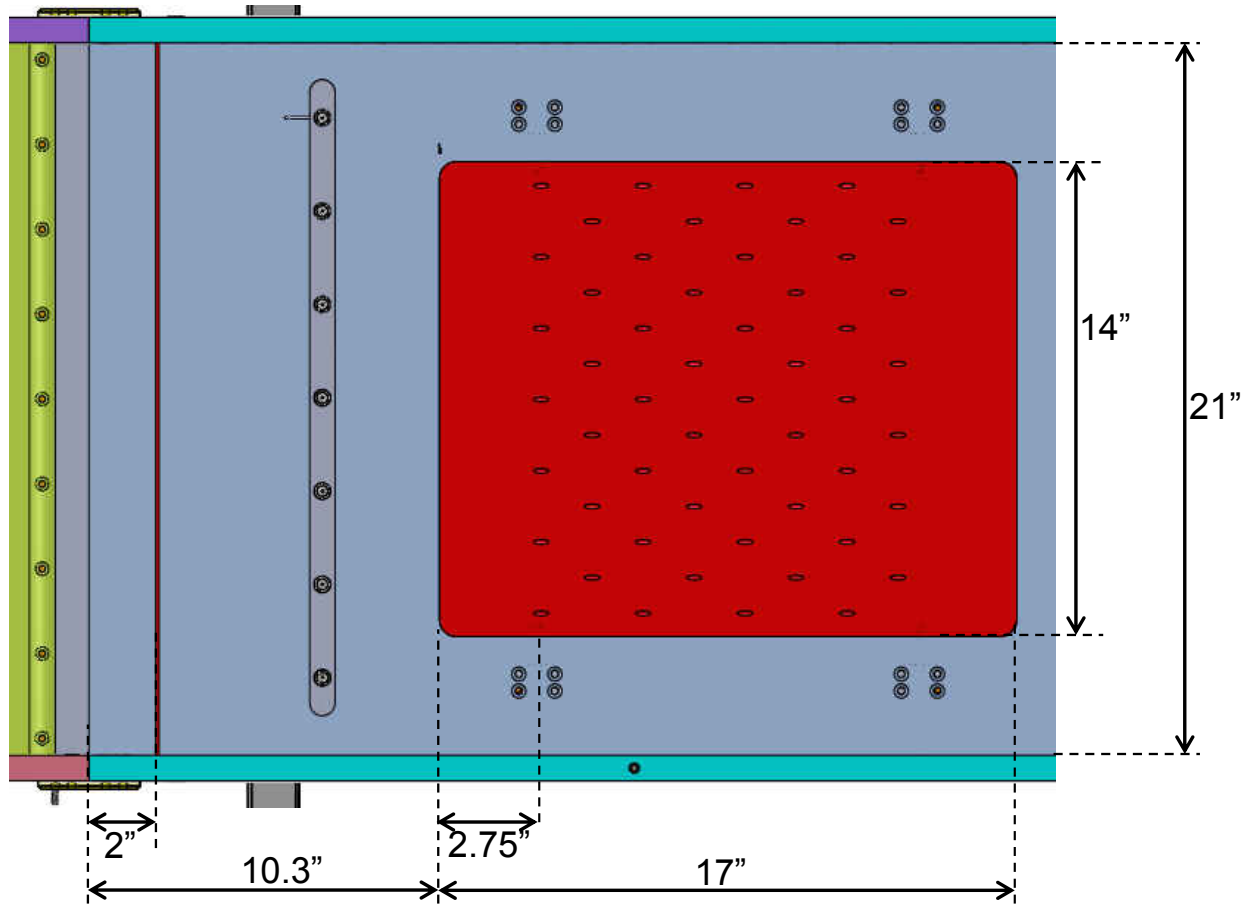


Figure 2.6: Physical test section dimensions

The tunnel is fitted with three pitot probes downstream of the boundary layer extraction, and used to measure the mainstream total pressure. Four thermocouples located at the same streamwise location as the pitot probes are used to measure the mainstream temperature. Static pressure is measured from multiple static pressure ports along the side wall. Typical pressures inside of the wind tunnel are shown in Figure 2.7. Three thermocouples are located in the plenum to measure the coolant temperature just before it reaches the film holes. A thermocouple is placed just downstream of the venturi to measure the temperature of the coolant as it passes through the venturi. T-type thermocouples were used in this experiment. Pressure data is recorded using a mechanically multiplexed Scanivalve®. Temperatures are recorded with two NI-USB 9211 thermocouple data acquisition systems. Data acquisition is automated, and recorded using an in-house code made in LabVIEW software. Pressure and temperature data is recorded for every set of images required to obtain an effectiveness measurement.

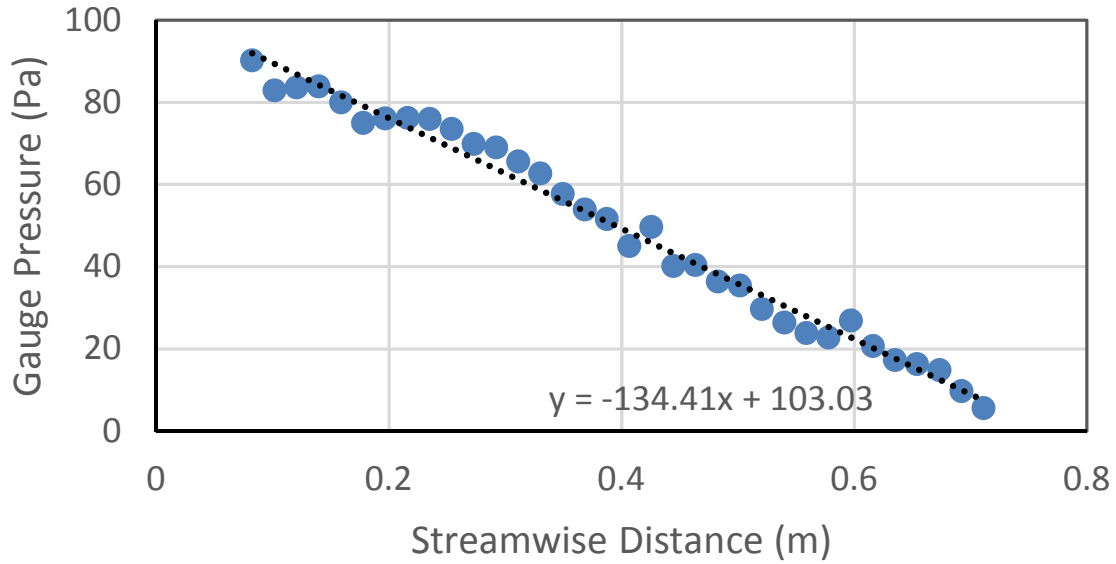


Figure 2.7: Streamwise pressure gradient in wind tunnel primary flow

2.2.1 Pressure Gradient at the Test Section

The test is nominally a zero pressure gradient experiment. However, due to boundary layer growth and a constant cross-sectional area of the test section there is a slight favorable streamwise pressure gradient which results in some acceleration of the mainstream through the tunnel. To quantify this a non-dimensional acceleration parameter, K , is used, defined by Equation 2.1. This can be calculated from the wall pressure taps and the pitot probes at the inlet (assuming no loss of total pressure in the core flow). The results of this calculation are shown in Figure 2.8.

$$K = \frac{\nu}{U_\infty^2} \frac{dU_\infty}{dx} \quad (2.1)$$

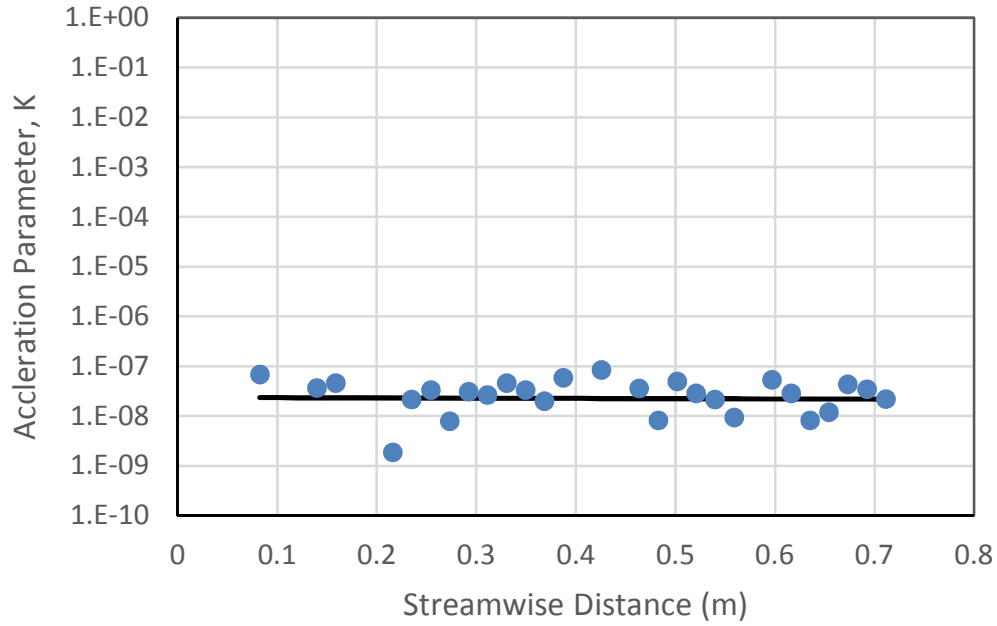


Figure 2.8: $K(x)$, acceleration parameter throughout the test section

A K value of 2.16×10^{-8} is measured throughout the test section. The gauge pressure plot comes from data taken from static pressure taps located every 0.75 in along the streamwise position of the channel. Three total pressure measurements are taken at an upstream location and averaged. Freestream velocity is calculated as it develops in the streamwise direction. A first order finite difference is applied to obtain the velocity gradient (very noisy right now) and thus the acceleration parameter. The acceleration parameter is shown in a log-linear plot in Figure 2.8.

2.2.2 Inlet Boundary Layer

The distance from this leading edge to the first row of holes is $67.5d$. The turbulent boundary layer was characterized with a hotwire anemometry at two locations. Location 'L-1' is far upstream of the film cooling array ($x/d = -50.3$) in order to provide a boundary layer profile which a CFD simulation might use as an inlet boundary condition. Location 'L0' is location $1d$ upstream of the leading edge breakout for row 1 ($x/d = -2.2d$) to provide the boundary layer which the first row will see and to assess a CFD prediction of boundary layer growth from an inlet plane to the film cooling array. Both of these measured profiles are plotted in inner-scaled coordinates in Figure 2.9. The parameters describing the boundary layer are summarized in Table 3. These measurements are described in detail in Chapter 4.

Table 2.4: Measured boundary layer parameters

Streamwise Location	x/d	-	100
Hole Diameter	d	mils	150
Freestream Velocity	U	m/s	39.3
99% Boundary Layer Thickness	δ_{99}	mils	334
Displacement Thickness	δ_1	mils	40
Momentum Thickness	δ_2	mils	29
Shape Factor	$H = \delta_1/\delta_2$	-	1.37
Reynolds Number on δ_2	$Re_{\delta_2} = U\delta_2/\nu$	-	1.8k
Reynolds Number on d	$Re_d = Ud/\nu$	-	9.4k
99% Boundary Layer Thickness to Hole Diameter Ratio	δ_{99}/d	-	2.2
Displacement Thickness to Hole Diameter Ratio	δ_1/d	-	0.27
Momentum Thickness to Hole Diameter Ratio	δ_2/d	-	0.19

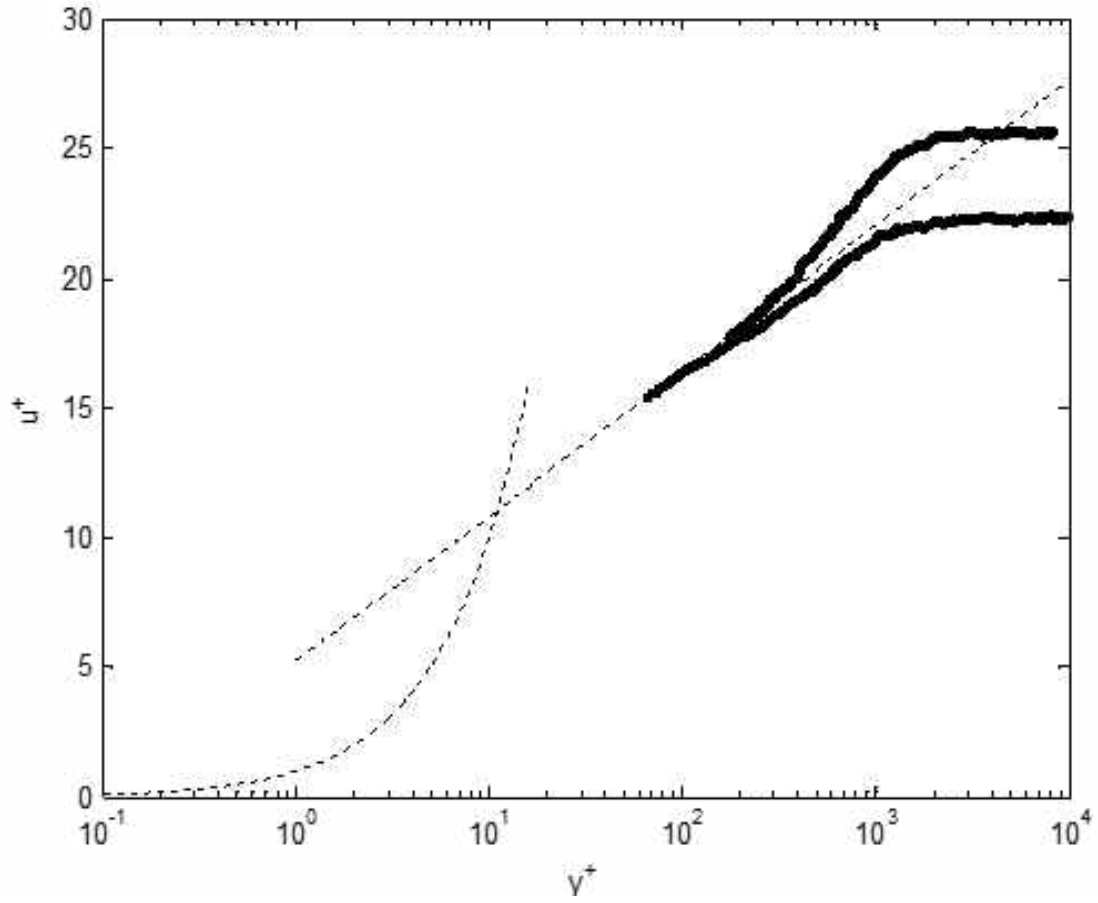


Figure 2.9: Inner scaled boundary layer upstream of film cooling array

Table 2.5: Parameters describing equation to recover boundary layer

Friction Velocity	U_τ	m/s	1.71
Outer-Inner Length Scale Ratio	$\delta^+ = \delta_{99} U_\tau / \nu$	-	915
Cole's Wake Strength	Π	-	0.37
Constant in van Driest's Damping Function	A^+	-	26
von Karman's Constant	κ	-	0.41

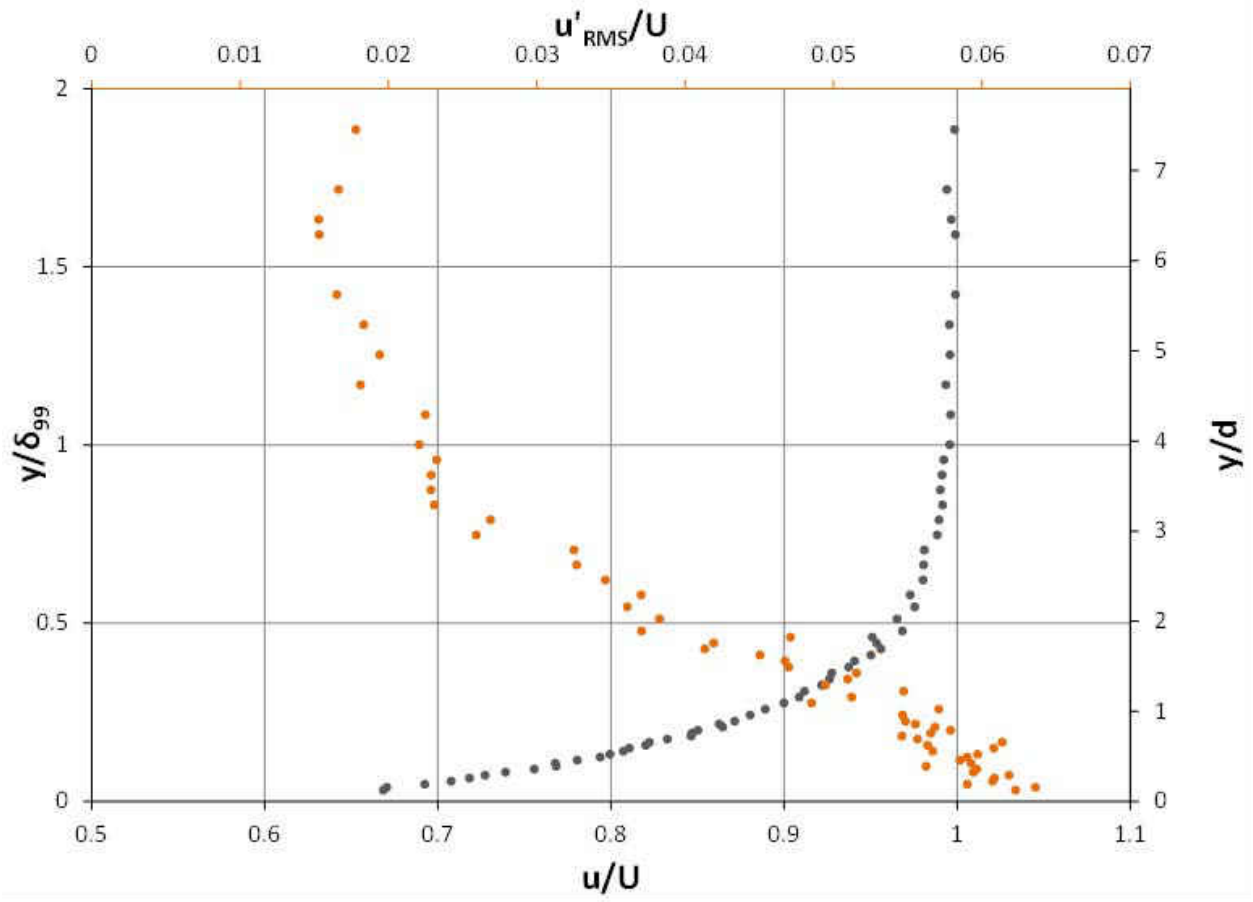


Figure 2.10: Outer scaled boundary layer upstream of film cooling array

Table 2.6: Hot wire details

Wire Diameter	d_{hw}	μm	3.8
Wire Length (Sensing Area)	l	mm	1.27
Wire Length to Diameter Ratio	l/d_{hw}	-	334
Inner Scale	ν/u_τ	μm	9.75
Viscous-Scaled Wire Diameter	d^+	-	0.39
Viscous-Scaled Wire Length	l^+	-	130
Sampling Frequency	f_s	kHz	300
Low Pass Frequency Cutoff	f_{lp}	kHz	150
Time Between Samples	Δt	μs	3.3
Viscous-Scaled Sample Time	Δt^+	-	0.61

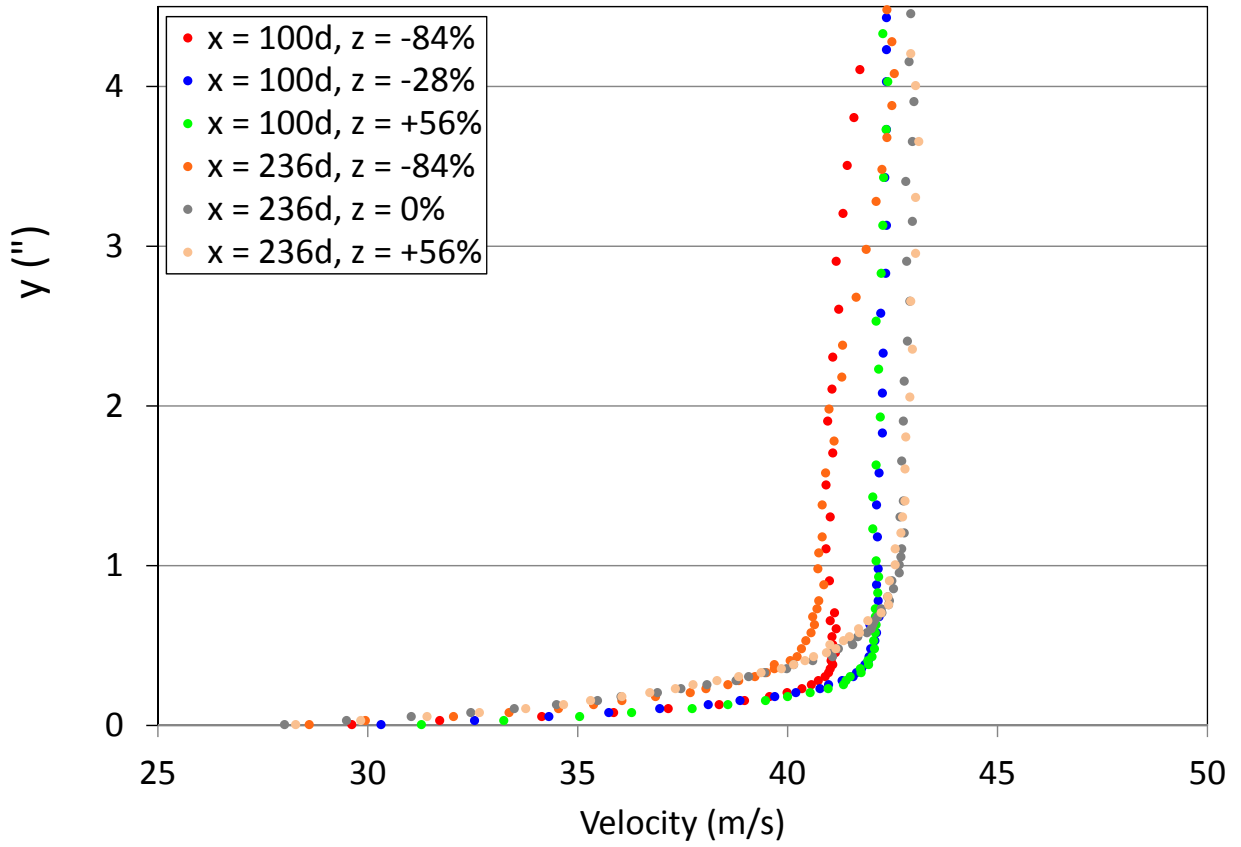


Figure 2.11: Lateral uniformity and streamwise development of boundary layer within test section

2.2.3 Coolant Supply

Carbon dioxide, CO₂, is supplied as a cryogenic liquid. A MicroBulk CO₂ tank (3500 lb capacity) supplies liquid CO₂ to a 30kW electric vaporizer which turns the liquid into a gas at flow rates up to 130 SCFM. The gas then passes through an ambient vaporizer which increases the temperature as close to the mainstream temperature as possible (70-90°F). Typical ΔT between mainstream and coolant is 0 – 3°C (the coolant is never hotter than the mainflow). Typically this ΔT is larger for low blowing ratios than for high blowing ratios due to the Reynolds number effect in the upstream heat exchangers.

The coolant flows through a venturi flow meter, in order to measure the flow rate of the coolant. The differential pressure across the venturi, static pressure at the throat and temperature are recorded. The coolant then flows into an acrylic plenum, which contains a splash plate and a series of screens to condition the coolant before it reaches the film cooling holes.



Figure 2.12: CO₂ microbulk tank with electric and ambient vaporizers

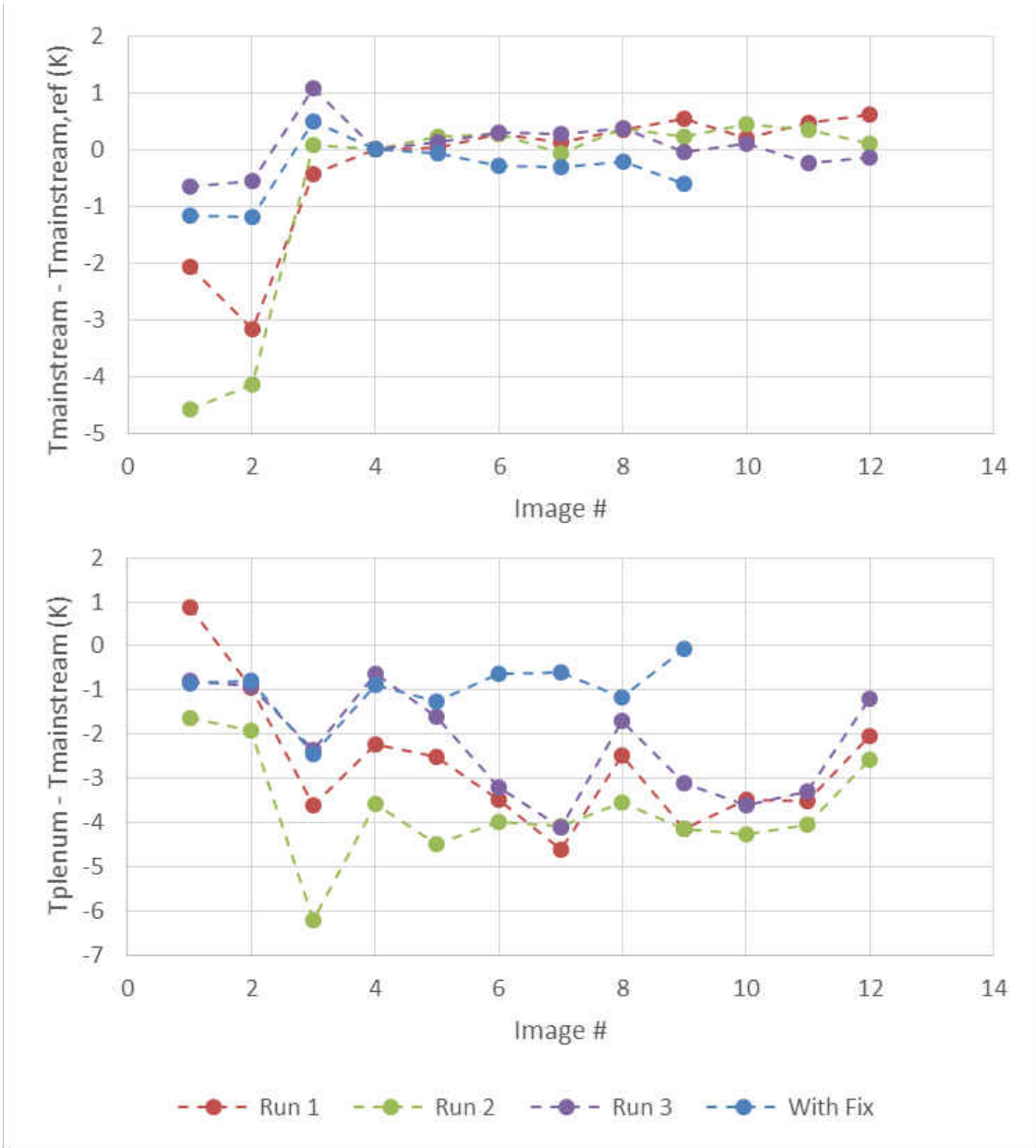


Figure 2.13: Efficacy of the ambient vaporizer for reducing temperature different between mainstream and coolant flows

CHAPTER 3

TIME RESOLVED FLOWFIELD

This chapter describes the time resolved velocity measurements taken of the multi-row film cooling geometries with the hot wire anemometry technique (constant temperature anemometry, constant resistance anemometry). The benefit of hot wire measurements is the very high temporal resolution, up to 300 kHz in this study. First the fundamentals of thermal anemometry are review in §3.1 and §3.2. Then, some relevant aspects of turbulence and turbulent boundary layers are described in §3.3. The specifics of the processing and testing methodologies used are then described in §3.4 and §3.5. Finally, hot wire measurements, including mean velocity, RMS velocity, integral lengthscale, boundary layer development and wall shear stress, are presented in §3.6.

3.1 Thermal Anemometry Background

Thermal anemometry devices are based off the principle of heat removal through convection of a heated rod. A current is passed through fine sensor ($2 - 20\mu m$) which then dissipates energy in the form of Joule heating throughout the element. This heat is removed by convection imposed by the measured flow field. The amount of heat removed is a function of the velocity and temperature of the flow. To obtain velocity data, the heat input to the probe is monitored and used to deduce desired quantities of the flow. The most commonly imposed condition across the probe is to maintain the wire at a constant temperature which would make the probe a constant temperature anemometer (CTA). The sensitivity of this configuration is least sensitive to temperature variations and is most commonly used to measure velocity. If a constant current is maintained across the probe the measurement device is called a constant current anemometer (CCA). Due to the larger dependence on temperature and lower dependence upon velocity, this mode of operation is commonly used to measure temperature fluctuations.

3.1.1 Heat Transfer to a Heated Wire

For an infinite cylinder in a cross flow, the steady state solution of an energy balance can be shown to be expressed by Equation 3.1

$$i^2 R = hA(T_w - T_\infty) \quad (3.1)$$

Substituting Nusselt number for heat transfer coefficient,

$$i^2 R = \frac{ANuk_f}{d}(T_w - T_\infty) \quad (3.2)$$

Introducing a correlation for Nusselt number for a cylinder in a crossflow [47],

$$Nu = A_1 + B_1\left(\frac{d}{\nu}\right)^2 U^n \quad (3.3)$$

Substituting into the energy balance,

$$i^2 R = \frac{Ak_f(T_w - T_\infty)}{d}\left(A_1 + B_1\left(\frac{d}{\nu}\right)^2 U^n\right) \quad (3.4)$$

The previous analysis is general to any probe, for a CTA, the temperature difference driving heat transfer can be reasonably considered constant, multiplying both sides by the electrical resistance of the wire, and substituting voltage across the wire into the equation it

can be simplified to,

$$E^2 = \alpha + \beta U^n \quad (3.5)$$

in which

$$\alpha = \frac{Ak_f(T_w - T_\infty)A_1R}{d} \quad (3.6)$$

$$\beta = \frac{Ak_f(T_w - T_\infty)B_1R(d/\nu)^n}{d} \quad (3.7)$$

α and β are constants made up from a combination of probe parameters and properties of the flow, n is a constant coming from an empirical relation for heat transfer from a cylinder. This form of energy balance on a heated wire, Equation 3.5, is known as King's Law and is the theoretical form to which CTA calibrations would be fit.

In real application, not all parameters are known exactly, the coefficients of the heat transfer correlation for example. This along with deviations from this ideal heat transfer model dictates the coefficients α , β and n to be determined through an experimental calibration of the probe.

One factor which causes this model to deviate from reality is the fact that the wire is actually not infinite. The prongs which support the sensing element cause the ends of the wire to act as fins, encouraging heat transfer and causing the heat transfer of the wire to be two dimensional. This added heat transfer causes the ends of the wire to drop in temperature which reduces the accuracy of the measurement. This factor is hard to avoid and is dealt with by making the wire length to diameter ratio very large, minimizing this effect to a very small fraction of the probe length.

3.1.2 Wheatstone Bridge

The heart of the electronics enabling CTA's to maintain their constant sensor temperature is known as a Wheatstone bridge. Wheatstone bridge circuits are used to measure an unknown resistance by maintaining zero current passing through the bridge.

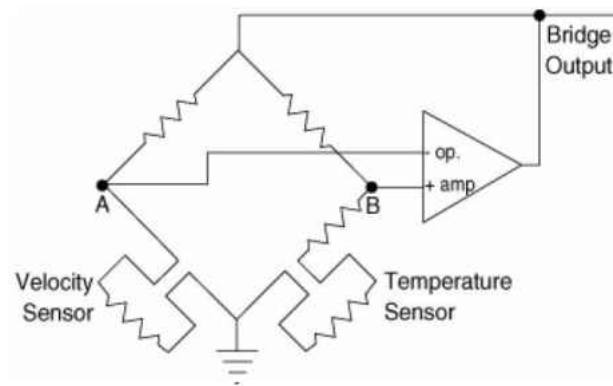


Figure 3.1: Bridge circuit

The temperature sensor allows for a measurement of the flow temperature and provides the required information for the sensor to stay at a constant overheat ratio. The overheat ratio is the ratio of a reference resistance to the probe hot resistance. Due to the temperature dependence of resistance, this holds the anemometer to a constant temperature. Modern anemometers have become much more complex with additional circuits for signal conditioning, response modifications and filtering.

3.2 Measurements with a Single Wire

The output signal from an anemometer system is in the form of a voltage. Hence there is a need to relate the desired measurable quantity (velocity) with the voltage output from the system. This is accomplished by means of a calibration curve which relates the effective velocity which the wire is exposed to with the output voltage of the system. The calibration can take the form of King's Law, or more conveniently a polynomial curve fit of the form,

$$V_E = K_3E^3 + K_2E^2 + K_1E + K_0 \quad (3.8)$$

in which K_{0-3} are curve fitting constants. The polynomial form provides accurate results and is sufficient when measuring a single velocity component.

3.2.1 Probe, Stem, Flow Coordinate Systems

There are many coordinate systems applicable to measurements by thermal anemometry. The probe coordinate system is described by the normal, binormal and tangential directions. The probe based coordinate system shown in Figure 3.2 applies to any arrangement of hot-wire probes including multi probe anemometry analysis.

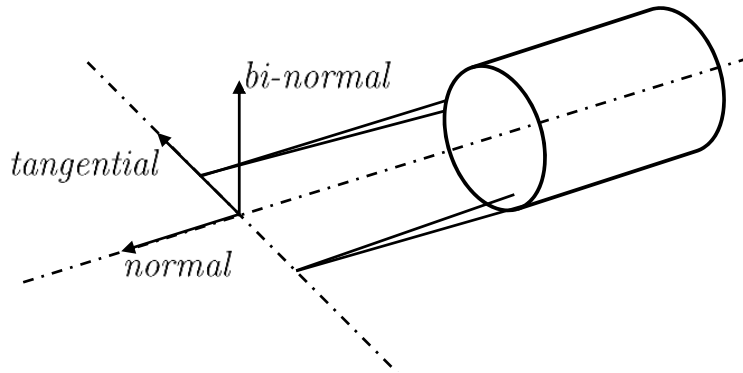


Figure 3.2: Probe coordinate system

To relate the probe coordinate system to the stem coordinate system, a 3-D rotation is likely to be necessary. Another rotation may be needed to relate the stem coordinate system to the flow coordinates. These last rotations are trivial in comparison to the determination of equivalent velocities; however, must be considered when analyzing results.

3.2.2 Velocity Analysis

Voltages are measured and velocity is calculated through a correlation such as Equation 3.5 or Equation 3.8 and an effective velocity is calculated for each sensor. For a given wire the relation, suggested by Jörgensen which is now known as Jörgensen's Equation, between effective velocity to the wire coordinate system velocity components is given by Equation 3.9.

$$U_E^2 = U_N^2 + k^2 U_T^2 + h^2 U_B^2 \quad (3.9)$$

In single wire measurements, the wire is assumed to be aligned such that the main flow direction is aligned with the U velocity vector ($v \approx w \approx 0$). A first order series expansion of Equation 3.9 gives rise to,

$$U_E = U_N = u = \langle u \rangle + u' \quad (3.10)$$

which is valid for low turbulence flows. In flows of higher turbulence levels errors will be incurred by neglecting higher order terms. For higher turbulence level flows, assuming the same sensor orientation with the flow and realizing $k^2 \ll h^2$ (the heat transfer tangential to the wire is less than that bi-normal to the wire for a given velocity), it follows that Equation 3.9 takes the form of

$$V_E = \langle u \rangle \left[1 + \frac{h^2}{2} \frac{\langle w'^2 \rangle}{\langle u'^2 \rangle} \right] \quad (3.11)$$

This equation does not allow calculation of the desired velocity without conducting multiple experiments due to the unknown bi-normal fluctuating component; hence, single wire probes are not well suited for measurements in high turbulence flows.

3.3 Turbulent Boundary Layers

Some aspects of turbulence and turbulent boundary layers are relevant for the measurements taken and will be reviewed. Let us assume a stationary flowfield, i.e. the only time dependence is due to turbulent fluctuations. A Reynolds decomposition can be applied to the Navier-Stokes equations. This would decompose any quantity, say streamwise velocity u , which would vary with time due to turbulent fluctuations, into a mean ($\langle u \rangle$) which is independent of time and fluctuating component (u') which is time dependent, according to Equation 3.12.

$$u(\mathbf{x}, t) = \langle u(\mathbf{x}) \rangle + u'(\mathbf{x}, t) \quad (3.12)$$

where the operator $\langle \cdot \rangle$ represents an ensemble average given by Equation 3.13.

$$\langle \cdot \rangle \equiv \lim_{N \rightarrow \infty} \frac{1}{N} \sum_{n=1}^N (\cdot)_n \quad (3.13)$$

This process can be repeated for any fluctuating quantity. With these definitions applied to the momentum equation it becomes very messy; however, if a time averaging procedure is applied to the equations many terms drop out. There do remain some additional terms which act as additional stresses within the fluid. These are known as Reynolds stresses. There are 6 in total; however, this study only encounters the following 3 of them because no lateral velocities are measured.

$$R_{xy} = -\rho \langle u'v' \rangle \quad (3.14)$$

$$R_{xx} = -\rho \langle u'^2 \rangle \quad (3.15)$$

$$R_{yy} = -\rho \langle v'^2 \rangle \quad (3.16)$$

The introduction of these 6 Reynolds stresses (6 additional unknowns) is known as the turbulence closure problem [48].

A new variable turbulent kinetic energy, k , which represents the average kinetic energy of the fluctuations per unit mass can be defined.

$$k \equiv \frac{1}{2} \left[\langle u'^2 \rangle + \langle v'^2 \rangle + \langle w'^2 \rangle \right] \quad (3.17)$$

If all three components are not measured it is not possible to obtain an exact measurement of k and assumptions are often made to relate the energy of one fluctuating component to another.

Prandtl's boundary layer theory was important to the understanding of wall bounded flows. No matter the Reynolds number of a flow, if it is contacting a surface, there must be length scales appropriate to preserve the viscous term in the Navier-Stokes equations. Therefore, a characteristic feature of boundary layers is the presence of multiple scales. It is sufficient to name two in our study of the mean velocity profile: an outer length scale and an inner length scale. The outer scaling of a boundary layer is given by the boundary layer thickness, δ and the freestream velocity, U_∞ .

A Buckingham Pi analysis will yield the following velocity scale for the inner region of a boundary layer, given by Equation 3.18, known as the friction velocity u_τ .

$$u_\tau = \sqrt{\frac{\tau_{y=0}}{\rho}} \quad (3.18)$$

With this and the molecular diffusivity, ν , non-dimensional inner coordinates and velocities can be defined according to Equations 3.19 and 3.20.

$$y^+ = \frac{yu_\tau}{\nu} \quad (3.19)$$

$$u^+ = \frac{u}{u_\tau} \quad (3.20)$$

Order of magnitude analysis with this in mind results in the conclusion that in the near wall region of an infinite Reynolds number boundary layer the total shear stress within the fluid (molecular and turbulent) is a constant. Specifically, near the wall, Equation 3.21 is true.

$$u_\tau^2 = \nu \frac{\partial \langle u \rangle}{\partial y} - \langle u'v' \rangle \quad (3.21)$$

Several different descriptions of different regions of the boundary layer are plotted in Figure 3.3. These profiles are described in the following sections.

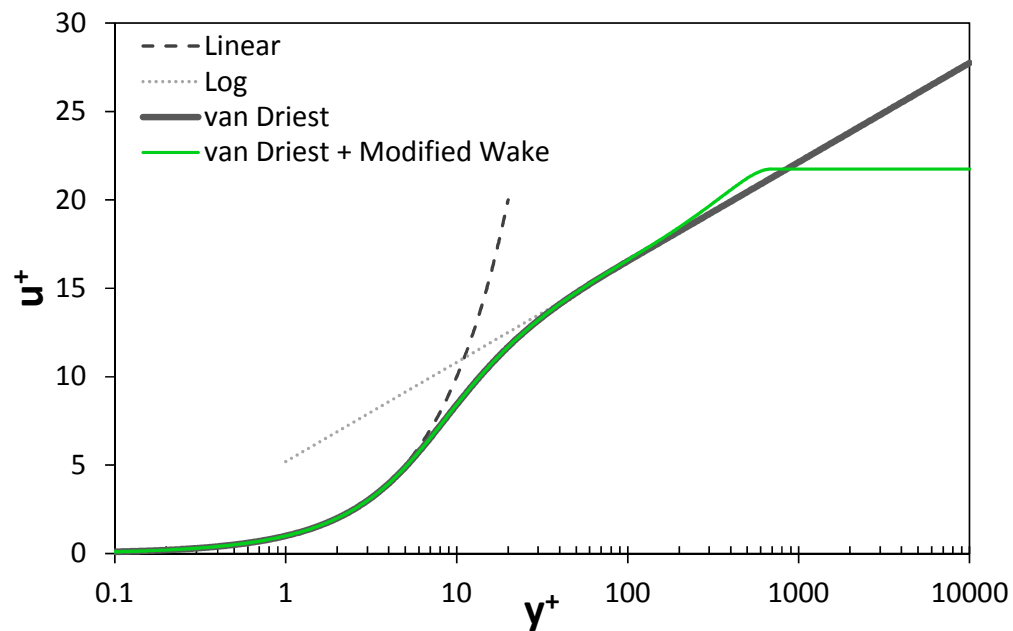


Figure 3.3: The different laws and functions describing a turbulent boundary layer

3.3.1 Linear Sublayer

In the limit that $y \rightarrow 0$ any turbulent fluctuations will be damped by the wall such that molecular stresses will dominate turbulent ones. In this case, very near the wall at locations corresponding to $y^+ < 3$, molecular viscosity dominates and Equation 3.21 can be integrated to yield a linear velocity profile given by Equation 3.22.

$$u^+ = y^+ \quad (3.22)$$

3.3.2 Logarithmic Layer

Farther away from the wall but still within the near wall region the effects of molecular viscosity will become negligible and turbulent stresses will dominate. A turbulent viscosity mixing length model applied to Equation 3.21 can result in a logarithmic profile. Don't forget, this corresponds to the limit that: $Re \rightarrow \infty$.

$$u^+ = \frac{1}{\kappa} \ln(y^+) + C \quad (3.23)$$

κ is von Karman's constant and is taken as 0.41 here

C is an additive constant taken as 5.2 here

There is recent debate as to whether these values are a constant, [48][45], but for the purposes of this study they will be assumed universal and constant and the log profile will be assumed to be correct and applicable.

3.3.3 van Driest Damping Function

Based on Stokes' solution for an oscillating plate in a flow a damping factor for the effect of a smooth wall in an oscillating fluid was deduced. This along with a mixing length assumption from Prandtl, a continuous description for a turbulent flow over a smooth wall was developed, [49].

The effect of the wall is to modify von Karman's constant from κ to $K[1 - \exp(-y/A)]$, a Stokes damping-type modification. After non-dimensionalization, solving for the wall normal velocity gradient and then integrating, a continuous expression for the velocity is obtained.

$$u^+ = \int_0^{y^+} \frac{2dy}{1 + \sqrt{1 + 4\kappa^2 y^2 [1 - \exp(-y/A^+)]^2}} \quad (3.24)$$

3.3.4 Cole's Wake Function

Noting that the outer boundary layer does not maintain the constant stress seen near the wall and that it must be dictated by the outer length scale, y/δ , Coles proposed a law of the wake, [50]. He proposed a universal wake profile which is given by Equation 3.25.

$$u^+ = f(y^+) + \frac{\Pi(x)}{\kappa} W\left(\frac{y}{\delta}\right) \quad (3.25)$$

where Π is a profile parameter which can be related to the wall shear stress and the function $w(y/\delta)$. Coles examines several experimental datasets and provides an empirical table for the wake function. Hinze found that a \sin^2 function provides good agreement with the data from Coles.

3.3.5 Modified Wake Function

An addition of a cubic term to the traditional Wake Law was proposed by Guo and Julien [51]. The addition of this term ensures the profile satisfies the axisymmetric condition for flow through a pipe, i.e. the velocity gradient is zero at the outer edge of the boundary layer. Even for non-pipe-flows this term can provide a better match with experimental results than a traditional sine squared wake profile.

$$W\left(\frac{y}{\delta}\right) = \frac{2\Pi}{\kappa} \sin^2\left(\frac{\pi y/\delta}{2}\right) - \frac{(y/\delta)^3}{3\kappa} \quad (3.26)$$

3.3.6 Clauser Fit

When conducting hot wire measurements it is difficult to determine the exact wall normal position of the probe to within the accuracy of $10\nu u_\tau$. Hence; it is desirable to have some verification or correction process to refine the wall normal position recorded during measurements. Also, when it is not possible to measure within $y^+ < 5$ or so, determination of wall shear stress is difficult. Both of these parameters can be obtained by comparing measurements near the wall with the logarithmic velocity profile given by Equation 3.23. To do this a sum squared difference, Equation 3.27, is calculated between near-wall measurements and the expected logarithmic profile. This is done for several different guesses of $\tau_{y=0}$ and $Y_{offset} = Y_{true} - Y_{estimated}$.

$$\varepsilon_{Clauser} = \sum \left[u_i^+(y_i^+) - u_{log}^+(y_i) \right]^2 \quad (3.27)$$

An example of the results from this calculation is given in Figure 3.4. The $(\tau_{y=0}, y_{offset})$ pair which minimizes the sum squared difference between measurements and the expected velocity profile is used to correct the wall normal position and inner scale the profiles in the following measurements. This process was automated in Matlab, the code is shown in Appendix D.

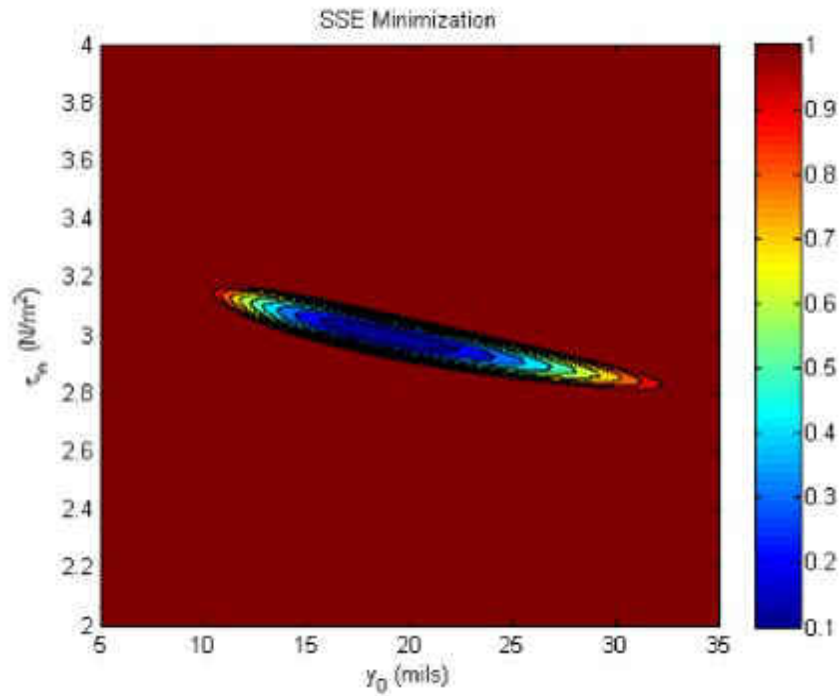


Figure 3.4: Clauser fit to obtain $\tau_{y=0}$ and y_{offset}

3.3.7 Length Scales

In this study the autocorrelation coefficient function of streamwise velocity is used to calculate integral time-scales which can be converted to length-scales. This process has to be carried out for each wall normal position (150) for each streamwise location (7-15) for all three cases; therefore, it was necessary to automate this process. An algorithm was developed to carry out this process automatically and is shown in Appendix E.

The basis of characterizing turbulence depends on G. I. Taylor's Frozen-Flow Turbulence hypothesis. This hypothesis states that the larger integral scales provide the majority of the advection energy compared to the turbulent circulation advection. This is only valid when the smaller integral scales have sufficiently less power than the larger scales [52]. The significance of this hypothesis is that it allows the spatial fluctuations of turbulent velocity from the temporal fluctuations at a single point. An extensive review of different methods of calculating a turbulent length scale was performed by Barrett [53]. Barrett concluded that the length scale created from a modification of the energy scale created by Ames [54] is the best suited for standardization of a length scale.

This length scale assumes isotropy of the convecting field as well as the convected field which allows for the use of a single hot wire anemometer. The dimensions of the hot wire were selected such that the wire length to wire diameter ratio was greater than the minimum accepted value of 150-200, which is required to keep the heat conduction losses to the wire prongs to a minimum [55]; however, if the wire length is smaller than the smallest eddies existing in the flow, unavoidable error exists in the measurement.

The integral time scale is obtained here with the integration of the autocorrelation function. An alternate definition based on the Fourier energy spectrum is performed in addition to the autocorrelation integration, in order compare results with a method that avoids the errors inherent to numerically integrating the autocorrelation function [56]. This requires the use of the energy spectrum at zero frequency. An approximation can be had by taking a well converged part of the Fourier spectrum and extrapolating it to the lower frequencies. These results though however for performed for internal validation, and will not be presented here. Also, internal analysis was performed by calculating the Taylor microscales for each test, to help validate the integral scales of the flow.

When comparing the different techniques for calculating length scale, the best results for length scale were obtained through using an integral of the autocorrelation function.

To calculate the integral length scale, the autocorrelation function was first generated. A part of generating the autocorrelation function, was to analyze the velocity time series at every individual particular point in space that velocity measurement were made. From this data, 1000 lags are taken for the autocorrelation function. This corresponds to the being statistically judged on its self-similarity for the samples taken up to the first 10 ms, or 2000 samples. This plot is truncated at the first zero crossing (the first positive, real root), where the truncation error is minimal after the autocorrelation function plateaus at zero. By multiplying the integral time scale by the locally averaged velocity, the length scale is calculated. This corresponds to the longest distance between two points in the flow field where there velocities are correlated.

Autocorrelation coefficient is given by

$$\rho(\tau) \equiv \frac{C(\tau)}{C(0)} = \frac{\langle u(t)u(t + \tau) \rangle}{\langle u'^2 \rangle} \quad (3.28)$$

$$T_{int} \equiv \int_0^{\infty} \rho(\tau) d\tau \quad (3.29)$$

Expanding the auto-correlation about the origin gives

$$\rho(\tau) = 1 + \frac{1}{2} \frac{d^2 \rho}{dt^2} \Big|_{\tau=0} \tau^2 + \dots \quad (3.30)$$

This is used to define a special time scale, λ_τ called the Taylor microscale

$$\lambda_\tau^2 \equiv -\frac{2}{\rho''(0)} \quad (3.31)$$

so

$$\rho(\tau) \approx 1 - \frac{\tau^2}{\lambda_\tau^2} \quad (3.32)$$

this approximation of the autocorrelation approaches zero in the same way the autocorrelation approaches zero. The Taylor microscale, λ_τ , is the positive intercept of this approximate autocorrelation.

3.4 Data Reduction

A one dimensional velocity measurement will yield information about the mean and variance of the flow velocity in the measured direction. A sample size of N measurements are averaged to determine the mean (this assumes the flow is stationary),

$$\langle u \rangle = \frac{1}{N} \sum_{i=1}^N U_i \quad (3.33)$$

By taking the series of data and subtracting off the mean from each point leaves a value for the fluctuating component of velocity for each measurement,

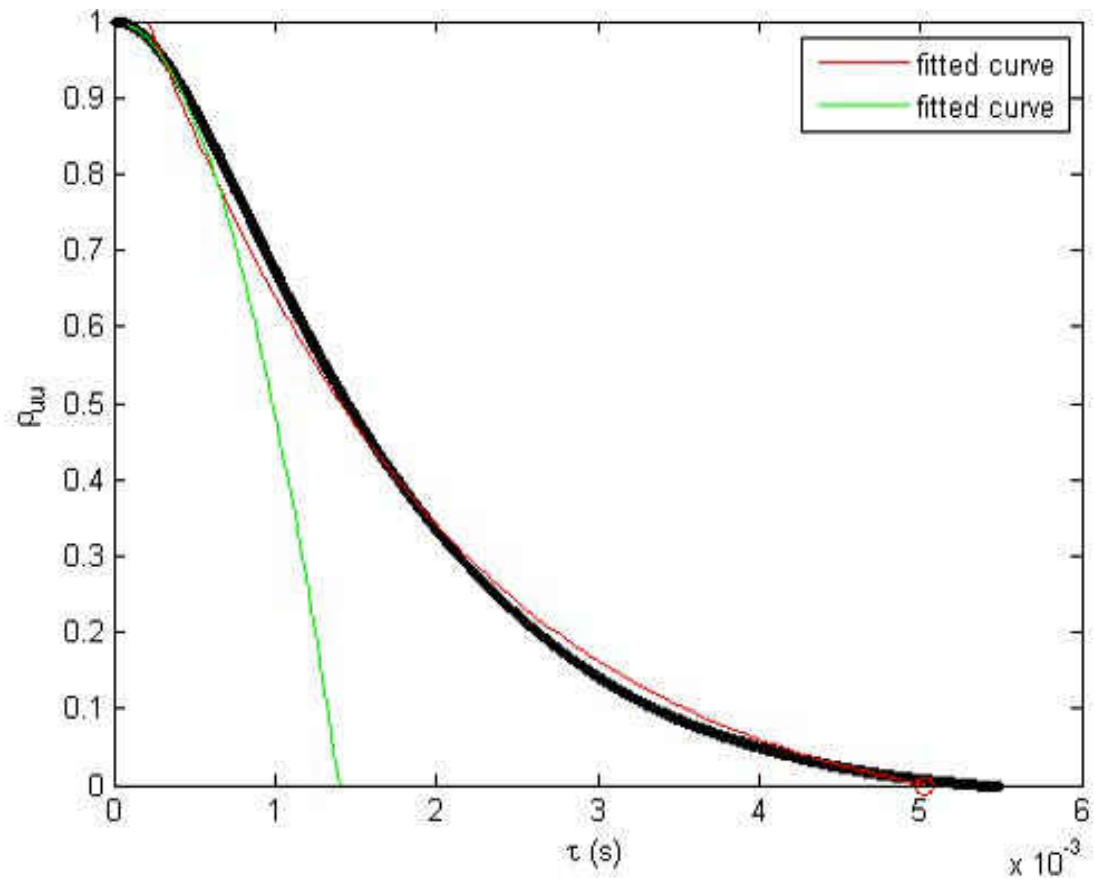


Figure 3.5: Autocorrelation function and associated curve fits for the calculation of Λ_I and λ_τ

$$u'_i = u_i - \langle u \rangle \quad (3.34)$$

With knowledge of the instantaneous velocity, the second central moment of the velocity fluctuations can be calculated from,

$$\langle u'^2 \rangle = \frac{1}{N} \sum_{i=1}^N u_i'^2 \quad (3.35)$$

Higher order moments can be calculated from the sample, the third moment known as the skewness is expressed as

$$skewness = \frac{\sum u_i'^3}{(n-1)\langle u'^2 \rangle^{3/2}} \quad (3.36)$$

and the fourth moment known as the kurtosis can be calculated by

$$kurtosis = n \frac{\sum u_i'^4}{\langle u'^2 \rangle^2} \quad (3.37)$$

The moments act to characterize the probability density function associated with the measured random variable. One can estimate the probability density function directly by computing a histogram of the velocity measurements. With sufficiently large N a reasonable estimate is obtainable.

3.5 Experimental Methodology

3.5.1 Hotwire Calibration

Prior to sampling the flow field surrounding the film cooling holes, a hot wire calibration is performed to accurately account for the ambient conditions as well as the electrical circuit properties with the anemometer system. A TSI Model 1127 Manual Velocity Calibrator is used to generate a relation between flow velocity and bridge voltage. The calibration unit consists of a controllable jet orifice which provides steady, well-conditioned flow directly over the hot wire. A range of velocities were imposed over the hot wire sensor within the jet orifice. A sample calibration can be seen in Figure 3.6.

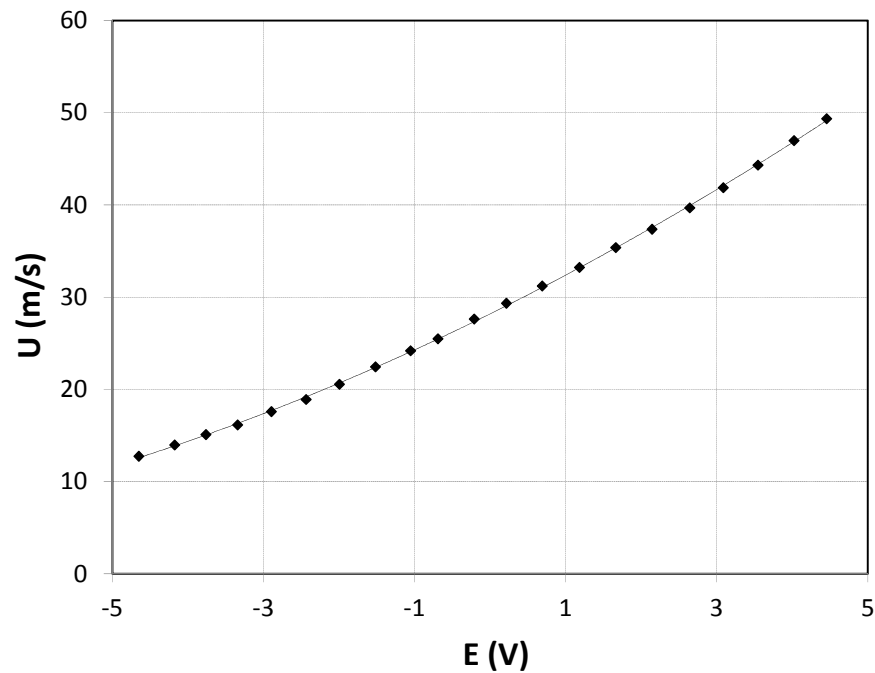


Figure 3.6: Sample hot wire calibration relating bridge voltage with flow velocity

3.5.2 Hardware

The sensor chosen for the study is a TSI Model 1243 boundary layer single hot wire with a wire diameter of $3.2 \mu\text{m}$ and wire length of 1.27 mm, as seen in Figure 2. The hot wire is calibrated using a TSI Model 1127 Manual Velocity Calibrator. A TSI IFA-300 anemometer controls the hot wire probe and utilizes a high pass filter at 1 Hz and a low pass filter at 300 kHz. For the power spectrum calculations, measurements are made at 20 kHz for 200k samples. A data sampling convergence study was conducted prior to test matrix data acquisition, where variations in sampling criteria were performed with the resulting hot wire measurements documented. The sampling frequency was varied over a large range, between 5 kHz and 250 kHz. The results show that the quality is a function of the ratio of samples to sampling frequency, but not ether one explicitly. Measurements are digitized utilizing a National Instruments PXIe-6366 DAQ card using a PXIe-1062Q chassis. The DAQ card features 8 channels and 16-bit resolution and is capable of 2 MS/s per channel. Traverses are made using a Velmex model #A2512P40 – S2.5 combined with model #A1509P40 – S1.5, giving X-Z movement at $2.5 \mu\text{m}$ resolution.

Table 3.1: Hotwire specifications

-T1.5 (Platinum coated tungsten wire)			
Wire diameter	d	μm	3.8
Wire length (sensing area)	l	mm	1.27
Wire length to diameter ratio	l/d	-	334
Inner scale	ν/u_τ	μm	9.75
Viscous scaled wire diameter	d^+	-	0.39
Viscous scaled wire length	l^+	-	130

Model 1261A Miniature Boundary Layer Probe

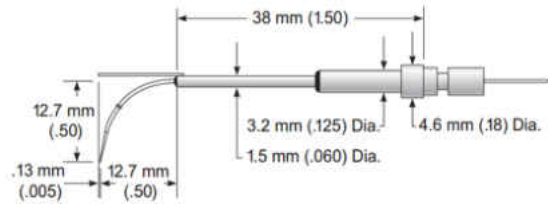


Figure 3.7: Hotwire probe used in experiment



Figure 3.8: Hotwire probe in tunnel at the lowest wall normal position

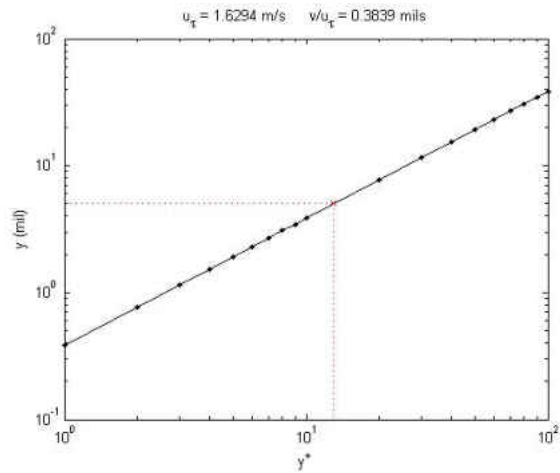


Figure 3.9: Relation between physical wall normal coordinate and y^+ location

3.5.3 Sampling Convergence

A convergence study to determine sampling rate and number of samples for the tests. Different combinations of sampling rate and total samples were varied from 10-250 kHz and 3-60 s per data point. One 2.5 MS and 250 kHz per location was subsampled to obtain most of these reduced sets. One additional 25 kHz 1.5 MS traverse was also taken to represent entitlement for Λ_I calculation. Each sample is used to calculate $\langle u \rangle$, $\langle u'^2 \rangle$ and Λ_I , the results of which are shown in Figures 3.10, 3.11 and 3.12.

Figure 3.10 shows that the mean velocity profile converges very quickly. Only 1 case stands out (0.001 MS at 10 kHz) as being noisy from the samples. Interesting to note is that the extreme sample of 1.5 MS at 25 kHz seems to differ significantly from the other series. This is because the sample takes 2.5 hours to complete the data acquisition. In this time there must have been appreciable temperature changes within the room (the tunnel is in an un-conditioned space) which resulted in the mean profile coming out incorrectly. As we will see later this did not affect the turbulent quantities.

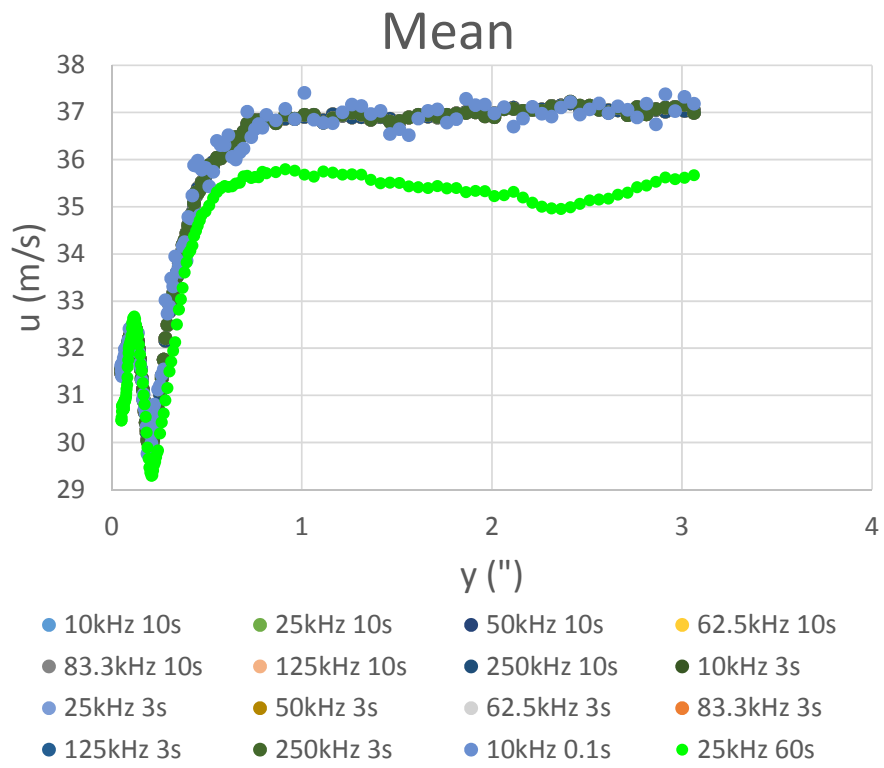


Figure 3.10: Convergence of $\langle u \rangle$

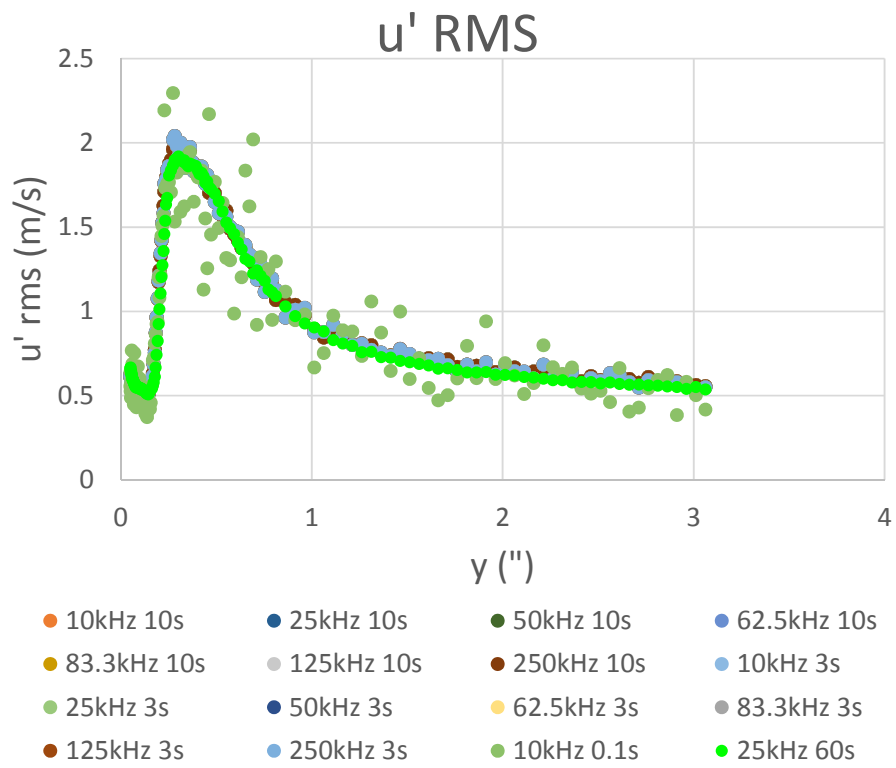


Figure 3.11: Convergence of $\langle u'^2 \rangle$

Figure 3.11 exhibits slightly more scatter than the convergence of the mean profile; however, we see that all sampling combinations still yield a profile which clearly exhibits the proper trend and smoothness expected. Note that the undersampled case, 0.001 MS at 10 kHz, is noisier than for the mean. This is because the higher order moments are more difficult to resolve. Also note that the extreme sampling case, 1.5 MS at 25 kHz, now falls in line with the other trends. This is because the relative fluctuations are captured despite the mean results changing.

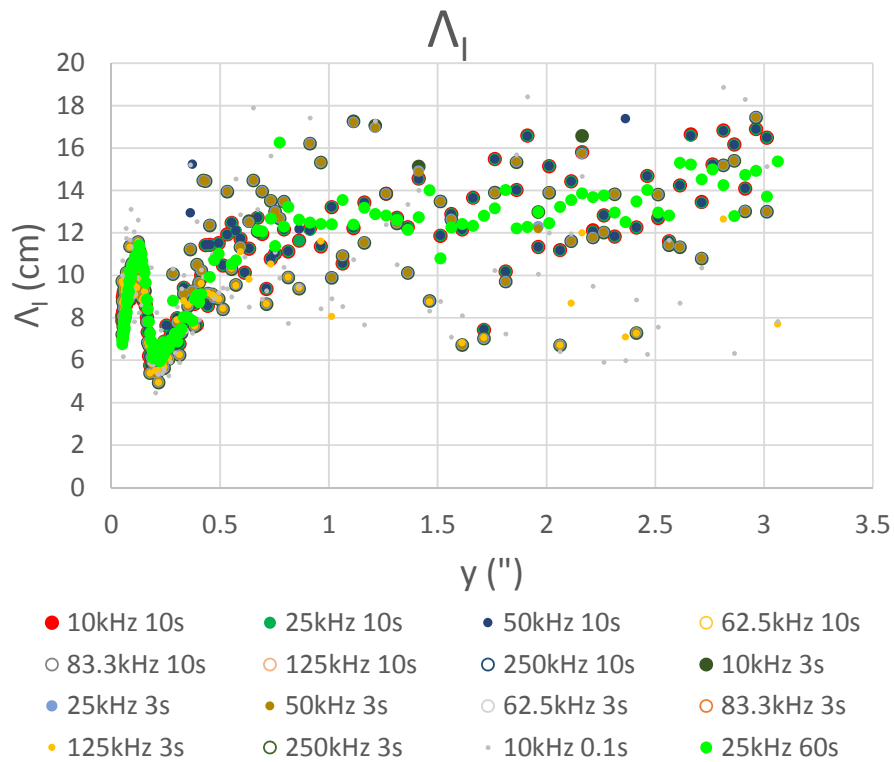


Figure 3.12: Convergence of Λ_I

3.6 Results

If CO₂ were used as the coolant there would be a Reynolds number effect on the wire due to fluid properties which would be confound the interpretation of velocity; hence, a density ratio of $DR = 1$ was necessary for the hot wire testing. The test conditions are listed in Table 3.2.

Table 3.2: Hotwire test matrix

Hotwire Case No.	Geometry	M	I	VR
1	1	0.3	0.1	0.3
2	1	0.9	0.8	0.9
3	5	0.9	0.8	0.9

3.6.1 Measurement Locations

Seventeen streamwise locations were chosen for detailed boundary layer measurements. The non-dimensional streamwise locations of the traverses are listed in Table 3.3. All traverses presented in this section or obtained from the array centerline. The wall normal resolution is adjusted from 25 μm near the wall to 1 mm once in the mainflow. Each wall normal traverse consists of 152 wall normal measurements locations covering a distance of 77 mm.

Table 3.3: Streamwise locations for hot wire traverses

<u>Position No.</u>	<u>x/d location</u>
-1	-50.3
0	-2.5
1	1.5
2	5.2
3	9.0
4	12.7
5	16.5
6	20.2
7	24.0
8	27.7
9	31.5
10	35.2
11	39.0
12	42.7
13	46.5
14	50.2
15	54.0

3.6.2 Mean Velocity

The mean streamwise velocity profiles for the cases tested are shown in Figure 3.13. The profiles are in physical units; however, the different streamwise locations are shifted by a constant to show all profiles in a single plot. The lower blowing ratio cases add low velocity fluid to the boundary layer. This may speed up the very near-wall region which isn't measured but the affect seen most in these measurements is to retard the outer layer. This effect is most clear at streamwise locations immediately after injection. At locations $7.5d$ downstream the boundary layer seems to recover and approach a more typical profile. The high blowing ratio case tested adds high velocity (90% of the mainflow speed) fluid into the boundary layer. The jet is clearly seen by the local velocity peak nnear the wall. This peak spreads out as the jet advects downstream but a deformed velocity profile can be seen even $11d$ downsteram of injection heading into the following row. The lifted jet is likely protruding into the inviscid flow of the mainstream at this point, yet it leaves a wake of some kind which hasn't relaxed to a typical boundary layer yet.

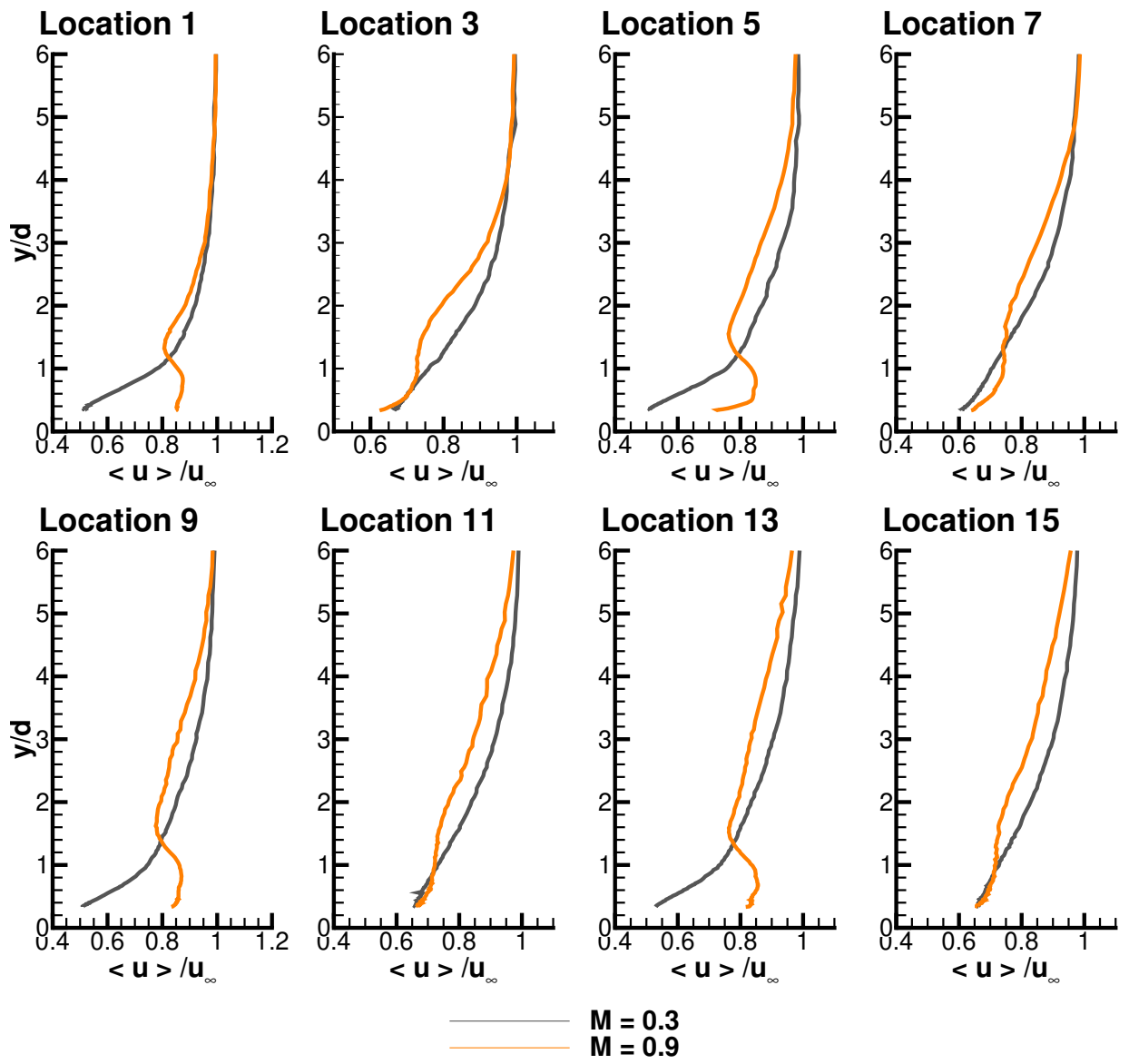


Figure 3.13: Mean streamwise velocity, $\langle u \rangle$, measurements throughout Geometries 1 and 5

3.6.3 $\sqrt{\langle u'^2 \rangle}$ Results

Streamwise fluctuations are evidence of turbulence production. The low blowing cases (cases 1 and 3) show qualitatively the same trend as the upstream boundary layer $\sqrt{\langle u'^2 \rangle}$ profiles, just with exaggerated levels. Because low momentum fluid is pushed farther away from the wall than normal, it is creating stronger shearing with the high speed freestream than if there was no injection. This causes increased production of turbulence resulting in higher levels of $\sqrt{\langle u'^2 \rangle}$. By downstream rows the film has significantly altered the shape although it is qualitatively the same as a typical boundary layer it is thicker and of higher peak magnitude.

The high blowing case (case 2) is distinctly different from the low blowing cases because it affects the overall qualitative shape of the $\sqrt{\langle u'^2 \rangle}$ profiles. The jets themselves have low turbulence level cores so a minimum of $\sqrt{\langle u'^2 \rangle}$ is seen at the jet cores. Immediately downstream of injection the jet is relatively close to the wall and a single large peak is seen above the jet. The profiles show that the jet moves away from the wall (seen by the location of the $\sqrt{\langle u'^2 \rangle}$ minima) and then a dual peak is seen in $\sqrt{\langle u'^2 \rangle}$. The two peaks highlight the tops and bottoms of the jets. The lower peak is washed at by $7.5d$ after injection.

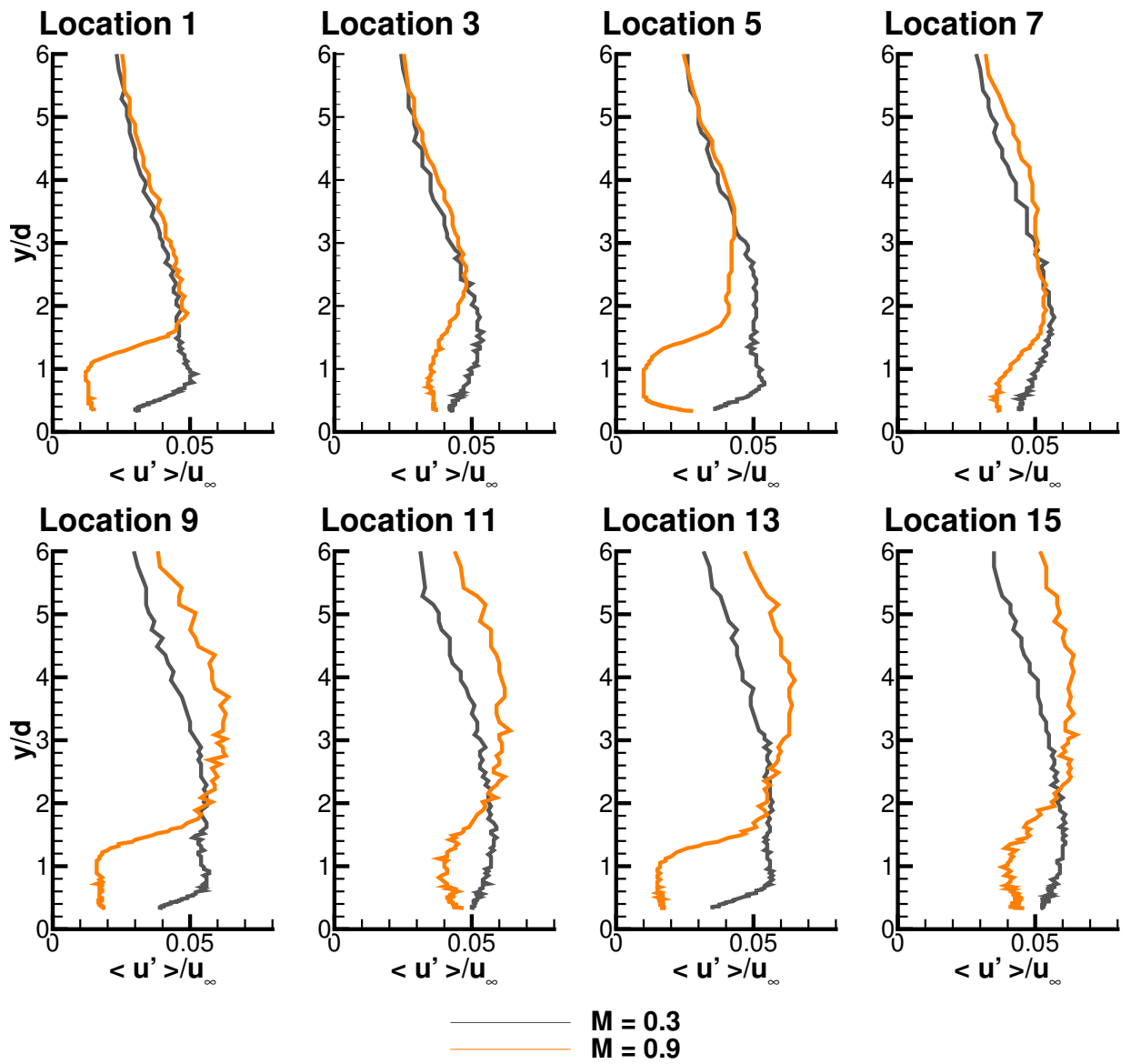


Figure 3.14: RMS of streamwise velocity fluctuations, $\langle u' \rangle$, measurements throughout Geometries 1 and 5

3.6.4 Length-Scale Calculations

Integral length scale (Λ_I) and Taylor micro scale (λ_τ) values were calculated for all measurements locations. An estimate for the relative size of these parameters is given by Tennekes and Lumley [57] and is repeated in Equation 3.38. It seems that the measured ratio is orders of magnitude different from expected. The integral scales are on the order of the wind tunnel channel height so the micro scale measurements are in question.

$$\frac{\lambda_\tau}{\Lambda_I} \propto Re_I^{-1/2} \quad (3.38)$$

Hutchins et al. [3] listed several guidelines related to hot wire measurements for the determination of turbulent quantities. Table 3.4 shows the guideline values presented in [3] compared with estimates for the values used in the current measurements. These values are out of the experiments control without custom designing a new experiment or hot wire probe. Because the non-dimensional length of the wire is relatively large, it is expected to dampen very small scale effects and result in a type of integration of the eddys along the sensor. This results in longer than expected correlations at very small time scales. For this reason measurements of the Taylor micro scale, λ_τ , are deceptively large and are not presented.

This fact does not have appreciable influence on the calculation of integral length scales which are presented in Figures 3.15 for the two upstream locations and 3.16 for the three conditions tested. The calculation of integral length scale in the freestream is very noisy due to the very low turbulence levels. The data is scattered about $\Lambda_I = 17.5$ cm. The channel height is 15.2 cm so this is very reasonable. Near the wall the Λ_I estimates go down as low as 6 cm.

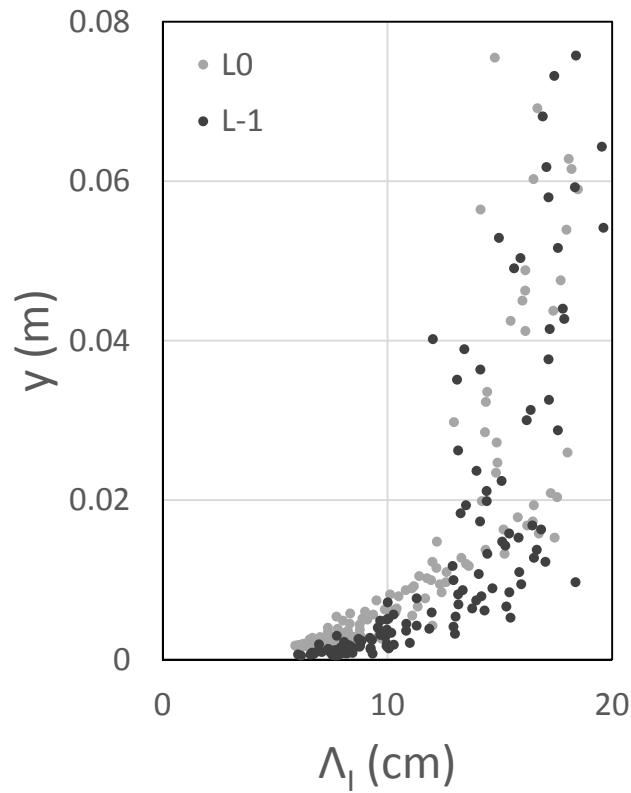


Figure 3.15: Integral length-scale, Λ_I , measurements of the approach flow

Figure 3.16 shows that the very attached cases (Geometry 1, $M = 0.3$ and Geometry 5, $M = 0.9$) have very little influence on the correlations. The diffuser case has a slight increase in Λ_I near the wall but not much. The penetrating case (Geometry 1, $M = 0.9$); however, has the distinct influence of increasing Λ_I near the wall, especially immediately after injection. The Λ_I values approach freestream levels. This is an indication of larger scales driving the mixing for the lifted jets.

3.6.5 Derived Quantities

A Clauser fit was applied to each of the measured streamwise velocity profiles. There are big assumptions made by fitting a film cooled velocity profile to a logarithmic velocity profile; however, this process was carried out anyway and resulted in corrections for the wall normal position as well as shear stress at the wall. With these values, calculated for each measurement traverse, the 99% boundary layer thickness (δ_{99}) and wall shear stress can be plotted as a function of streamwise location in the multi-row film boundary layer at the array centerline.

Boundary layer thickness as a function of streamwise location is shown for all three cases tested in Figure 3.19. The wall shear stress at the array centerline as a function of streamwise location is shown for all three cases tested in Figure 3.20.

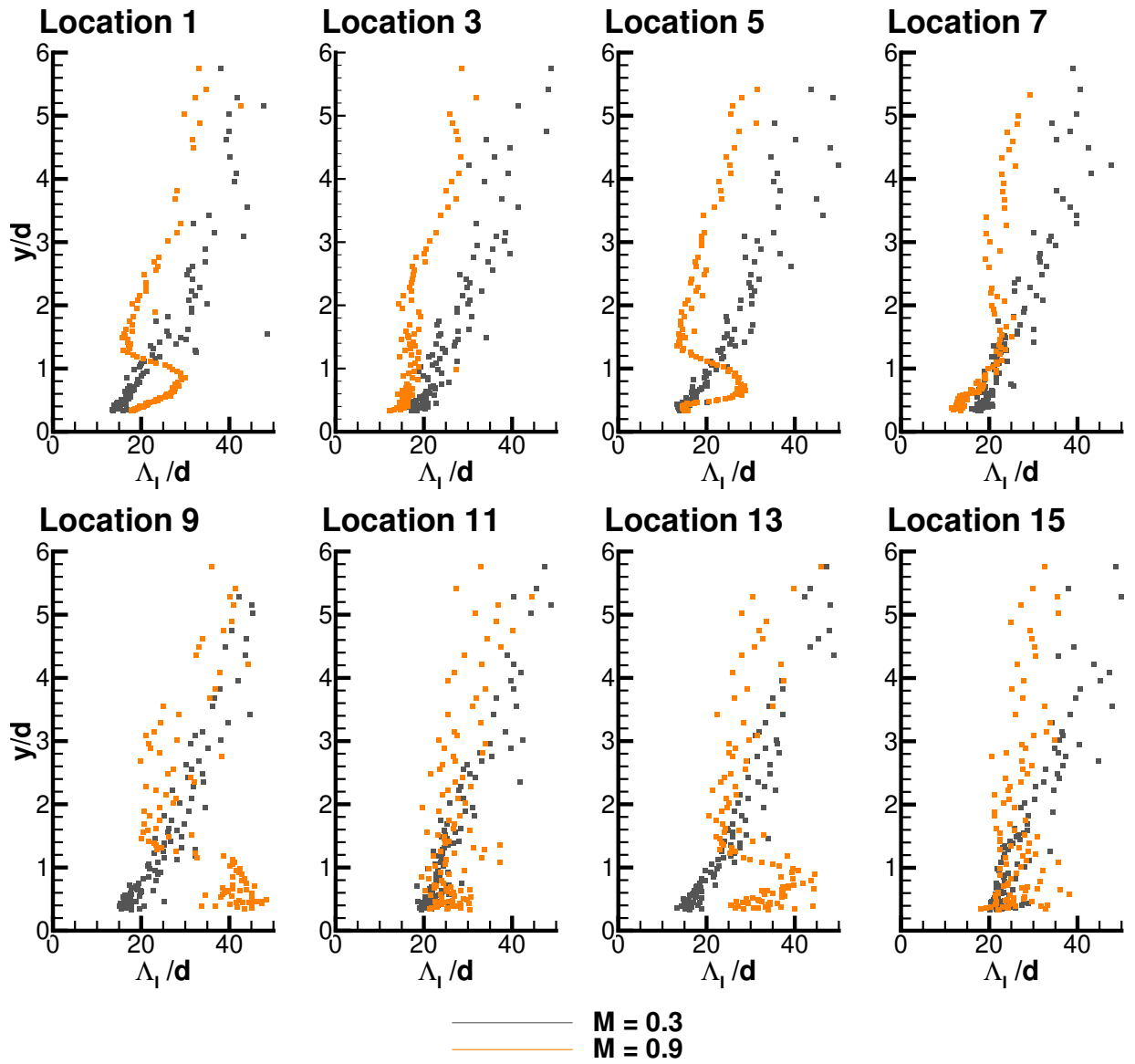


Figure 3.16: Integral length-scale, Λ_I , measurements throughout Geometries 1 and 5

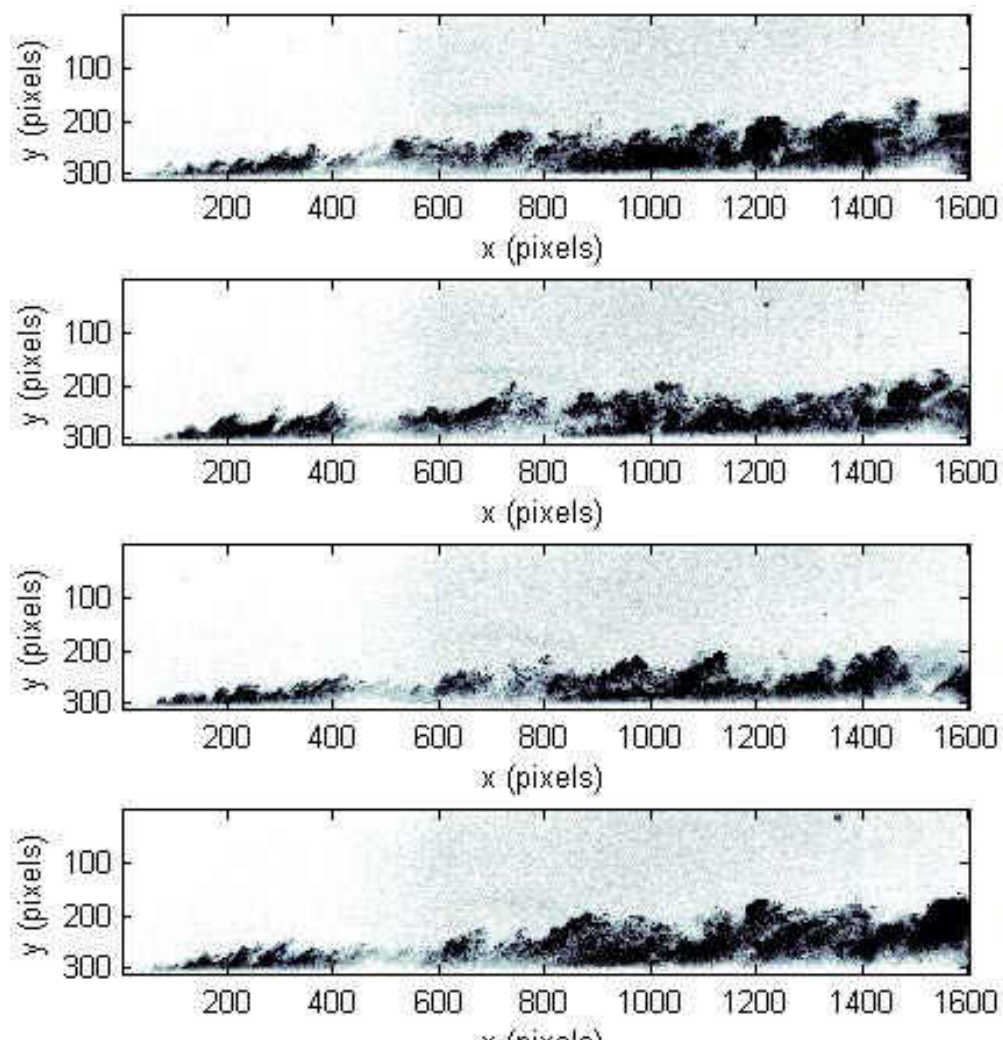


Figure 3.17: Particle density flow visualization for $M = 0.45$ showing rows 1 and 3

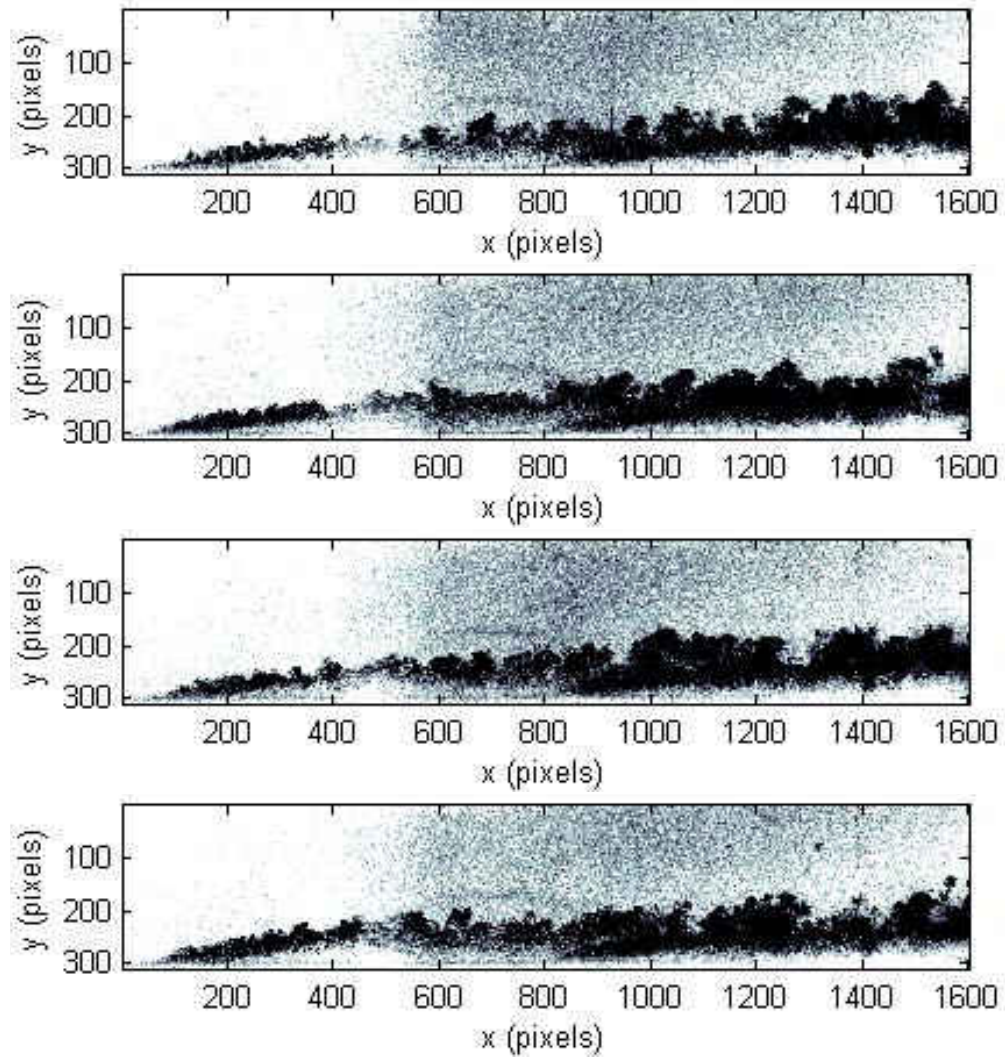


Figure 3.18: Particle density flow visualization for $M = 1.05$ showing rows 1 and 3

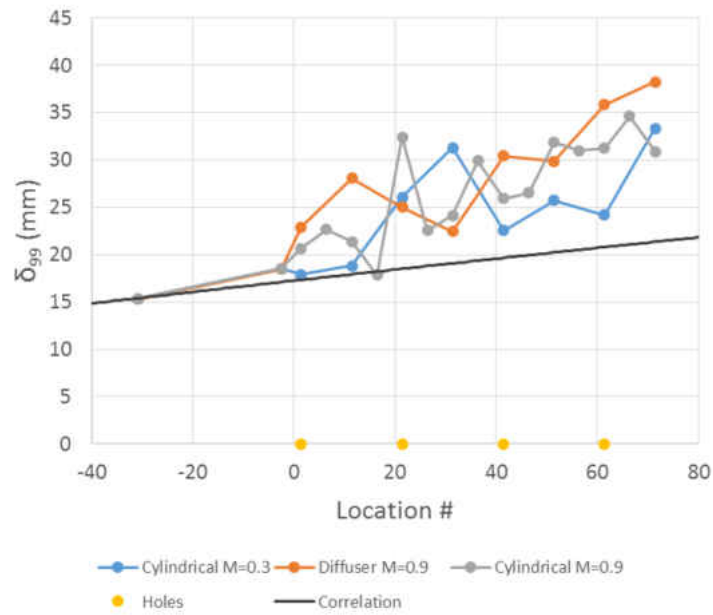


Figure 3.19: Boundary layer thickness development throughout the multi-row arrays

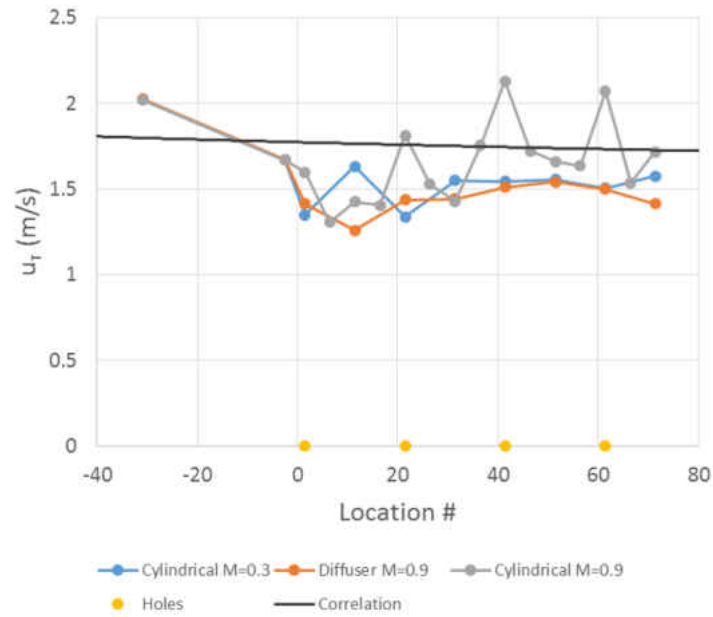


Figure 3.20: Streamwise development of wall shear stress

3.7 Summary of Hot Wire Findings

Statistically converged measurements of $\langle u \rangle$, $\sqrt{\langle u'^2 \rangle}$ and Λ_I were presented. δ_{99} and $\tau_{y=0}$ values were calculated from the measured profiles. From these measurements, several conclusions can be made which are listed below.

- Injection thickens the boundary layer significantly
- Due to the low turbulence mainstream and jets, turbulence production takes place primarily at regions of high shear between mainflow and coolant or in wakes for the lifted case
- Length scale is proportional to effective blowing ratio, i.e. higher blowing ratios result in longer correlation of streamwise velocities
- Array is spaced far enough ($7.5d \times 7.5d$) to allow flow to approach typical flat plate boundary layer for the low blowing cases
- High blowing case influences flow enough to not allow it to reach a BL flow by the following row ($15d$ later)

Table 3.4: Hotwire parameters compared with guidelines from [3]

Guidelines	Study Parameters
$l^+ < 20$	$l^+ = 130$
$l/d > 200$	$l/d = 334$
$t^+ < 3$	$t^+ = 0.6$

CHAPTER 4

SPATIALLY RESOLVED FLOWFIELD

This chapter describes the spatially resolved velocity measurements taken of the multi-row film cooling geometries with particle image velocimetry (PIV). The strength of PIV is its ability to measure two components, streamwise and wall-normal in this case, of velocity over an entire plane.

Previously reported measurements from literature of the hydrodynamics of film cooling are presented in §4.1. Then, the PIV technique is described in §4.2. The experimental setup used in this experiment is detailed in §4.3. Testing methodology for the PIV experiments is described in §4.4. Next, the processing algorithm implemented in this experiment is described in §4.5. The correlation statistics method of uncertainty quantification is described in §???. Finally the test results are presented in §4.6.

4.1 Flowfield Measurements of Film Cooling

In the near wake of a film cooling jet, there is a separation region which is a factory of turbulent kinetic energy. In gas turbines the main stream is already highly turbulent. The challenge is to predict the interaction of a stream jetting into a turbulent boundary layer and generating more turbulence. What is needed is more insight into the role of turbulence in film cooling. Pietrzyk [58] insists the fundamental limitation to improving film cooling performance is a lack of understanding of the fluid mechanisms governing the flow. This issue remains, as Kohli [59] asserts that our current knowledge still lacks a fundamental understanding of the mechanisms governing transport of heat and momentum.

There are few studies which report turbulent quantities in a film cooled boundary layer. Recently the topic has been receiving more attention. Burd [60] measured length-scale and spectra of velocity at hole exits with different inlet boundary conditions. Kohli [59] used a cold-wire to obtain spectra and probability density functions of the fluctuating temperature field to study the mechanisms behind the rapid dispersion of coolant near injection. Kohli [61] simultaneously measured two components of velocity and temperature by means of a cold-wire and LDV combination to obtain turbulent Prandtl numbers; confirming that they are far from constant, as they are commonly modeled.

Aga [62] studied the flow structure of a compound angle hole with stereoscopic PIV in order to validate a computational model. El-Gabry [63] measured all three components of velocity by means of two X-wire probes; the focus being the generation of data for validating CFD. Wright [64] measured velocity at planes parallel to the flow with PIV and introduced a thickness parameter which correlates well with the cooling seen on the surface; thus linking the flow-field with the cooling effectiveness in a simple term.

4.2 Particle Image Velocimetry

The particle image velocimetry (PIV) used in this study is more specifically planar high image density PIV in which a thin laser sheet illuminates a particle laden flow and is recorded via a CCD camera. Two images are taken in short succession of one another ($10 - 20\mu s$) and an image pair of particle patterns are obtained. Through interrogation by spatial correlation a most probable displacement is estimated. With information on the system magnification and timing between successive pattern images a velocity can be calculated. This process can provide quantitative measurement of two components of velocity over a plane within the flowfield.

4.3 PIV Experimental Setup

The laser used is an EverGreen laser by Quantel. It is an Nd:YAG laser providing light at 532nm. There are two lasers within the unit which can be externally triggered to provide laser pulses of arbitrary separation times. The maximum frequency of each individual laser is 14 Hz.

The laser sheet is formed with a pair of optics. A 1 m focal length spherical lens is used to converge the beam axisymmetrically. The beam then passes through a 10 mm focal length cylindrical lens to expand the beam quickly along one axis. The sheet is then turned 90° with a dichroic mirror. A schematic of this setup is shown in Figure 4.1.

A pco.1600 in dual frame mode is used to record the droplet patterns. Two seeders are required for this experiment. The mainflow is seeded with a TSI 9307-6 oil droplet generator. The secondary flow is seeded with a LaVision model 1108926 seeder. The seed used is Bis-ethyl-hexyl-sebacate (*DEHS*; Di-ethyl-hexyl-sebacate; Dioctyl-sebacate) in the coolant supply and olive oil (Pompeian Imported Classic Pure Olive Oil, 100% Pure and Natural, Rich Flavor) is used in the mainstream. This results in a seed diameter of 0.5 - 1.0 μm .

Particle Reynolds number can be calculated as follows,

$$Re_p = \frac{U d_p}{\nu} \quad (4.1)$$

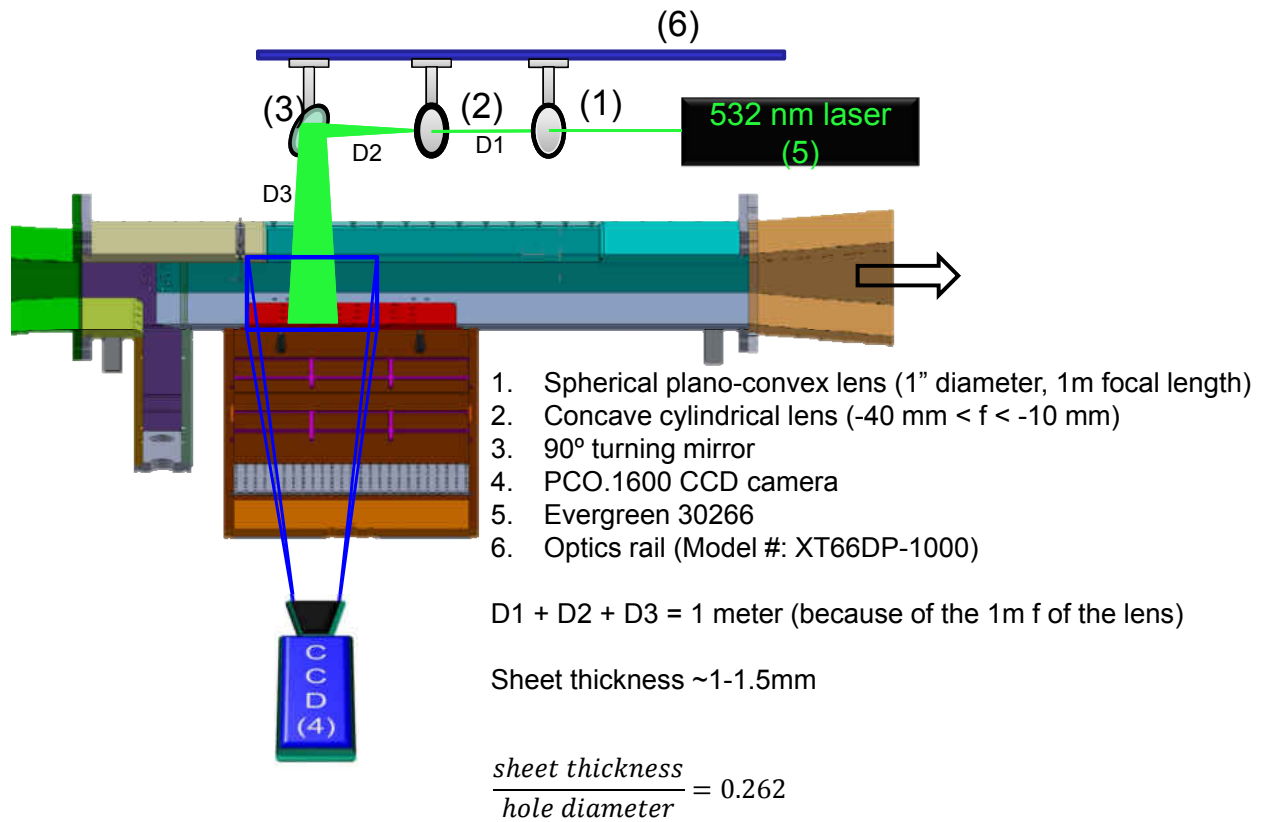


Figure 4.1: Experimental setup for PIV testing

Particle Reynolds numbers range from 1 - 2.5. For $Re_p < 1$, a Stokes flow estimate of drag is valid. For heavy particles, $\rho_p \gg \rho_f$ the particle response time is given by,

$$\tau_p = d_p^2 \frac{\rho_p}{18\mu}. \quad (4.2)$$

Particle response times range from 0.6 - 2.8 μs . The characteristic frequency, which is given by,

$$C = \frac{18\mu}{\rho_p d_p^2} = \frac{1}{\tau_p} \quad (4.3)$$

ranges from 0.36 - 1.66 MHz. Dissipation rate can be estimated according to Equation 4.4 [57].

$$\epsilon \approx \frac{U^3}{L} \quad (4.4)$$

For a 40 m/s mainflow with a 6" characteristic length this estimate comes out to $\epsilon = 420$ kJ/kg/s.

Kolmogorov length scale can be estimated according to

$$\eta = \left(\frac{\nu^3}{\epsilon} \right)^{(1/4)} \quad (4.5)$$

This comes out to 10 μm . Using Taylor's Hypothesis this would be a time scale of 0.25 μs .

Stokes number defined by relating the particle time constant to the Kolmogorov time scale is given by,

$$St = \frac{\tau_p}{\tau_k} \quad (4.6)$$

This estimate for the Stokes number range used in these experiments is 2.4 - 11. Another way to estimate the Stokes number is by comparing particle inertia to its drag according to,

$$St = \frac{\rho_p d_p^2 U C_c}{18\mu L} \quad (4.7)$$

This estimate yields a Stokes number range of 2×10^{-4} - 8×10^{-4} . This large discrepancy between Stokes number estimates is likely due to the way turbulence dissipation rate (and then the Kolmogorov time scale) is estimated. Due to the low particle Reynolds numbers in the experiment, Equation 4.7 is a valid estimate of the Stokes numbers. In either case the Stokes numbers are sufficiently small to capture the desired effects. As $St \rightarrow 0$ the particles follow the flow perfectly. As $St \rightarrow \infty$ the particles are unresponsive to the flow.

A Berkeley Nucleonics Corporation Model 565 Pulse Delay Generator is used to externally trigger both flash lamps and the camera.

4.4 Testing Methodology

First everything must be aligned properly. The laser should pass through the axis of each lense. The sheet must lie in the streamwise aligned plane corresponding the the desired measurement plane and but be aligned with the geometry. Meaning the sheet must be parallel with the freestream as well as perpendicular to the surface. This is ensured by using a very flat calibration block and shooting the laser such that it glances the entire surface of the block. The camera must also be aligned orthogonally to the sheet / calibration block.

Once alignment is completed the seeding density must be fine tuned in the crossflow and the mainflow. Both fluid streams are seeded so both seeding loops must be optimized. In this experiment the mainflow seeder can be operated at full and the coolant seeding must be adjusted to provide as much seed as possible while still maintaining the ability for the CCD to distinguish individual droplets.

There are four guidelines given by Adrian [?] related to particle densities and particle displacements in an image pair. The first guideline states that there should be 10 or more droplets in a given interrogation region. This implies a high seeding density is desirable to have the smallest window, highest resolution, possible. The next states that the displacement should be less than 1/4 of the interrogation region. This dictates the timing between laser pulses. The third states that the out of plane motion should be less than 1/4 the sheet thickness. This also dictates the timing between laser pulses due to a fixed minimum sheet thickness. The last relates to the camera magnification.

$$N_I > 10 \tag{4.8}$$

$$|\delta X| < \frac{1}{4}D_I \tag{4.9}$$

$$|\delta z| < \frac{1}{4}\delta z_0 \tag{4.10}$$

$$M_0|\delta u|\delta t < t_\tau \tag{4.11}$$

Ultimately the camera aperture, lense focal length, laser timing and focus of the camera must be refined to obtain the best possible droplet pattern images for high quality results.

4.5 PIV Processing

There are several existing software packages which can be used to process, post-process and manipulate PIV data. Some of the more popular softwares are listed below:

- *LAvision DaVis 8.0*
- TSI Insight 4GTM
- PIVLAB [65] [66] [67]
- Fluere

- PIVMAT
- OpenPIV
- PIVview by PIVtec

This study uses DaVis 8.0 from LAvision for processing the droplet pattern image pairs.

In PIV processing, the main goal is to compute a spatial cross-correlation between the two droplet pattern images calculates a most probable displacement for each interrogation window. This displacement is calculated within the laser plane (i.e. a two-component displacement). At this point it is a pixel displacement. With knowledge of the spatial resolution (pixels per mm) from a reference image such as that shown in Figure 4.2 and the timing between laser pulses ($10 \mu s$) the pixel displacement can be converted to a velocity vector. This conversion is applied to each interrogation window. The specific process and steps are explained in detail in the following sections.

4.5.1 Image Calibration

The same block that was used during laser sheet alignment also serves the purpose of a calibration block for spatial mapping. An image of this calibration block allows a spatial mapping between physical space and pixel space in the recorded images. Several dots, 2 mm diameter, are placed on a 2-D cartesian grid, 5mm spacing in each direction, and are printed onto the block. After alignment an image is taken of the calibration block and this image is used for the spatial calibration. A sample calibration image is shown in Figure 4.2. The processing software automatically finds each dot, rotates each image to make the dots line up properly, and transforms the image coordinates to physical dimensions. In this experiment any dewarping that the software would try to apply is not desirable because everything is aligned so well so there is no dewarping applied by the software.

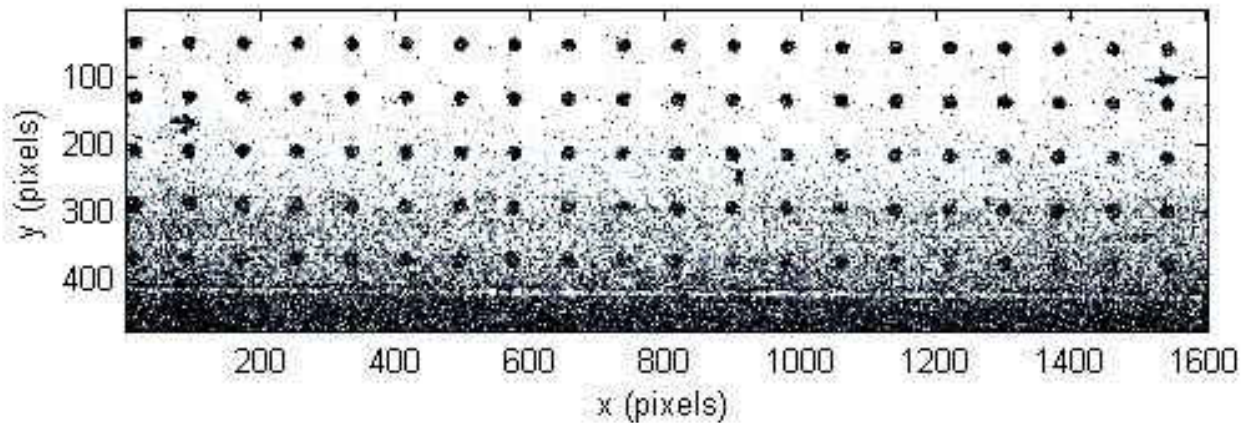


Figure 4.2: Reference image used for determining spatial resolution

4.5.2 File Formats and Timing Attributes

Image pairs are acquired as two separate `.tif` files. To allow the software to work with them properly they must first be stacked appropriately and put into a format the software can handle. After this step the inter-frame timing attribute is applied. In all cases presented the delay between pulses is $10 \mu s$.

4.5.3 Pre-Processing

The next step is an image pre-processing step. For each pixel, a 10×10 window is sampled to calculate a median. This value is subtracted from the pixel of interest. This single pre-processing step is very effective at eliminating noise and adding contrast to the image to allow easy identification of even very dim particles by the software. This step is crucial in obtaining high resolution results to get the most out of the droplet pattern images.

4.5.4 Geometric Mask

Regions which are not relevant are best to be removed from the processing domain. The regions masked in the present study correspond to the wall and fastening locations. A geometric mask is used to block these regions.

4.5.5 Interrogation Algorithms

A multi-pass cross correlation algorithm is used to process the results in this study. There are first 2 passes with a 64 x 64 pixel² interrogation window. Then there are 4 passes with a 24 x 24 pixel² adaptive interrogation window from Wieneke [68]. The adaptive window is Gaussian weighted and can change its shape, to make the center of the window more important than its edges. Elliptical windows are used, the aspect ratio and angle of the major axis is adapted to align with large gradients to provide best accuracy and resolution while maintaining robustness of the calculations.

4.5.6 Vector Validation

To remove spurious vectors a vector validation step is necessary. It is unavoidable for every window in every image to yield a proper vector [69]. For a given interrogation window, neighboring windows are sampled to yield a mean and standard deviation. If vector for the interrogation window of interest falls outside the mean by a certain amount the vector is removed and the next highest correlation peak is put in its place. This process is repeated 4 times until the criterion is satisfied. If the criterion is not met, the vector is left blank for that image.

4.5.7 Extraction of Scalar and Vector Fields

The result of a PIV processing algorithm is a series of instantaneous velocity vector fields. These can be analyzed to yield mean streamwise ($\langle u \rangle$) and wall normal velocity ($\langle v \rangle$), three Reynolds stress fields ($\langle u'v' \rangle$, $\langle u'^2 \rangle$ and $\langle v'^2 \rangle$) and z-vorticity, ω_z . A minimum of 500 valid vectors at interrogation window are required to calculate any of these quantities. Most regions have 1000+ valid vectors.

$$\boldsymbol{\omega} = \nabla \times \mathbf{U} \quad (4.12)$$

$$\omega_z = \frac{\partial v}{\partial x} - \frac{\partial u}{\partial y} \quad (4.13)$$

Turbulent kinetic energy, k , is calculated only from the two components measured.

$$k = \frac{1}{2} \left(\langle u'^2 \rangle + \langle v'^2 \rangle \right) \quad (4.14)$$

The Reynolds stresses presented are ensemble averages velocity fluctuations and do not incorporate density.

$$\langle u'v' \rangle = \frac{\sum_{i=1}^N u'_i v'_i}{N} \quad (4.15)$$

$$\langle u'^2 \rangle = \frac{\sum_{i=1}^N u'_i u'_i}{N} \quad (4.16)$$

$$\langle v'^2 \rangle = \frac{\sum_{i=1}^N v'_i v'_i}{N} \quad (4.17)$$

Uncertainties were calculated according to the correlation statistics method from [70].

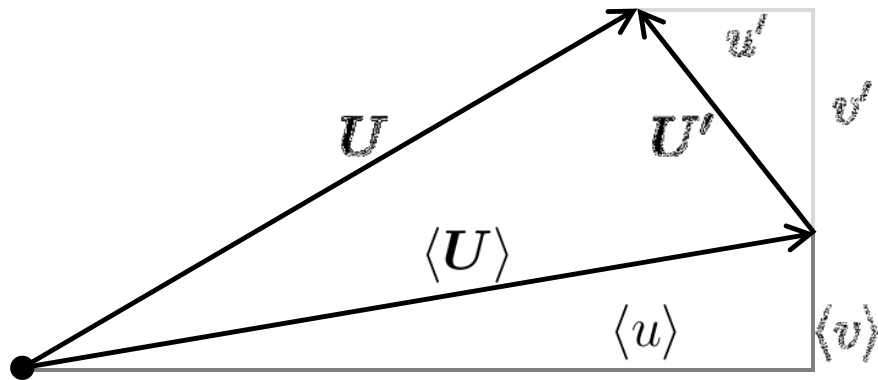


Figure 4.3: Diagram explaining nomenclature for instantaneous, mean and fluctuating components of velocity

4.6 Results

PIV measurements were taken at two different planes, $z/d = 0$ and $1/2$, which correspond to centerline and hole edge. Only Geometry 1 is measured with PIV. Three blowing ratios are tested to yield an attached case, a lifted case and one in between. The coolant is CO_2 and the seed is assumed to not influence the density. This yields a density ratio of $DR = 1.52$, the same as the PSP tests. The influence on momentum flux ratio, I , and velocity ratio, VR , is recorded. These test conditions are listed in Table 4.1.

Table 4.1: Conditions and measurement plane locations tested with PIV

Test #	z/d location	Geometry	M	I	VR
1	0	1	0.45	0.13	0.30
2	0	1	0.75	0.37	0.49
3	0	1	1.05	0.73	0.69
4	$d/2$	1	0.45	0.13	0.30
5	$d/2$	1	0.75	0.37	0.49
6	$d/2$	1	1.05	0.73	0.69

Test cases 1-3 from Table 4.1 are shown in Figures 4.4 through 4.9. Figures 4.4 through 4.6 show mean streamwise velocity (u), mean wall-normal velocity (v), mean lateral vorticity (ω_z) and turbulent kinetic energy (k).

The mean streamwise velocity near the wall at a blowing ratio of $M = 0.45$ ($VR = 0.3$) is low and attached to the wall. There are small regions of wall normal velocity at the holes which are quickly re-oriented to the mainflow direction. The lateral vorticity is all negative for this blowing ratio. This is due to the high speed mainstream shearing the top of the slow moving jets. The turbulent kinetic energy is high for this low blowing case. This is, again, due to the large amount of shearing between the mainflow and the slow moving coolant. There are large gradients in streamwise velocity which result in a large amount of turbulence production above the jets.

The middle blowing ratio of $M = 0.75$ still has a low velocity ratio of $VR = 0.5$ so there are still regions of slow moving fluid near the wall. In this case, the slow regions extend farther in the streamwise direction. The wall normal velocities are also extending farther in the streamwise direction, maintaining some vertical component all the way to the following row. The vorticity magnitude is still all negative; however, the magnitude decreased compared to the low blowing case. This is due to smaller velocity gradients. The turbulent kinetic energy is of lower magnitude compared to the lower blowing ratio, and is displaced farther from the wall. This implies the jets are extending farther into the mainflow compared to the low blowing case.

The high blowing ratio of $M = 1.05$, shown in Figure 4.6, is detached from the wall. We will see that a blowing ratio of $M \approx 0.6 - 0.7$ is optimum for these cylindrical holes in regards to cooling effectiveness. This momentum flux ratio of $I = 0.7$ is enough for the jets to lift off the wall. There is a significant wall normal velocity which envelopes the entire centerline plane. Now the lateral vorticity has positive and negative regions. The positive lobes are on the upstream edge of the jet where the jet is faster than the slow fluid near the wall. Downstream of the jets where is a wake region with negative vorticity. The upper edge of the jets now has no vorticity due to the jet matching the freestream velocity by that point. There is a layer of turbulent kinetic energy at the upper edge of the boundary layer; however, it is very low in magnitude compared to the lower blowing ratios.

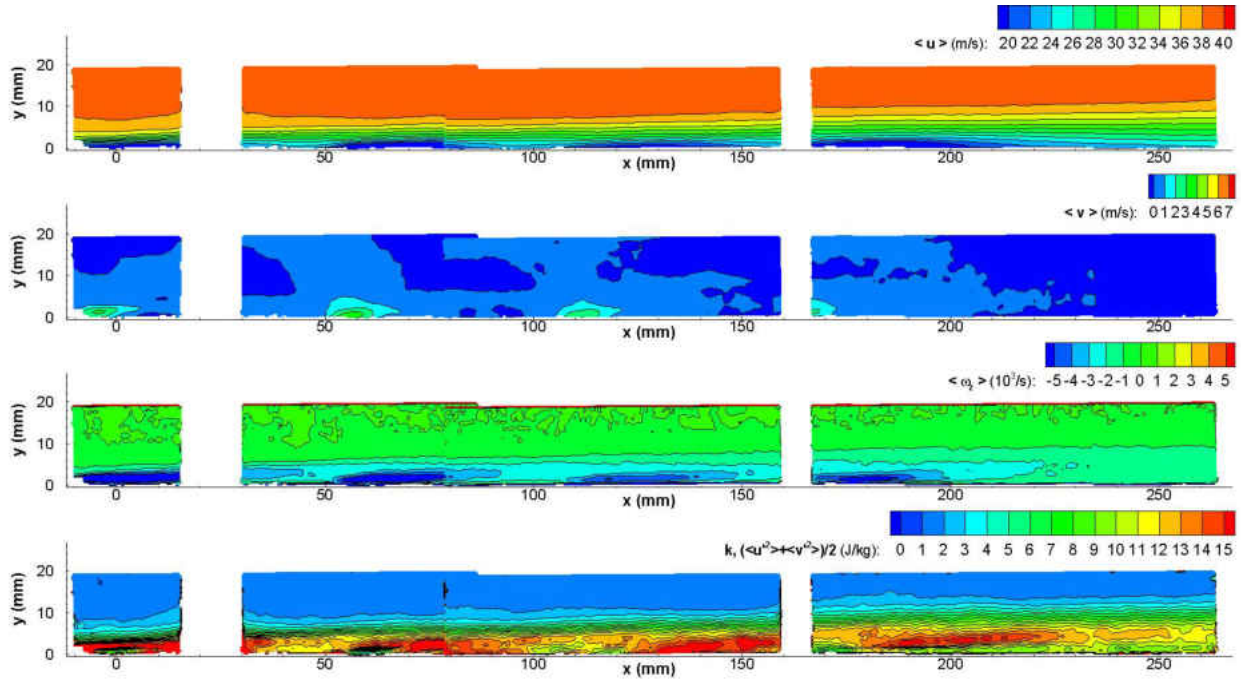


Figure 4.4: $u(x, y)$, $v(x, y)$, $\omega_z(x, y)$ and $k(x, y)$ for $M = 0.45$ at the centerline plane

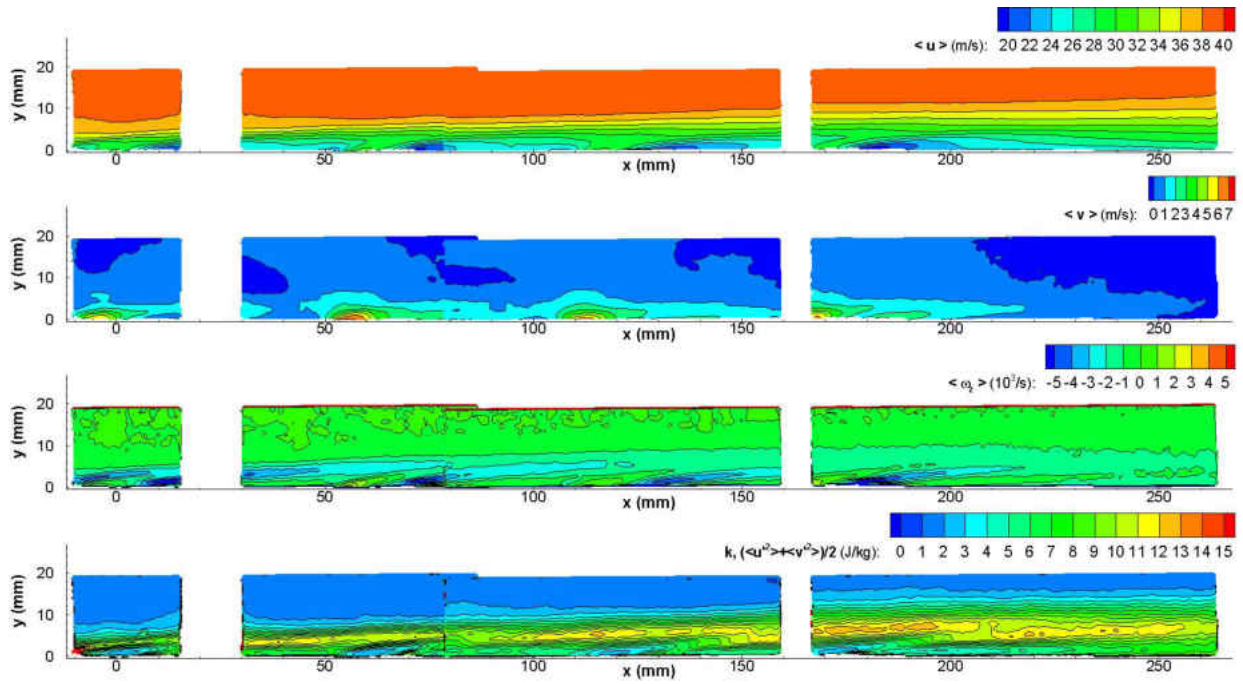


Figure 4.5: $u(x, y)$, $v(x, y)$, $\omega_z(x, y)$ and $k(x, y)$ for $M = 0.75$ at the centerline plane

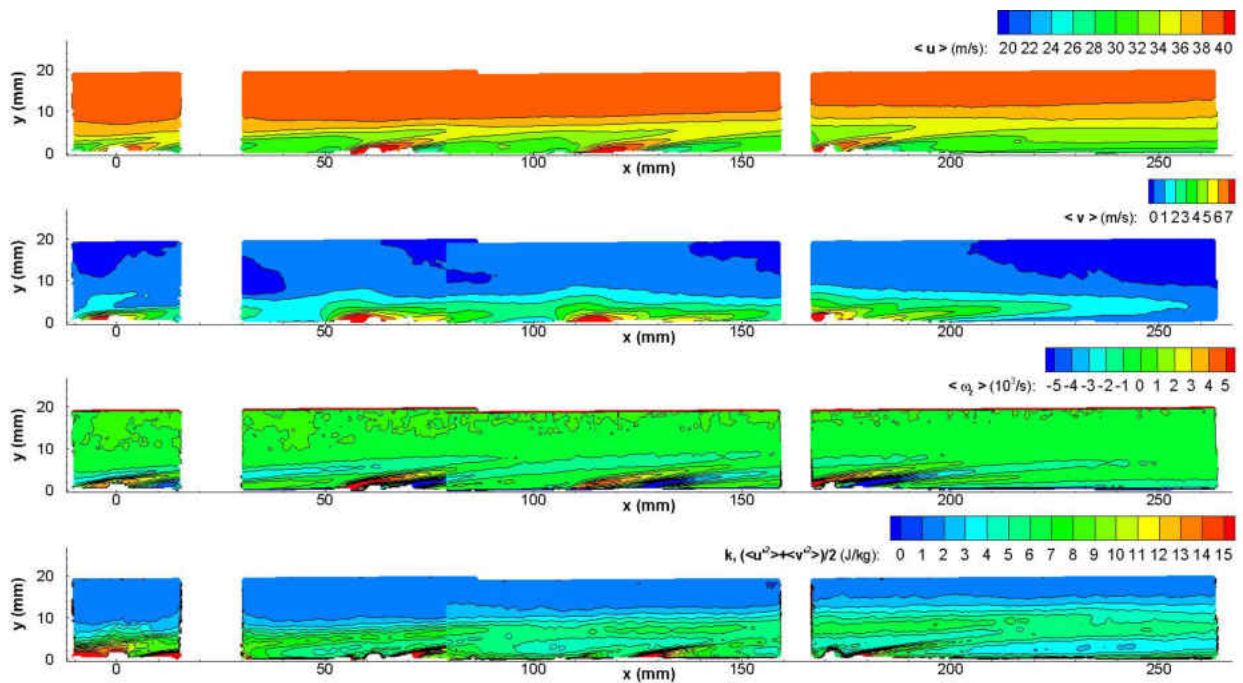


Figure 4.6: $u(x, y)$, $v(x, y)$, $\omega_z(x, y)$ and $k(x, y)$ for $M = 1.05$ at the centerline plane

Figures 4.7 through 4.9 repeat turbulent kinetic energy (k) and show the three in-plane Reynolds stresses ($\langle u'v' \rangle$, $\langle u'^2 \rangle$ and $\langle v'^2 \rangle$).

In the turbulent quantities the low blowing ratio case of $M = 0.45$ are large in magnitude compared with the higher blowing cases. There is a thick region of negative turbulent shear stress, $\langle u'v' \rangle$, near the wall. This is due to strong shearing producing k . The turbulent normal stresses, $\langle u'^2 \rangle$ and $\langle v'^2 \rangle$, exhibit the same shape as the shear stress. The turbulent normal stresses do not contribute to mean momentum exchange as much as the turbulent shear stress [57]. The magnitude of $\langle u'^2 \rangle$ is approximately 3 times that of $\langle v'^2 \rangle$. This shows there are potential problems with assuming the magnitude of 1 component from another.

The middle blowing ratio of $M = 0.75$ has regions of high turbulence which are displaced from the wall. There is a strong turbulent shear at the upper edge of the boundary layer. Figure 4.8 shows very clearly that turbulence production occurs where the mainflow interacts with the coolant jets. There is no turbulence in either the mainflow or the jets, only where they meet. Again, the magnitude of $\langle u'^2 \rangle$ is significantly larger than the magnitude of $\langle v'^2 \rangle$, despite their shape being the same.

The high blowing ratio case of $M = 1.05$ has turbulent both positive and negative turbulent shear stress values. Similar to the vorticity for this case, the high velocity jets shears the low velocity fluid near the wall and this different sign gradient causes an opposite sign shear stress at the upstream edge of the jets. The wakes of the jets have peaks in normal turbulence stresses; however, the magnitude of turbulence is notable lower than for the lower blowing ratios. Interesting to note is that the magnitude of $\langle u'^2 \rangle$ and $\langle v'^2 \rangle$ are approximately the same for this blowing ratio.

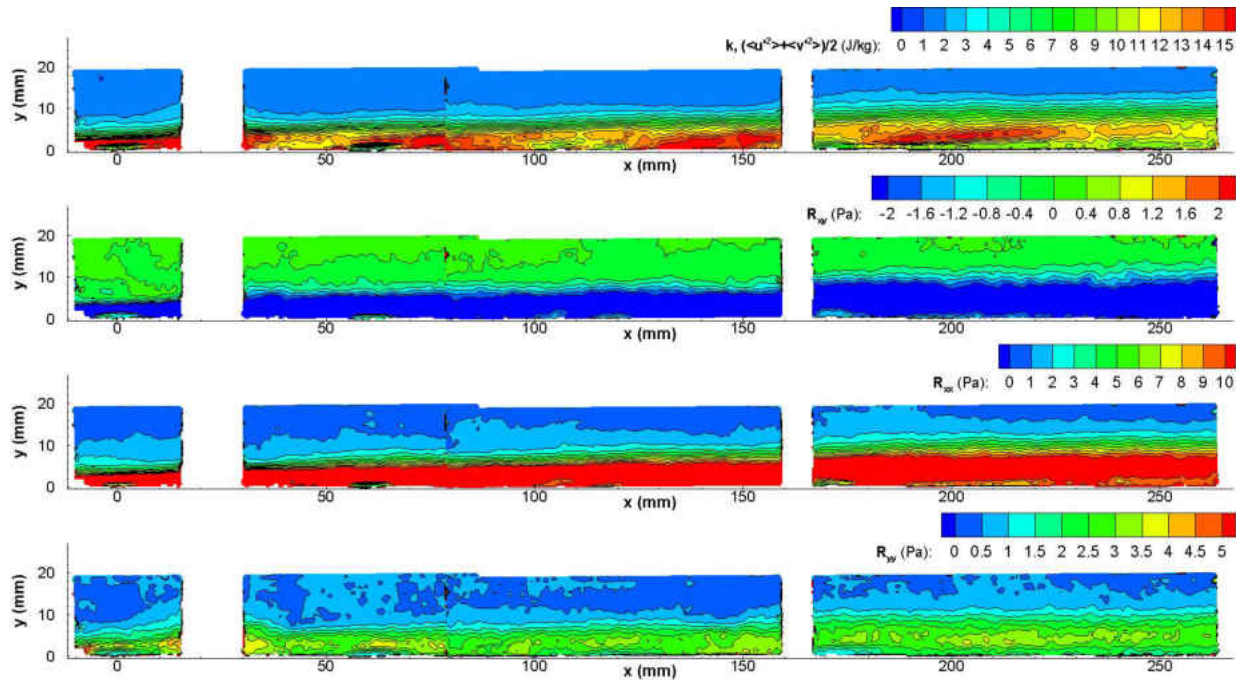


Figure 4.7: $k(x, y)$, $R_{xy}(x, y)$, $R_{xx}(x, y)$ and $R_{yy}(x, y)$ for $M = 0.45$ at the centerline plane

Test cases 4-6 from Table 4.1 are shown in Figures 4.10 - 4.15. Figures 4.10 - 4.12 show mean streamwise velocity (u), mean wall-normal velocity (v), mean lateral vorticity (ω_z) and turbulent kinetic energy (k). Figures 4.13 - 4.15 show turbulent kinetic energy (k) and the three in-plane Reynolds stresses ($\langle u'v' \rangle$, $\langle u'^2 \rangle$ and $\langle v'^2 \rangle$).

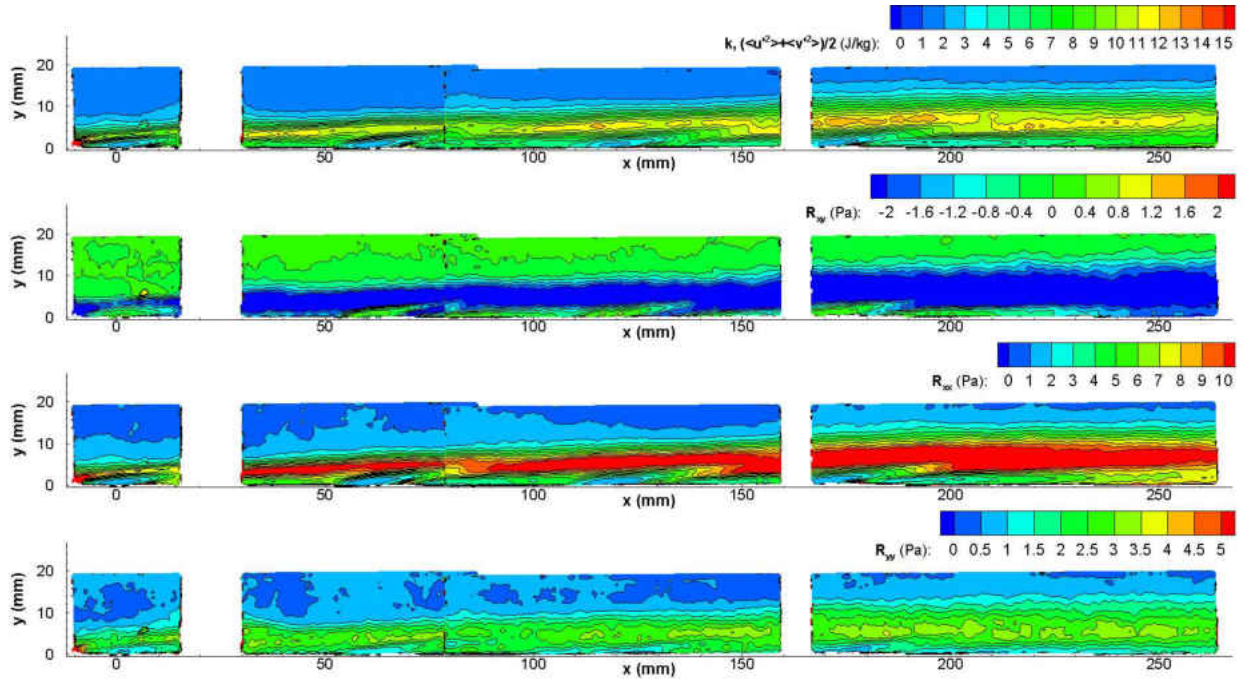


Figure 4.8: $k(x, y)$, $R_{xy}(x, y)$, $R_{xx}(x, y)$ and $R_{yy}(x, y)$ for $M = 0.75$ at the centerline plane

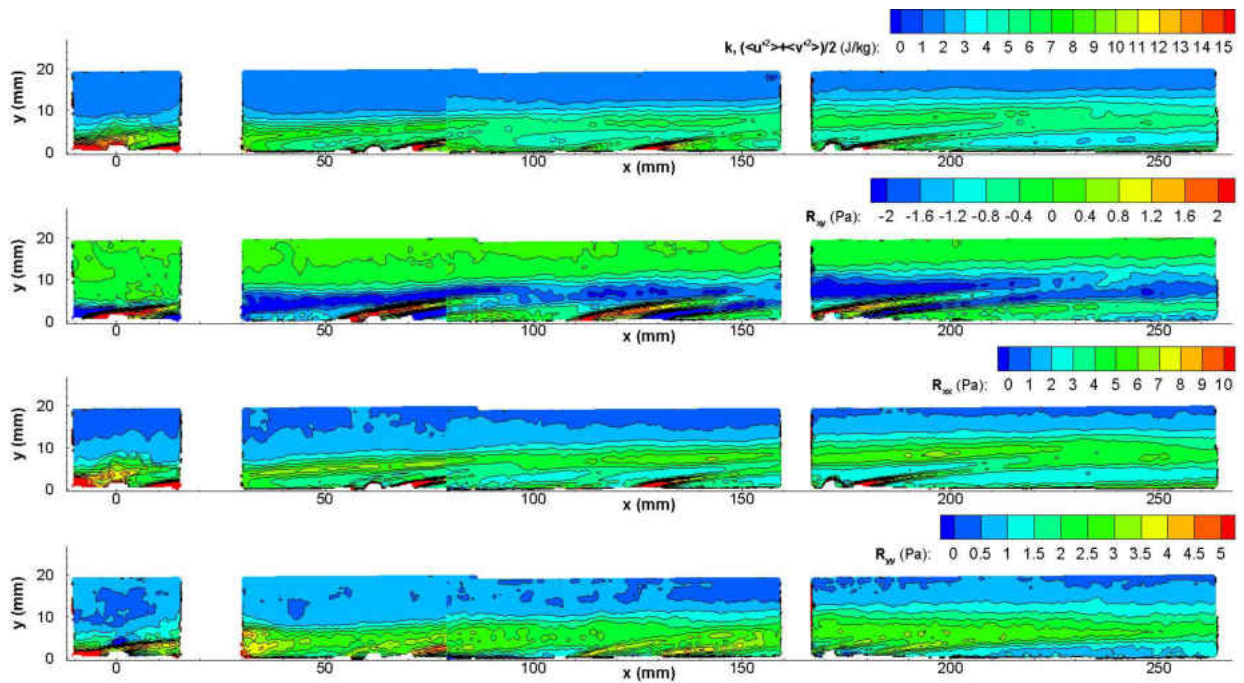


Figure 4.9: $k(x, y)$, $R_{xy}(x, y)$, $R_{xx}(x, y)$ and $R_{yy}(x, y)$ for $M = 1.05$ at the centerline plane

This $z/d = 1/2$ planes exhibit the same exact physics as the centerline planes just with some attenuation. Magnitude are smaller but the trends are identical. In the medium and high blowing ratios there are some negative velocities seen which indicates the presence of counter-rotating vortex pairs at this location.

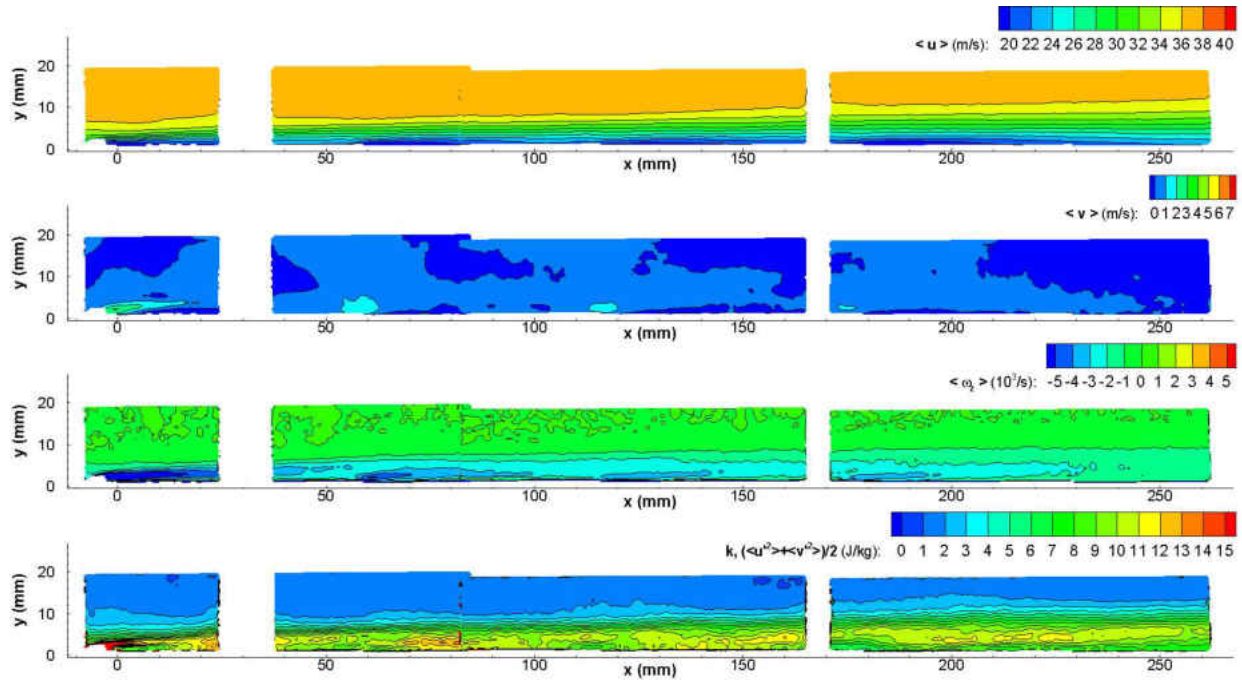


Figure 4.10: $u(x, y)$, $v(x, y)$, $\omega_z(x, y)$ and $k(x, y)$ for $M = 0.45$ at the $d/2$ plane

4.7 Summary of PIV Findings

PIV measurements were taken of Geometry 1 at two lateral planes ($z/d = 0$ and $1/2$) for three blowing ratios ($M = 0.45, 0.75$ and 1.05).

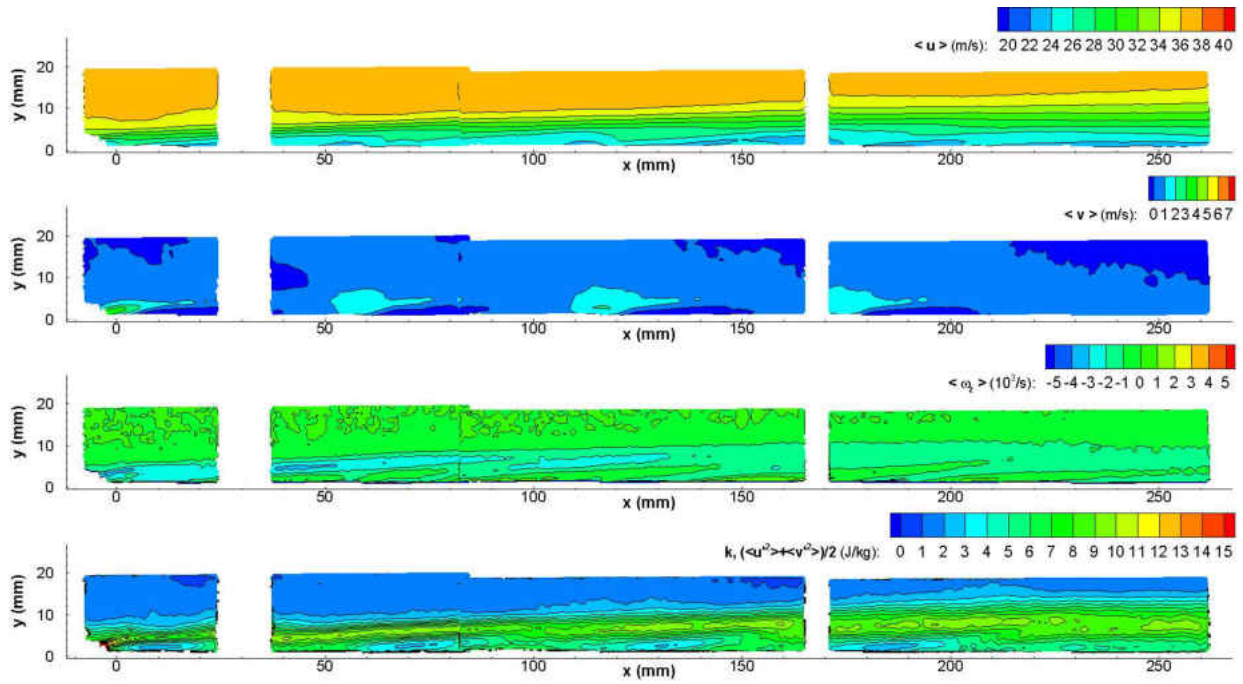


Figure 4.11: $u(x, y)$, $v(x, y)$, $\omega_z(x, y)$ and $k(x, y)$ for $M = 0.75$ at the $d/2$ plane

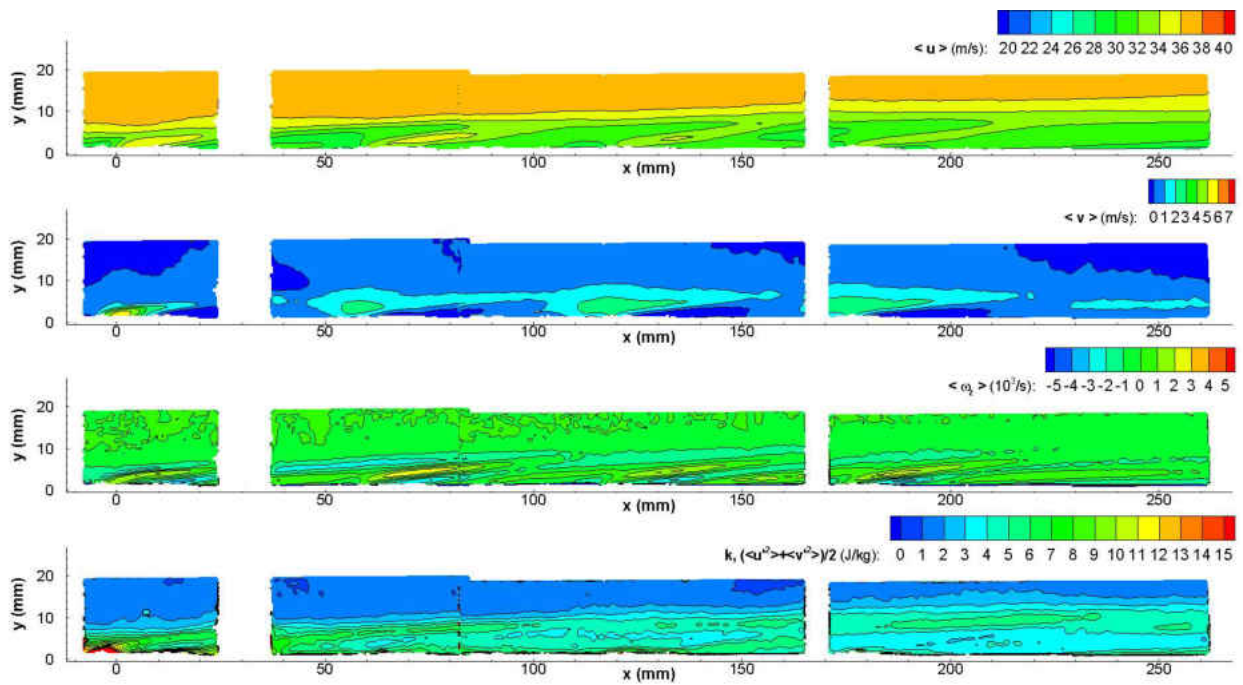


Figure 4.12: $u(x, y)$, $v(x, y)$, $\omega_z(x, y)$ and $k(x, y)$ for $M = 1.05$ at the $d/2$ plane

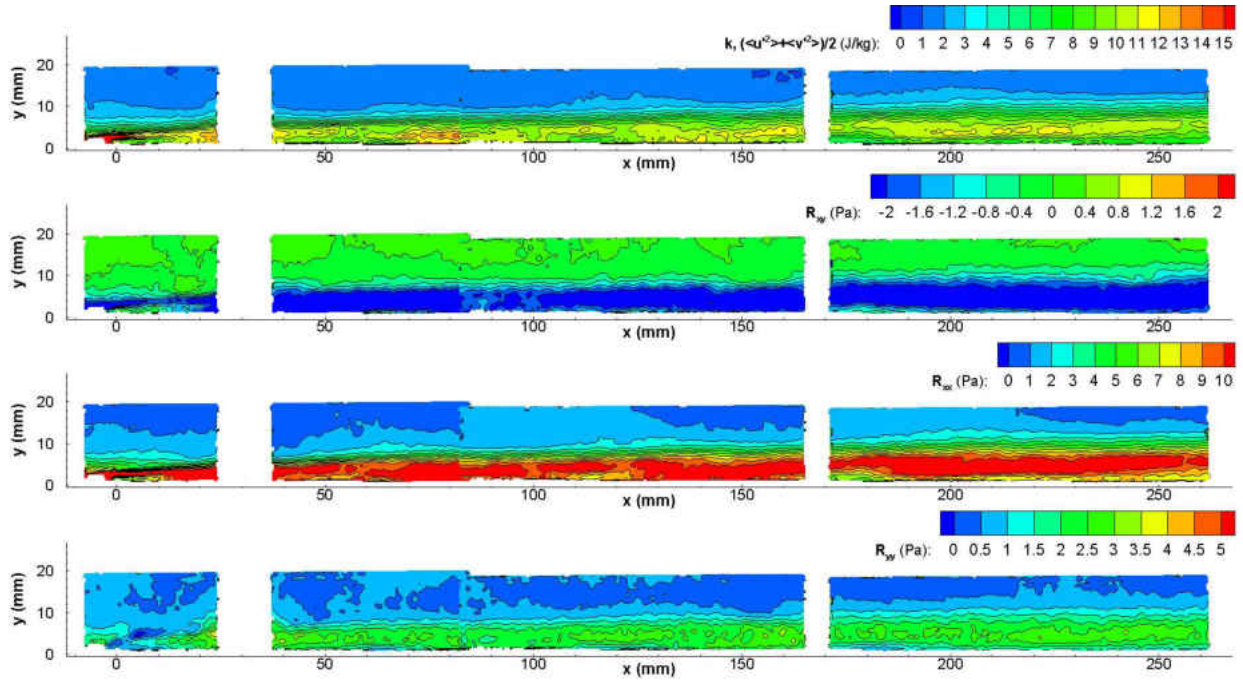


Figure 4.13: $k(x, y)$, $R_{xy}(x, y)$, $R_{xx}(x, y)$ and $R_{yy}(x, y)$ for $M = 0.45$ at the $d/2$ plane

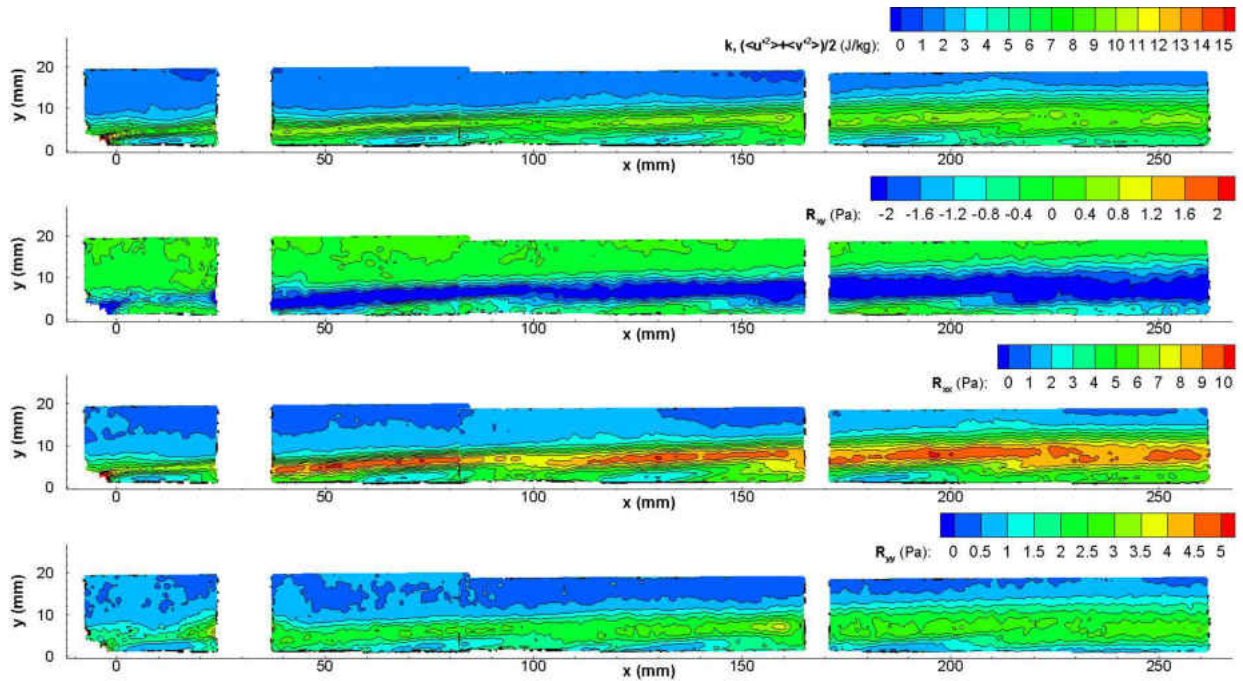


Figure 4.14: $k(x, y)$, $R_{xy}(x, y)$, $R_{xx}(x, y)$ and $R_{yy}(x, y)$ for $M = 0.75$ at the $d/2$ plane

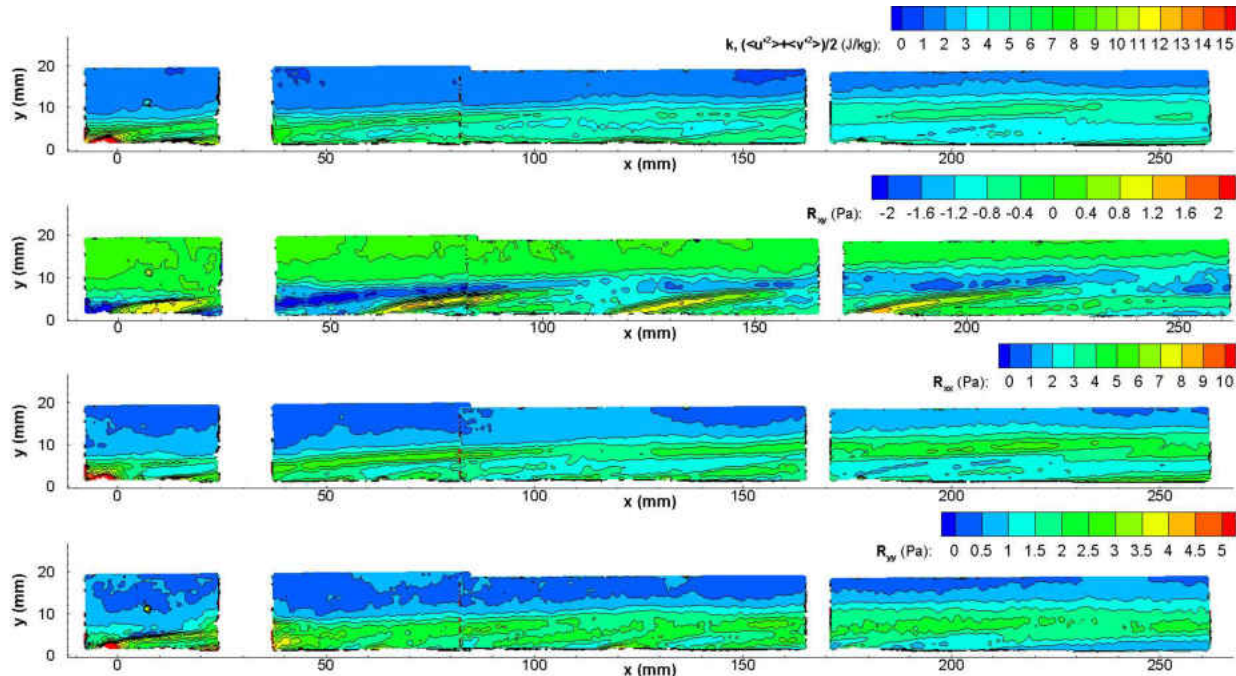


Figure 4.15: $k(x, y)$, $R_{xy}(x, y)$, $R_{xx}(x, y)$ and $R_{yy}(x, y)$ for $M = 1.05$ at the $d/2$ plane

- Turbulence levels are higher for $M = 0.45$ compared with the other blowing ratios tested. This is a result of more shearing between coolant jets and primary flow.
- Reynolds stresses are seen to be highly anisotropic
- Vorticity mimics turbulent shear stress, both track the flow gradient closely
- As blowing ratio increases, peak turbulent kinetic energy values drop in magnitude and location of peak moves away from the wall
- Lateral plane of $z/d = 1/2$ exhibits similar trends to centerline plane with the difference being lower magnitudes for most values

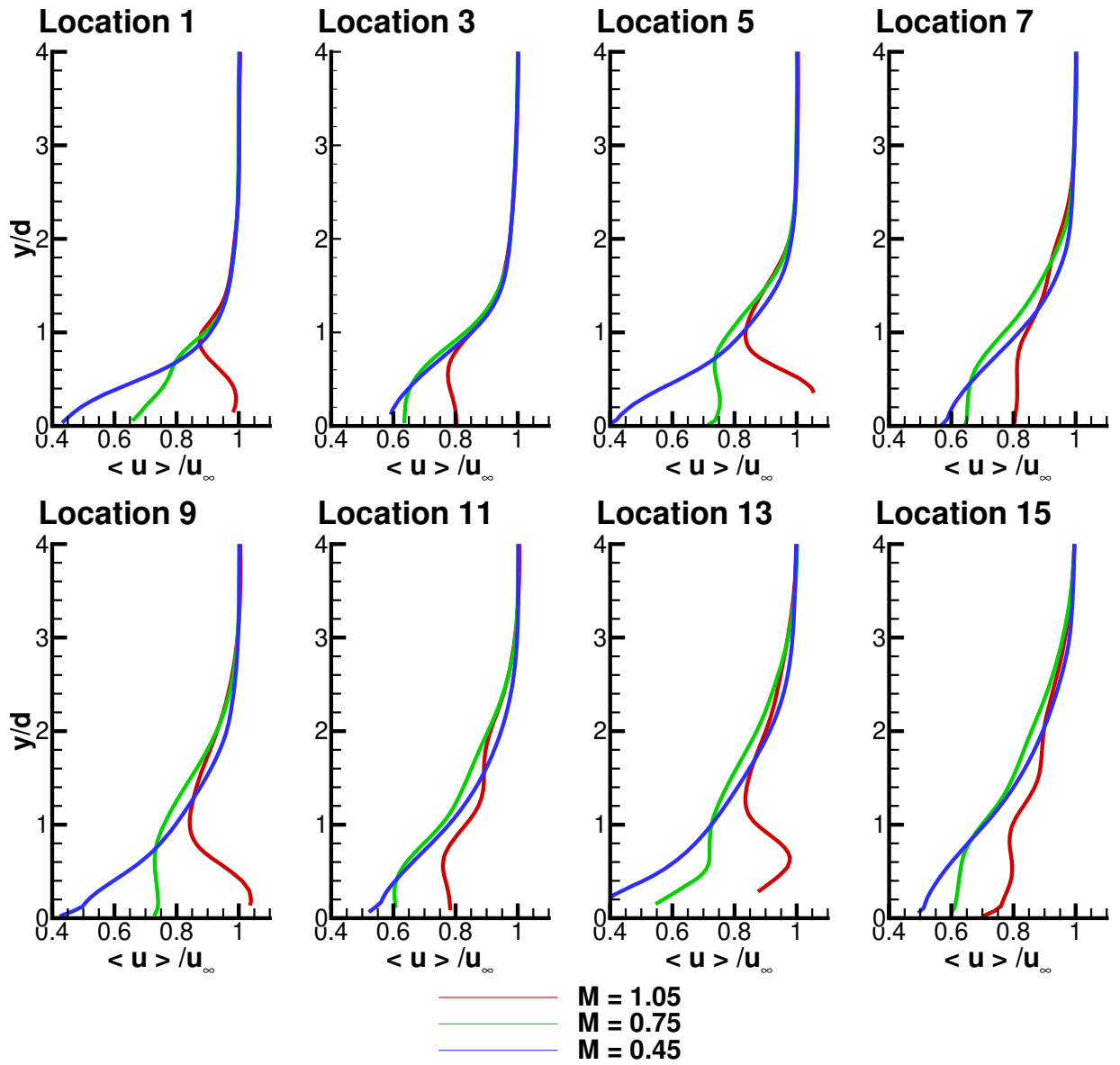


Figure 4.16: PIV measurements of streamwise velocity at row trailing edge breakout locations

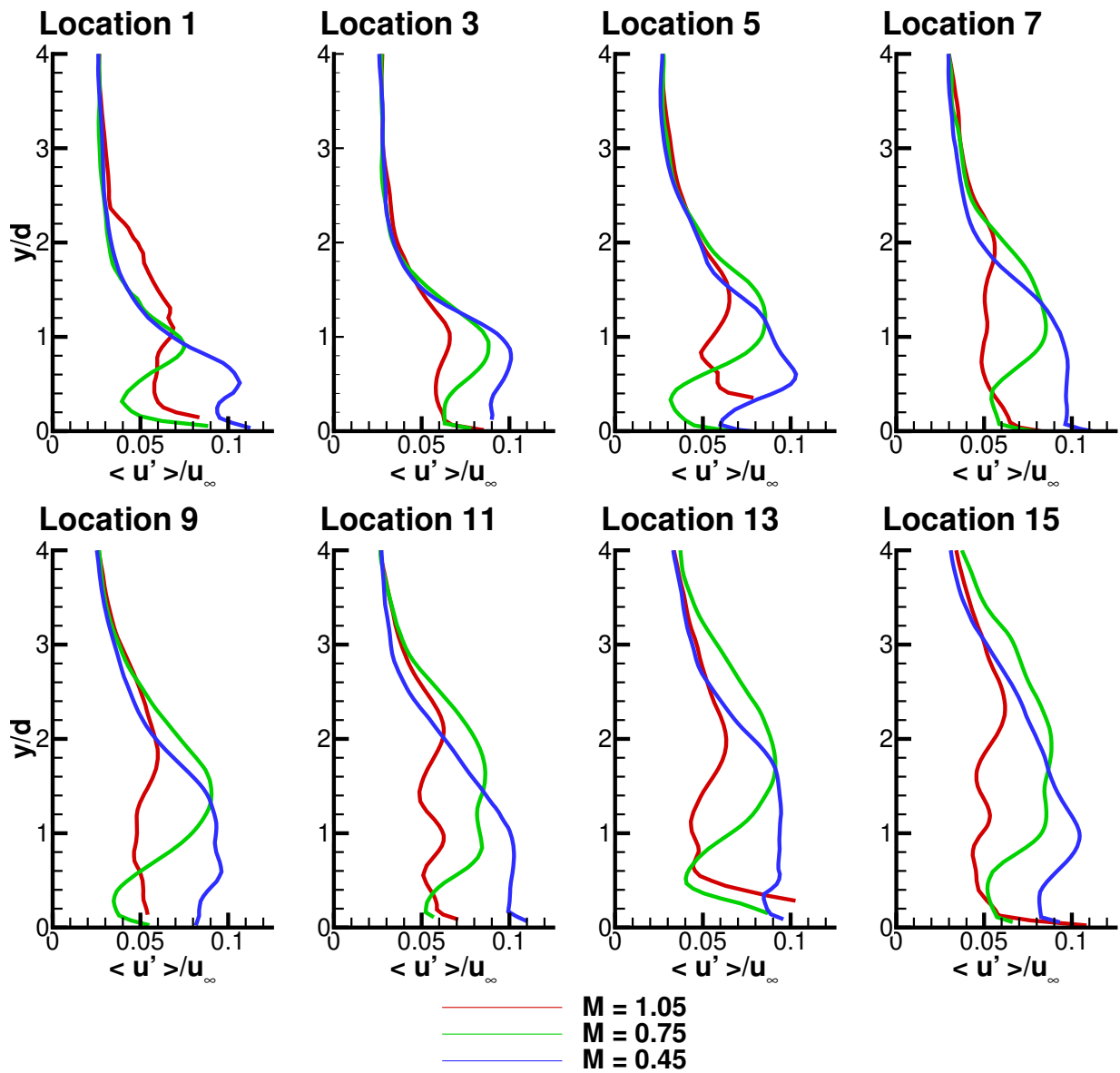


Figure 4.17: PIV measurements of RMS streamwise velocity at row trailing edge breakout locations

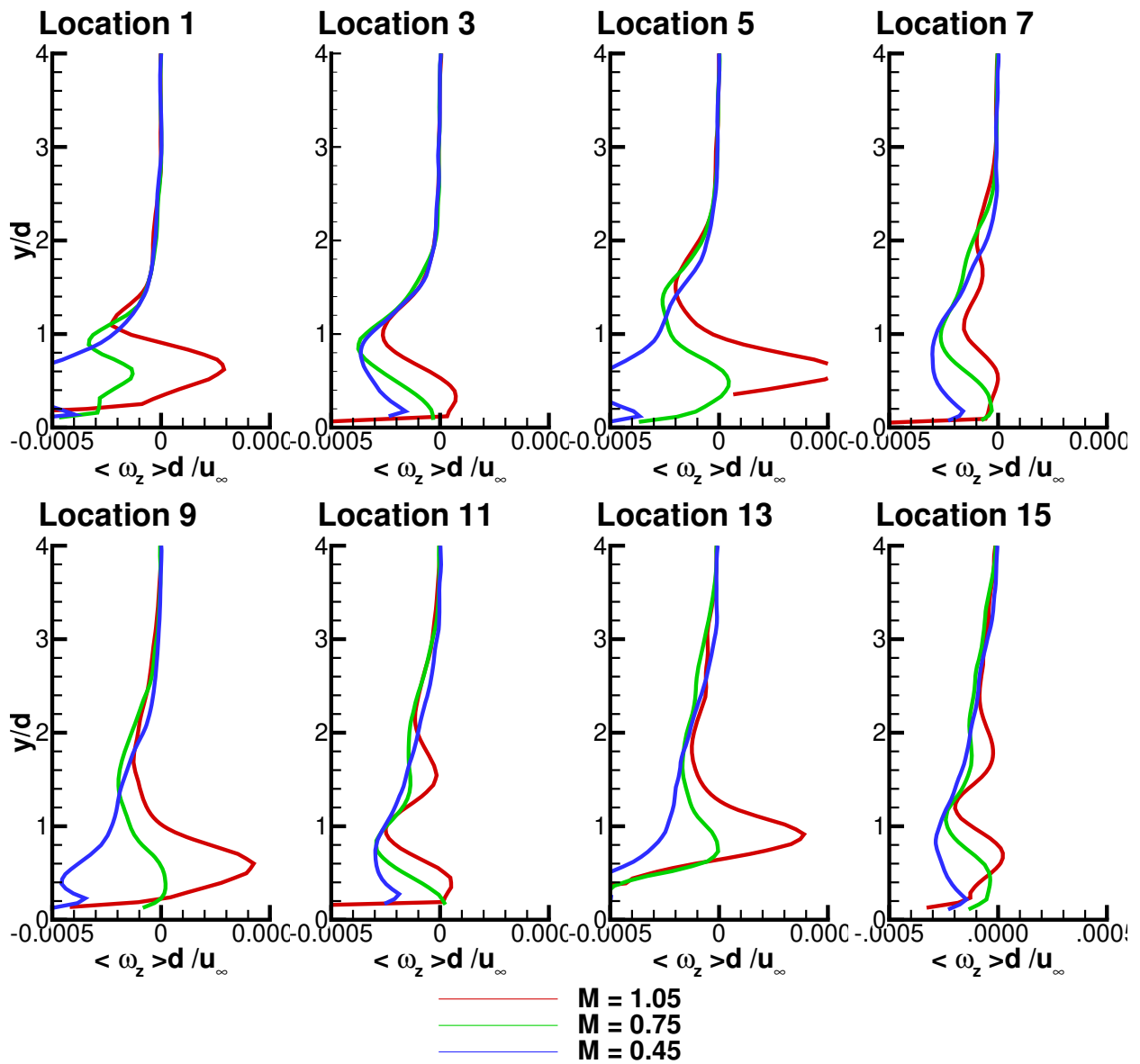


Figure 4.18: PIV measurements of mean lateral vorticity at row trailing edge breakout locations

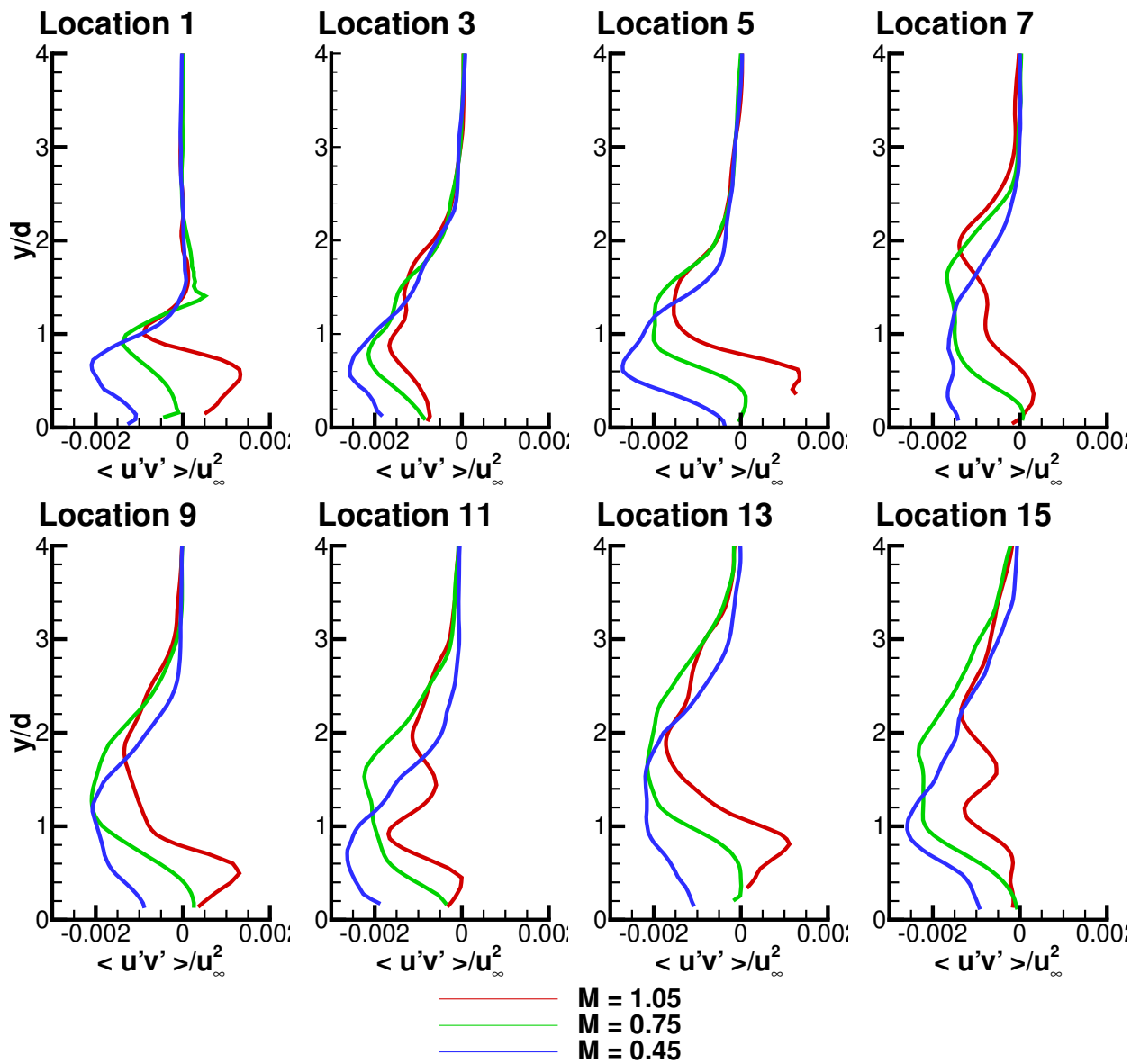


Figure 4.19: PIV measurements of turbulent shear stress at row trailing edge breakout locations

CHAPTER 5

ADIABATIC FILM COOLING EFFECTIVENESS

In this chapter measurements of adiabatic film cooling effectiveness, η , are presented. These measurements can be broadly divided into PSP experimental methodology and uncertainty and multi-row testing results.

First the heat and mass transfer analogy is reviewed, with historical examples of its use for measuring heat transfer scenarios by analogous mass transfer experiments, §5.1. Then an introduction of the PSP technique is presented in §5.2. The PSP measurement system and some methodologies are described in §5.3. PSP calibration hardware and methodology are described in §5.4. The processing procedure for PSP results is documented in §5.5. Several aspects related to PSP uncertainty are discussed in §5.6. Single row film cooling results are presented in §5.7. Aspects related to uncertainty quantification which incorporate the system values which required experimental data are discussed in §5.8. Next, multi-row results are presented in §5.9. Finally conclusions are presented in §5.10.

5.1 The Heat and Mass Transfer Analogy

Mass transfer measurements of the thermal film cooling problem date as far back as film cooling itself. Pedersen [9] and Whitelaw [71] used discrete gas sampling ports to draw out near wall fluid mixtures, from which adiabatic film cooling effectiveness was obtained. Goldstein and Jin [72] used naphthalene sublimation to obtain film effectiveness.

The basis of this comparison is the similarity between the transport equations for species and energy. The differential equations of a laminar boundary layer after some assumptions are given by Equations 5.1 and 5.2, [73].

$$\mathbf{G} \cdot \nabla i - \nabla \cdot (k \nabla T) = 0 \quad (5.1)$$

$$\mathbf{G} \cdot \nabla m_j - \nabla \cdot (\rho D_j \nabla m_j) = 0 \quad (5.2)$$

γ_j : mass-diffusion coefficient for substance j in a mixture, ρD_j $kg/m/s$

D_j : mass-diffusion coefficient for component j in a mixture, m^2/s

m_j : mass concentration (mass fraction) of substance j in a mixture

If the two diffusion coefficients, $\alpha \equiv \frac{k}{\rho C_P}$ and D are equal, i.e. the Lewis number, $Le \equiv \frac{\alpha}{D} = \frac{k}{\rho C_P D} = 1$, then temperature and species should behave the same. The non-dimensional temperature difference should equal the non-dimensional concentration difference given in Equation 5.3

$$\eta = \frac{T_{aw} - T_1}{T_2 - T_1} = \frac{C_{iw} - C_1}{C_2 - C_1} \quad (5.3)$$

5.2 Pressure Sensitive Paint

Pressure sensitive paint (PSP) is composed of luminescent molecules suspended within an O₂ permeable binder. The luminescent molecules used are quenched in the presence of O₂ which limits the emissions intensity when the paint is exposed to higher O₂ concentrations.

5.2.1 PSP Photophysics

Due to oxygen quenching mechanisms the PSP emission is inversely proportional to the local O₂ concentration on the paint surface. It is convenient to compare any given emission or concentration to reference values. This is done by defining intensity ratio, IR , and pressure ratio, PR . The definitions are given in Equations 5.4 and 5.5 respectively.

$$IR = \frac{I_{ref} - I_{bg}}{I - I_{bg}} \quad (5.4)$$

$$PR = \frac{P}{P_{ref}} \quad (5.5)$$

One can determine the theoretical relationship between IR and PR . This is known as the Stern-Volmer relation, given in Equation 5.6

$$\Theta = A(T) + B(T)\Phi \quad (5.6)$$

where $A(T)$ and $B(T)$ are known as the Stern-Volmer coefficients. The temperature dependence of $A(T)$ is due to the thermal quenching as in TSP, while the temperature dependence of $B(T)$ is related to the temperature dependence of the oxygen diffusivity in the binder. Typically the coefficient $B(T)$ has a stronger temperature dependence.

In practice the relation between Θ and Φ is not strictly linear so it is recommended by Liu and Sullivan [74] to use a third order polynomial such as Equation 5.7.

Calibration relation

$$PR = c_3 IR^3 + c_2 IR^2 + c_1 IR + c_0 \quad (5.7)$$

In calibration the intensity is recorded as a function of pressure ratio and then this is inverted to yield a relation for pressure ratio as a function of intensity ratio.

5.2.2 Effectiveness from Pressure Ratio

Traditionally the PSP technique was applied to high speed flows but has also produced promising results in film cooling studies. Zhang and Fox [75] pioneered the use of pressure sensitive paint to measure film cooling effectiveness, and compared the results using PSP to those obtained via gas chromatography. They determined that the data obtained using the pressure sensitive paint technique was superior to that of data obtained using gas chromatography. Jones [76] analyzed the effect of studying the film cooling thermal problem with foreign gases as the coolant. He related the temperature definition of adiabatic film cooling effectiveness to a mass fraction ratio, even in the presence of temperature differences. Charbonnier [77] worked from Jones analysis and represented adiabatic effectiveness in terms of partial pressures, what PSP is intended to measure, and a molecular weight ratio between the foreign (coolant) gas and the mainstream. The Charbonnier definition of effectiveness, Equation 5.8, is the definition most commonly used by researchers. Figure 5.1 plots Equation 5.8 with values for $MW > 1$, $MW = 1$ and $MW < 1$.

$$\eta = 1 - \left[1 + MW \left(\frac{PR_{air}}{PR_{fg}} - 1 \right) \right]^{-1} \quad (5.8)$$

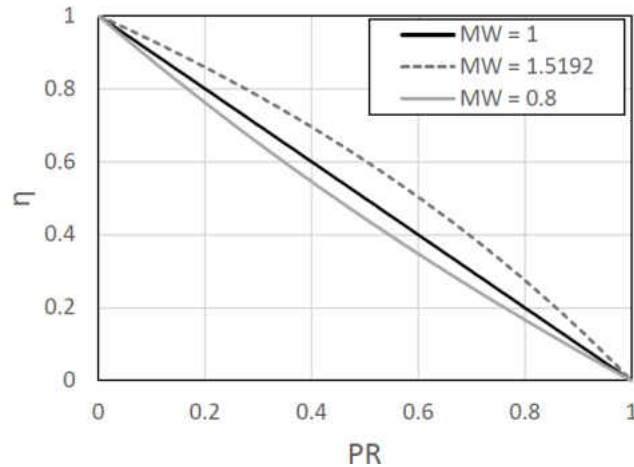


Figure 5.1: Relation between pressure ratio and adiabatic film cooling effectiveness for different molecular weight ratios ($MW = 1.5192$ corresponds to injection of pure CO_2)

Wright et al. [?] assessed three different steady state techniques for measuring flat plate film cooling effectiveness: PSP, TSP, and IR thermography. They concluded the superior technique is PSP. Data obtained from heat transfer techniques are known to have conduction effects around areas near the film holes. This lowers the integrity of the data, and is an unavoidable problem associated with heat transfer techniques. PSP utilizes a mass transfer analogy, which allows for data near the holes to be obtained. Han and Rallabandi [78] tie in the aforementioned studies and provide a comprehensive review of film cooling in gas turbines. They provide insight into the theory and assumptions that must be taken into account when utilizing PSP and invoking the mass transfer analogy, and then describe the uncertainties that should be taken into consideration when using the technique.

5.3 PSP Experimental Setup

5.3.1 PSP Preparation and Test Methodology

The aluminum film cooling test coupon was prepared (painted and cured) in the same manner as the calibration coupon which was previously described in this manuscript. Once the coupon is painted and cured, it is placed inside the test section. The plenum is then mounted to the test section. The same camera and LED spotlight are already in the correct location directly above the aluminum test coupon, from the semi-in-situ calibration. The frame of the wind tunnel is made of 80/20 aluminum extrusion. Roc-lon blackout fabric is mounted around the frame of the wind tunnel in order to block out any ambient lighting which could leak into the tunnel and affect the tests.

There are three different series of images required to obtain adiabatic effectiveness measurements. 20 images are taken for each type. The images are taken using the same camera, camera orientation, and camera location described in the calibration setup. The first image type is a background image, which is an image with all house lights and LEDs off, and flow off. This image is subtracted from all subsequent images to reduce systematic CCD error. The second image is a reference image taken twenty minutes after the tunnel has been turned on with the LEDs on and the coolant flow off. It is taken after twenty minutes to allow for the tunnel to achieve a thermal steady state, and minimize the difference between the reference temperature and the mainstream temperature of the other test images. The third image is the test image, taken with the house lights off, the LEDs on, flow on, and coolant on. Before taking this image, care must be taken in order to make sure that the coolant plenum is fully purged of all air, and that only CO₂ is flowing in the plenum and film holes. The coolant flow rate is measured using a venturi flow meter.

5.3.2 CCD camera

The camera used in this experiment is a Cooke Corporation pco.1600.

The parameters relevant to the camera are listed in Table 5.1,

Table 5.1: pco.1600 camera characteristics

	Setpoint	pco.1600
Pixel Array		1600x1200
Full Well (e^-)		40,000
Temperature ($^{\circ}$ C)	@ 20 $^{\circ}$ C typ.	-30
Dark Current ($e^-/pixel$)	@ 20 $^{\circ}$ C typ.	0.5
	@ -20 $^{\circ}$ C typ.	0.01
Readout Noise (e^-)	@ 10 / 40 MHz	10 / 21
Quantum Efficiency (%)	@ 500 nm typ.	55

5.3.3 Paint

UniFIB PSP from ISSI was used in this experiment [79]. UniFIB is a blend of FIB, dye, and a white pigment. It is a single application system. It is designed to yield a high pressure sensitivity with a low temperature sensitivity (FIB). Pressure sensitivity of 0.7% per kPa. Temperature sensitivity 0.5 % per $^{\circ}$ C. Photo-degradation rate of 1% per hour.

5.4 PSP Calibration

The calibration of PSP involves a controlled experiment to determine the quantitative relation between O_2 pressure ratio, PR , and PSP emission intensity ratio, IR .

This section describes the calibration hardware and coupon preparation procedure in §5.4.1. The calibration procedure is described in §5.4.2.

The theoretical relation between IR and PR is given by the Stern-Volmer equation, Equation 5.6; however, it is recommended to use a third-order polynomial such as Equation 5.9.

$$PR = c_3IR^3 + c_2IR^2 + c_1IR + c_0 \quad (5.9)$$

UniFIB PSP from Innovative Scientific Solutions, Inc. (ISSI) was used in this study. UniFIB is a blend of FIB, dye, and a white pigment. It is a single application system designed to yield a high pressure sensitivity with a low temperature sensitivity (FIB). It has a pressure sensitivity of 0.7% per kPa and temperature sensitivity of 0.5% per °C. UniFIB has a photo-degradation rate of 1% per hour, when being exposed to an excitation wavelength [79]. Kameda et al. [80] studied the effect of humidity on a pressure sensitive paint. They found a linear relation between relative humidity and PSP emission. This is only a problem when the relative humidity changes in between reference and test images. The relative humidity of the air is measured during each calibration experiment and during the effectiveness testing. Throughout a single test, the relative humidity varies no more than 5%.

A proper calibration is necessary in order to correctly quantify the uncertainty in pressure ratio and in converting pressure ratio into effectiveness. A series of calibrations are performed at our facilities in order to quantify and understand this uncertainty.

5.4.1 Calibration Setup

The calibration chamber is connected to a vacuum pump (0.4 kW direct drive Hitachi). There is a Peltier heater placed on a heat sink which allows calibration at several temperatures. The coupon is mounted on the heater with thermal paste in order minimize contact resistance. There is a acrylic plate on the top section of the pressure vessel to allow optical access.

The calibration coupon is aluminum. Half the surface is milled down to expose non-oxidized aluminum. There are embedded thermocouples (RTD) just under the painted surface.

Calibration coupon preparation

- coupon is cut from aluminum and half the surface is milled down by 0.005" on a router
- Holes are drilled into the edge of the coupon to allow insertion of TC/thermistor near the painted surface
- TC is thermally cemented into the coupon
- Primer is applied to half of each side
- Paint is applied
- Paint is cured

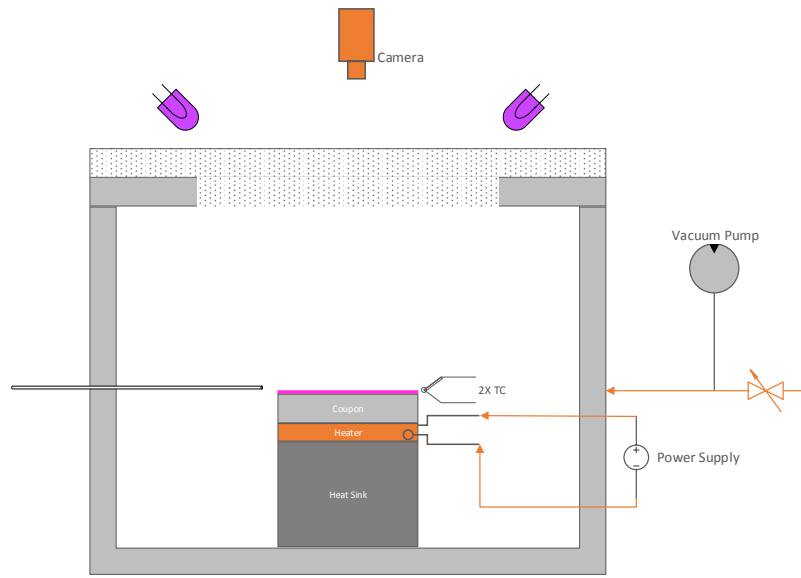


Figure 5.2: PSP calibration facility

A $5 \times 5 \text{ cm}^2$ aluminum coupon is used for the calibration. The calibration vessel is also made of aluminum, and is fitted with an acrylic plate on the top section of the pressure vessel to allow optical access.

The preparation of the calibration coupon and test section are identical. The coupon for this study has two halves: a factory surface or oxidized surface, and a surface milled down 0.005, to expose non-oxidized aluminum in order to examine the effect of surface finish on the painting and calibration. Primer was not used on the coupons because they are aluminum, which means they are already ideal surfaces to apply PSP to.

The coupon is painted with UniFIB PSP from ISSI using a Paashe TG-3F airbrush. Eight cross-coats of the paint are applied as directed by ISSI. One coat consists of spraying the coupon from left to right, and then right to left. The coupon is then turned 90°C and coated again from left to right, and right to left. This is done in order to prevent streaking and to produce an even coat of paint on the whole surface [10]. The coupon is then baked at 70°C for 3 hours, in order to minimize the temperature sensitivity of the paint.

An Omega HHP-242 0-30 PSI pressure transducer is used to measure the pressure inside the vessel. The absolute accuracy of this pressure transducer is found to have a noticeable impact on the overall uncertainty of using PSP for adiabatic film cooling effectiveness measurements. In the results present in this work, the accuracy is 206.8 Pa. The aluminum coupon and the calibration vessel are each fitted with two T-type thermocouples to ensure a minimum temperature difference between the ambient temperature inside the vessel (which can affect the temperature of the painted surface) and the temperature of the coupon.

The coupon is glued onto a Peltier heater with Dow corning 340 silicon heat sink compound (thermal paste) and placed inside a sealed chamber. The Peltier heater not only allows the difference in temperature between the coupon and the vessel to be minimized, but also allows calibration at several temperatures.

A 460 nm LED from ISSI (model: LM2X-460) is used to illuminate the calibration coupon. A 14-bit CCD camera (pco.1600) with a 590 nm long pass filter was used to obtain the calibration data. The calibration chamber sits on top of the wind tunnel. The camera is mounted above the wind tunnel and the lens looks down towards the floor. The camera and lighting orientation used during calibration is the same set up used for the effectiveness tests, and the camera is in the same location for the calibration of the PSP and for the film cooling experiments.

5.4.2 Calibration Procedure

The calibration vessel is connected to a vacuum pump (0.4 kW direct drive Hitachi). During the calibration, air is systematically drawn from the vessel using the vacuum pump. The calibration begins at atmospheric pressure and the cavity is incrementally purged to the lowest pressure achievable using the vacuum pump, then incrementally allowed to reach atmospheric again. This cycling is important to allow a real estimate of the variability of the PSP at $PR = 1$ ($\eta = 0$). Pictures are taken using Camware, a software from PCO. The lowest pressure ratio the calibration system used could achieve was $PR = 0.04$. In order to achieve a pressure ratio of 0, the calibration vessel is purged with CO_2 . This is important in order to avoid non-physical extrapolations of the calibration outside the calibration range. A pressure ratio of 0 corresponds to $\eta = 1$ which is an important point which cannot be overlooked.

Three different coupons, each with two different surface finishes, were painted and calibrated over 6 different days. All calibration data obtained from every coupon from every day of testing are used to generate the calibration curve which is used to calculate effectiveness. This results in a larger, albeit more realistic, uncertainty. Both the oxidized and milled sides provided the same calibration results.

There are three different types of images taken during the calibration. The first image is a background image, which is taken and subtracted from all images to reduce the background noise. This image is taken with house lights off and LEDs off, at reference (atmospheric) pressure. The second image is the reference image, which is taken with house lights off and LEDs on, at reference pressure. The third type of image is the test image, which is taken with the house lights off, LEDs on, at the test pressure.

Each image set consists of 20 images, averaged to reduce noise. Initially, 100 images were taken and averaged. Figure 2 illustrates that the mean intensity converges to less than 0.5% error after averaging only 20 images, which is why 20 images are taken for the rest of the experiments. The entire region of the calibration coupon is averaged (65k pixels) for a single calibration point.

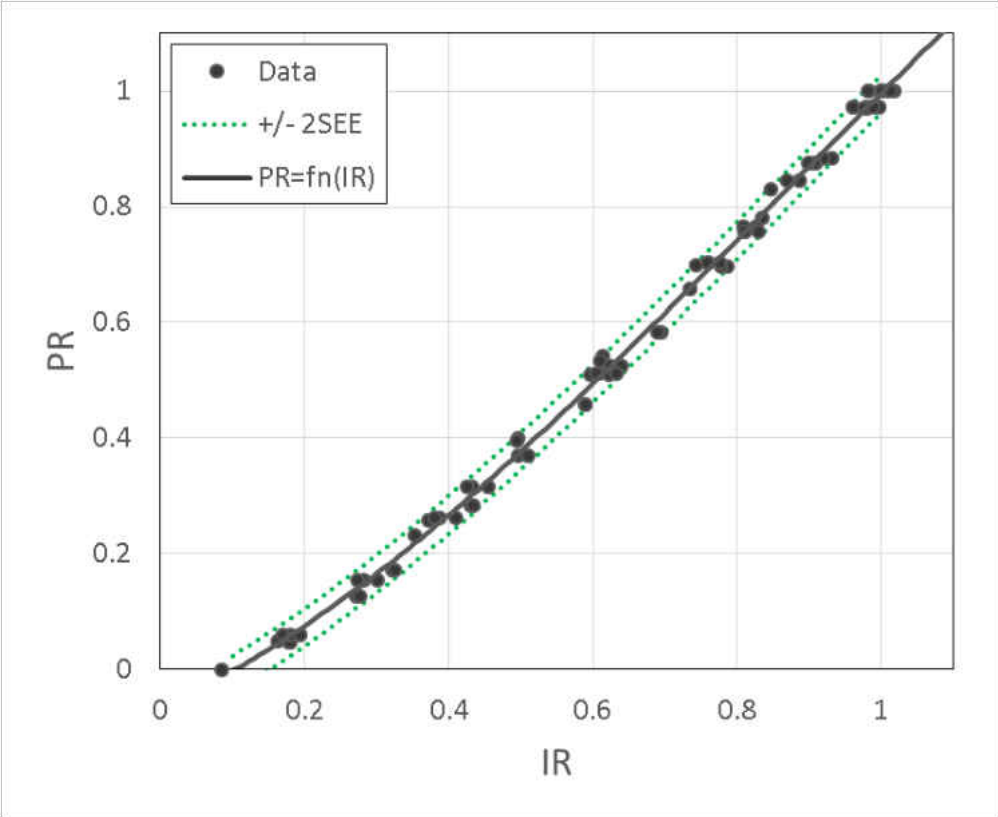


Figure 5.3: PSP calibration

5.5 Processing

The overall steps from going to the raw PSP images to final adiabatic effectiveness results are outlined below. This process was carried out by a custom Matlab code which is included in Appendix F.

1. Beginning with `.tif` images of the PSP emission and a table of measured pressures and temperatures
2. Take the image sets and calculate average and standard deviation
3. Calculate spatial resolution of images, pixels per meter, using film holes as reference marks
4. Generate x/d and z/d vectors
5. Define thermophysical properties of coolant and mainstream
6. Load averaged images
7. Calculate intensity ratio according to Equation 5.4
8. Map to a set x/d and z/d (every $d/10$ in both directions) coordinate system to allow point by point comparison between tests such as that shown in Chapter 5 §5.7.1
9. Calculate PR from IR according to Equation 5.9 with the constants obtained during calibration
10. Calculate η according to Equation 5.8
11. Calculate $\bar{\eta}$ according to Equation 5.37
12. Extract centerline profiles from horizontal lines shown in Figure 5.4
13. Extract η values obtained from gas sampling tap regions (detailed in Chapter 5 §5.9.6))
14. Extract $\eta = 0$ samples for uncertainty quantification (detailed in Chapter 5 §5.8.1)

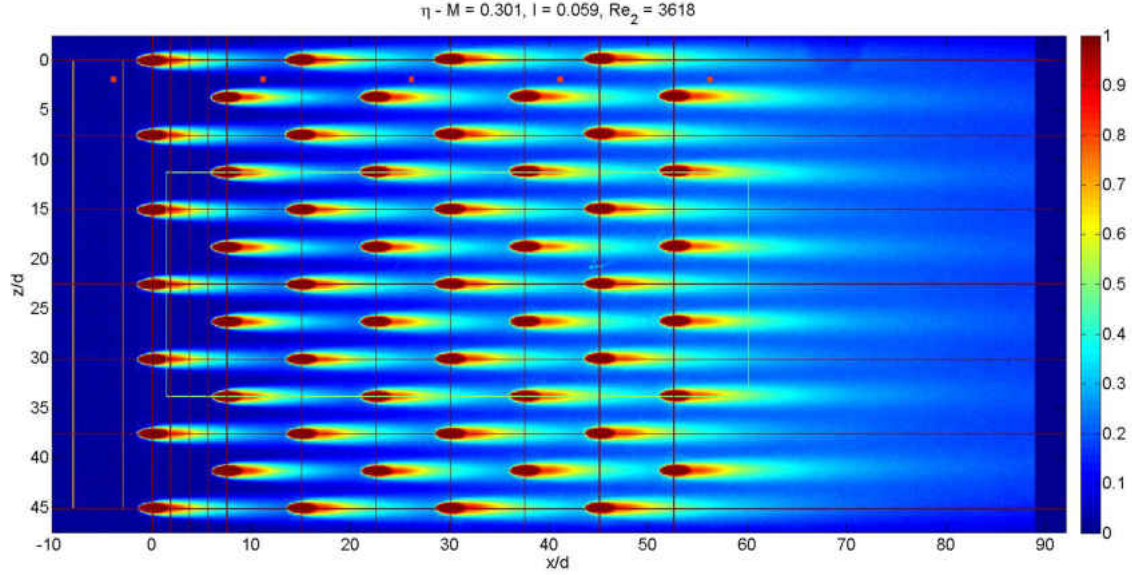


Figure 5.4: Locations from which data was taken for centerline, gas sampling, lateral average, area average and $\eta = 0$ sampling

5.6 Uncertainty Estimation

Liu and Sullivan describe sources of PSP error in [74] which are repeated here in Table 5.2. This section quantitatively assesses some of these error sources. The sensitivity coefficients for the PSP data reduction equations are determined in §5.6.1. CCD parameters and their impact on uncertainty are discussed in §5.6.2. Convergence of the intensity sample means is shown in §5.6.3. Temporal degradation of the PSP emission and thermal effects influencing PSP emission are discussed in §5.6.4 and §5.6.5 respectively.

Table 5.2: Sources of PSP error

#	Error Source	Category	Studied
1	Paint degradation	PSP property	y
2	Model motion (spatial variation of intensity)	Model motion / deformation	n
3	Illumination (time variation of intensity)	LED property	y
4	Photodetector noise, reference	CCD property	y
5	Photodetector noise, test	CCD property	y
6	Model motion (camera distance)	Model motion / deformation	n
7	Illumination (spectral variation)	LED property	n
8	Model motion (paint thickness)	Model motion / deformation	n
9	Model motion (measurand spatial variation)	Model motion / deformation	n
10	Model motion (excitation spatial variation)	Model motion / deformation	n
11	Measurement uncertainty in P_r	Measurement uncertainty	N/A
12	Temperature effect of PSP	PSP property	y
13	Calibration coefficient uncertainty	Measurement uncertainty	y
14	Calibration coefficient uncertainty	Measurement uncertainty	y
15	Model deformation	Model motion / deformation	n

5.6.1 Propagation of Error Sensitivity Coefficients

At this point we would like to understand the sensitivity of certain inputs and their impact on the parameter of interest, film effectiveness η .

We would like to control the uncertainty in PR because that will directly impact the uncertainty in effectiveness. To understand the sensitivity with respect to PR we take Equation 5.8 for the definition of effectiveness and calculate the sensitivity coefficient according to ASME PTC 19.1 [81]:

$$\frac{\partial \eta}{\partial PR} = \frac{MWPR_{air}}{PR^2 \left[MW \left(\frac{PR_{air}}{PR} - 1 \right) + 1 \right]^2} \quad (5.10)$$

Figure 5.5 shown the uncertainty in effectiveness, u_η , for different errors in PR .

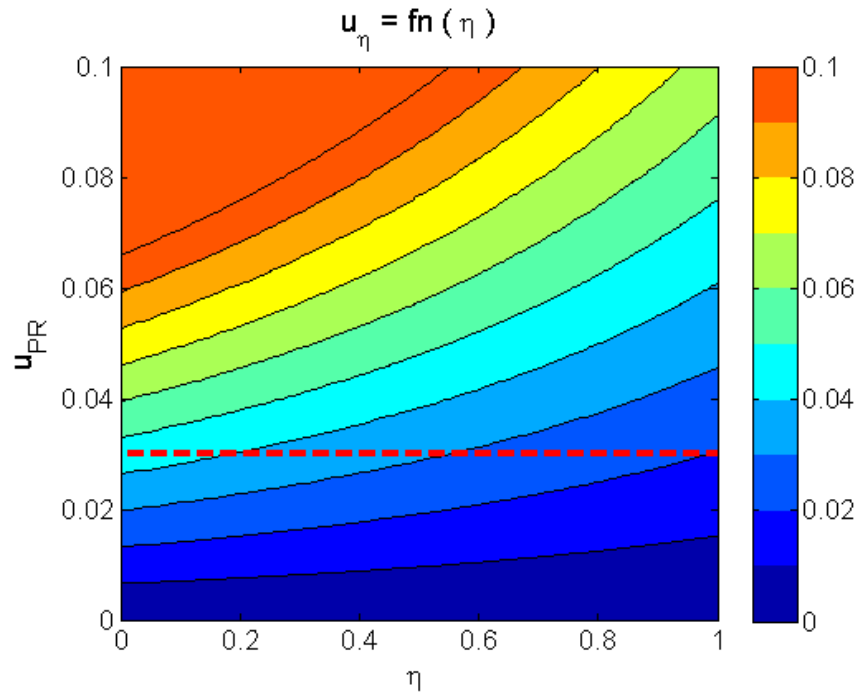


Figure 5.5: Propagation of error estimate, using Equation 5.8, for uncertainty in effectiveness due to error in pressure ratio (red dashed line shows $2SEE = 0.032$ error from calibration)

A slice from Figure 5.5 corresponding to the red dashed line, $2SEE = 0.032$, is shown in Figure 5.6.

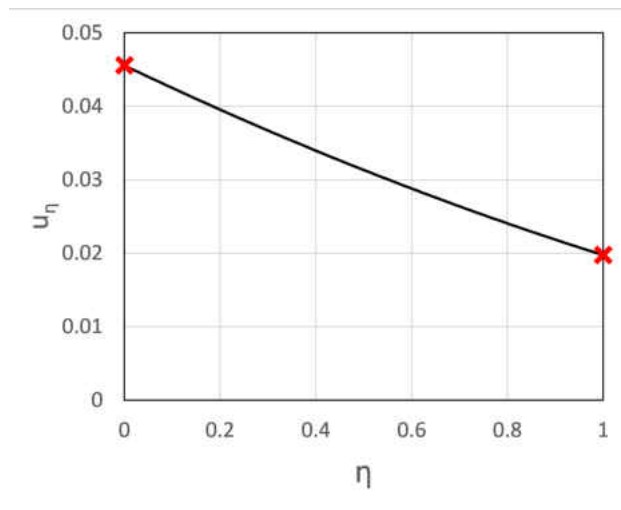


Figure 5.6: $u_{\eta}(\eta)$

It helps to take the limits for the ranges of PR corresponding to the bounds of effectiveness (for CO_2 injecting into air, $MW \equiv MW_{fg}/MW_{air} = 1.5192$).

$$u_\eta(\eta = 0) = MW u_{PR} \quad (5.11)$$

$$u_\eta(\eta = 1) = \frac{u_{PR}}{MW} \quad (5.12)$$

In the case of CO_2 injection the molecular weight ratio MW is greater than 1. As a result the uncertainty of a low effectiveness measurement is higher than that of a high effectiveness measurement. These expressions also allow a quantitative goal for u_{PR} in order to meet certain uncertainty requirements. For example, if no more than 0.01 uncertainty is required at $\eta = 0$, an uncertainty in PR of 0.0065 is necessary.

Currently, the pressure ratio with air as coolant, PR_{air} , is taken as 1 over the entire field. The experiments of interest for this study are low speed ($Mach < 0.15$) and hence will experience a maximum error of 1% due to this assumption. There is a trade off between this error due to compressibility effects and the error associated with taking the PR_{air} image. From the uncertainty analysis presented already, it is clear that more random uncertainty will be incurred by taking this image than systematic uncertainty due to the assumption of $PR_{air} = 1$. However, in cases where this is not the case, higher Mach number flows, Equation 5.13 can be used to understand the uncertainty.

$$\frac{\partial \eta}{\partial PR_{air}} = \frac{PRMW}{[PR(MW - 1) - MW(PR_{air})]^2} \quad (5.13)$$

Now, spatially resolved uncertainty of film effectiveness is calculated considering the parameters shown in Figure 18 and according to the methodologies described in [81]. Systematic errors are surely present; however, they are considered negligible for the analysis to avoid improper estimations. For a third-order curve fit, the sensitivity of PR with respect to IR is given by Equation 5.14 for a third-order calibration.

$$\frac{\partial PR}{\partial IR} = 3c_3IR^2 + 2c_2IR + c_1 \quad (5.14)$$

The calibration data is fit to a third-order polynomial shown in Figure To estimate the error of the curve fit the Standard Estimate of Error (SEE) from this calibration Equation 5.15 is used,

$$SEE = \sqrt{\frac{1}{N-4} \sum_{i=1}^N (y_i - y_c)^2} \quad (5.15)$$

$$s_{\hat{y}} = \frac{S_{yx}}{\sqrt{N}} \quad (5.16)$$

This error estimate is combined with other sources of error for PR , such as uncertainty in IR and potentially uncertainty in temperature, according to the ASME PTC 19.1 [81]. For the current study, values of $SEE = 0.016$ and $s_{\hat{y}} = 0.0017$ were calculated which correspond to a linear least squares analysis. If a more detailed analysis considering uncertainties in IR and PR were needed, a total least squares analysis would be used. This study will use the linear least squares, consistent with ASME PTC 19.1.

In this experiment, 20 samples are taken for each image set ($\nu_{I_{bg}} = \nu_{I_r} = \nu_I = 19$). Three image sets are required to build intensity ratio. The standard deviation of the sample is calculated for each image set. The random standard uncertainty of the sample mean is calculated for each image set. This uncertainty is propagated through to intensity ratio (s_{IR}, ν_{IR}). The partials of IR are given by the following expressions:

$$\frac{\partial IR}{\partial I_r} = \frac{1}{I_t - I_{bg}} \quad (5.17)$$

$$\frac{\partial IR}{\partial I_t} = -\frac{I_r - I_{bg}}{(I_t - I_{bg})^2} \quad (5.18)$$

$$\frac{\partial IR}{\partial I_{bg}} = \frac{I_r - I_t}{(I_t - I_{bg})^2} \quad (5.19)$$

The sensitivity coefficient, θ_i , defined in Equation 5.20, relates the sensitivity of a parameter to a measured input.

$$\theta_i = \frac{\partial R}{\partial \bar{X}_i} \quad (5.20)$$

In this case we would like to determine the sensitivity of the calculation of η with respect to the measured intensity values. The expression for the individual sensitivity coefficients of effectiveness with respect to the measured parameters can easily be implemented via the chain rule and are shown in Equations 5.21 - 5.23.

$$\theta_{I_r} = \frac{\partial \eta}{\partial PR_{fg}} \frac{\partial PR}{\partial IR} \frac{\partial IR}{\partial I_r} \quad (5.21)$$

$$\theta_{I_t} = \frac{\partial \eta}{\partial PR_{fg}} \frac{\partial PR}{\partial IR} \frac{\partial IR}{\partial I_t} \quad (5.22)$$

$$\theta_{I_{bg}} = \frac{\partial \eta}{\partial PR_{fg}} \frac{\partial PR}{\partial IR} \frac{\partial IR}{\partial I_{bg}} \quad (5.23)$$

The uncertainty in pressure ratio takes the random standard uncertainty of the sample mean of intensity ratio into account as well as the uncertainty in the PSP calibration, $s_{\hat{y}}$. The calibration in this case takes 87 samples to provide a third-order polynomial relationship between intensity ratio and pressure ratio. The calibration resulted in a standard error of the curve fit $s_{\hat{y}} = 0.0017$. This standard curve fit error is an elemental error source which is combined with the elemental uncertainty in intensity ratio to yield an RMS of elemental random standard uncertainties of the mean from all sources for PR , i.e. $s_{PR} = \sqrt{((d(PR)/d(IR) * s_{IR})^2 + s_{\hat{y}}^2)}$. The RMS of elemental random standard uncertainties in PR , s_{PR} , is propagated through to effectiveness. The standard uncertainty, s_{η} , is then multiplied by 2 (t_{95} for $N = large$) to yield the total expanded uncertainty, [81] (systematic errors are not considered). This procedure is applied to each pixel of the test domain. Sample results of this process are shown in Figure 19.

5.6.2 CCD System Considerations

There are several variables contributing to the number of photons collected by each pixel in a given image. According to Crites and Benne [82]:

$$N = f(I_L, \lambda_L, R_l, \theta_l, \Omega, localpaintfilmefficiency(T), Q_{CCD}, N_D, N_Q, N_R, P) \quad (5.24)$$

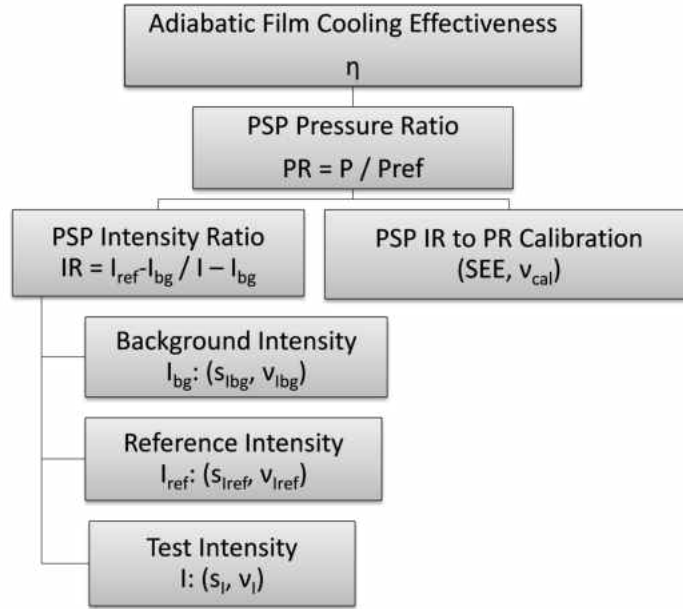


Figure 5.7: η propagation of error uncertainty tree

If we assume ideal conditions, i.e. no model deformation or motion and excitation source is perfectly stable in intensity and spectral content with no physical motion, then taking an image ratio removes all sources of error except dark current, read noise, and photon shot noise. Dark current is effectively removed as an error source by subtracting a dark image from all test images.

Based on this, the full well capacity of each pixel in the CCD is 40,000 photons.

Considering the random nature of light, the maximum signal to noise ratio can be calculated as 200. This is because light obeys a the Poisson distribution which, for large sample sizes, can be approximated as a normal distribution with the variance equal to the mean.

$$Signal \propto N \tag{5.25}$$

$$RandomNoise \propto \sqrt{N} \tag{5.26}$$

$$SNR_{max} \approx \sqrt{N_{max}} \tag{5.27}$$

For a full well capacity of 40,000 the maximum SNR is 200. On the other hand, if we consider the error introduced by camera resolution (bit count) the intensity or photon count resolution is $N_{max}/2^n$ where n is the number of bits. For the 14 bit camera used in the present study this resolution is 2.4 photons.

5.6.3 Sampling Convergence

To quantitatively assess the convergence of our estimator of a mean a series of 100 images was taken. A running average was calculated for each pixel. Figure 5.8 shows the convergence of several pixels normalized by their mean after 100 samples. This would be the convergence for an unbiased estimator. After 20 samples a 0.25% uncertainty can be obtained. For the experiments in this study 20 samples are taken to calculate each mean.

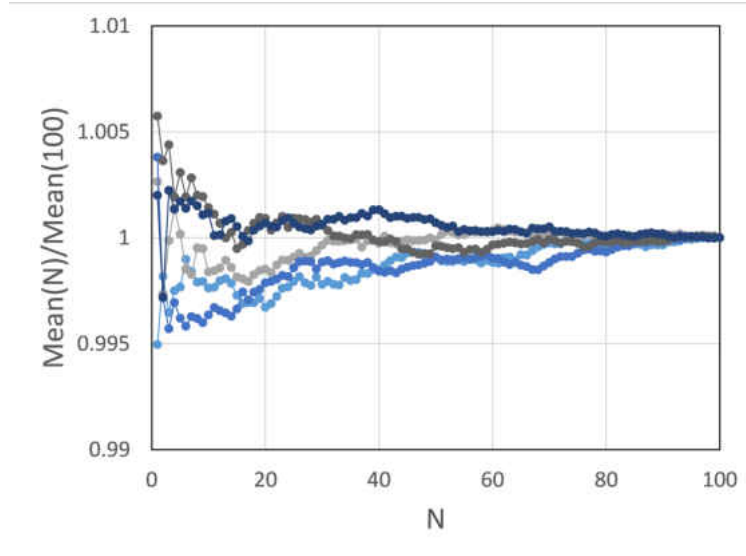


Figure 5.8: Convergence of estimator over 100 images

5.6.4 Temporal Degradation of Intensity

When testing film cooling in a wind tunnel, the paint can experience a degradation of intensity over time. Ideally, the intensity of PSP would not change over time. The luminescent intensity decreases with time due to photo-degradation of a luminophore (Egami and Asai [83]). There are two ways in which this can happen: the first is a prolonged exposure to the excitation light, and the second is the addition of any dust particles or oils that deposit on the painted test surface. According to Liu [84], this effect is irreversible, and is accelerated with temperature and excitation intensity.

Degradation testing - during initial calibrations time between successive points was very short so the lights were left on continuously. This resulted in a 5% difference between the pre-calibration reference image and the post-calibration reference image. This motivated a thorough look at the intensity degradation of the UniFIB.

- This is a semi-in-situ calibration (lights are mounted same as in testing, vessel is placed on test section)
- The aluminum coupon is prepared the same as in normal calibrations
- The temperature is maintained at room temperature (nominally 23 °C)
- The lights are left on the entire duration of the test (4 hours)
- Several images are taken over the course of the test
- After approximately 4 hours the lights were then turned off in between images to observe the degradation stop

To capture this effect, the calibration coupons were tested under constant exposure to the excitation LED. The tests were taken at reference (atmospheric) pressure and temperature. The coupons were exposed for 2 hours, the results from this test are shown in Figure 5.9. The first initial 30 minutes there is an increase of intensity. This is due to the LED approaching a steady state. This shows that a 1.5% error for an intensity measurement can be incurred if proper testing methodologies are not in place to allow the excitation source to reach a steady operating condition. The decrease of intensity over time after the 30 minutes mark is attributed to the photodegradation of the PSP. For this system a 0.75% loss of intensity is observed if the paint is exposed to constant excitation for 90 minutes.

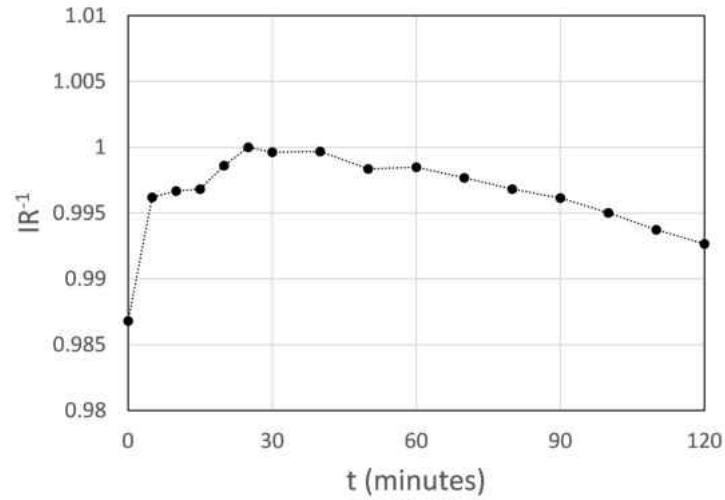


Figure 5.9: PSP emission over time

Over the course of two hours, there was no more than a 1% change in intensity due to degradation. This results in an uncertainty in effectiveness the same order of magnitude. If this additional uncertainty is too high, or the testing duration (exposure to excitation intensity) is too long, then a procedure must be put into place to mitigate these effects. The photo-degradation can be avoided by covering the test coupon or the LED in between taking images.

5.6.5 Temperature Dependence of PSP

PSP emission is has a temperature dependence as well. According to ISSI the temperature sensitivity of UniFIB PSP is 0.5 % per $^{\circ}C$, [79]. When there is a temperature difference on the paint between reference image and flow on image there is potential for intensity changes which are due to temperature to be superimposed on the variation due to pressure. To quantify this effect serparate tempearture calibrations were ran. The reference image aws taken at room temperature and then with the use of a Peltier heater the temperature of the calibration coupon was raised and lowered relative to the reference image and calibration data was taken at this offset temperature. Results for this are below.

PSP emission has a temperature dependence as well. There are two potential ways this can cause uncertainty in a film cooling measurement. The first way is when the coolant and mainstream temperatures are the same, but shifted from the reference temperature. The second source is when the coolant and mainstream temperatures are different. Shifting may be acceptable, as long as the temperature shift is small. Having different coolant and mainstream temperatures can result in trends that are functions of both temperature and concentration, not just concentration alone. If you cannot minimize this temperature difference, these tests would require binary paint.

To quantify this impact these different setpoint curves were collapsed to 1 curve which yields an empirical functional relationship between intensity ratio, pressure ratio, and temperature ratio. This equation can now be used to calculate partial derivatives and quantify the error which will be incurred in the presence of a temperature shift.

Ahn et al. [85], Mhetras et al. [86], and Narzary et al. [87] proved that if the temperature doesn't change between the reference images and the test images, then the relation between intensity ratio and pressure ratio does not change. But it is desirable to quantify the impact of a change in temperature between the reference and test image. According to the manufacturer the temperature sensitivity of UniFIB PSP is 0.5% per °C. When there is a temperature difference on the paint between reference image and flow on image, there is potential for intensity changes which are due to temperature to be superimposed on the variation due to pressure. To quantify this effect, separate temperature calibrations were performed. The reference image was taken at room temperature, and then with the use of a Peltier heater, the temperature of the calibration coupon was raised and lowered relative to the reference image, and pressure calibration data was taken at this offset temperature. Results for this are shown in Figure 5.10.

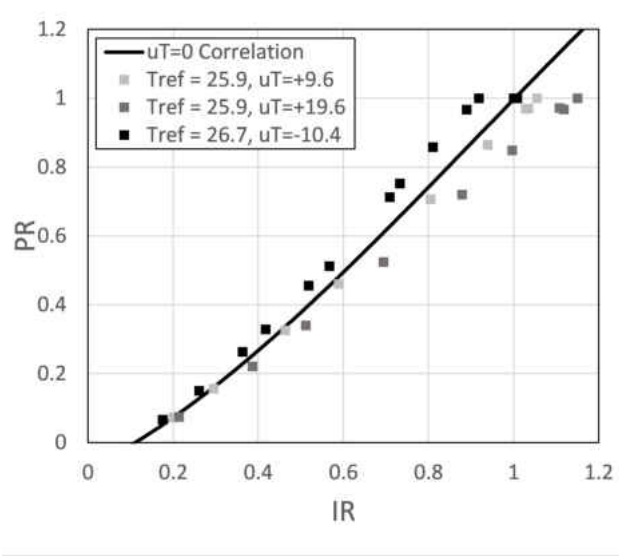


Figure 5.10: Calibration of PSP for different dT relative to reference temperature

To quantify this impact, these different setpoint curves were collapsed to one curve, shown in Figure 5.11, which yields an empirical functional relationship between intensity ratio, pressure ratio, and temperature ratio. This equation can now be used to calculate partial derivatives and estimate the error which will be incurred in the presence of a temperature shift. An optimum value of $\alpha = 2.492$ was found by minimizing the deviation from the constant temperature calibration. The data used to generate this relationship used; $-10.4^{\circ}C < u_T < 19.6^{\circ}C$ so the expected range of validity of this analysis easily covers applicable ranges (results of $u_{\eta} < 0.1$).

$$PR_{mod} = \frac{P}{P_{ref}} \left(\frac{T}{T_{ref}} \right)^{\alpha} = fn(IR) \quad (5.28)$$

$$PR = \frac{P}{P_{ref}} = fn(IR) \left(\frac{T}{T_{ref}} \right)^{-\alpha} \quad (5.29)$$

$$\frac{\partial PR}{\partial T} = -\alpha \frac{PR}{T} \quad (5.30)$$

With a propagation of error expression for u_{PR} which assumes the only source of error is temperature an estimation of uncertainty in adiabatic film cooling effectiveness is available

$$u_{\eta} = \frac{\partial \eta}{\partial PR} \frac{\partial PR}{\partial T} u_T \quad (5.31)$$

Figure 5.12 shows the resulting standard uncertainty in effectiveness due to different temperature shifts, u_T , at different effectiveness levels. With no temperature shift, there is no uncertainty (due to temperature). Also, common of film measurements with PSP, this figure shows maximum values of uncertainty occur at low effectiveness levels. From Figure 5.12 it is clear that these temperature effects become important very quickly. Even at a u_T of $2^{\circ}C$, uncertainty in effectiveness is already as high as $u_{\eta} = 0.03$.

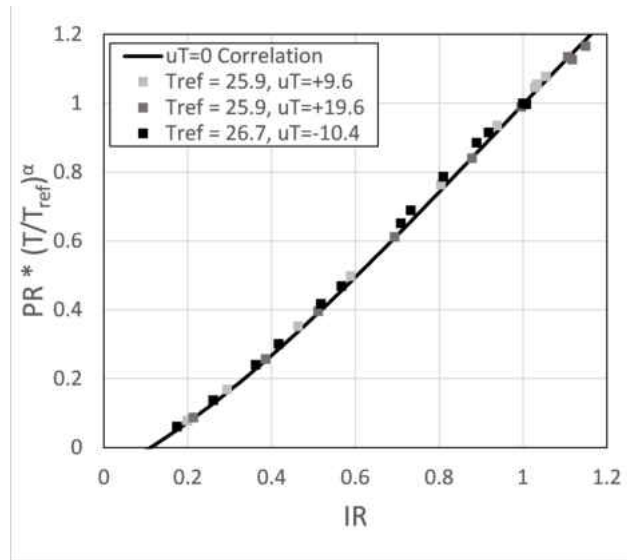


Figure 5.11: Collapse of different temperature curves

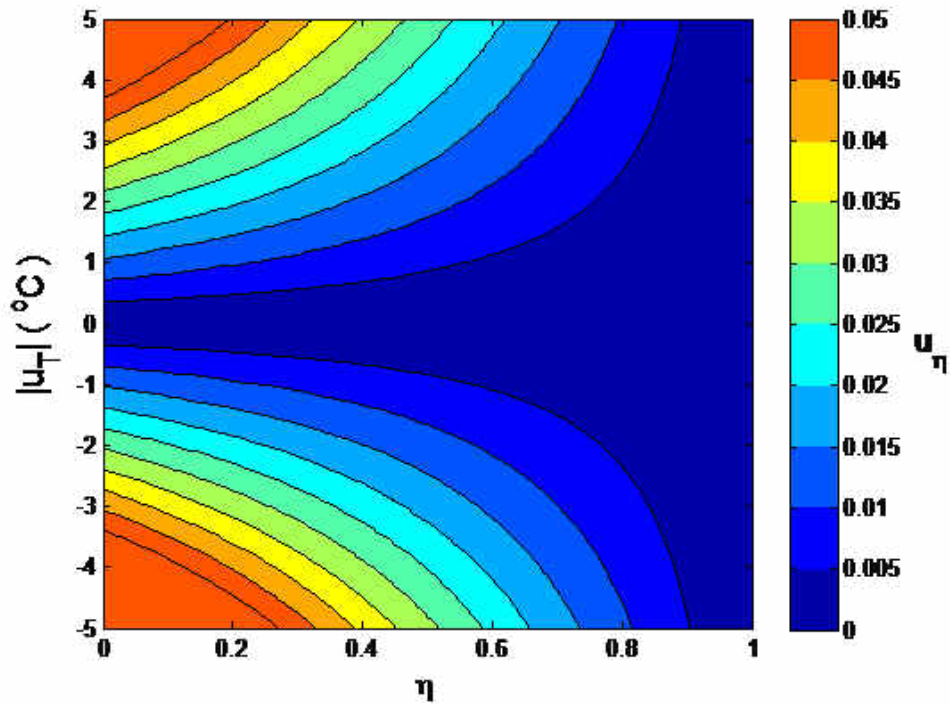


Figure 5.12: Propagation of error based on power law collapse of different temperature curves

5.7 Single Row Results

A single row of cylindrical holes is tested. The holes are inclined at 20° and spaced 7.8 hole diameters apart laterally. The parameters describing the film cooling geometry used for repeatability testing are described in Table 5.3.

Table 5.3: Single row geometry

Hole Type	-	-	Cylindrical
Diameter	d	mm	3.66 ± 0.04
Inclination Angle	α	$^\circ$	20
Hole Length	L/d	-	11.67 ± 0.17
Lateral Pitch	P_z/d	-	7.79 ± 0.09

Spatially resolved effectiveness, $\eta(x_i/d, z_j/d; M)$, profiles of near field results for a range of blowing ratios in Figure 5.13. Blowing ratios range from $M = 0.3$ to 1.2 which corresponds to a momentum flux ratio range of $I = 0.06$ to 0.95. This covers all regimes of the geometry, from a very attached film (mass addition regime) at the low end through a penetrating film by $M = 1.2$. The operating conditions are listed in Table 5.4.

Table 5.4: Single row flow conditions

M	I	VR
0.3	0.06	0.20
0.5	0.16	0.33
0.6	0.26	0.39
0.8	0.42	0.53
0.9	0.53	0.59
1.2	0.95	0.79

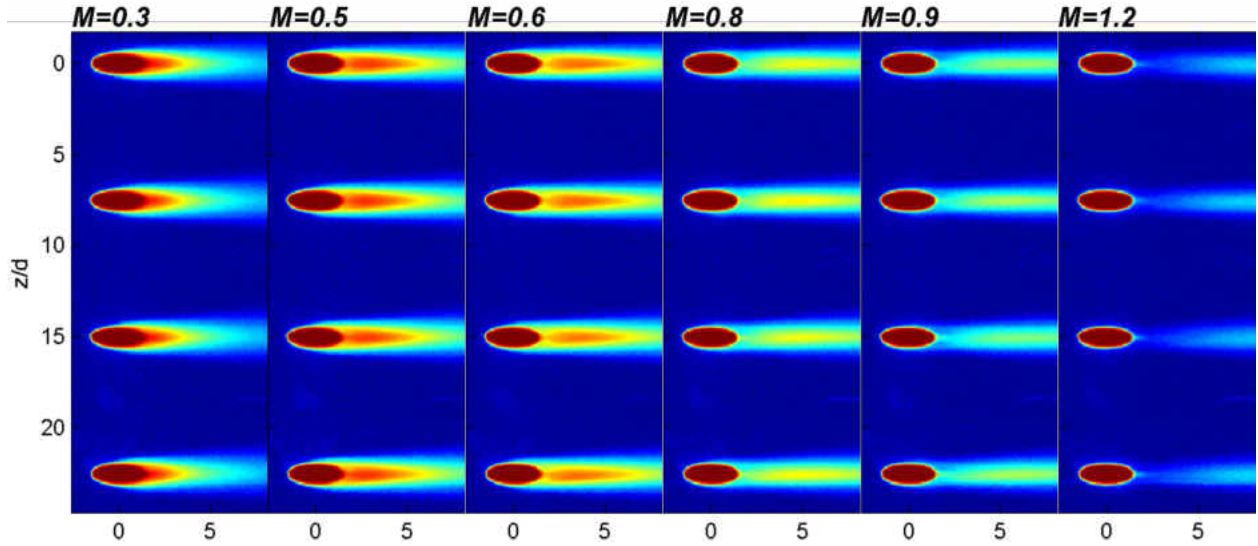


Figure 5.13: Spatially resolved effectiveness for single row case

Centerline effectiveness, $\eta(x_i/d, z/d = 0; M)$ results for all blowing ratios tested are shown in Figure 5.14. This shows a strength of PSP is its ability to resolve detailed results near the hole without the effect of diffusion damping out large gradients in the measured field. Values of $\eta = 1$ are recovered within the hole which transition quickly to $\eta = 0$ upstream of injection. This Figure clearly shows signs of coolant jet liftoff even at blowing ratios as low as $M = 0.5$. By a blowing ratio of $M = 0.8$ there is no benefit seen in increasing the coolant flow rate.

Figure 5.15 shows the area averaged effectiveness, $\bar{\eta}$, for the single row cases as a function of blowing ratio. The averaging region is from $d/\sin \alpha/2 < x/d < 3P_x/d$ in the streamwise direction and spans 2 lateral pitches. It seems the optimal blowing ratio is near $M = 0.6$.

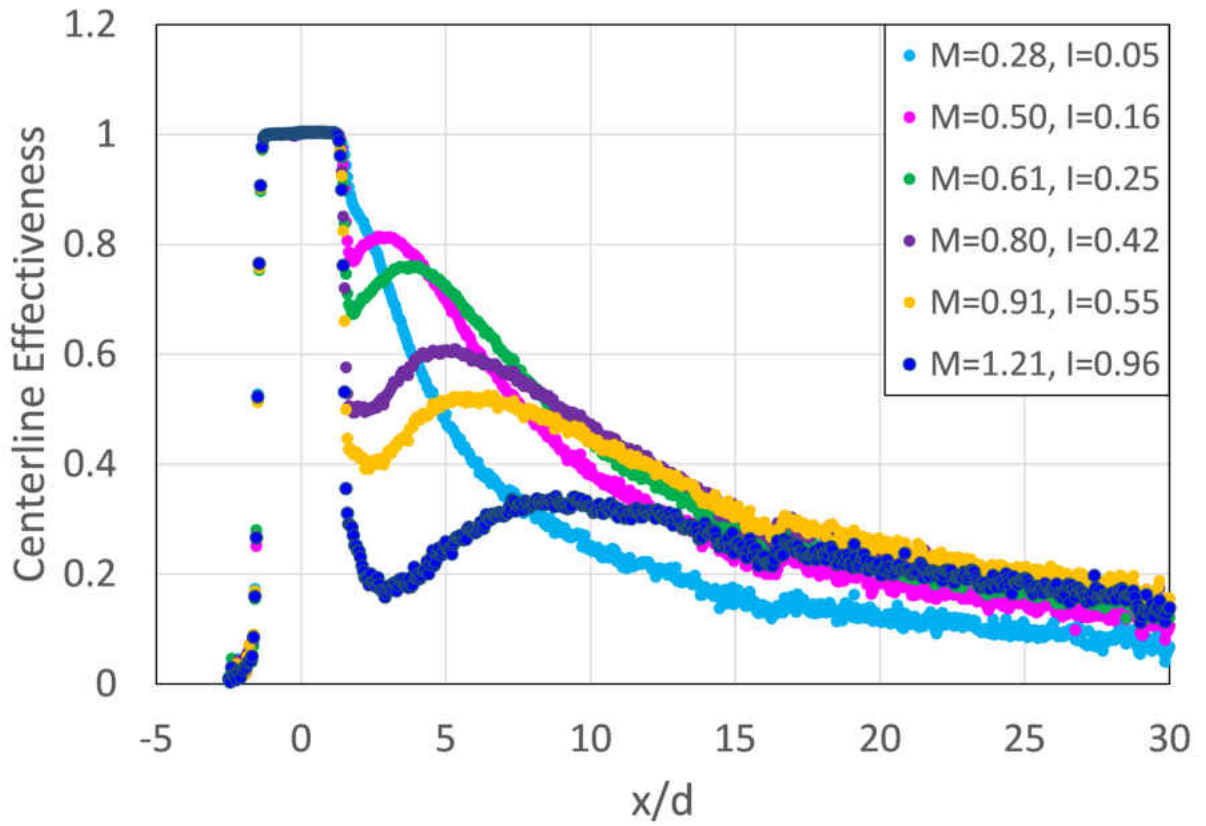


Figure 5.14: Centerline effectiveness for single row

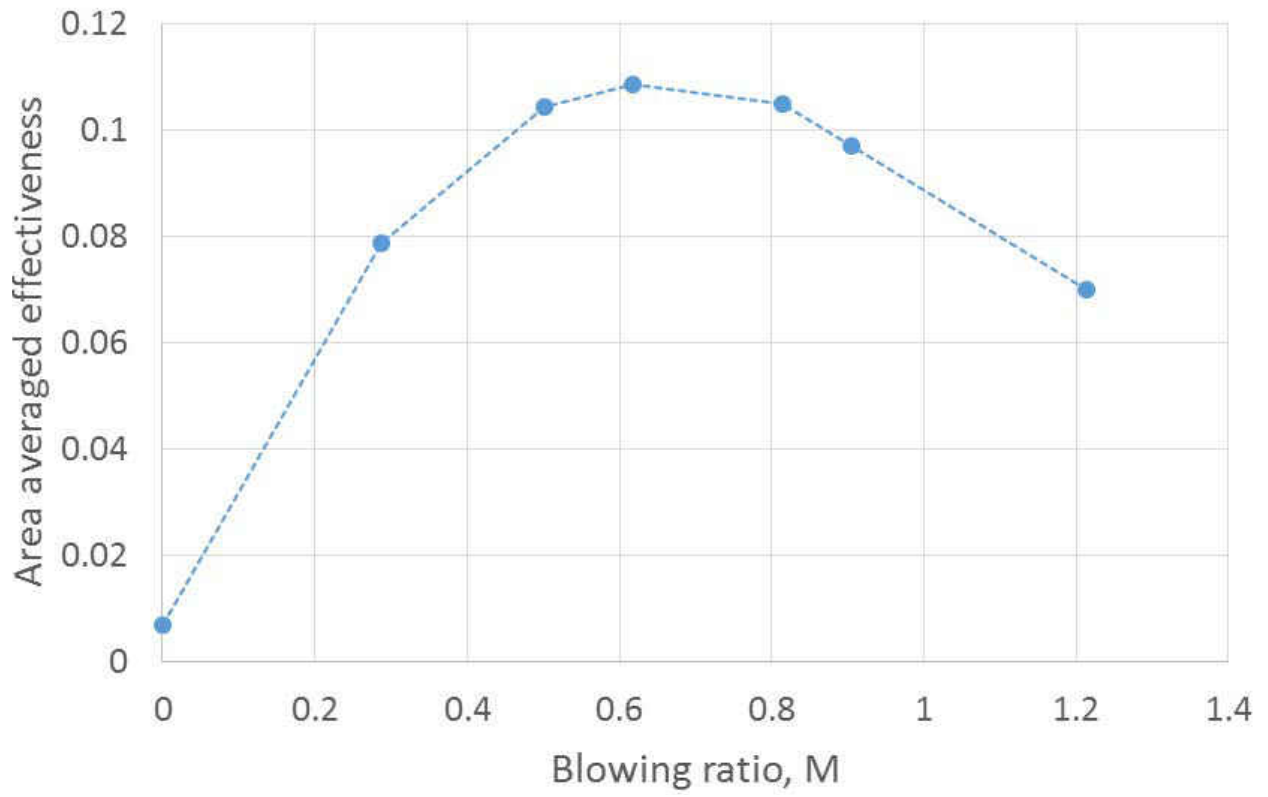


Figure 5.15: Single row area averages

5.7.1 Repeatability

Adiabatic film cooling effectiveness data was obtained for a single row of film cooling holes at six different blowing ratios. Four sets of data were taken over the course of a month. To quantify day-to-day variations of lateral averaged effectiveness some ensemble statistics were calculated. The mean measurement of η was calculated according to Equation 5.32, the variation of the different measurements was quantified via an RMS given by Equation 5.33 and a normalized version to represent a percent error is given by Equation 5.34.

$$Avg(x/d) = \sum_{i=1}^N \eta_i(x/d)/N \quad (5.32)$$

$$Sdv(x/d) = \sqrt{\frac{\sum_{i=1}^N (\eta_i(x/d) - Avg(x/d))^2}{N - 1}} \quad (5.33)$$

$$Nrm(x/d) = \frac{Sdv(x/d)}{Avg(x/d)} \quad (5.34)$$

$$Dlta(x/d) = max(\eta_i(x/d)) - min(\eta_i(x/d)) \quad (5.35)$$

The repeatability measurements for laterally averaged results are plotted in Figures 5.16 - 5.21. The lateral average is taken over 3 pitches. The maximum deviation observed between any test across all blowing ratios is 0.022, and was seen at the highest blowing ratio ($M = 1.2$). The highest standard deviation observed is 0.009 and also occurred at the most downstream location of the highest blowing ratio ($M = 1.2$).

Qualitatively correct, repeatable trends are observed throughout all tests. At a blowing ratio of 0.3, the jets are in the mass addition regime, and are still attached. By a blowing ratio of 0.5, the onset of the mixing regime is observed. The jets are observed to lift off, and then impinge back onto the test surface. The jets enter a penetration regime by a blowing ratio of 1.2, where the jets lift off, but reattach much further downstream than the lower blowing ratios. There is a peak in effectiveness moving downstream as blowing ratios and momentum flux ratios increase. These trends are in agreement with reported results in the literature.

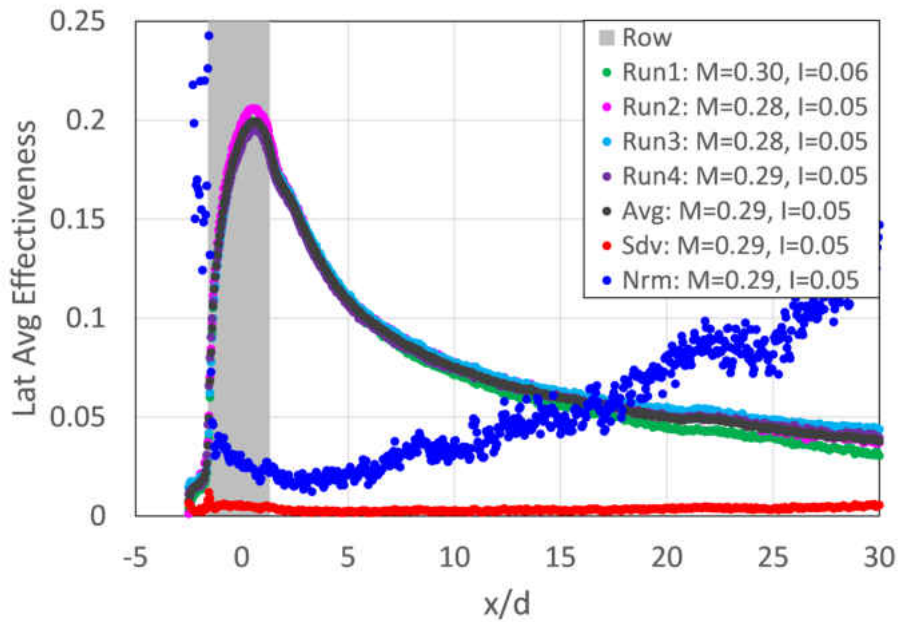


Figure 5.16: Day-to-day repeatability of $\bar{\eta}$ for $M = 0.3$

Figure 5.22 shows day to day repeatability of centerline effectiveness. Lateral uniformity is shown by plotting centerline effectiveness following each of the four holes for a single days test in Figure 5.23.

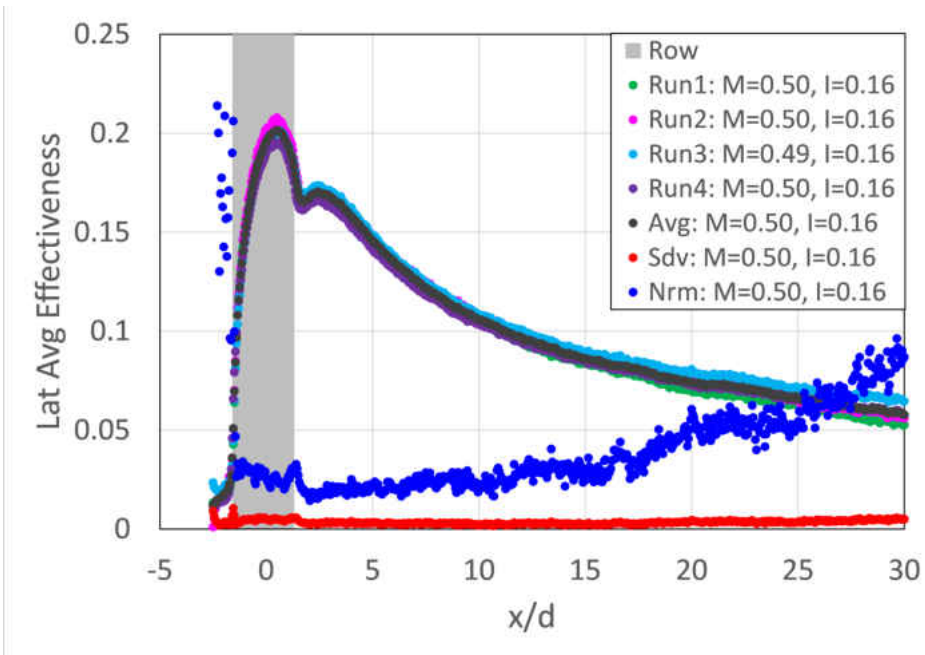


Figure 5.17: Day-to-day repeatability of $\bar{\eta}$ for $M = 0.5$

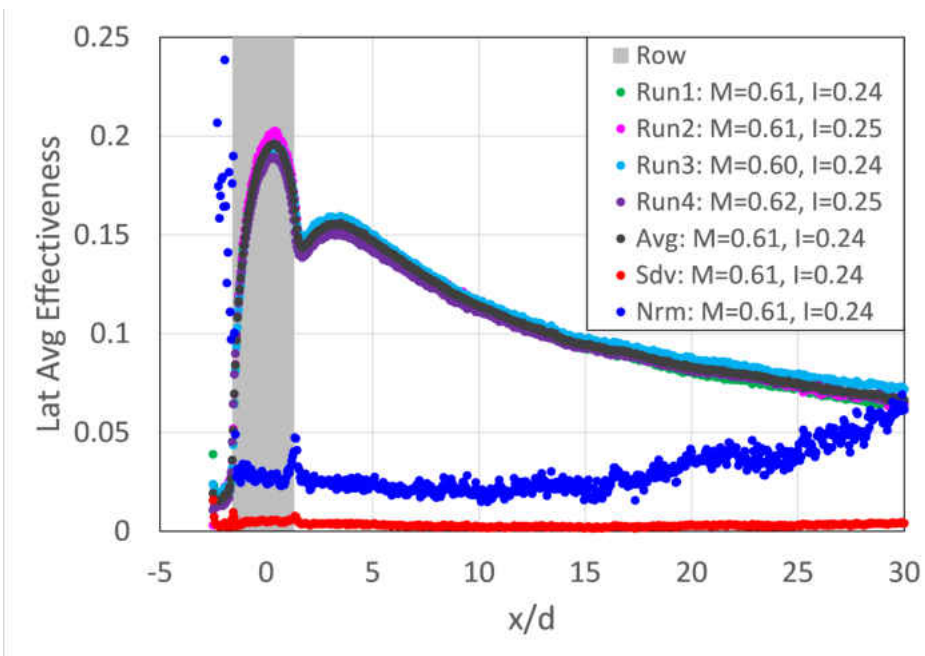


Figure 5.18: Day-to-day repeatability of $\bar{\eta}$ for $M = 0.6$

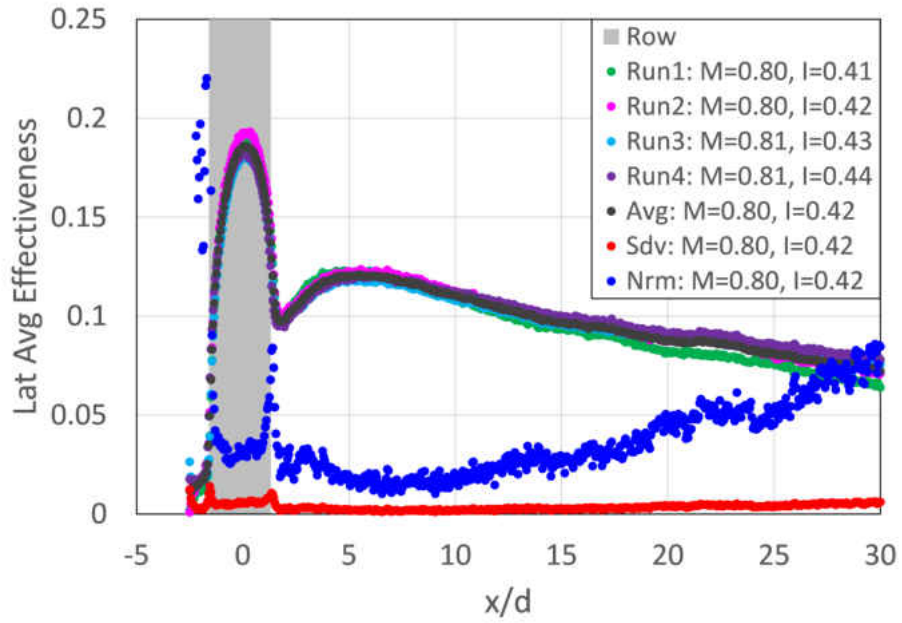


Figure 5.19: Day-to-day repeatability of $\bar{\eta}$ for $M = 0.8$

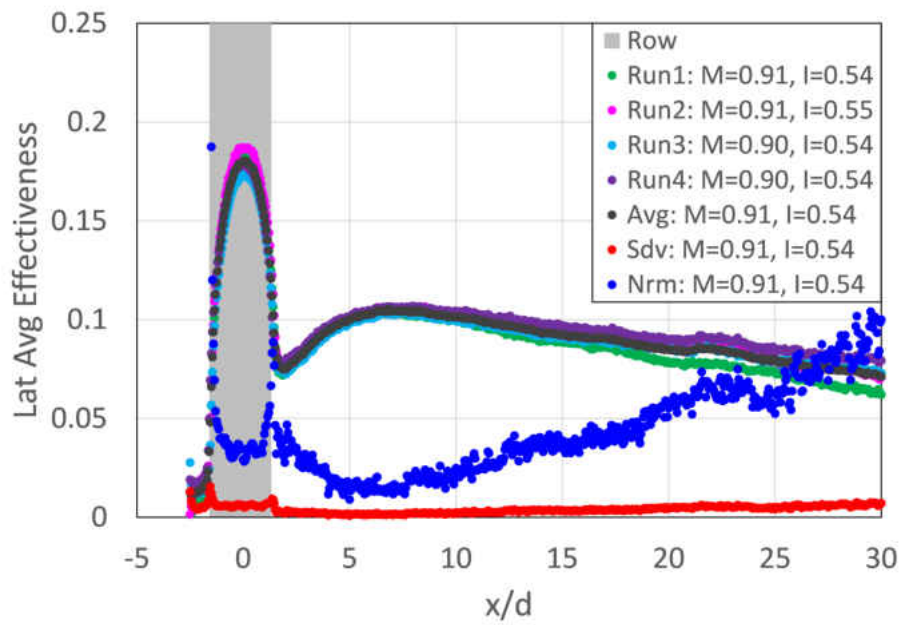


Figure 5.20: Day-to-day repeatability of $\bar{\eta}$ for $M = 0.9$

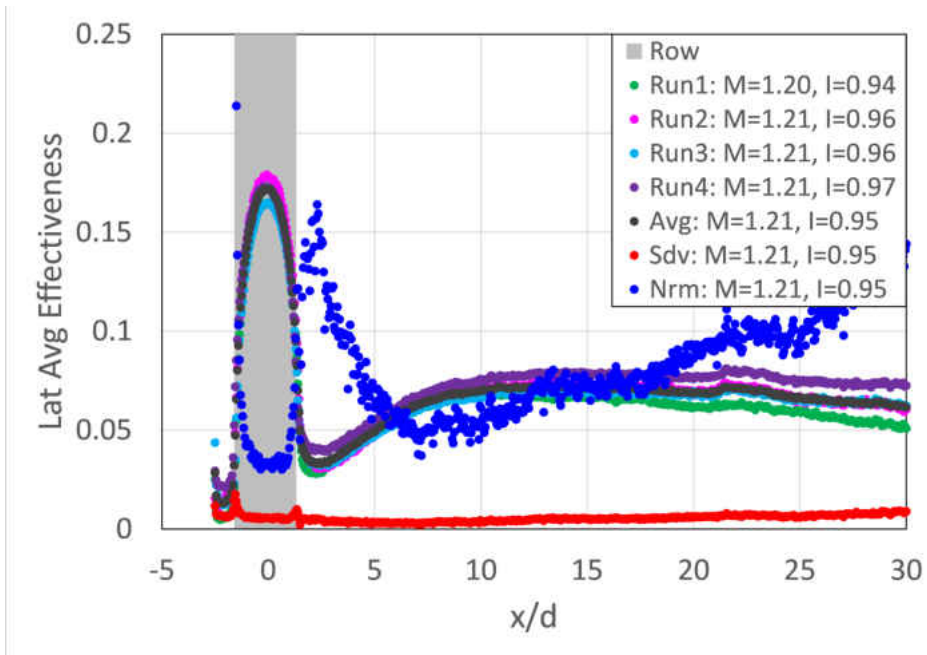


Figure 5.21: Day-to-day repeatability of $\bar{\eta}$ for $M = 1.2$

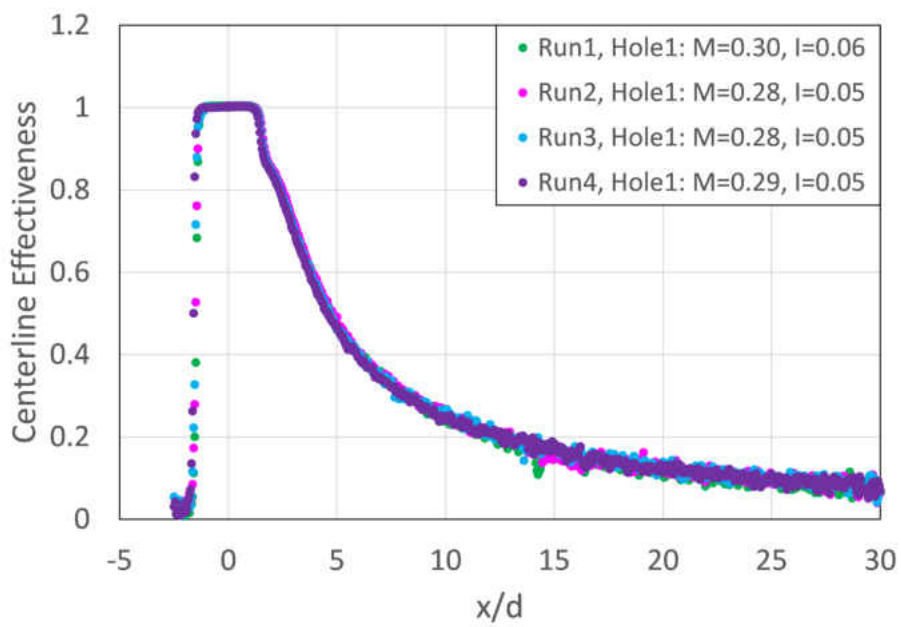


Figure 5.22: Day to day repeatability of centerline film effectiveness, η_{cl}

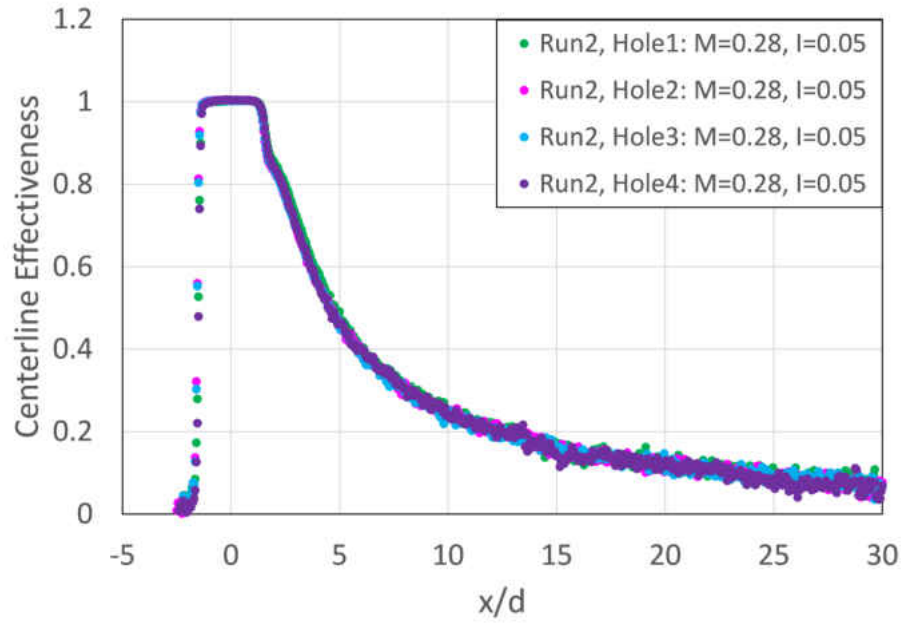


Figure 5.23: Lateral uniformity of η_{cl}

The results we see here are consistent with what has been estimated in the prediction of uncertainty, and all data sets fall within the bounded uncertainty previously calculated.

5.7.2 Validation

The results obtained were then compared with previous literature, [9] [10] [88] [2] [89] [90] [29] [91] [64] [92], in Figure 5.24 and Figure 5.25. All holes compared with are cylindrical holes. Other relevant parameters such as inclination angle, P_z/d , blowing ratio, and density ratio listed in Table 5.5. The author and technique employed are also included in the Figure legends. A direct comparison with 20° inclination angle results is sparse, so the current data is compared with many different studies. No study is the same as the current one. These studies include blowing ratios ranging from 0.25 to 0.75 and density ratios ranging from 0.9-1.6 and are compared with the present study's data at a blowing ratio of 0.5 and density ratio of 1.5. Studies are also scaled to match a lateral pitch of $7.5d$ according to Equation 5.36 for the sake of comparison.

$$\bar{\eta}_{scaled} = \bar{\eta} \frac{(p/d)_{original}}{(p/d)_{new}} \quad (5.36)$$

Qualitatively the results match those from literature. Due to the large differences in geometries, test condition and measurement techniques; however, there is not good quantitative agreement. Consistently the results from the present study are higher than those from literature. This is likely due to the 20° holes performing better than the higher angle holes more commonly found in literature.

Table 5.5: Literature for comparison with single row results

Year	Technique	α	L/d	P_z	M	DR	Author
1991	TCs	35	1.75, 3.5	3	0.25 - 1	1.2 - 2	Sinha et al. [10]
1996	?	35	4	3, 6	0.5 - 2.5	0.5 - 2.5	Schmidt et al. [88]
1997	TLC	35	4.6	4	0.5 - 2	1.46	Ekkad et al.
1997	GS	35		3	0.25 - 2.5	0.75 - 4	Pedersen et al. [9]
1998	IR	30	6	-	0.4 - 1.8		Gritsch et al. [2]
2000	TLC	35	4	3			Jung and Lee [90]
2001	IR	30	6	3	0.2 - 2.5	1.8	Baldauf [13][14]
2002	TLC	30	10	3	0.5, 1	1	Yu et al. [91]
2011	PSP	35	4.66	4	0.25 - 2	1, 1.4	Wright et al. [64]
2012	IR	20, 35	6	6, 3	0.5, 1, 2		Abdullah et al.
2012	IR	20	8.35	3, 5, 7	2, 5, 10	1.15-1.25	Ling et al. [29]
2014	IR	30, 35	4.7	3, 6.7	0.5 - 2	1.2, 1.6	Eberly, Thole [92]

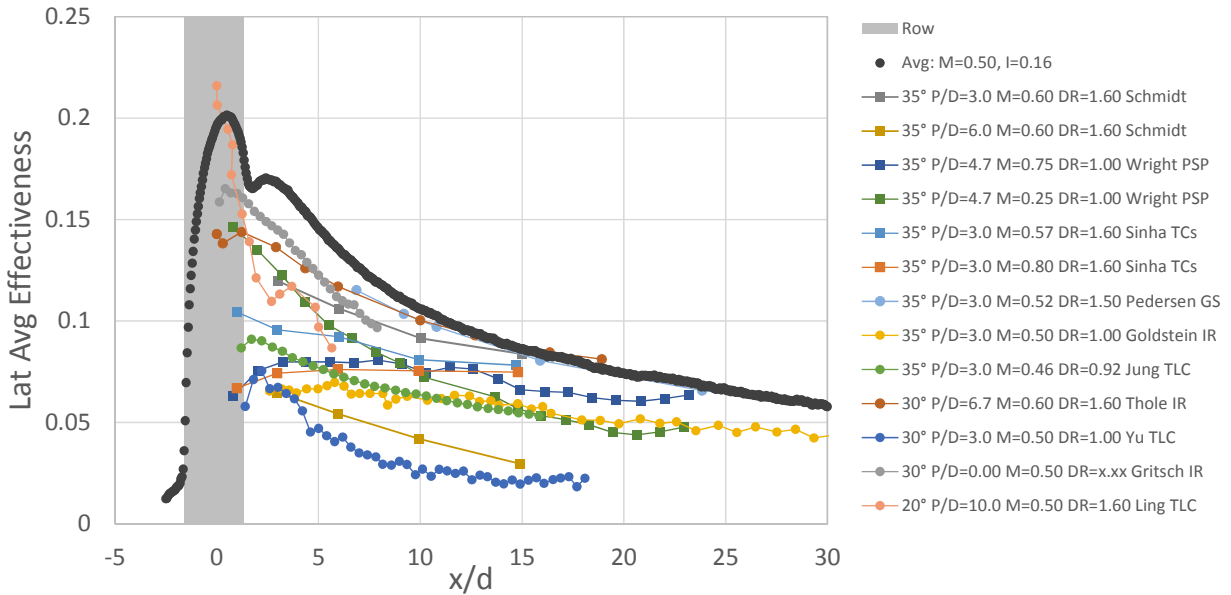


Figure 5.24: Single row validation for $M \approx 0.5$

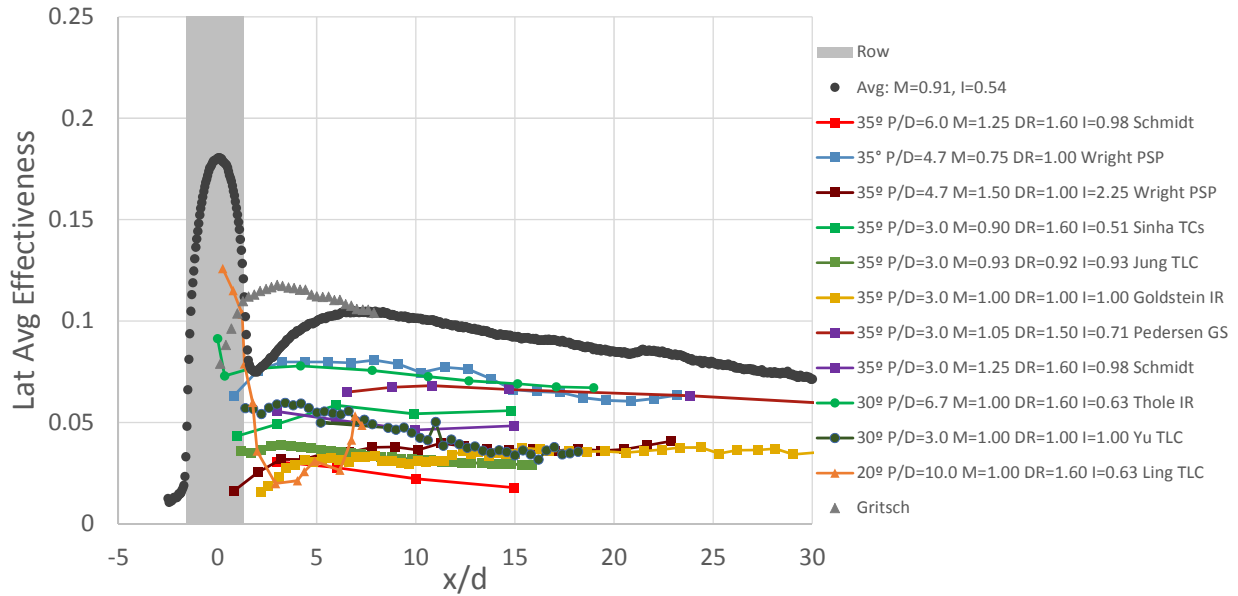


Figure 5.25: Single row validation for $M \approx 0.9$

5.8 Evaluation of Test Uncertainty

The test methodologies described were then applied to the testing of a single row of inclined cylindrical holes. This data allows a detailed look at the zero level effectiveness as well as a comparison of laterally averaged film effectiveness curves from several days.

From the spatially resolved profiles of adiabatic film cooling effectiveness results shown in Figure 5.13 we can see two experiment-related features in the data. There is a blurriness to the edges of the holes and the effectiveness upstream of injection is not identically 0. These features are more visible in Figure 5.26. This Figure shows a slice of effectiveness corresponding to $x/d = 0$, the row axis breakout.

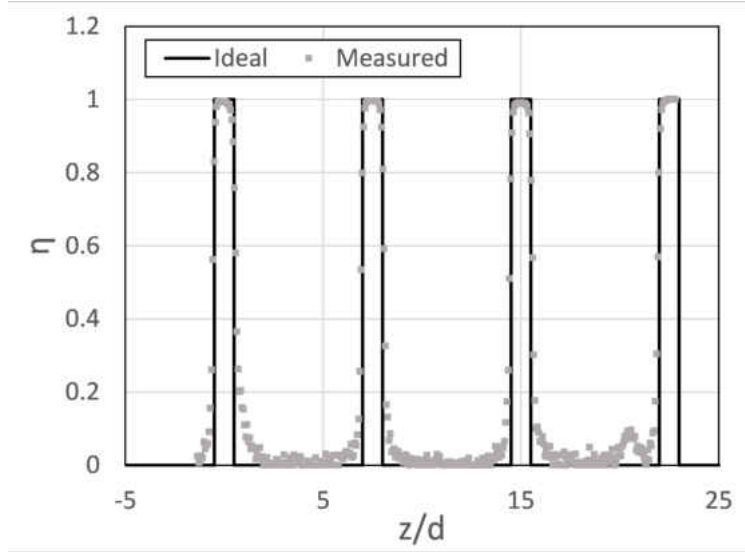


Figure 5.26: $\eta(x/d = 0, z/d)$ compared with ideal distribution

Transition: When taking a lateral slice of the data at the hole axis breakout ($\eta(z/d; x/d = 0)$) the transition from $\eta = 1$ to $\eta = 0$ is not sharp. The transition takes place over several pixels, evident from Figure 5.26. At low blowing ratios this could be conjectured to be physical; however, at the higher blowing ratio tested, $M = 1.2$, this should not be the case due to the jet immediately detaching from the surface. This is likely a result of the CCD cameras inability to resolve an infinite gradient. A stationary experiment (free from vibration and other movement) which provides a step input (calibration data is convenient for this) allowed an assessment of the PSP system output, data from which is shown in Figure 5.28. From this data, a 95% transition can be seen to occur over 8 pixels. This corresponds to $d/2$ for the current geometry and camera configuration.

Zero-level noise: There is a region in between the holes which should have $\eta = 0$, this region is highlighted red in Figure 5.29. The mean and standard deviation of this sample ($N \approx 6000$) was calculated for several series of tests. Examples of histograms of this sample are shown in Figure 5.30. They can be treated as normal distributions. The mean and standard deviation of several test sequences are shown in Figure 5.31 and Figure 5.32. Noise between holes has a mean of $-0.01 < \eta < 0.02$. Standard deviation of this noise is consistent at 0.016.

The results from Figure 5.27 reflect the prediction of uncertainty analysis in that we see low levels of uncertainty correspond to high levels of effectiveness. This is a result of the magnitude of intensity. Interesting to note, even in equal effectiveness areas, a region with a higher intensity will result in a lower effectiveness. Not only is it the effectiveness that impacts the uncertainty, but the uniformity of the lighting. This is an important fact because many places use LED spotlights, and not LED bars, the latter of which would provide a more uniform lighting. A bright spot in the excitation will result in a lower uncertainty, whereas a dark spot would result in a higher uncertainty.

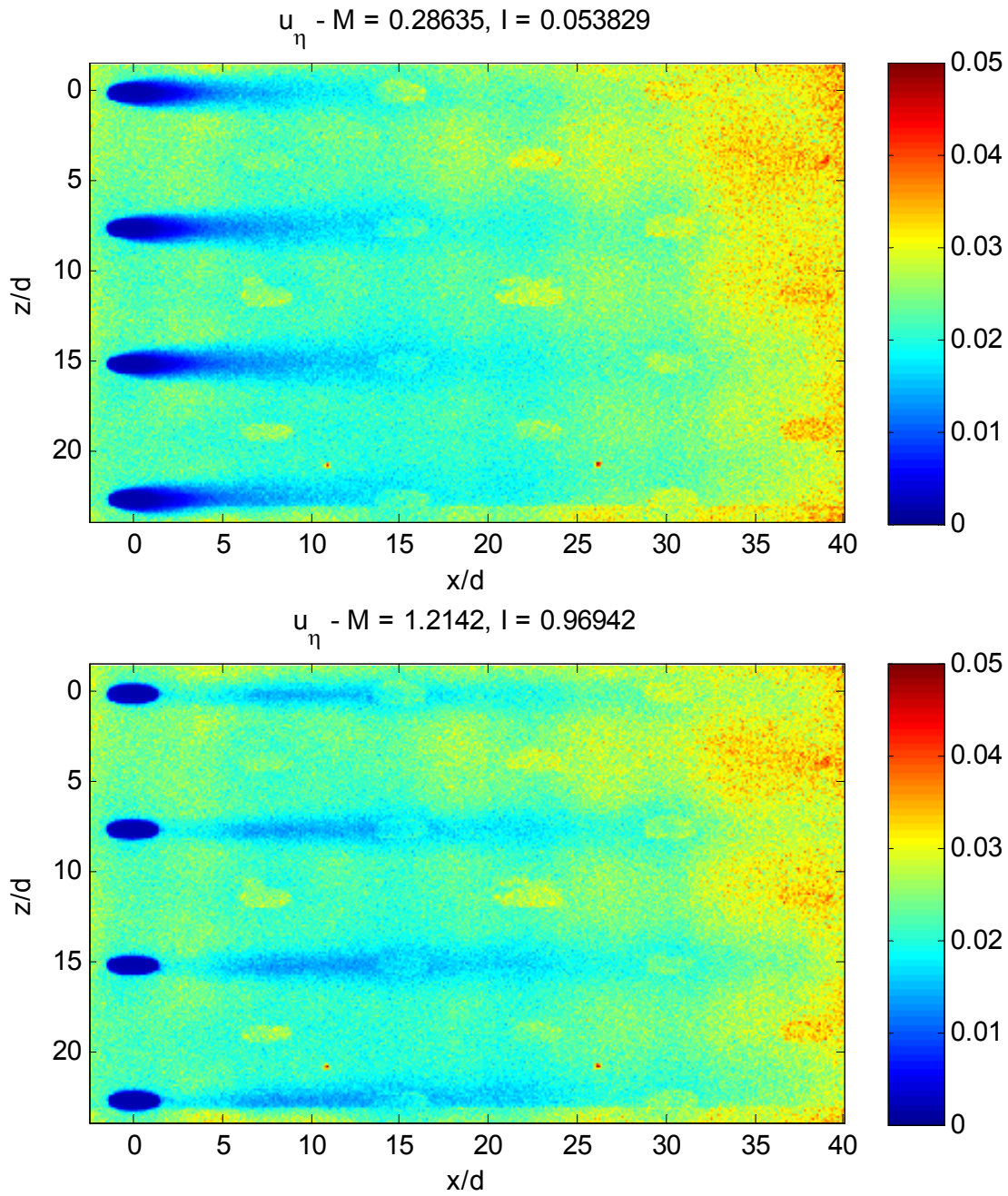


Figure 5.27: Maps of uncertainty, calculated according to [81], for $M = 0.3$ and 1.2

5.8.1 $\eta = 0$ Statistics

Regions in between holes and upstream of row 1 (5.29) would be expected to yield effectiveness values of $\eta = 0$. These regions were sampled to yield effectiveness values at each pixel. This sample allowed calculation of mean and standard deviation. Results for this zero-level effectiveness region are shown in Figure 5.30 through Figure 5.32.

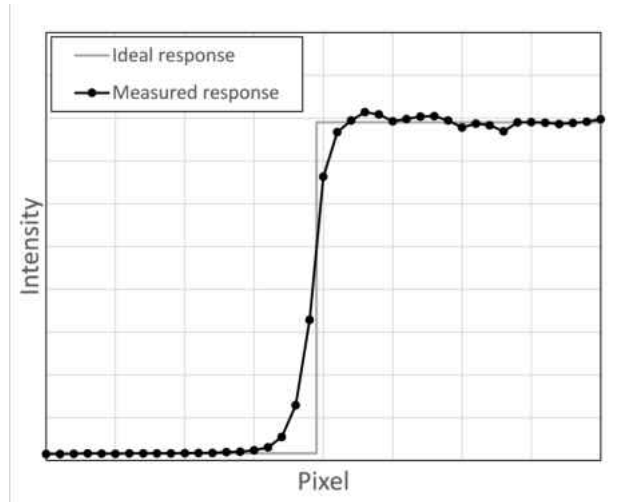


Figure 5.28: PSP system response to step input

5.9 Multi-Row Results

Results for adiabatic film cooling effectiveness measurements obtained with the PSP technique for the 5 test articles listed in Table 2.2 are shown in §5.9.1. Local distributions of experimental uncertainty estimates for Geometry 1 are shown in §5.9.2. Next, laterally averaged effectiveness results are presented in §5.9.3.

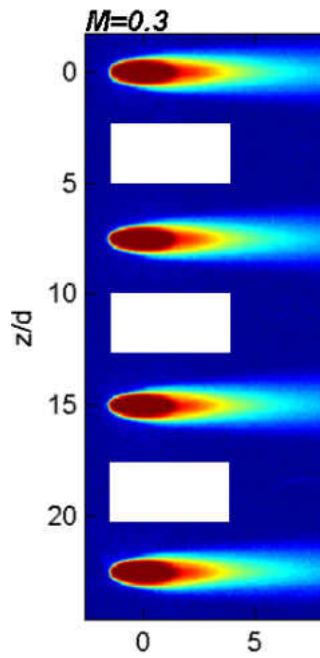


Figure 5.29: Region sampled for $\eta = 0$ statistics

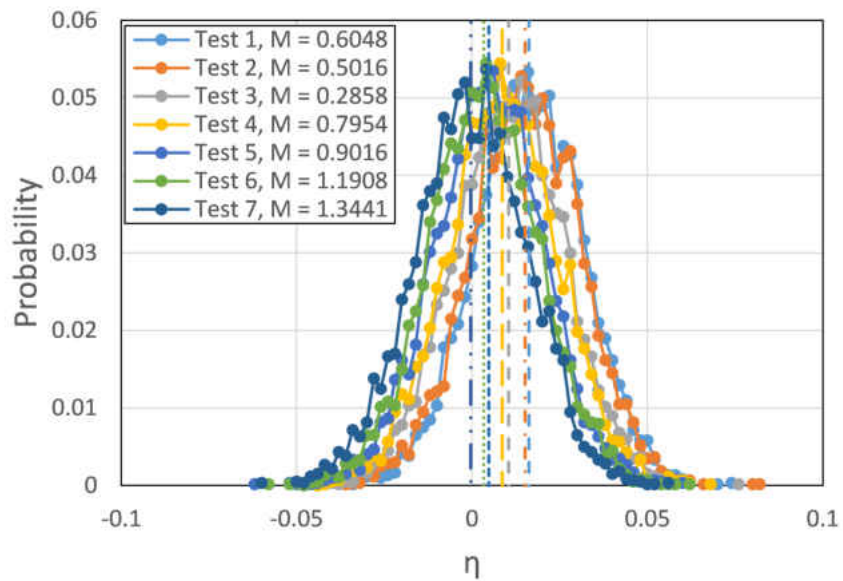


Figure 5.30: Probability density functions of a nominally $\eta = 0$ sample

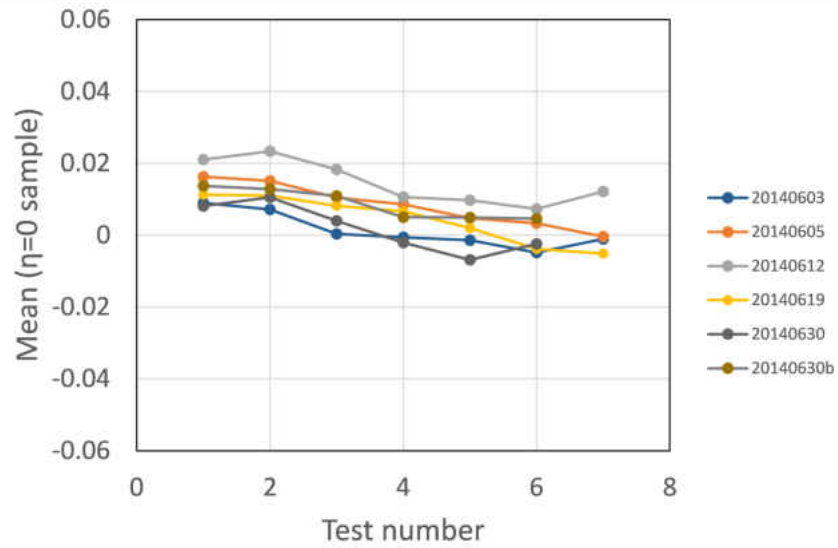


Figure 5.31: Compilation of means for several different tests from the $\eta = 0$ samples regions; represents an upper bound of bias error

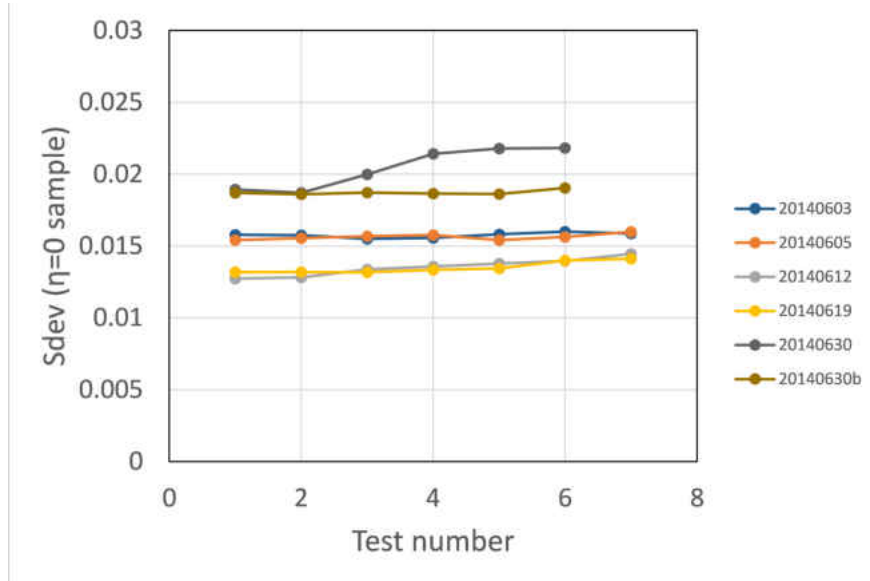


Figure 5.32: Compilation of standard deviations for several different tests from the $\eta = 0$ samples regions; represents an upper bound of random error

Some interesting experimental aspects encountered in the multi-row PSP measurements are presented next. Aspects of testing on SLA surfaces which are transmissive are discussed in §5.9.4. Then the topic of auto-illumination due to the increased emission intensity of the multi-row arrays is discussed in §5.9.5. Gas sampling measurements and their comparison with the PSP results are then presented in §5.9.6. Finally superposition predictions of multi-row performance using the single row results from §5.7 are presented in §5.9.7.

5.9.1 Spatially Resolved Film Cooling Effectiveness, $\eta(x_i/d, z_j/d)$

Local adiabatic film cooling effectiveness results are presented in this section. There are 5 geometries total. Each geometry was tested several times and repeatability results similar to those presented in §5.7.1 exist for each geometry and test condition. The presented results are representative results which differ only slightly within presented experimental uncertainty.

5.9.1.1 Geometry 1: 7.5 x 7.5 Cylindrical Array

Geometry 1 is the tight spacing cylindrical array and is also a multi-row version of the single row case investigated in §5.7. Results for several blowing ratios are shown in Figures 5.33 through 5.39. Similar to the performance of the single row, the coolant is attached at low blowing ratio providing distinct footprints of η near 1 immediately after injection. The traces are “short” or “stubby” in the streamwise direction at low M . As the blowing ratio is increased from $M = 0.3$ to 0.6 an increase in the length of the footprint is seen, accompanied by a decrease in peak effectiveness downstream of the hole. This is an indication that the film jet is leaving the wall slightly but it is still increasing in performance at this point. As the blowing ratio is increased past $M = 0.6$, a significant loss of performance is seen at the upstream rows. Despite upstream rows decreasing in performance the downstream rows see a rise in η . This is due to upstream rows buffering the mainflow and turbulent mixing bringing the coolant back near the wall.

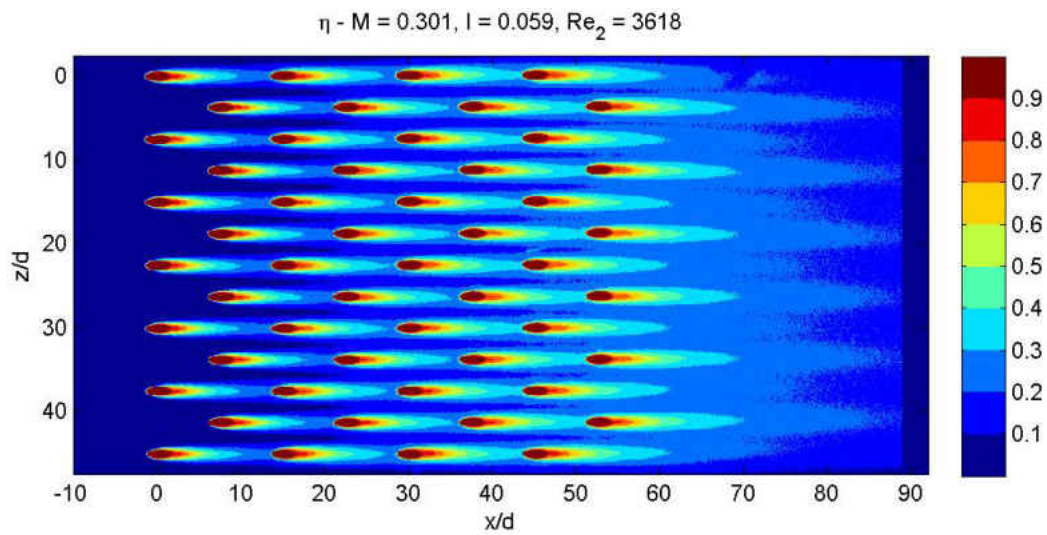


Figure 5.33: Geometry 1, $M = 0.30$; spatially resolved η

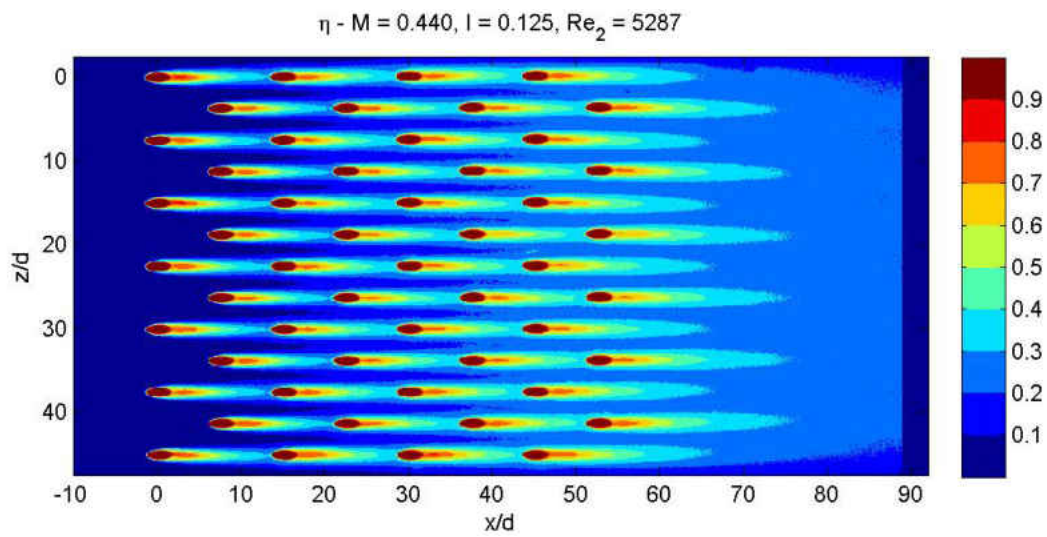


Figure 5.34: Geometry 1, $M = 0.44$; spatially resolved η

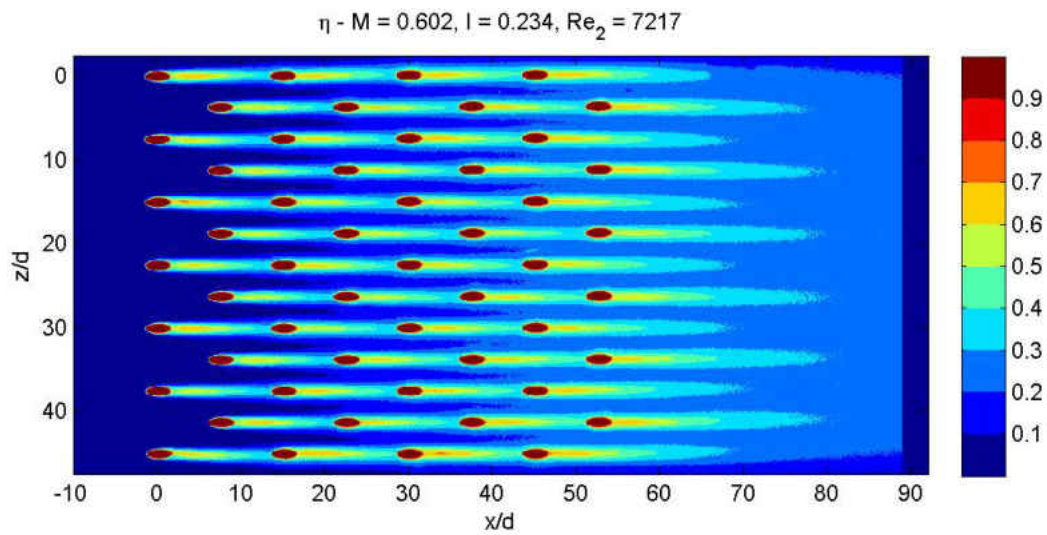


Figure 5.35: Geometry 1, $M = 0.60$; spatially resolved η

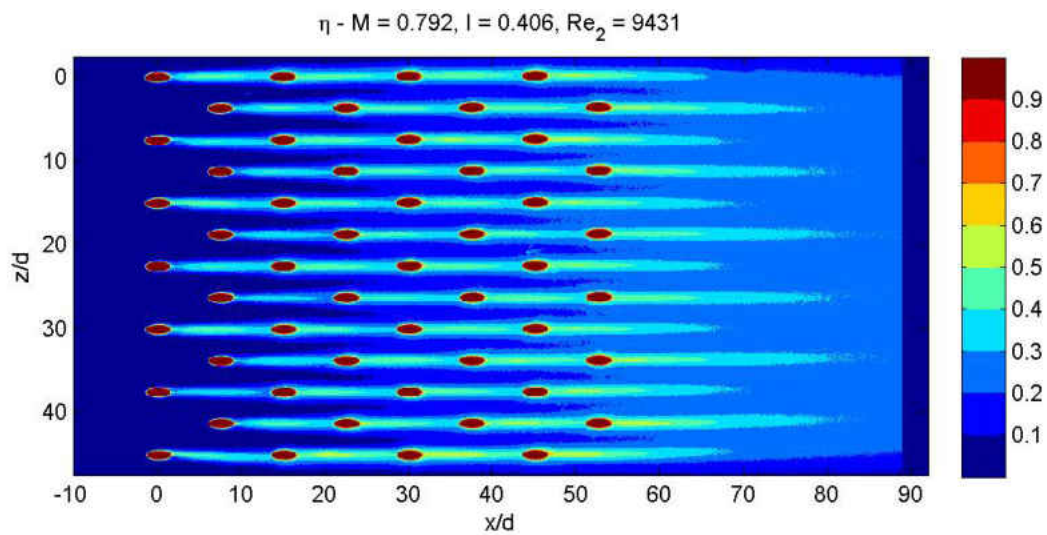


Figure 5.36: Geometry 1, $M = 0.79$; spatially resolved η

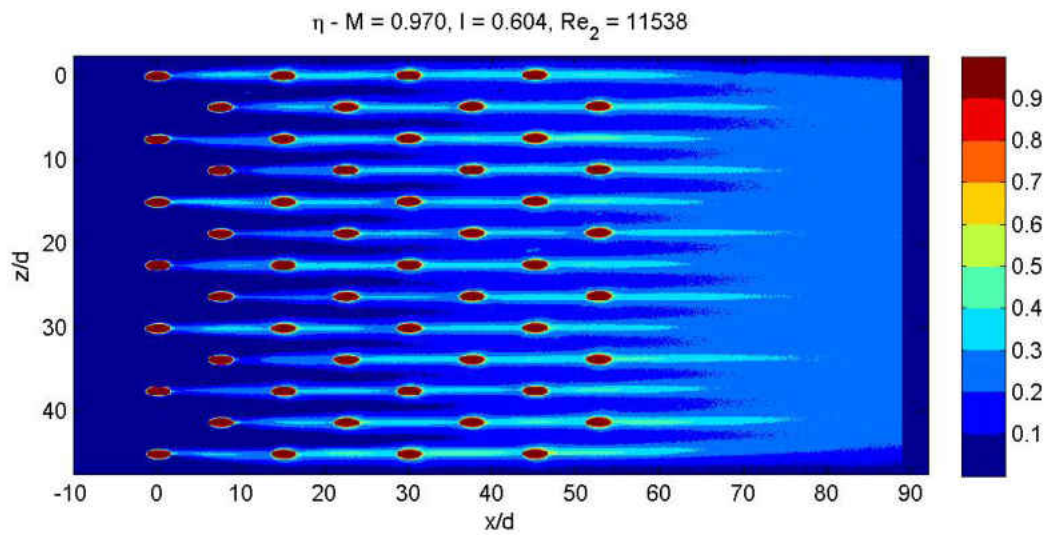


Figure 5.37: Geometry 1, $M = 0.97$; spatially resolved η

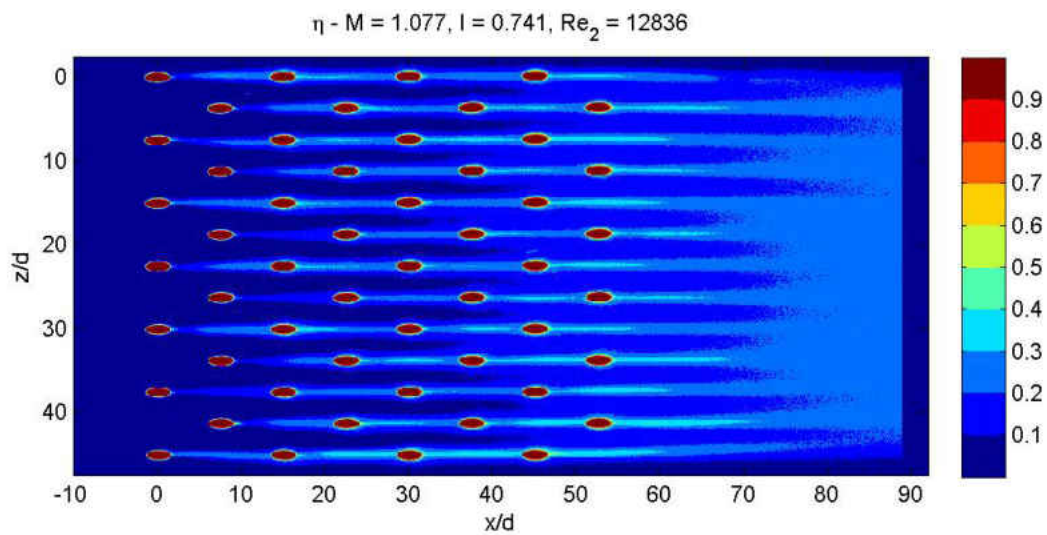


Figure 5.38: Geometry 1, $M = 1.08$; spatially resolved η

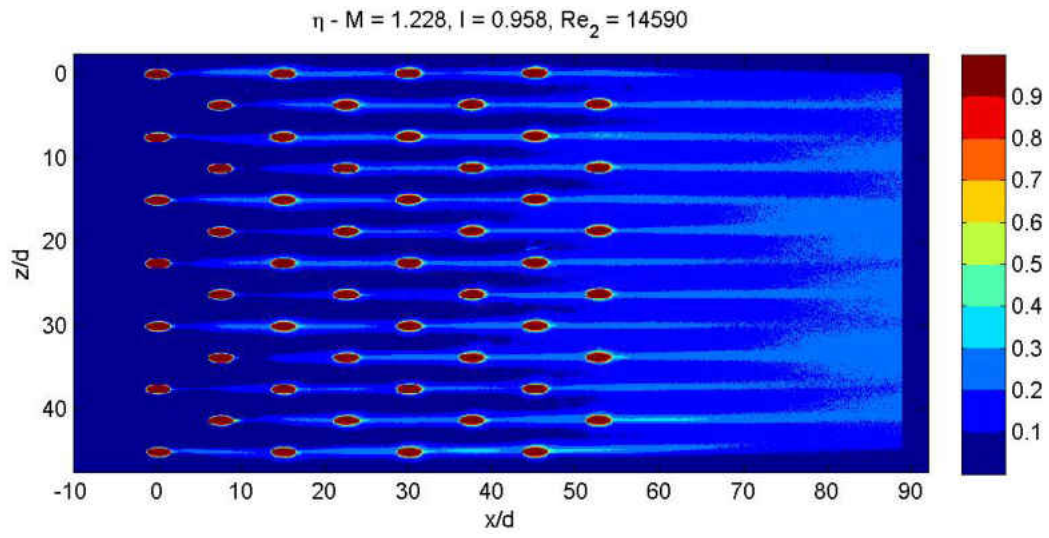


Figure 5.39: Geometry 1, $M = 1.23$; spatially resolved η

5.9.1.2 Geometry 1b: 7.5 x 7.5 Cylindrical Array, SLA

An additional tight spacing cylindrical geometry was manufactured from SLA. This extra hardware was tested in order to assess the impact of machining process and substrate on measurements of η . The results for Geometry 1b are presented in Figures 5.40 through 5.46. The results behave qualitatively and quantitatively very similar to those from the Aluminum equivalent. The same operating conditions are observed. The only differences which stand out relate to the quality of the measurement. There is a “noisiness” seen in the SLA results. This is related to the smoothness of the emission field being affected by the surface roughness and grain structure of the SLA substrate. Also, the SLA geometries result in slightly higher biases for the $\eta = 0$ samples taken upstream. This is due to the substrate being slightly transmissive to light despite efforts to prime the surface. These features are discussed in more detail, along with a quantitative comparison of Geometry 1 and Geometry 1b lateral averages, are shown in §5.9.4.

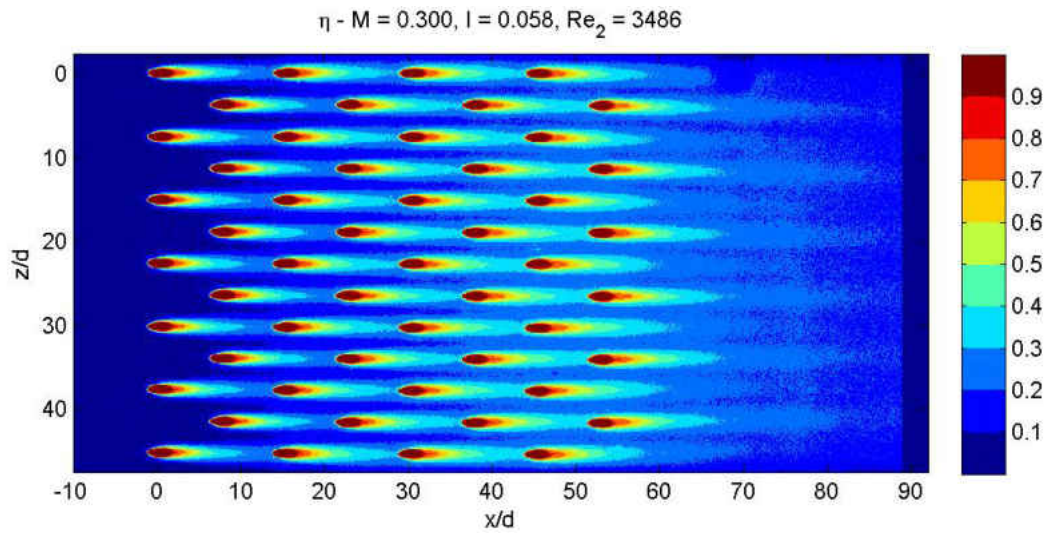


Figure 5.40: Geometry 1b, $M = 0.30$; spatially resolved η

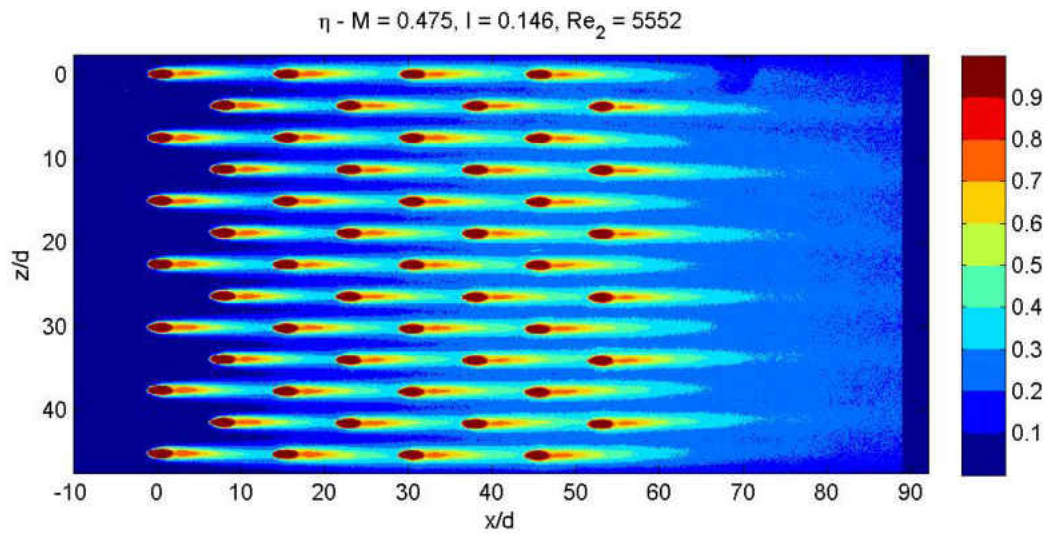


Figure 5.41: Geometry 1b, $M = 0.48$; spatially resolved η

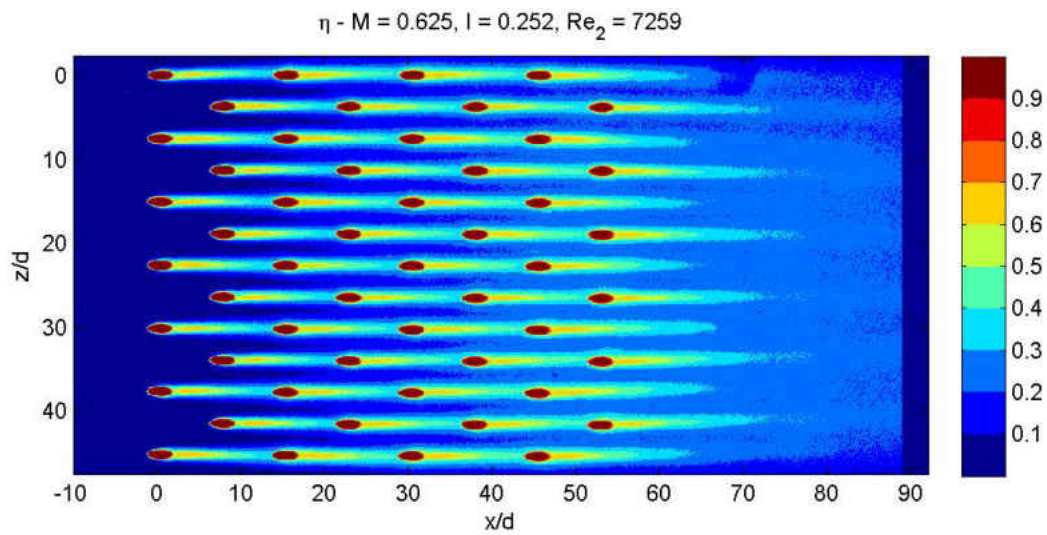


Figure 5.42: Geometry 1b, $M = 0.63$; spatially resolved η

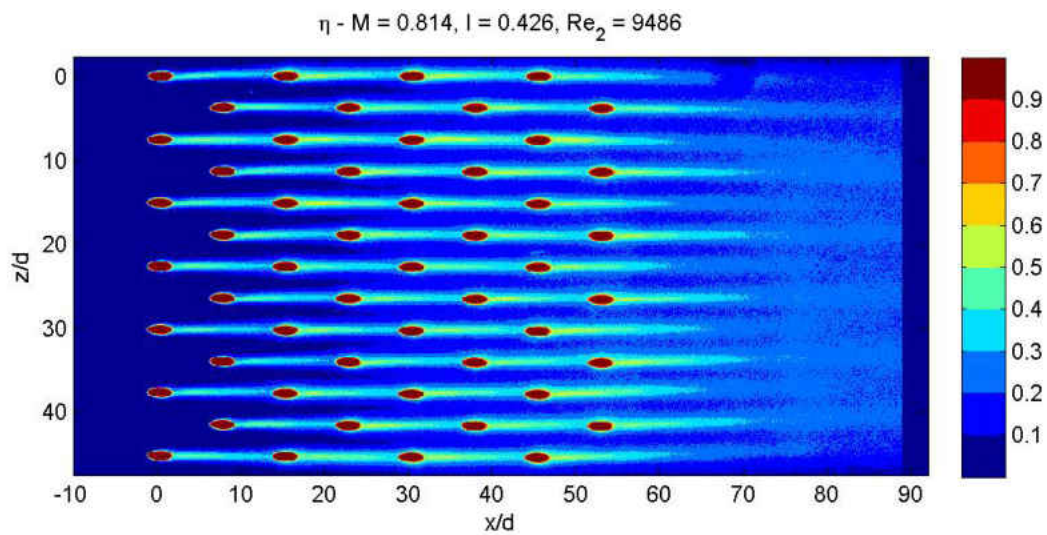


Figure 5.43: Geometry 1b, $M = 0.81$; spatially resolved η

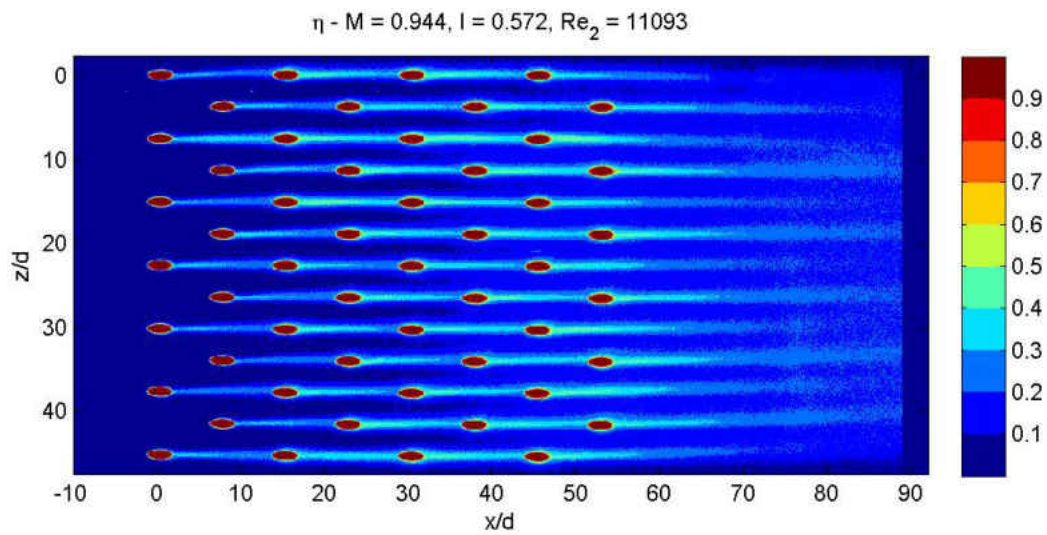


Figure 5.44: Geometry 1b, $M = 0.94$; spatially resolved η

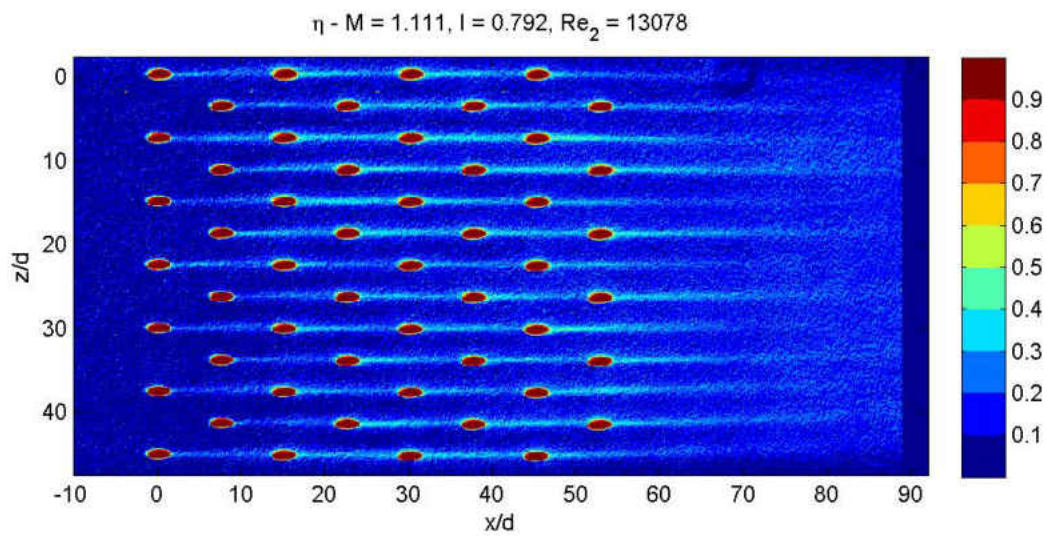


Figure 5.45: Geometry 1b, $M = 1.11$; spatially resolved η

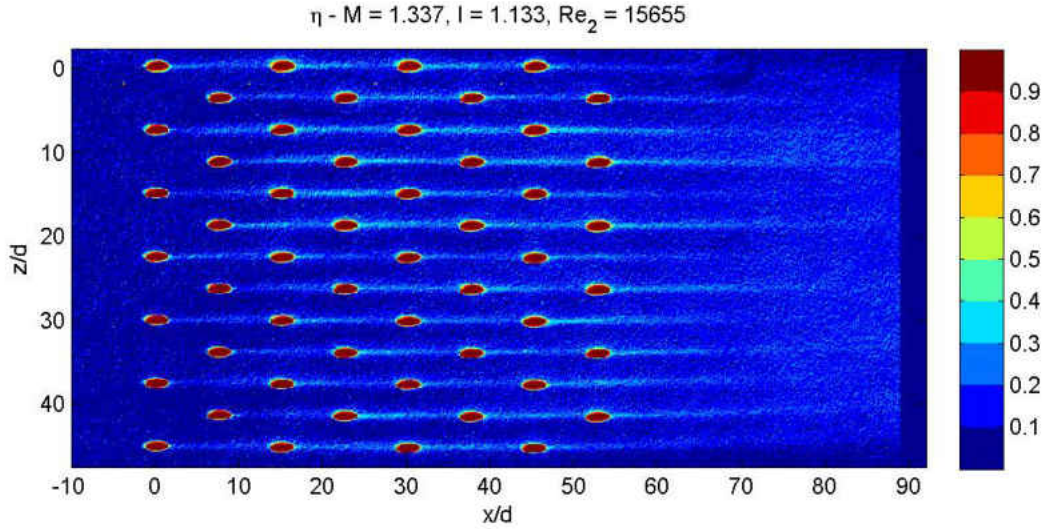


Figure 5.46: Geometry 1b, $M = 1.34$; spatially resolved η

5.9.1.3 Geometry 2: 14 x 10 Cylindrical Array

Geometry 2 is the large spacing round hole array. Results are shown in Figures 5.47 through 5.52. Qualitatively Geometry 2 behaves the same as Geometry 1; however, due to the increased spacing there is less row-to-row interaction. Adjacent jets do not meet each other for most conditions. This increased spacing results in significantly lower levels of effectiveness in mid-pitch regions. This will be shown quantitatively in §5.9.3 through lateral averages.

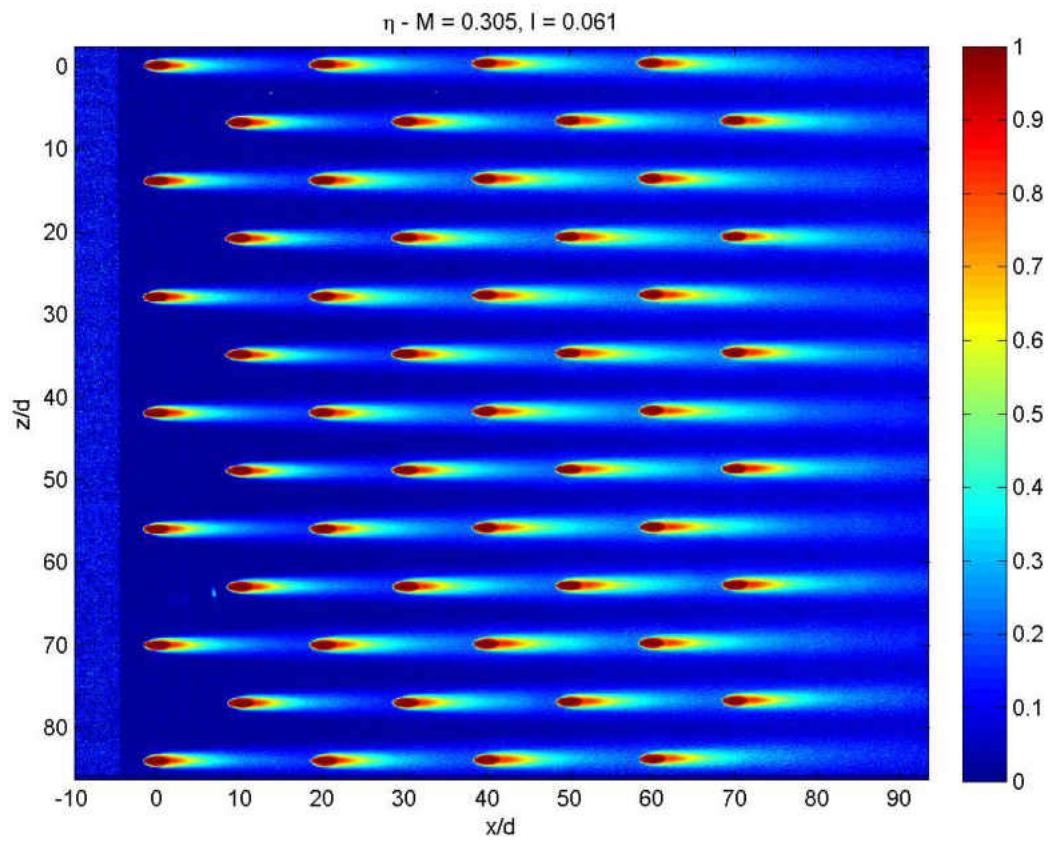


Figure 5.47: Geometry 2, $M = 0.31$; spatially resolved η

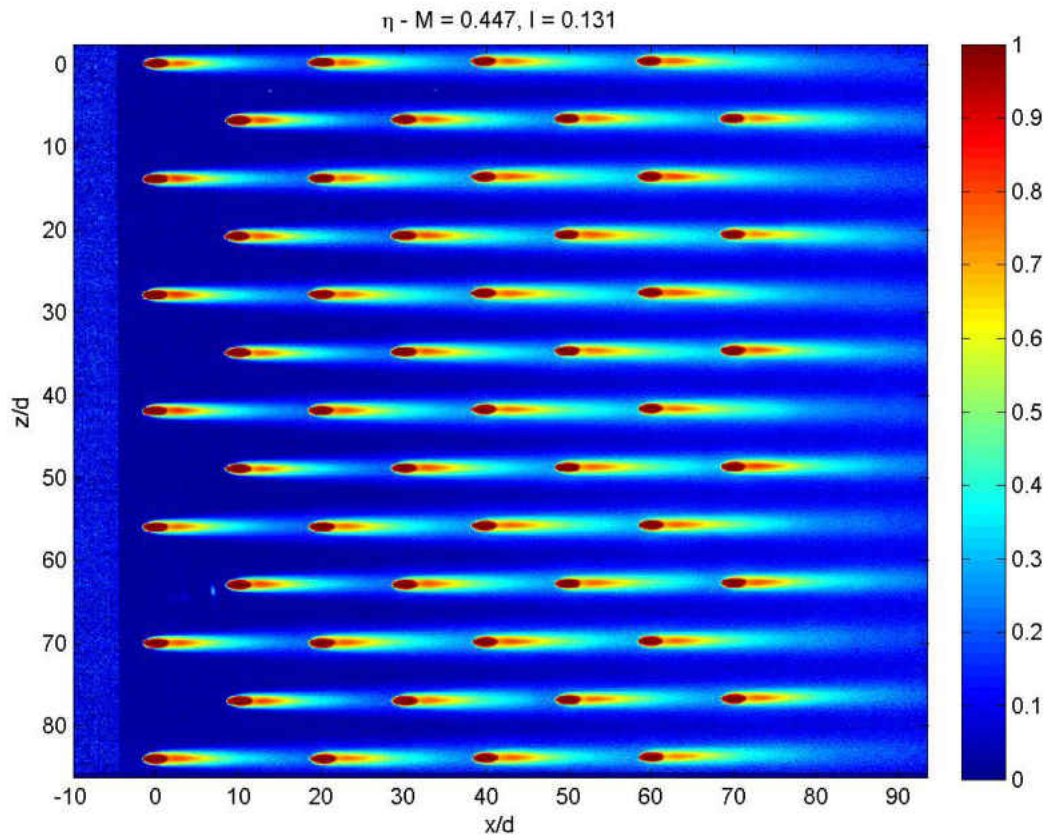


Figure 5.48: Geometry 2, $M = 0.45$; spatially resolved η

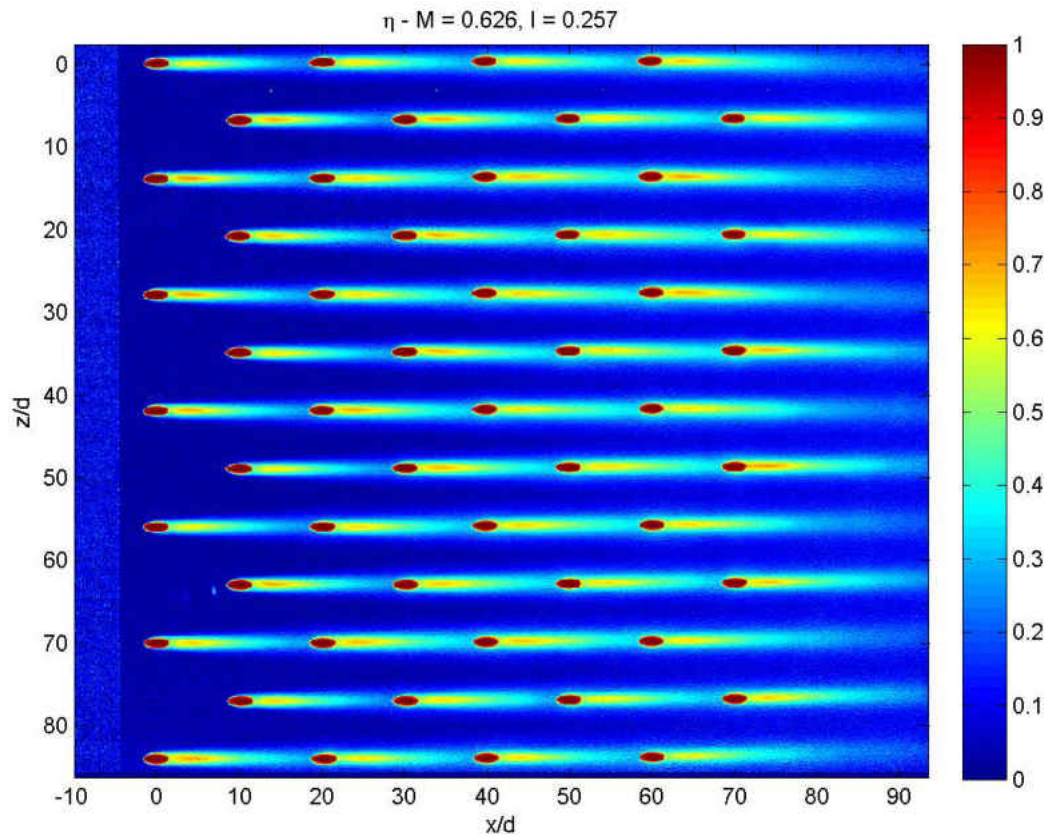


Figure 5.49: Geometry 2, $M = 0.63$; spatially resolved η

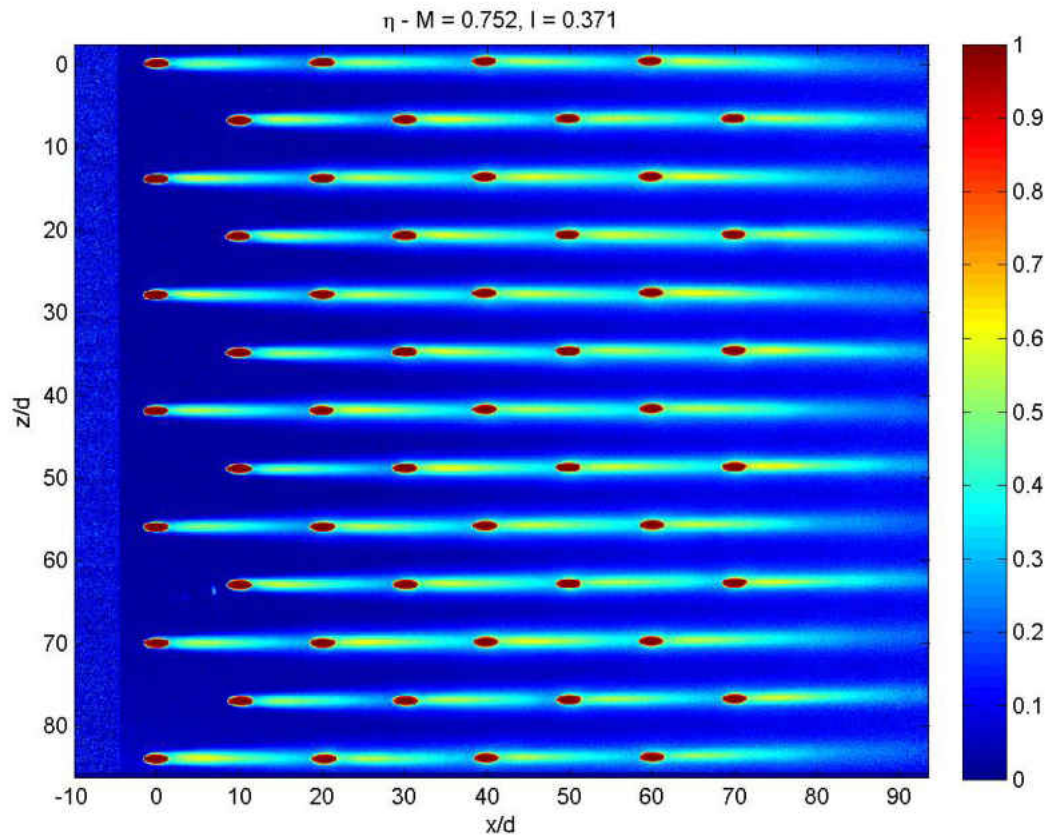


Figure 5.50: Geometry 2, $M = 0.75$; spatially resolved η

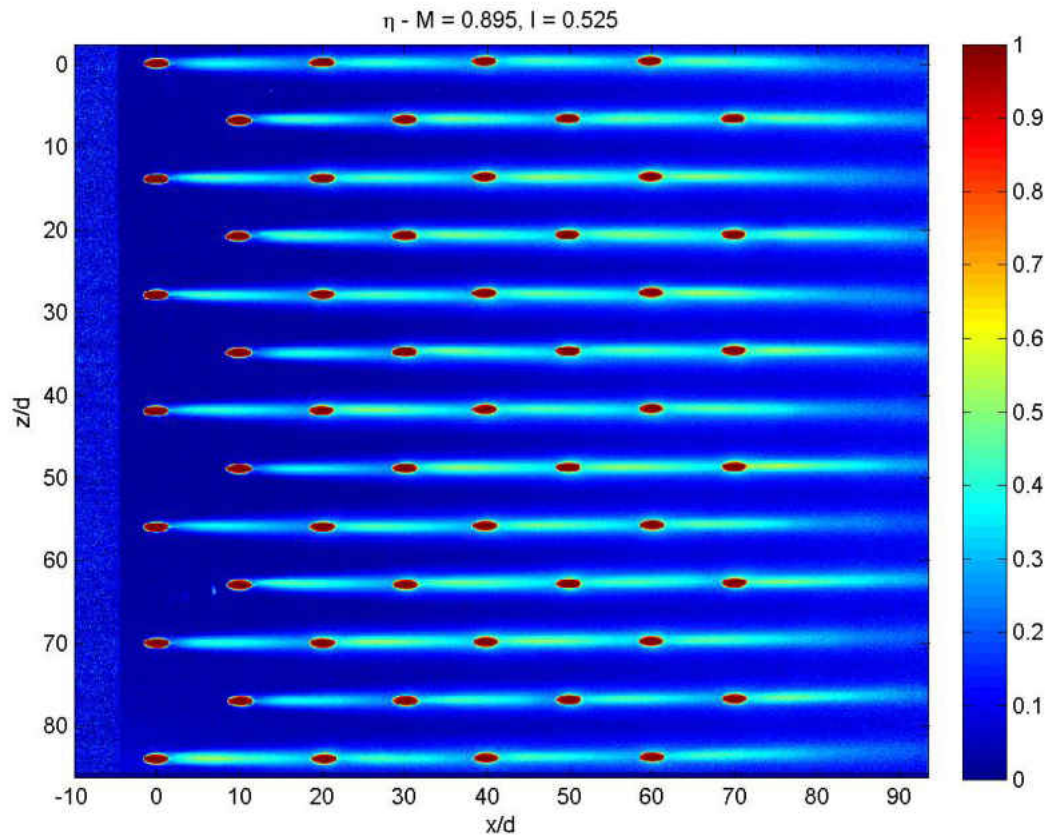


Figure 5.51: Geometry 2, $M = 0.90$; spatially resolved η

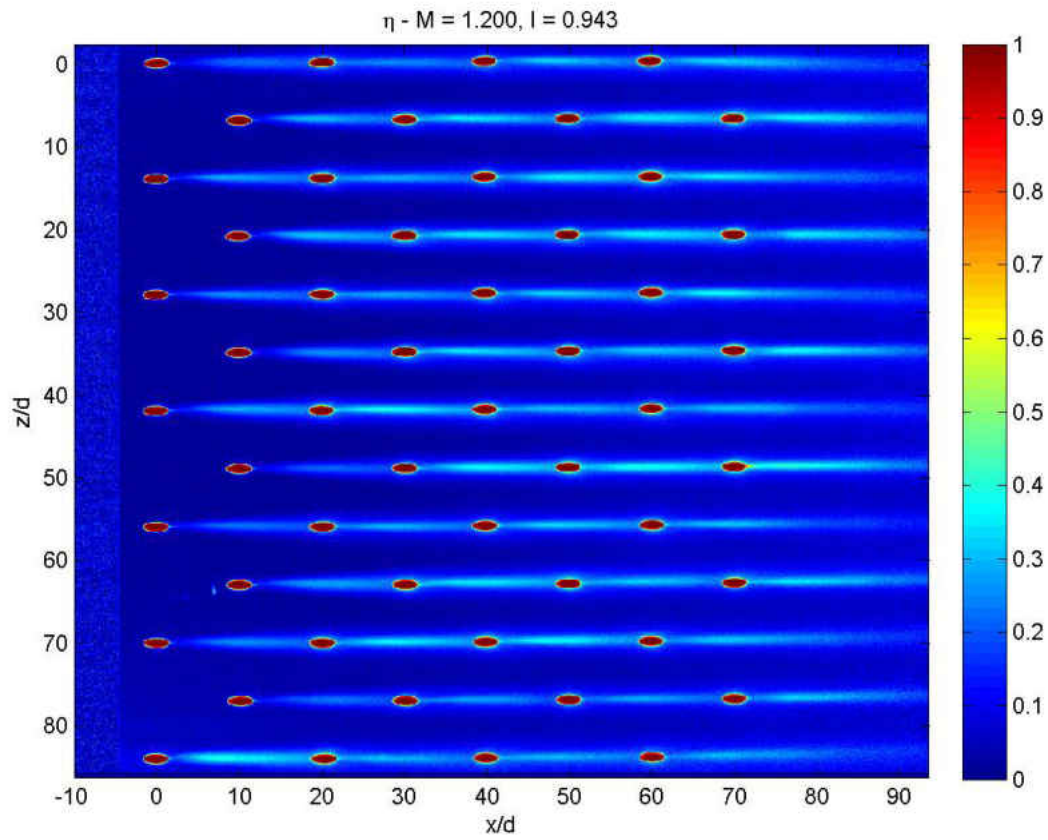


Figure 5.52: Geometry 2, $M = 1.20$; spatially resolved η

5.9.1.4 Geometry 5: 7.5 x 7.5 Diffuser Array

Geometry 5 is composed of the diffuser (described in Table 2.3) at the smaller spacing investigated. Significant local differences are observed in the effectiveness profiles shown in Figures 5.53 through 5.56. This non-uniformity is more apparent as the blowing ratio is increased. The large expansion angles, $\phi_1 = \phi_2 = 14^\circ$, causes the hole to act as an over expanded diffuser in which the coolant flow does not remain attached to both lateral walls. At high M there is typically a separation off either one or both lateral walls. At $M = 0.5$ most coolant jets remain attached to the lateral walls of the holes, but at $M = 1$ most holes are already looked slightly separated. Despite the apparent wasting of coolant the levels of η increase in the downstream region. By $M = 2.2$ the coolant jets are severely skewed to 1 lateral wall of the holes. Still, there are large streaks of local values of effectiveness as high as $\eta = 0.8$. Many jets coalesce and merge at this low spacing. This tight spaced diffuser array, Geometry 5, represents an over-cooled configuration for most applications.

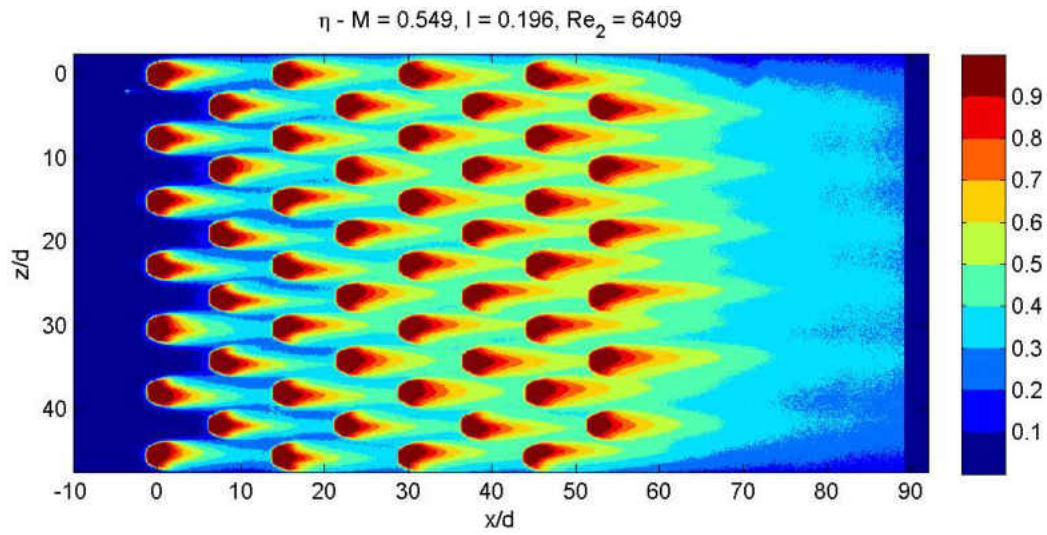


Figure 5.53: Geometry 5, $M = 0.549$; spatially resolved η

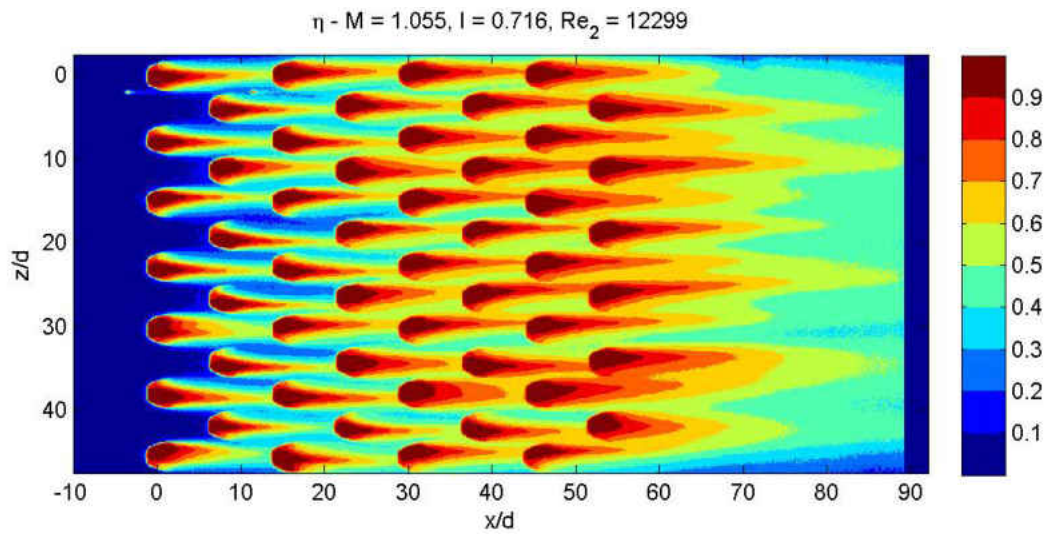


Figure 5.54: Geometry 5, $M = 1.06$; spatially resolved η

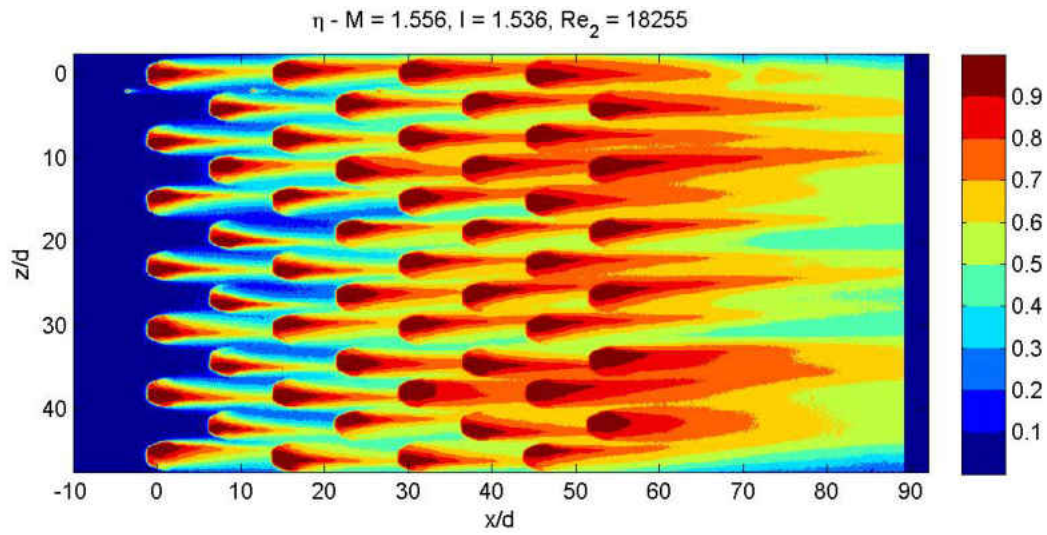


Figure 5.55: Geometry 5, $M = 1.56$; spatially resolved η

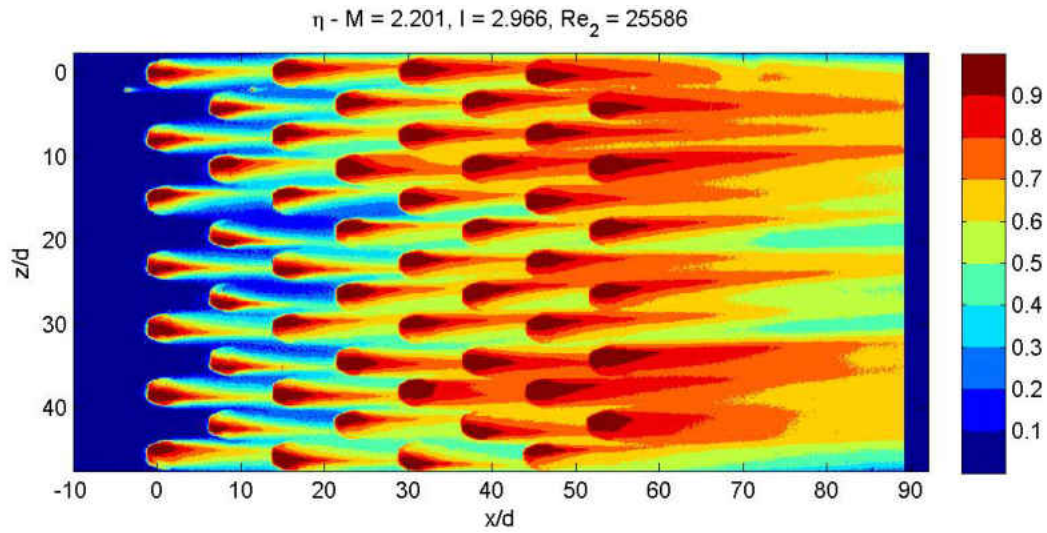


Figure 5.56: Geometry 5, $M = 2.20$; spatially resolved η

5.9.1.5 Geometry 6: 14 x 10 Diffuser Array

Geometry 6 is composed of the diffuser geometry at the large spacing investigated. Again, significant local differences are observed in the effectiveness profiles from Figures 5.57 through 5.60. In the low blowing ratio of $M = 0.5$ most of the coolant jets remain attached to both lateral walls of the diffuser holes. Again, at $M = 1$ many coolant jets are beginning to shift towards one side of their diffuser, yet many remain attached and the separation isn't sever in the ones that are showing signs of separating. By $M = 1.6$ most jets are separated from one of the lateral walls in the diffusers. Despite the lateral separation within the hole most jets do not seem to separate from the target wall. There is little to no evidence of jet liftoff. The main difference between this spacing and the lower spacing diffusers is that there is no jet coalescence. This results in much lower peak magnitudes of effectiveness downstream of the holes.

5.9.2 Spatially Resolved Uncertainty Estimates, $u_\eta(x_i/d, z_j/d)$

The procedure from [81] described in §5.8 was applied to the results from Geometry 1. Figures 5.61 through 5.67 show the uncertainty maps for Geometry 1. These uncertainty maps are representative of the other geometries.

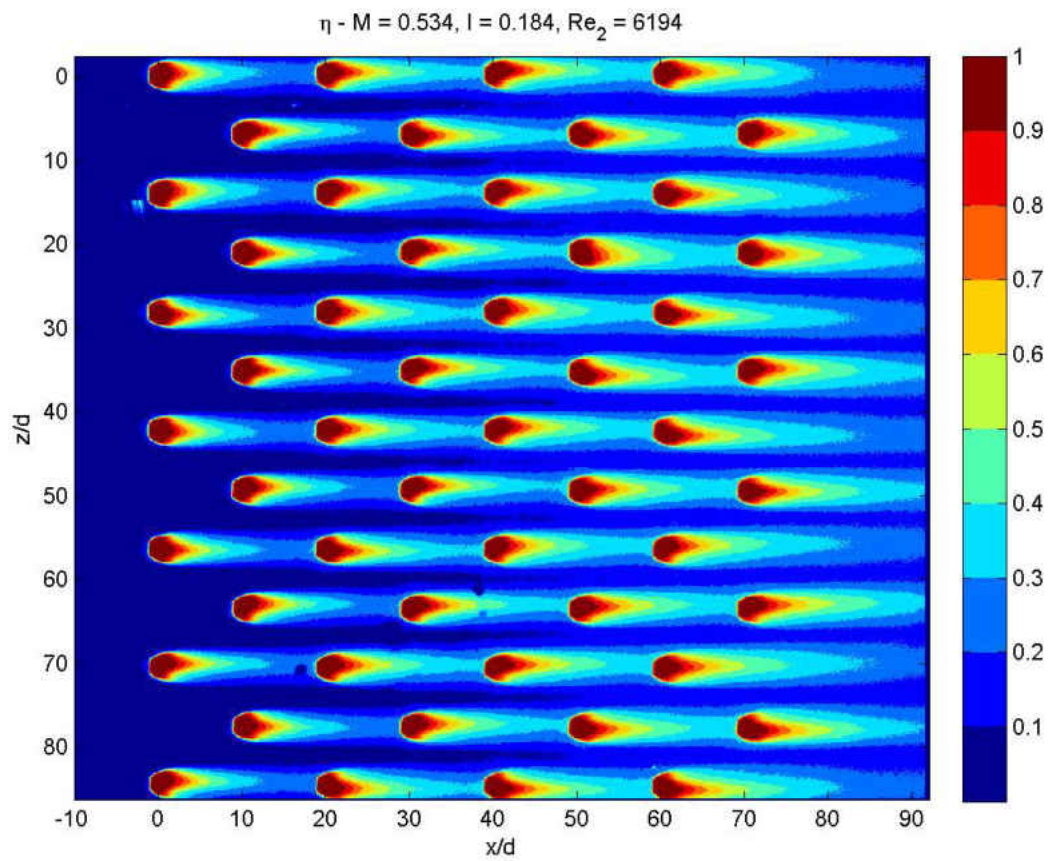


Figure 5.57: Geometry 6, $M = 0.53$; spatially resolved η

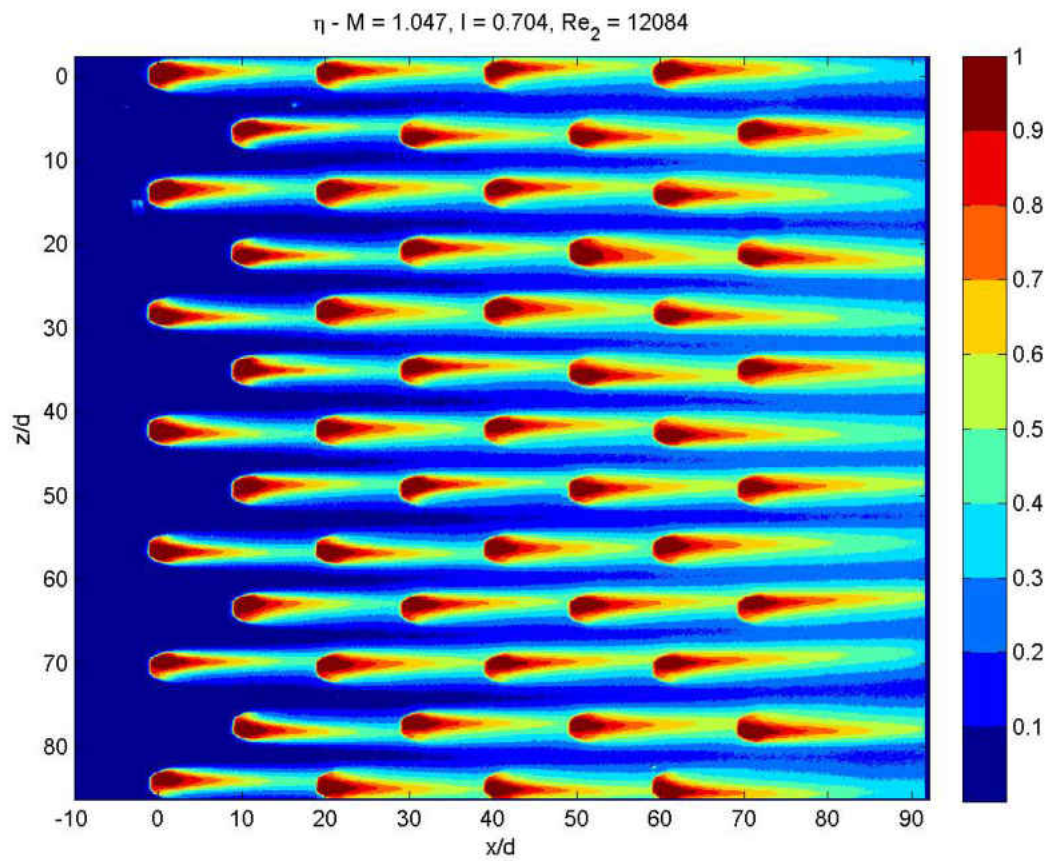


Figure 5.58: Geometry 6, $M = 1.05$; spatially resolved η

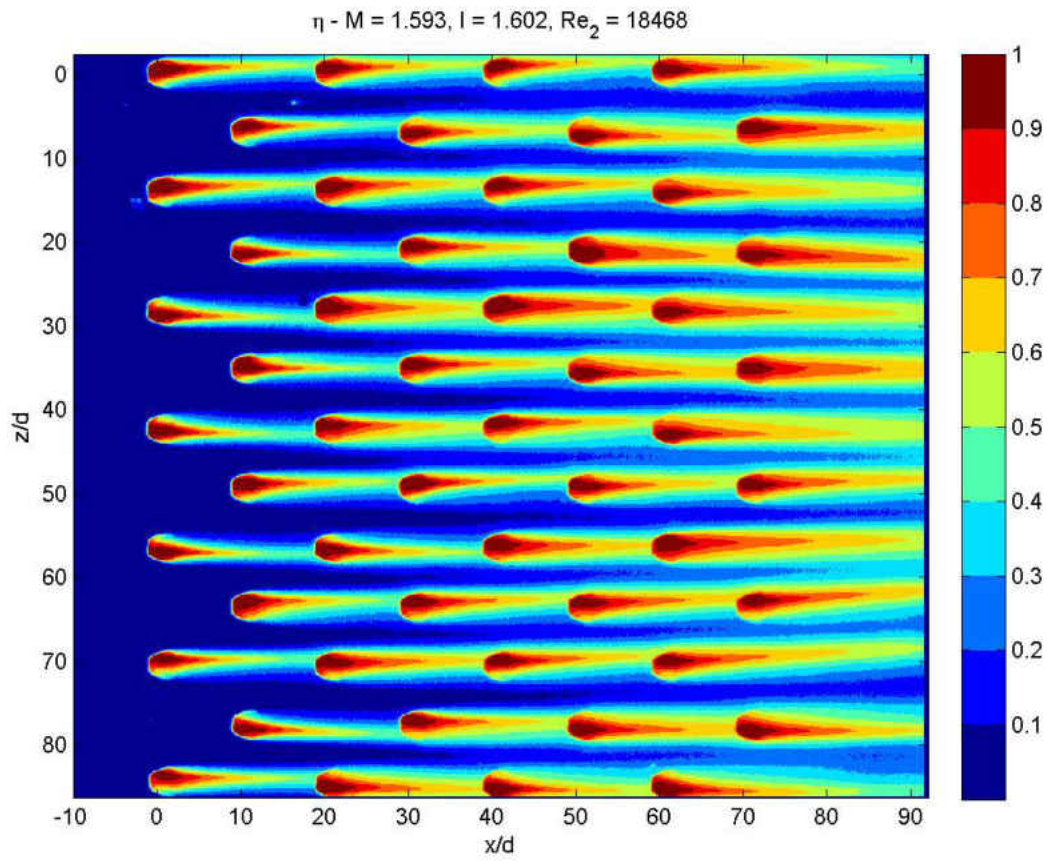


Figure 5.59: Geometry 6, $M = 1.59$; spatially resolved η

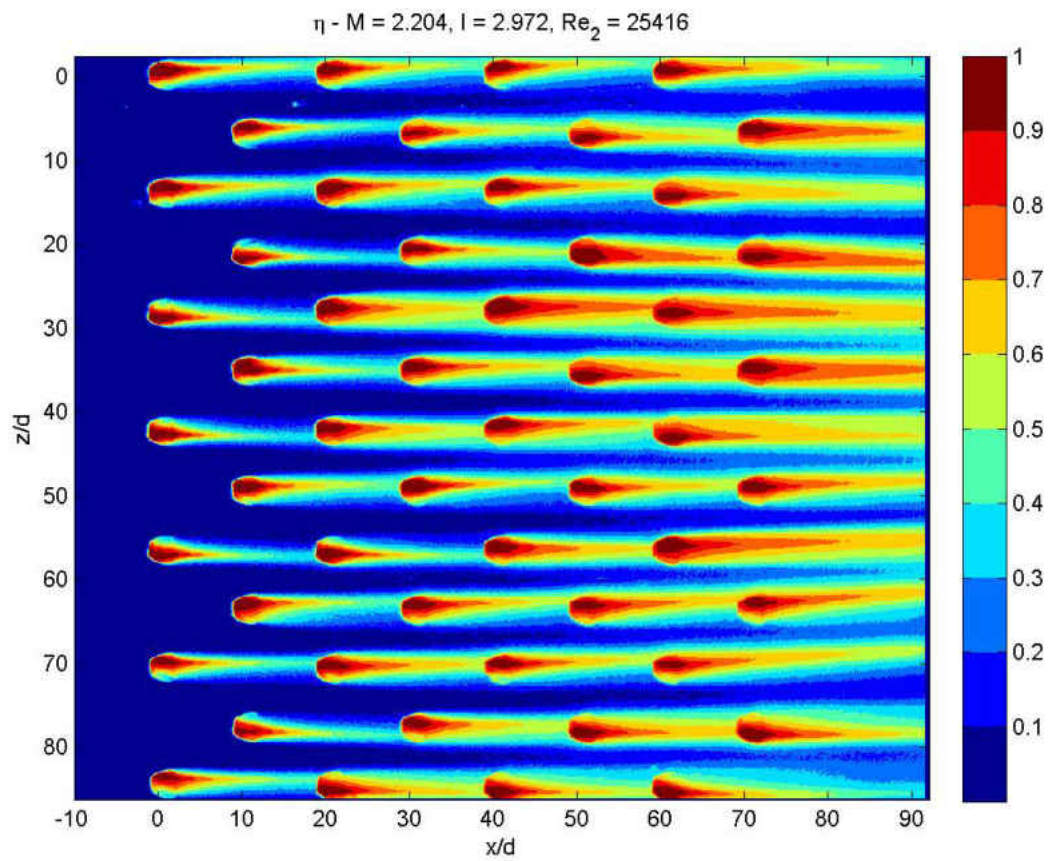


Figure 5.60: Geometry 6, $M = 2.20$; spatially resolved η

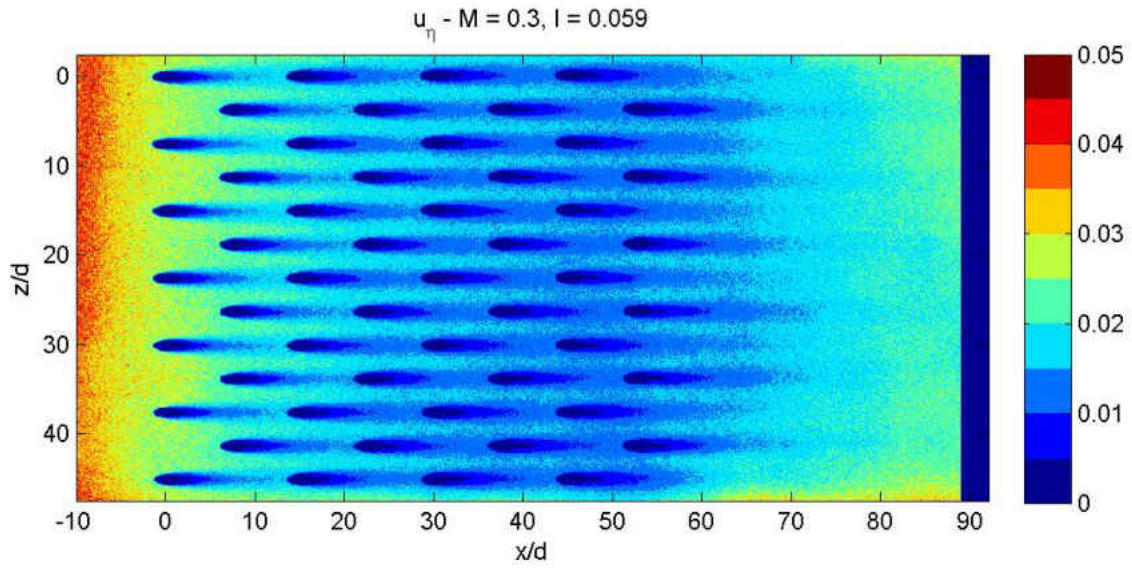


Figure 5.61: Geometry 1: $u_\eta(x_i/d, z_i/d; M = 0.30)$, spatially resolved uncertainty estimate

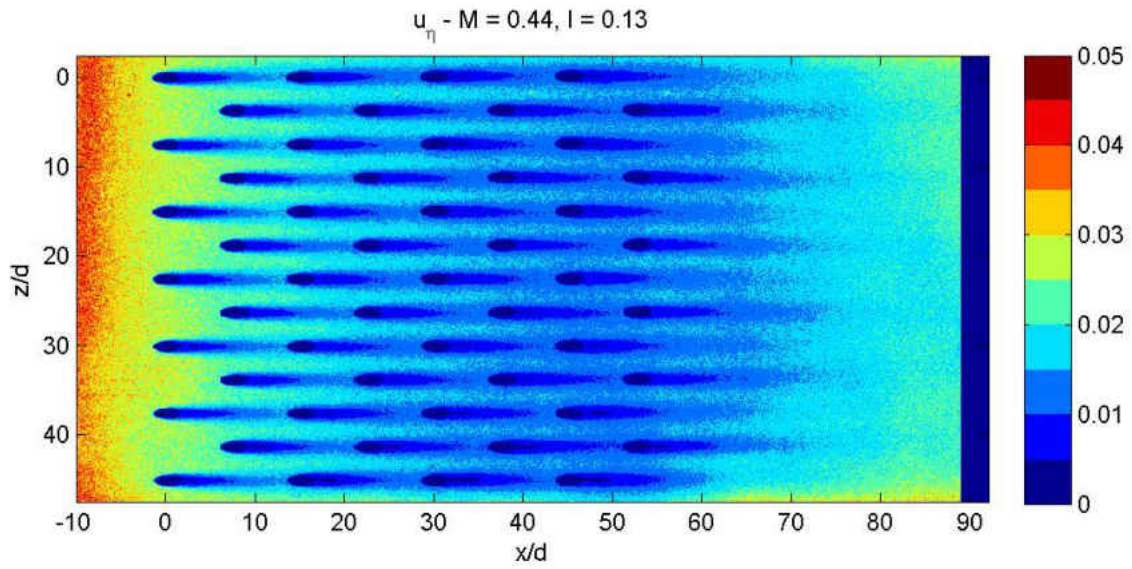


Figure 5.62: Geometry 1: $u_\eta(x_i/d, z_i/d; M = 0.44)$, spatially resolved uncertainty estimate

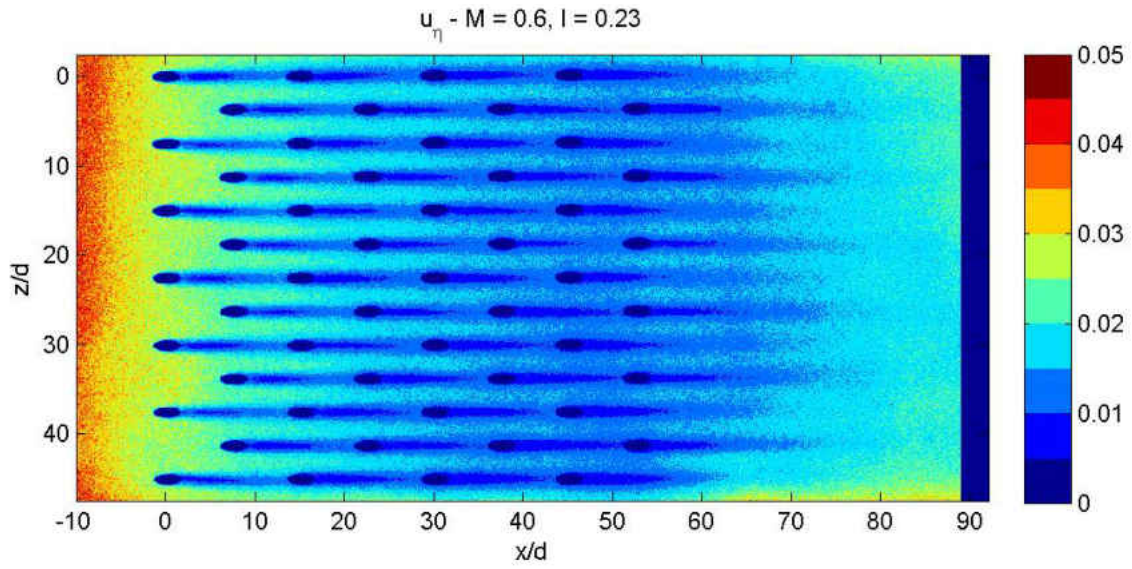


Figure 5.63: Geometry 1: $u_\eta(x_i/d, z_i/d; M = 0.60)$, spatially resolved uncertainty estimate

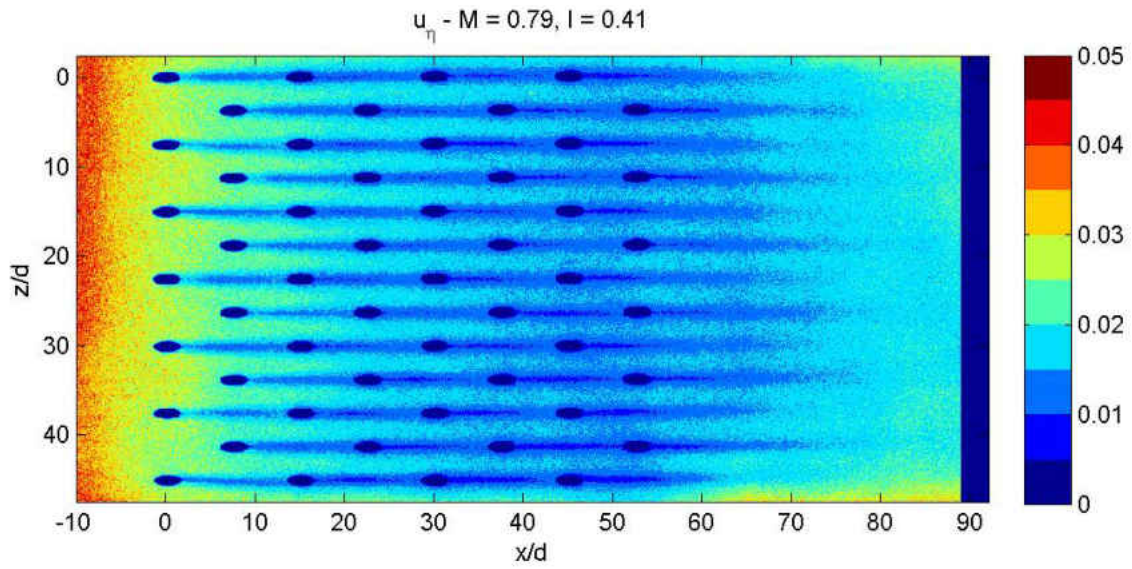


Figure 5.64: Geometry 1: $u_\eta(x_i/d, z_i/d; M = 0.79)$, spatially resolved uncertainty estimate

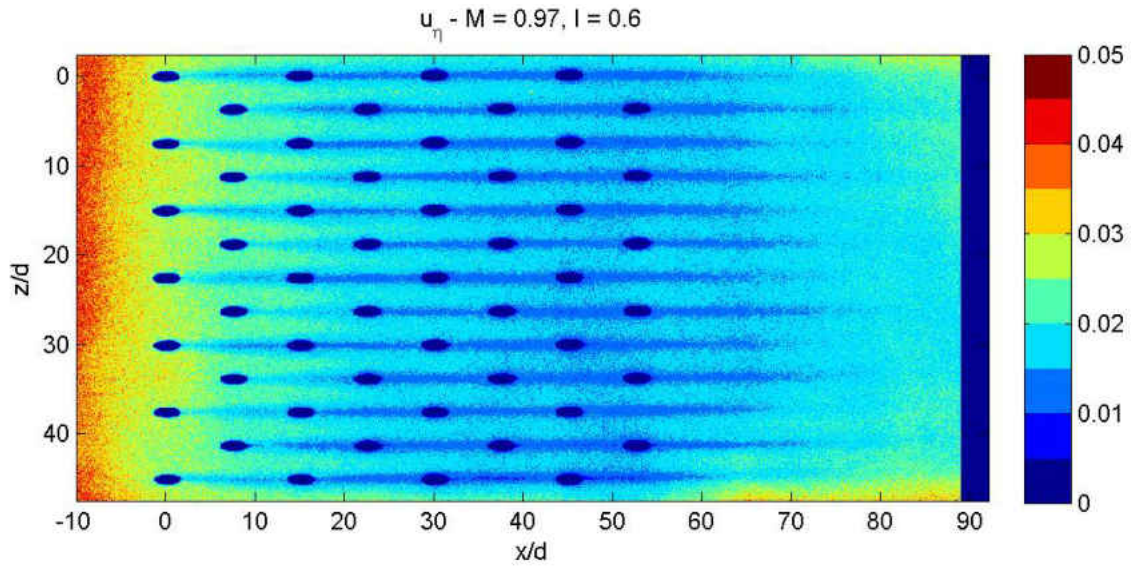


Figure 5.65: Geometry 1: $u_\eta(x_i/d, z_i/d; M = 0.97)$, spatially resolved uncertainty estimate

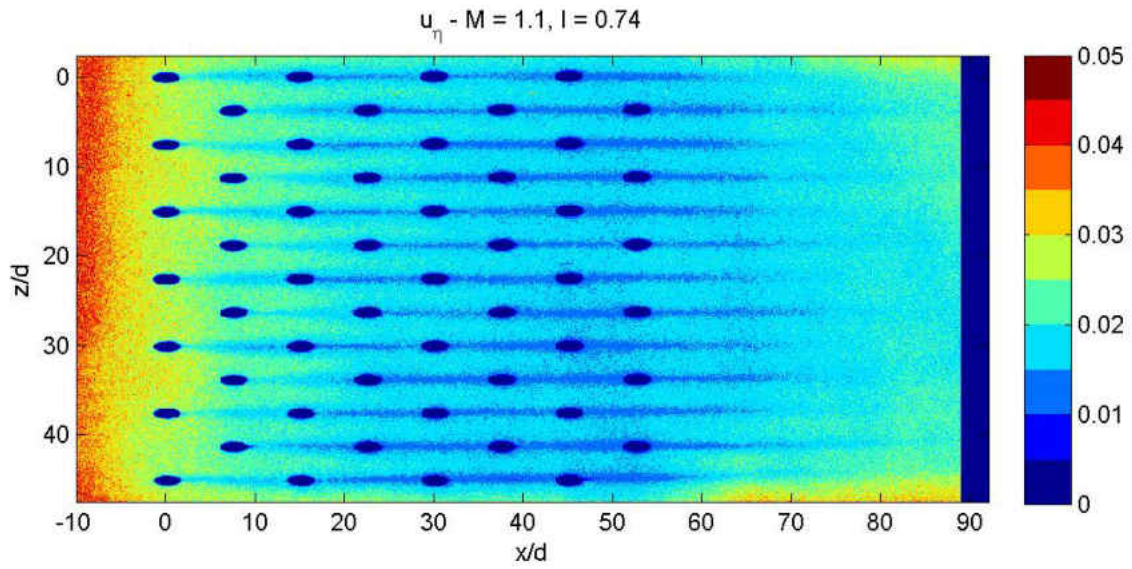


Figure 5.66: Geometry 1: $u_\eta(x_i/d, z_i/d; M = 1.08)$, spatially resolved uncertainty estimate

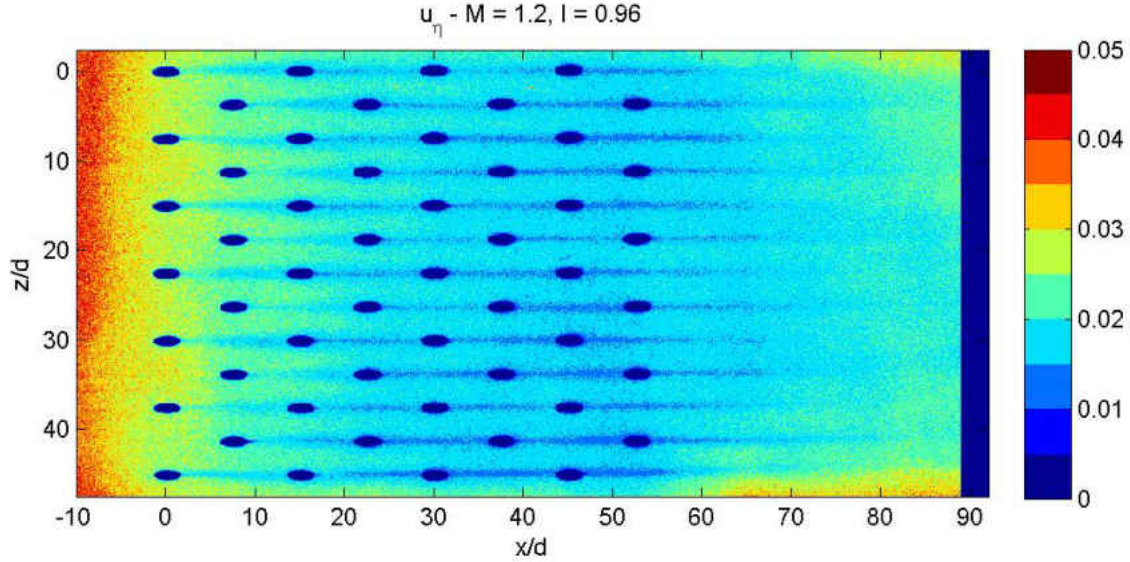


Figure 5.67: Geometry 1: $u_\eta(x_i/d, z_i/d; M = 1.23)$, spatially resolved uncertainty estimate

Two important observations can be made from these results. 1) The preliminary propagation of error analysis shows the proper trend for uncertainty (high u_η at low η) and 2) the raw reference intensity values influence the uncertainty in pressure ratio (high u_{PR} at low I_r). This is supported by Figure 5.68 which shows the relationship between u_η and η as determined from a propagation of error analysis of the experimental data. This takes into account all random error sources beginning from the intensity measurements and including the calibration curve fit uncertainty. The overall trend is consistent with the prediction shown by Figure 5.5 in §5.6. The vertical scatter in the results is due to the raw intensity values; with low intensity corresponding to higher uncertainty. This shows that at high η values the results are less sensitive to reference intensity while at low η values a high reference intensity is important in reducing experimental uncertainty.

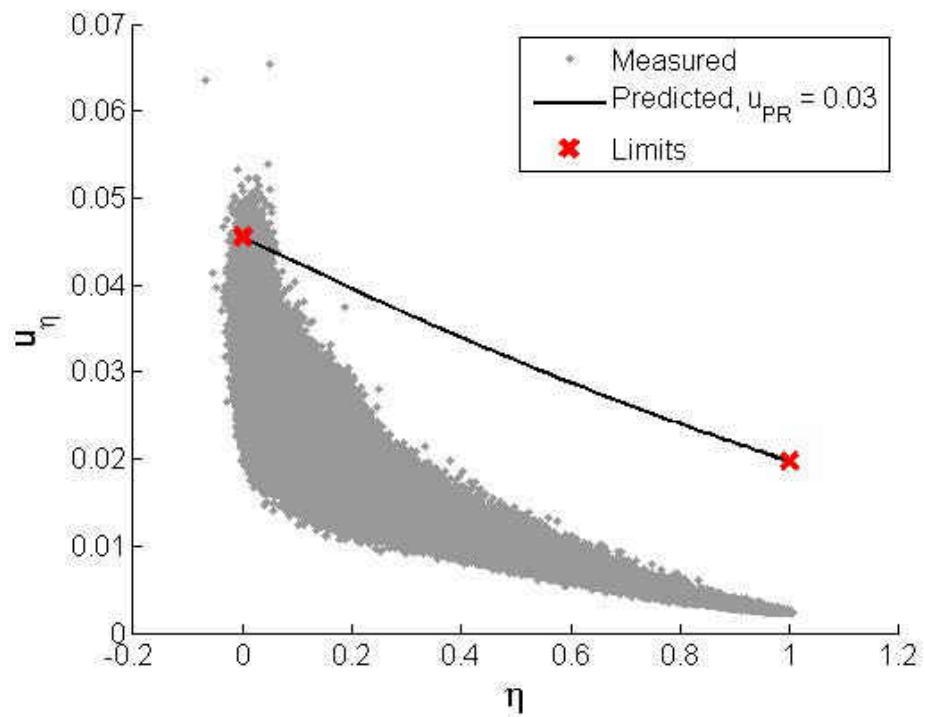


Figure 5.68: Geometry 1: $u_\eta(\eta; M = 0.30)$, relation between uncertainty in effectiveness with effectiveness, incorporating all random error sources beginning with intensities

5.9.3 Laterally Averaged Effectiveness for Multi-Row Geometries

Spatially resolved profiles can then be averaged over the lateral direction to yield a laterally averaged adiabatic film cooling effectiveness, $\bar{\eta}$. This averaging must be taken over integers of the lateral pitch to not bias the result in anyway. This averaging process is carried out over the center three pitches. In this way no edge effects are included in the averaged region and the lateral average represents the average of an infinitely wide multi-row film cooling array. The regions not at $y = 0$, i.e. within the holes, are included in this average. This could have been avoided with a spatial mask; however, it was decided to incorporate the pixel values obtained from looking into the hole. For the cylindrical geometries these values are within experimental uncertainty of $\eta = 1$. For the diffuser cases the onset of separation from the lateral walls of the hole interior causes some regions within the hole to be less than 1. These features are quantitatively incorporated in the lateral averaged profiles.

$$\bar{\eta}(x_i/d) = \sum_{z_i=z_0}^{z_i=z_0+N*P_z/d} \eta(x_i/d, z_i/d) \quad (5.37)$$

Laterally averaged effectiveness profiles, $\bar{\eta}$, are shown for all blowing ratios tested and all geometries in Figures 5.69 through 5.73. In all geometries studied, the the first blowing ratio tested is in the mass addition regime. This results in the second blowing ratio (a slight increase over the first) causing increased values of $\bar{\eta}$ throughout the entire domain. At the point the effect of increasing the blowing ratio results in increasing the downstream effectiveness while at the same time lowering the upstream effectiveness. For example take Geometry 1 shown in Figure 5.69; an increase of blowing ratio from $M = 0.44$ to 0.60 results in $\bar{\eta}$ decreasing throughout most of the array while increasing $\bar{\eta}$ in the recovery region, past $x/d = 60$. Something similar is seen increasing to $M = 0.8$. At this point the performance begins to drop everywhere as the blowing ratio is increased. This same behavior is representative of all multi-row film cooling arrays studied and was also observed by Natsui et al. [41].

The story is only slightly different for the diffuser arrays, Geometries 5 and 6. Figure 5.73 shows that as the blowing ratio is increased, Row 1 continues to drop off in performance, but, after a couple rows there is a continual increase in effectiveness as the blowing ratio is increased. The maximum blowing ratio tested for the diffuser arrays is $M = 2.2$ which is likely not high enough to get into the fully penetrating regime at which point we would expect to see the performance drop off even in the recovery region.

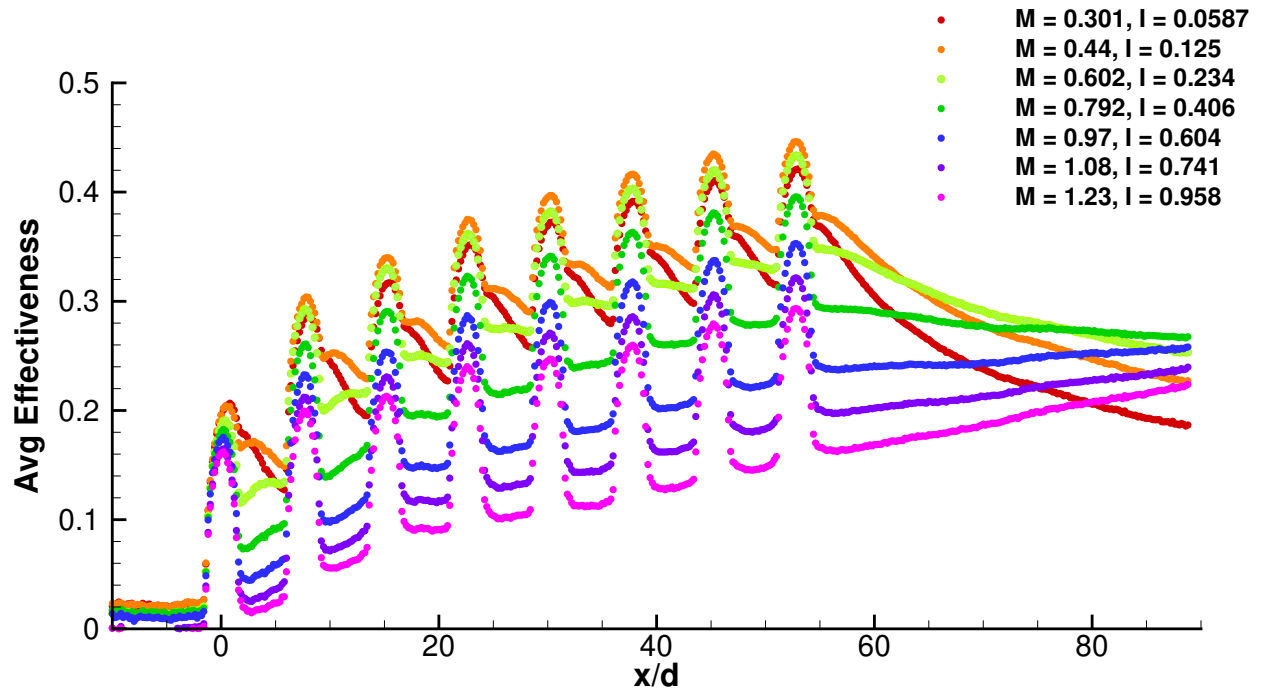


Figure 5.69: $\bar{\eta}(x_i/d; M)$ for Geometry 1

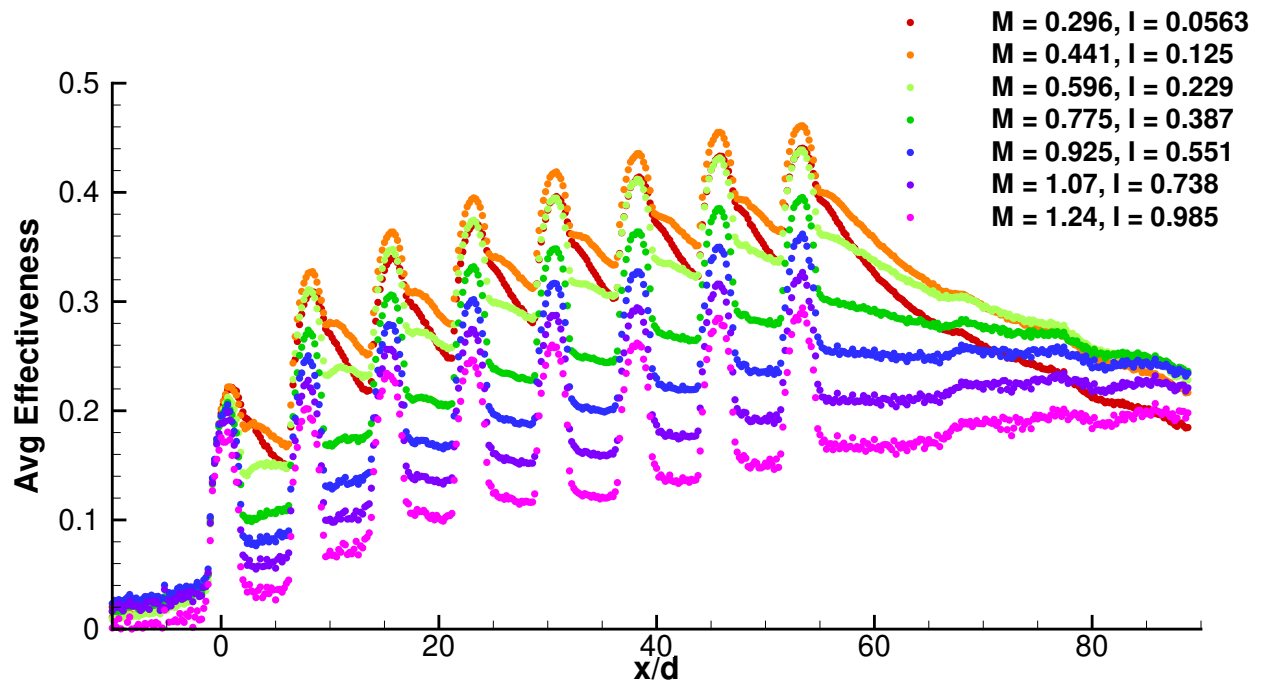


Figure 5.70: $\bar{\eta}(x_i/d; M)$ for Geometry 1b

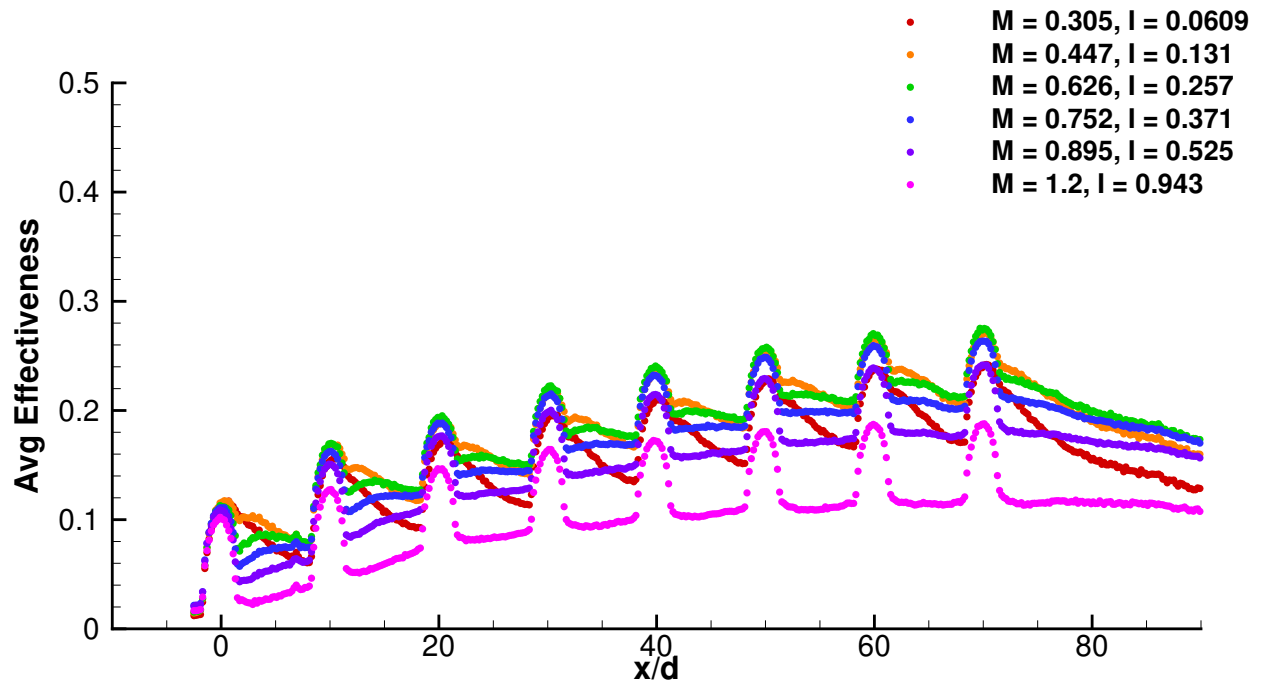


Figure 5.71: $\bar{\eta}(x_i/d; M)$ for Geometry 2

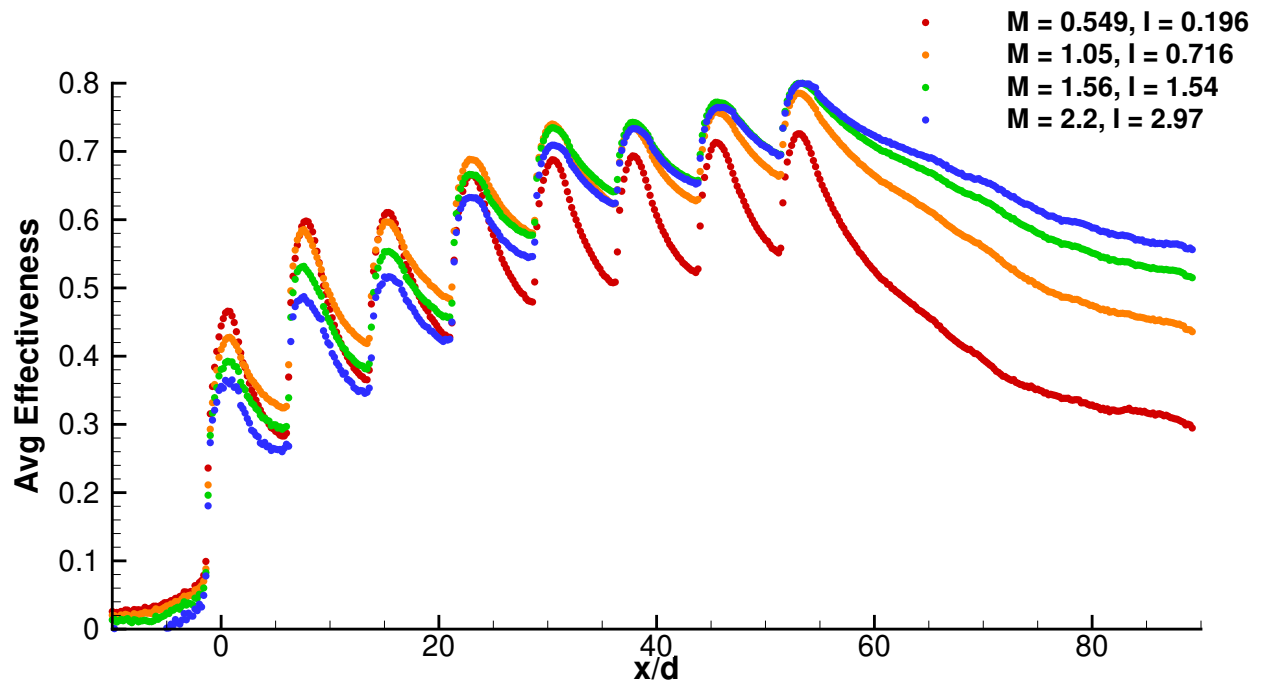


Figure 5.72: $\bar{\eta}(x_i/d; M)$ for Geometry 5

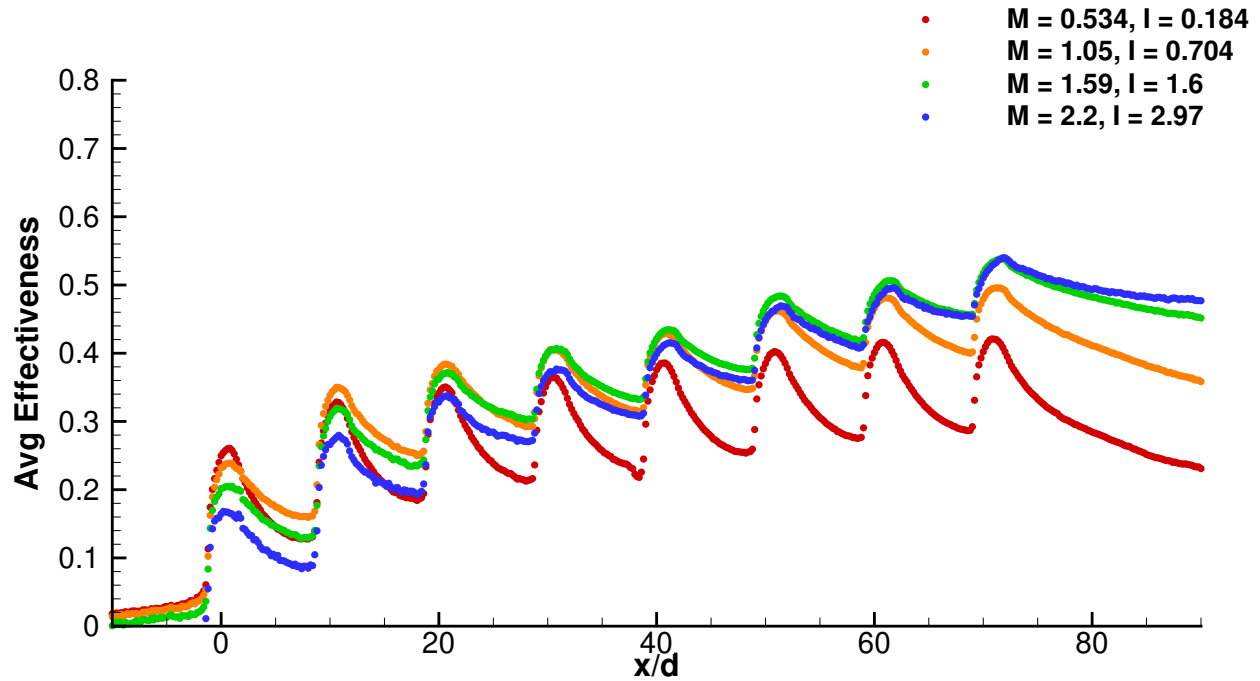


Figure 5.73: $\bar{\eta}(x_i/d; M)$ for Geometry 6

5.9.4 Testing of Stereolithography Manufactured Hardware

For lower cost compared to traditional machining, and to enable a faster work flow from geometry creation to testing, a rapid manufacturing technique is desirable. Stereolithography (SLA) is an additive manufacturing technique which involves curing a resin with a light source in order to build up a model in layers. Unfortunately the cured resin has some downsides which are listed below.

1. Glass point temperature is less than the PSP curing temperature
2. Stepping results in surface roughness
3. Transmissive to wavelengths of PSP emission and excitation

4. Geometric tolerances, especially after PSP preparation

Because of the many benefits associated with SLA manufactured parts it is worthwhile to find a way to mitigate these issues.

Figure 5.74 shows an image of SLA hardware which was prepared and tested the same way as Aluminum hardware, in which high intensity regions around the holes were seen. This is evidence of transmission through the SLA substrate.

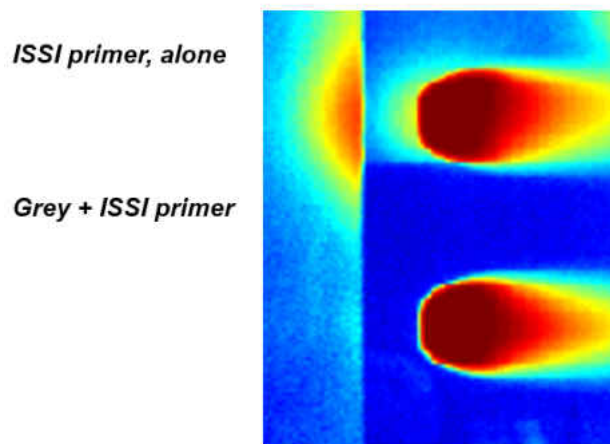


Figure 5.74: SLA Transmission

To verify the SLA substrate is transmissive, a LED was placed behind the material to make sure it is not fully opaque. Figure 5.75 shows the emission from the LED passes through the SLA. This is the reason there were bright spots around the holes.



Figure 5.75: LED shining through SLA test hardware

A diagram showing the mechanism for large errors in the vicinity of the hole is shown in Figure 5.76. Regions of paint which are exposed to CO_2 , less O_2 , emit more light during the test image. This is a diffuse emission which sends light in all directions. Some of the light encounters the SLA material around the paint and instead of being reflected or absorbed the transmissive SLA allows the light to pass. This light is then seen by the CCD in regions where there was no increase in emission due to the presence of CO_2 . The increased signal from these regions is due to emission from other sources passing through this region.

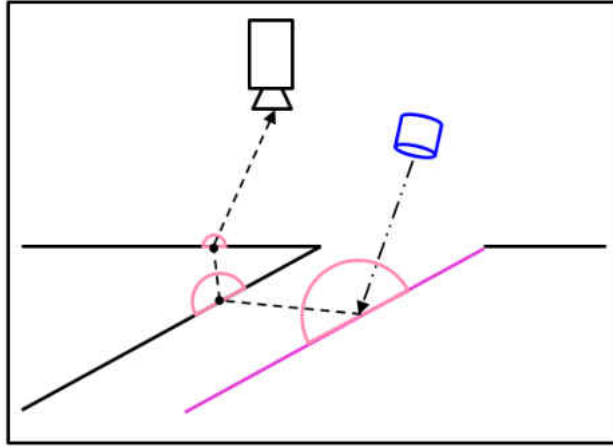


Figure 5.76: SLA Transmission

To eliminate this, a series of thick primers was applied to determine which primer combination best eliminates transmission of light through the substrate. The four primers tested are shown in Figure 5.77. A metallic primer was chosen because the goal is to make the SLA behave like the Aluminum substrate. White was chosen because it will yield the highest signal. Grey was chosen in hopes of absorbing as much incident light as possible. The ISSI FIB base coat was chosen because that is the most commercially available base coat specifically for PSP testing.



Figure 5.77: Four primers tested to see which combination can best eliminate transmission through the SLA substrate

Figure 5.78 shows the different combinations of primers which were evaluated. The left image shows their physical appearance and the right image shows results through the first two rows of results. After this screening a combination of 2 white layers then 3 silver layers then 2 white layers was chosen moving forward.

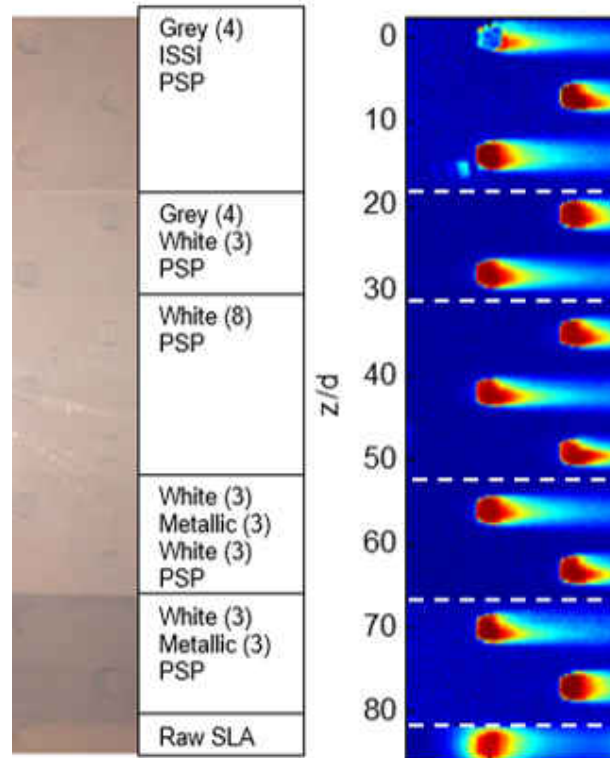


Figure 5.78: Different primer combinations tested

To assess the quality of the SLA measurements a comparison between Geometry 1 and 1b is shown in Figure 5.79. There is good quantitative agreement between the two results; however, there is a significant “waviness” to the SLA results. This effect can likely be minimized by thicker primer coats but this is a good example of the difficulties associated with obtaining high quality results from SLA hardware.

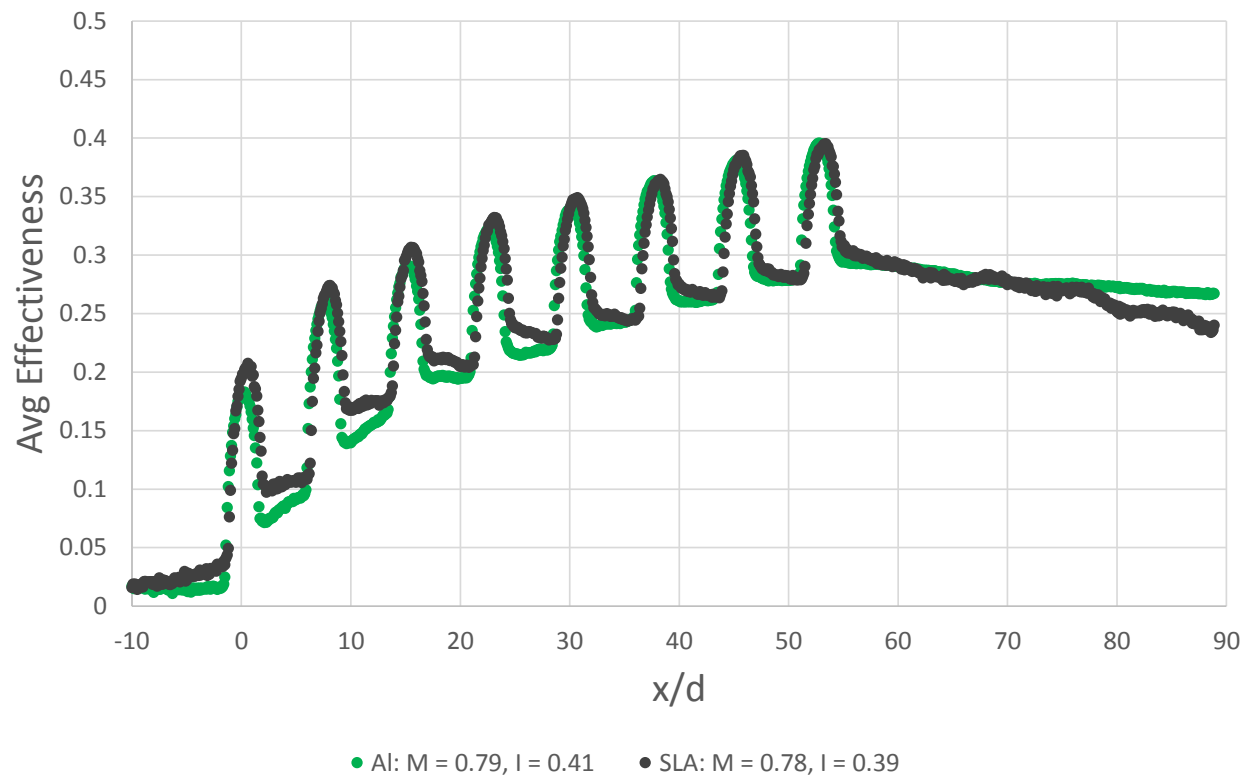


Figure 5.79: Aluminum hardware compared with SLA hardware

5.9.5 Auto-Illumination

Upstream bias, η_b , during single row testing was very low $-0.01 < \eta_b < 0.02$. During multi row testing values of η_b were as large as 0.1. Therefore, it is conjectured that the effectiveness in the array influences the level of bias seen upstream of injection. This could be explained by the increase of emission of the PSP reflecting within the tunnel. Stray light would increase the intensity values upstream resulting in non-zero values of effectiveness. There is evidence of stray emission in the tunnel which is shown in Figure 5.80. In this Figure there are 7 bright spots corresponding to the first row of holes which can be seen in a flange on the top wall.

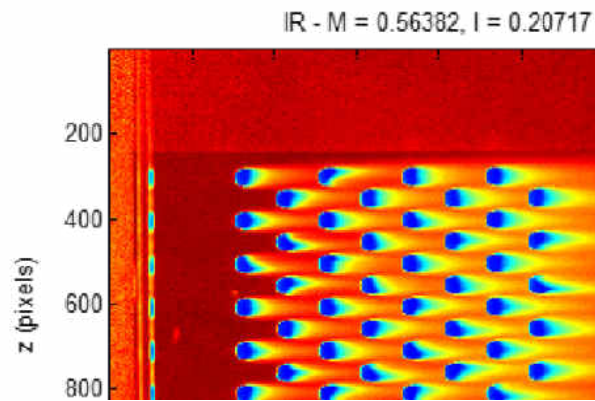


Figure 5.80: Evidence of reflections within the wind tunnel

The mechanism for one cause of upstream bias is shown in Figure 5.81. The PSP emission which was not present in the reference image is reflected within the tunnel, impacts a region and is then seen by the CCD. This apparent increase in intensity is taken as an increased concentration of CO_2 during processing which results in upstream bias. This shows that the reflectivity of the interior of the tunnel is important to control and minimize. For this reason the interior is painted with a matte black paint to best try to eliminate stray reflections.

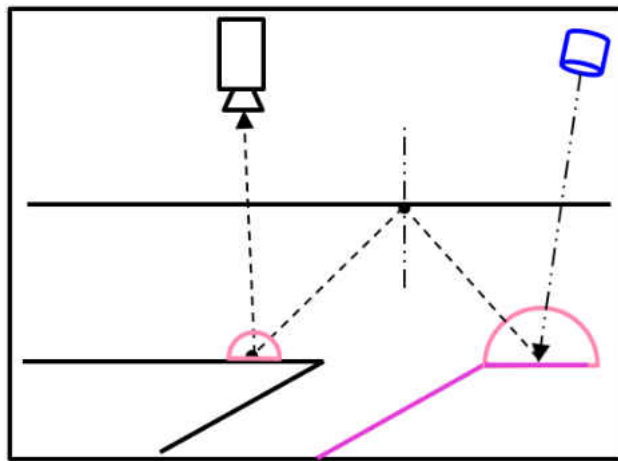


Figure 5.81: Schematic of how reflections can influence results

5.9.6 Gas Sampling

The gas sampling technique used by Pedersen et al. [9] was selectively used in this study to verify the PSP results. A Siemens Ultramat23 CO₂ analyzer, shown in Figure 5.82, was used to draw near wall fluid and analyze the concentration. This is analogous to a PR measurements and must then be input to Equation 5.8 to yield η . Taps are located at 75% pitch, $2d$ upstream of rows 1, 3, 5 and 7. Figure 5.83 shows the gas sampling tap locations.



Figure 5.82: Siemens Ultramat 23 gas analyzer used for gas sampling measurements

Suctions holes of $1/32$ " diameter are located in each plate. With a analyzer flow rate of 1.5 l/min this means a suction velocity at the wall of 50 m/s. This is expected not to influence the flow over the coupon despite the high velocity due to the very low amount of mass drawn through the tap. This was verified by taking images with and without the suction active and no difference was observed in the local profiles of η .

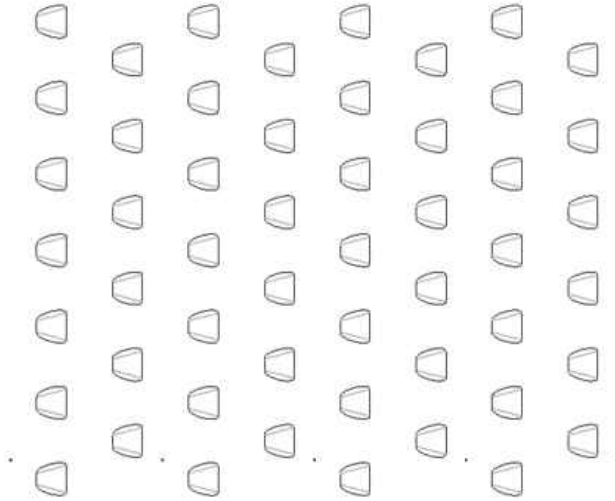


Figure 5.83: Gas sampling tap locations, shown on Geometry 5

In the following plots, Figures 5.84 - 5.90, *PSP* results are compared with gas sampling results. PSP results are taken from $\eta(x_i/d, z/d = P_z/d/4)$ corresponding to the lateral location of the taps and all streamwise locations. In this way any defects the tap would cause in η can be identified and ignored.

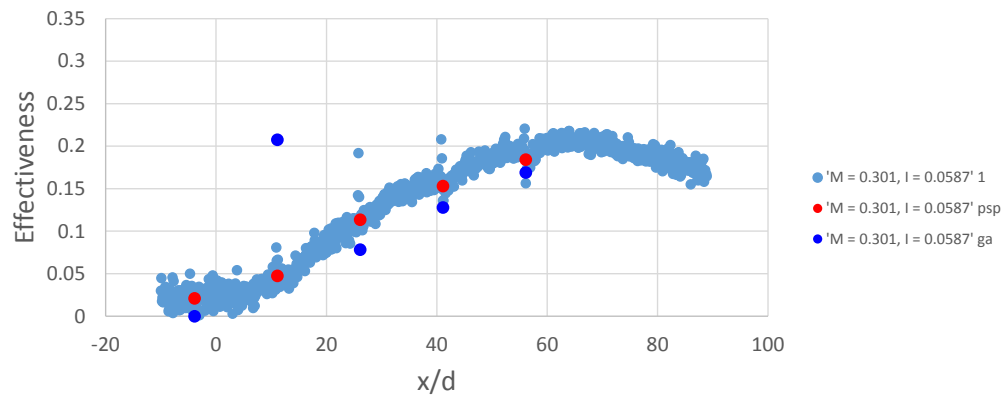


Figure 5.84: $\eta(x/d, P_z/4; M = 0.3)$ comparison to gas sampling results

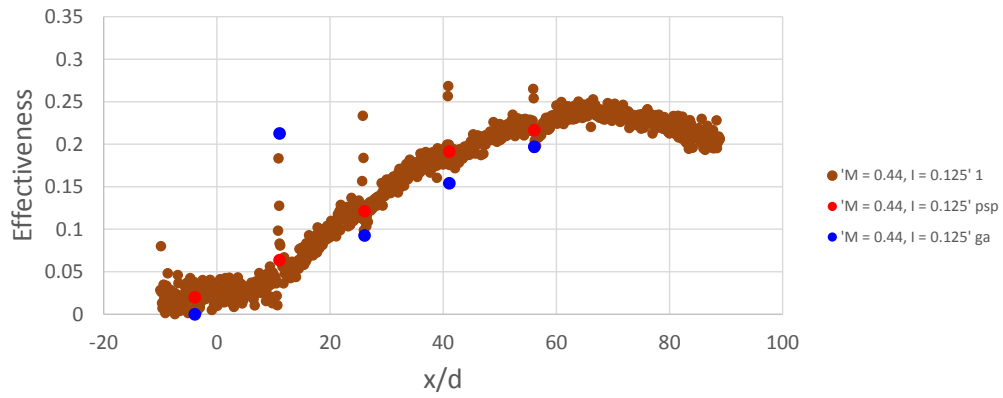


Figure 5.85: $\eta(x/d, P_z/4; M = 0.45)$ comparison to gas sampling results

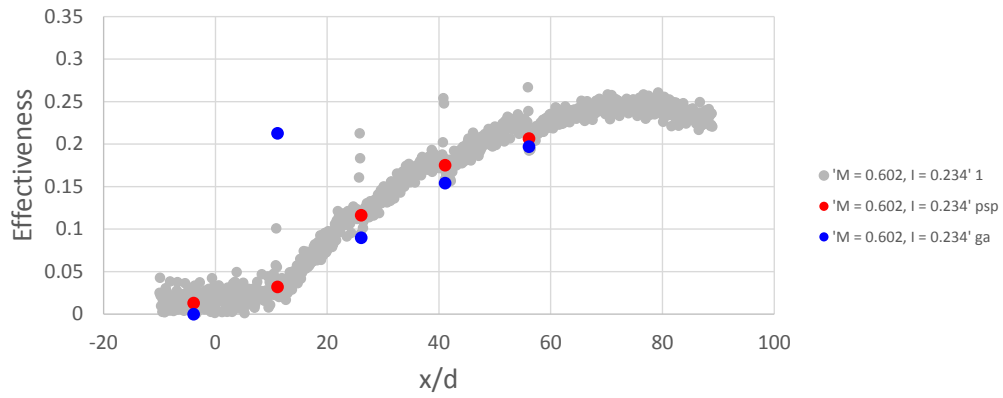


Figure 5.86: $\eta(x/d, P_z/4; M = 0.6)$ comparison to gas sampling results

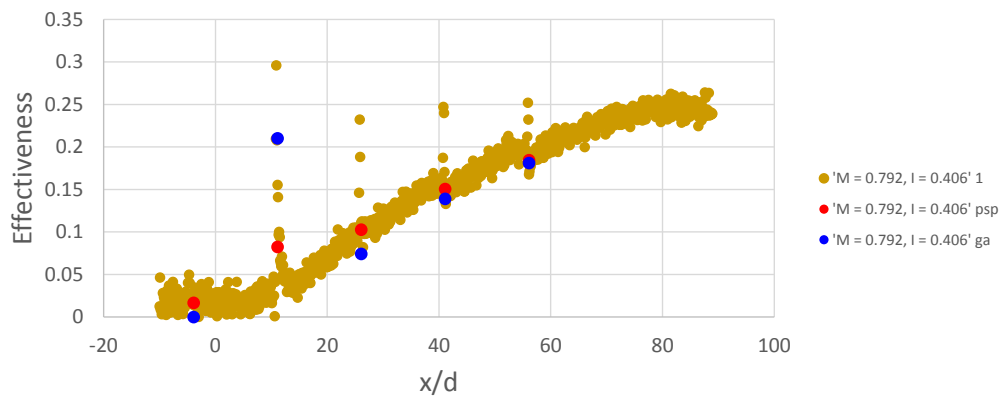


Figure 5.87: $\eta(x/d, P_z/4; M = 0.75)$ comparison to gas sampling results

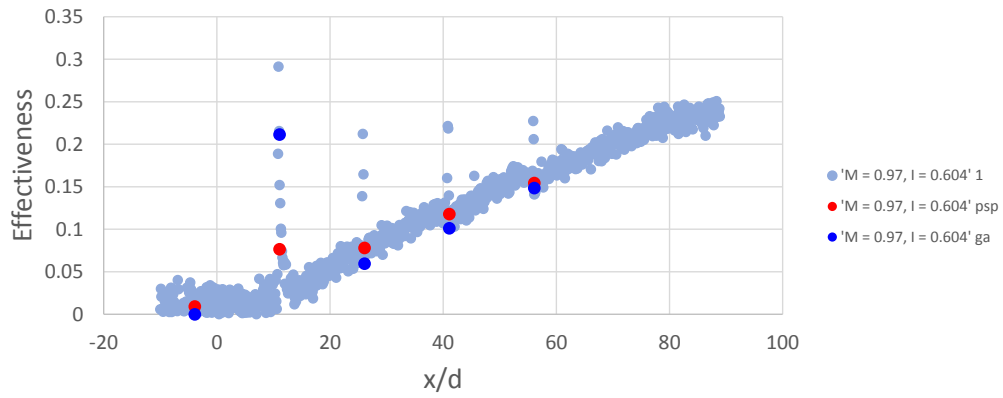


Figure 5.88: $\eta(x/d, P_z/4; M = 0.9)$ comparison to gas sampling results

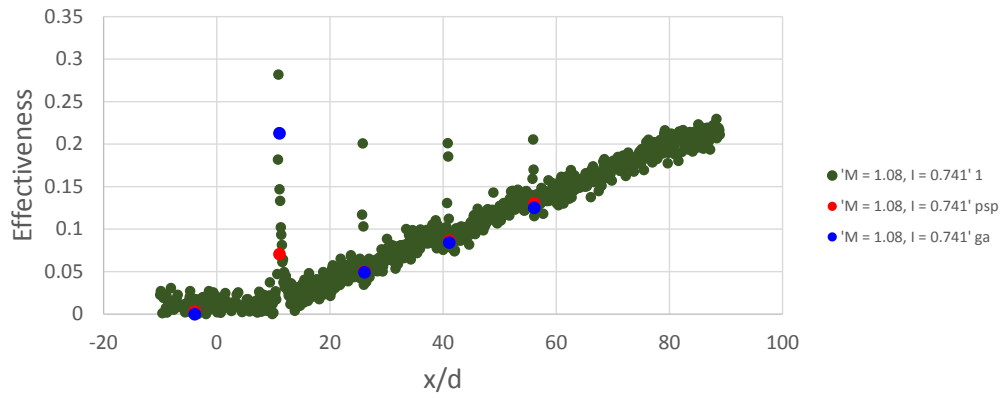


Figure 5.89: $\eta(x/d, P_z/4; M = 1.05)$ comparison to gas sampling results

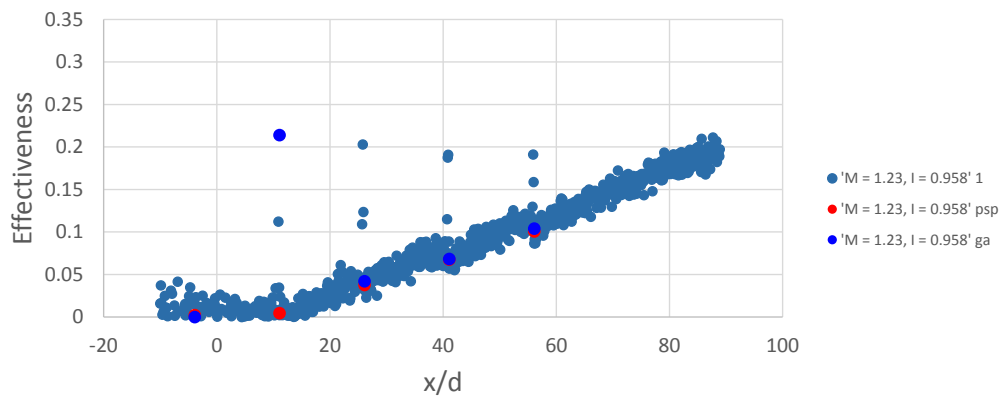


Figure 5.90: $\eta(x/d, P_z/4; M = 1.2)$ comparison to gas sampling results

The gas sampling results were repeated to ensure there is no test-to-test variability in their results. Figure 5.91 shows one of the taps on three different days of testing and how the results vary with blowing ratio. Gas sampling provides very repeatable results.

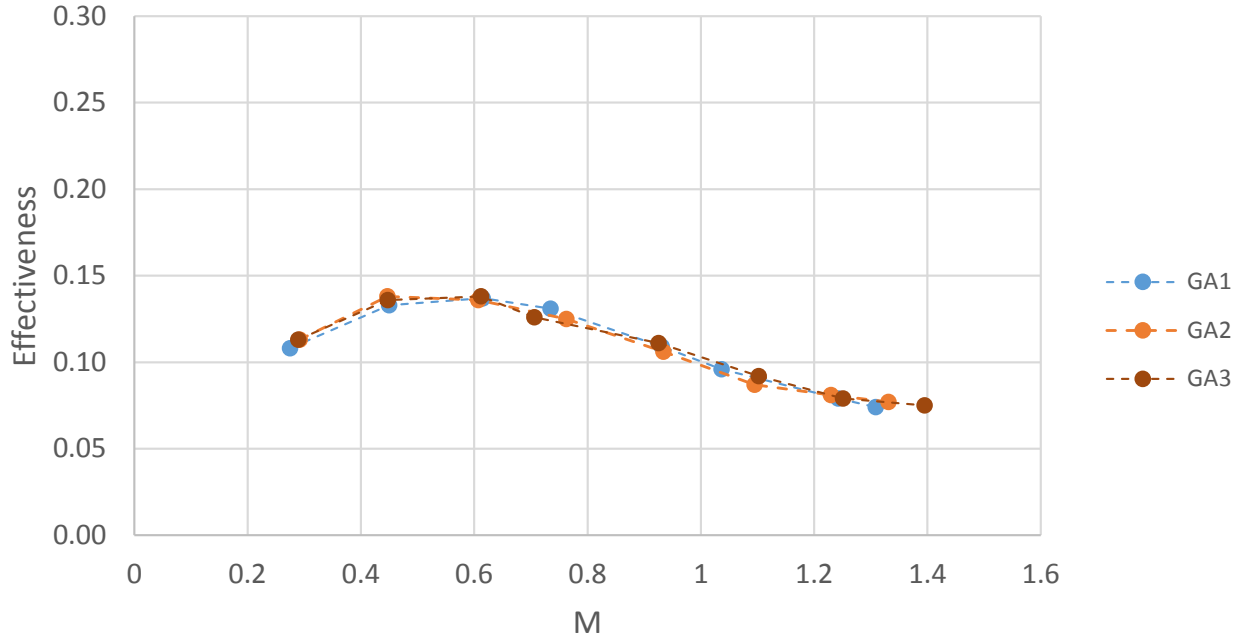


Figure 5.91: Repeatability of gas sampling results

5.9.7 Superposition Predictions of Multi-Row Performance

Seller's superposition method was applied to the single row results from §5.7 in order to predict the laterally averaged effectiveness, $\bar{\eta}$, results from §5.9. The superposition predictions based on a single row results and their comparison with multi-row results are shown in Figure 5.92.

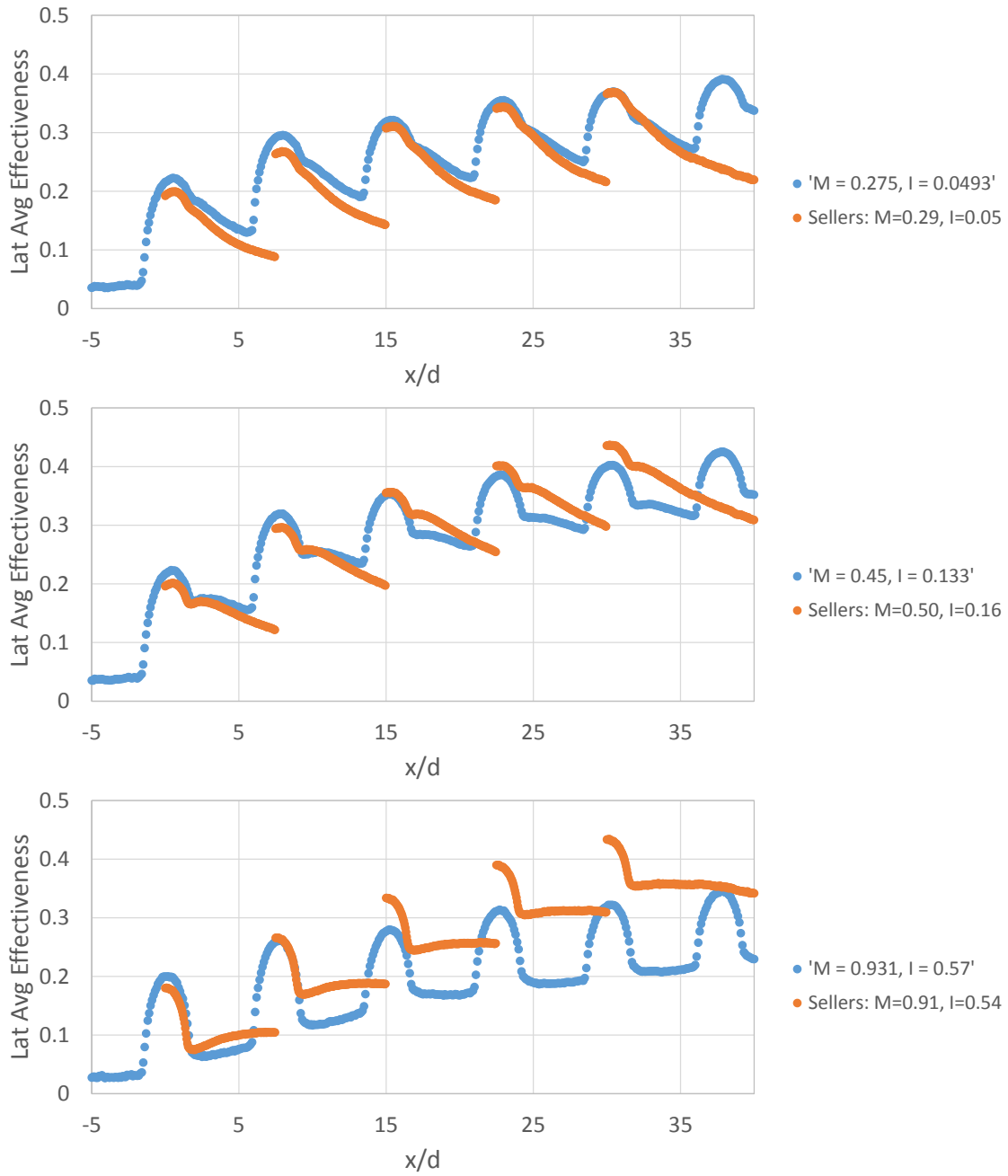


Figure 5.92: Superposition prediction of multi-row cooling based on single row results for $M = 0.3, 0.5$ and 0.9

For the very attached case still in the mass addition regime, $M = 0.3$, the single row superposition estimation of multi-row effectiveness properly accounts for the benefit of additional rows. Even at a blowing ratio of $M = 0.5$ the prediction is reasonable throughout 3 rows; however, by rows 4 and 5 the superposition approach over predicts effectiveness. For the higher blowing ratio predicted, $M = 0.9$, the superposition prediction does not account for the additional rows properly. It far over estimates the benefit of additional rows. This is due to the superposition technique by Sellers assuming the film act as laminates, smoothly flowing over one another. So for a detached case in which there are losses of coolant to the mainflow, the prediction breaks down.

5.10 Summary of Effectiveness Findings

Several experimental aspects of the pressure sensitive paint technique for measuring adiabatic film cooling effectiveness have been quantified. Recommendations for testing methodologies which minimize error have been reported. This paper has focused on CO_2 as the foreign gas; however, whenever applicable, expressions include a term for the molecular weight ratio. So, these methods can be applied to more general film cooling scenarios but these results are quantitatively specific to low speed film cooling with CO_2 .

Detailed PSP calibrations were performed. The uncertainty in these calibrations has been quantified and propagated through to assess the impact on the calculation of adiabatic effectiveness.

Data was collected in order to understand and quantify the effects of temperature and temporal degradation of intensity on the calculation of adiabatic effectiveness. This data has been described, and if care is taken and a meticulous experimental setup is put in place, then both of these effects can be maintained to have an arbitrarily low impact on effectiveness.

A thorough experimental procedure has been described and applied to both calibration and film cooling experiments. Adiabatic film cooling measurements were taken on a flat plate containing single row of cylindrical holes. These measurements provide a highly understood data set of 20° holes, data for which is sparse in the literature. Measurements were taken using the procedure described in this manuscript. A thorough uncertainty analysis has been provided for both the calibration and the effectiveness data, data which results in maps of effectiveness uncertainty. Laterally averaged results vary by less than 0.022 effectiveness throughout the entire domain ($x/d < 30$) for all blowing ratios tested. Day-to-day and hole-to-hole repeatability measurements are presented for centerline effectiveness. These results show less variation than the laterally averaged results due to the behavior of PSP having low uncertainty at high effectiveness values.

Measurements were made of multi-row arrays. Local adiabatic effectiveness results and laterally averaged results were presented for 5 geometries. Local uncertainty estimates were presented for Geometry 1. The issues of testing with SLA hardware were discussed and strategies were developed. A difficult-to-quantify error source, auto-illumination, was investigated and a method to mitigate the impact was discussed. Gas sampling measurements were compared with the PSP results. Finally superposition predictions were made of the multi-row geometries with single row results.

CHAPTER 6 FINDINGS

High fidelity measurements are necessary to validate existing and future models for the purpose of producing the next generation of more efficient gas turbines. The objective of the present study is to conduct several different measurements of multi-row film cooling arrays in order to better understand the physics involved with injection of coolant through multiple rows of discrete holes into a flat plate turbulent boundary layer.

Adiabatic effectiveness distributions are measured for several multi-row film cooling geometries. The geometries are designed with two different hole spacings and two different hole types to yield four total geometries. One of the four geometries tested for adiabatic effectiveness was selected for flowfield measurements. The wall and flowfield are studied with several testing techniques.

1. PSP measurements of adiabatic film cooling effectiveness
2. Gas sampling measurements of adiabatic film cooling effectiveness
3. Hotwire measurements of time resolved streamwise velocity
4. Particle image velocimetry measurements of wall normal and streamwise velocity
5. Particle density images for flow visualization

There are several novel aspects to this study listed below

- PIV measurements throughout multi-row array (Chapter 4)
- Back to back PSP and gas sampling measurements for film cooling (Chapter 5 §??)
- Lengthscale calculations throughout multi-row array (Chapter 3 §3.6.4)
- Multi-row shaped film cooling array (Chapter 5 §5.9.1.4 and §5.9.1.5)
- Testing of SLA geometries with procedures for successful tests (Chapter 5 §5.9.4)
- Quantification of PSP error sources in detail (Chapter 5 §5.6 and §5.8)
- Auto-illumination error quantification method (Chapter 5 §5.9.5)
- 20° inclination angle film cooling holes

Pressure sensitive paint and discrete gas sampling taps are simultaneously used to measure adiabatic film cooling effectiveness by taking advantage of the heat and mass transfer analogy. All cooling regimes documented by Goldstein [1] for a single row are seen in the multi-row geometries studied. As the blowing ratio increases from 0 the laterally averaged effectiveness increases everywhere, until a point is reached at which upstream rows begin to drop in performance while the downstream rows increase in performance. Finally a point is reached at which the cooling performance drops everywhere as the blowing ratio is increased.

Experiments are conducted in an effort to quantifiably bound expected errors associated with temperature non-uniformities in testing and photo-degradation effects. Results show that if careful experimental procedures are put in place, both of these effects can be maintained to have less than 0.022 impact on effectiveness.

Through accurate semi-in-situ calibration down to 4% atmospheric pressure, the near-hole distribution of effectiveness is measured with high accuracy. PSP calibrations are performed for multiple coupons, over multiple days. In addition, to reach a partial pressure of 0 the calibration vessel was purged of all air by flowing CO₂.

Testing of Stereolithography manufactured hardware was evaluated. Hardware preparation methodologies are discussed to alleviate the issues of testing these parts. Gas sampling measurements were taken in conjunction with pressure sensitive paint measurements and shown to provide consistent results. Superposition estimations of multi-row effectiveness are shown to predict low blowing ratio cases well while over-predicting cooling for higher blowing ratios.

Detailed boundary layer measurements are obtained with hot wire anemometry. The boundary layer is measured at two upstream locations to characterize the approaching flow and provide boundary conditions for computational predictions. The hot wire technique is then applied to the array at up to 15 streamwise locations to obtain measurements of mean velocity, RMS of the fluctuations and integral length scale, in the presence of film cooling. It was seen that injection thickens the boundary layer significantly. Due to the low turbulence mainstream and jets, turbulence production takes place primarily at regions of high shear between mainflow and coolant or in wakes for the lifted case.

Finally, particle image velocimetry measurements are taken to provide streamwise and wall normal velocity measurements at two streamwise aligned planes in the flow; an array centerline and $d/2$ plane corresponding to the edge of the jets. These measurements show how an increase in blowing ratio decreases turbulence levels throughout the array. The entire structure of the boundary layer changes from shearing at the top to a wall-bounded jet flow as the blowing ratio increases. Despite lower turbulence levels, the high blowing ratio case is seen to perform worse than the low blowing case from the effectiveness measurements. The particle image velocimetry measurements corroborate the hot wire measurements in that the turbulence production occurs where the mainflow and coolant jets meet and interact.

The next step is to generate models and simulations which can leverage these results with the goal developing a robust prediction tool for the design of multi-row film cooling hardware.

APPENDIX A
DESIGN CALCULATIONS

```

1  clc, clear all, close all;
2  %% DESIGN CALCULATIONS
3
4  % 1" = 0.0254m
5  mil2m = 0.0000254;
6
7  %% T E S T   A R T I C L E (geo)
8  geo_d_mils = 144;
9  geo_d = geo_d_mils*mil2m; % m
10 geo_Nx = 8; % # of rows
11 geo_Nz = 7; % # of holes per row
12 geo_N = geo_Nx*geo_Nz-4 - 16;
13 % 20131002 (p/d x x/d) 7.5 x 7.5 // 14 x 10
14 geo_Pd = 14;
15 geo_Xd = 10;
16 geo_RR_Xd = 40;
17 geo_PA_Xd = geo_Nx * geo_Xd;
18
19 geo_x_extent = (geo_Nx * geo_Xd + geo_RR_Xd) * geo_d;
20
21 geo_x_le_to_le = 7.25 * 0.0254; %m
22 geo_x_plate_to_hole = 2.75 * 0.0254; % m
23
24 %% T E S T   S E C T I O N (test)
25
26 % Blower capable of supplying air at ~4.72 m3/s
27 % Test section is of 1.2-m length, 0.53-m width, and 0.154-m height
28
29 %test section size
30 test_x = 1.2;
31 test_y = 5.5*1000*mil2m;
32 test_z = 21*1000*mil2m;
33
34 %test section size normalized by hole diameter
35 test_xd = test_x/geo_d;
36 test_yd = test_y/geo_d;
37 test_zd = test_z/geo_d;
38
39 %% C O O L A N T   P R O P E R T I E S (fluid)
40
41 fluid_1 = 'air'; % air
42 fluid_2 = 'co2'; % co2 or ??????????
43
44 if strcmp(fluid_1,'air') == 1;
45     prop_R1 = 287; %J/kg/K
46     prop_gamma1 = 1.4;
47     prop_Cp1 = 1007; %J/kg/K
48     prop_mu1 = 184.6e-7; %N*s/m^2
49     prop_Pr1 = 0.707;
50 else

```

```

51     display('Check fluid1');
52 end
53 if strcmp(fluid_2,'co2') == 1;
54     prop_R2 = 188.9; %J/kg/K
55     prop_gamma2 = 1.289;
56     prop_alpha2 = 11e-6; % m^2/s
57     prop_Pr2 = 0.766;
58     prop_mu2 = 149e-7; %dyn visc N*s/m^2
59     prop_Cp2 = 851; %J/kg/K
60 else
61     display('Check fluid2');
62 end
63
64 %% F L O W   C A L C U L A T I O N S (con) ((for conditions))
65
66 % inputs
67 con_P = 101350; %Pa
68 con_T1 = 30 + 273.15; %K
69 con_U1 = 40; %m/s
70 con_M = [0.5, 1.0, 1.5, 2.0, 2.5, 3.0, 3.5, 4.0];
71
72 % primary
73 con_a1 = (prop_gamma1*prop_R1*con_T1)^.5;
74 con_Ma1 = con_U1 / con_a1;
75 con_rho1 = con_P/prop_R1/con_T1;
76 con_G1 = con_rho1*con_U1; %kg/m3*m/s
77 con_Re1 = con_rho1*con_U1*geo_d/prop_mu1;
78
79 % coolant
80 con_T2 = con_T1; %in a perfect world
81 con_G2 = con_G1*con_M;
82 con_rho2 = con_P/prop_R2/con_T2;
83 con_U2 = con_G2/con_rho2;
84 con_Re2 = con_G2*geo_d/prop_mu2;
85 con_mdots_perhole = con_G2*pi()*geo_d^2/4;
86
87 % non-d
88 con_DR = con_rho2/con_rho1;
89 con_I = con_M.^2/con_DR;
90 con_VR = con_M/con_DR;
91
92
93 %% B O U N D A R Y   L A Y E R   C A L C U L A T I O N S
94
95 Re_x = con_U1 * (geo_x_le.to.le + geo_x_plate.to.hole) * con_rho1 / prop_mu1;
96
97 % Kays and Crawford pg. 493 ed.II
98 bl_delta99 = (geo_x_le.to.le + geo_x_plate.to.hole) * 0.37 * Re_x^(-1/5); %m
99 bl_delta1 = (geo_x_le.to.le + geo_x_plate.to.hole) * 0.046 * Re_x^(-1/5); %m
100 bl_delta2 = (geo_x_le.to.le + geo_x_plate.to.hole) * 0.036 * Re_x^(-1/5); %m

```

```

101
102 %non-d calcs
103 bl_Re_d_pri = con_rho1 * con_U1 * geo_d / prop_mu1;
104 bl_Re_d_sec = con_rho2 * con_U2 * geo_d / prop_mu2;
105 bl_Re_delta2 = con_rho1 * con_U1 * bl_delta2 / prop_mu1;
106 bl_99_d = bl_delta99 / geo_d;
107 bl_01_d = bl_delta1 / geo_d;
108 bl_02_d = bl_delta2 / geo_d;
109 bl_H = bl_delta1/bl_delta2;
110
111 %% M A S S   F L O W   R A T E S
112 test_mdot_2 = geo_N * con_G2 * pi() * geo_d^2 / 4;
113 test_time = 1 * 60 * 60; %seconds
114 test_mass_2 = test_mdot_2 * test_time;
115
116 % %gas analyzer - easier in for loop
117 % GA_vavg = 0.5:0.5:10; %avg suction velocity (m/s)
118 % GA_tapd = [1/32 , 1/16] * 1000 * mil2m; % tap diameter (m)
119 % GA_mdot = GA_vavg .* con_rho2 .* pi() .* GA_tapd.^2 / 4;
120
121 %% T A B L E
122 table_bl.1(1,1) = {'U1'};
123 table_bl.1(2,1) = {'delta_99'};
124 table_bl.1(3,1) = {'delta_1'};
125 table_bl.1(4,1) = {'delta_2'};
126 table_bl.1(5,1) = {'H'};
127 table_bl.1(6,1) = {'Re_delta2'};
128 table_bl.1(7,1) = {'Re_d'};
129 table_bl.1(8,1) = {'TI'};
130 table_bl.1(9,1) = {'delta_99/d'};
131 table_bl.1(10,1) = {'delta_1/d'};
132 table_bl.1(11,1) = {'delta_2/d'};
133
134 table_bl.2(1,1) = con_U1;
135 table_bl.2(2,1) = bl_delta99;
136 table_bl.2(3,1) = bl_delta1;
137 table_bl.2(4,1) = bl_delta2;
138 table_bl.2(5,1) = bl_H;
139 table_bl.2(6,1) = bl_Re_delta2;
140 table_bl.2(7,1) = bl_Re_d_pri;
141 table_bl.2(8,1) = 0;
142 table_bl.2(9,1) = bl_99_d;
143 table_bl.2(10,1) = bl_01_d;
144 table_bl.2(11,1) = bl_02_d;

```

APPENDIX B
MEASUREMENTS OF TEST GEOMETRIES

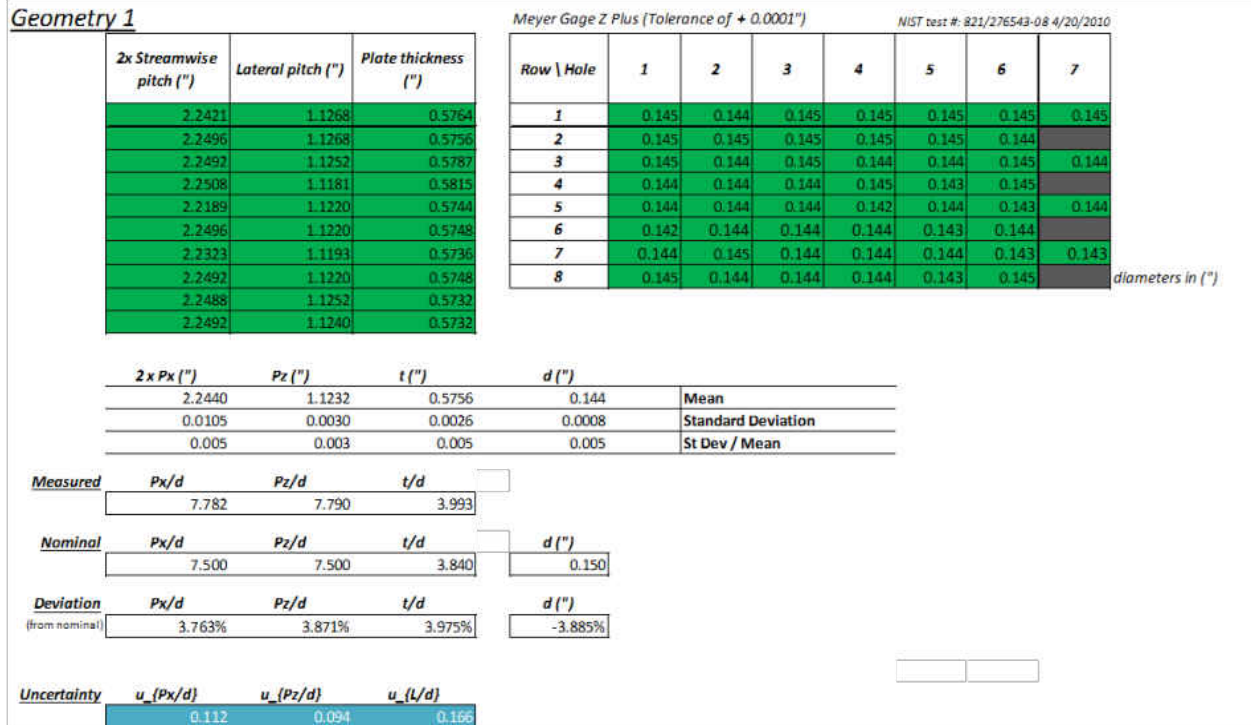


Figure B.1: Measurements of Geometry 1

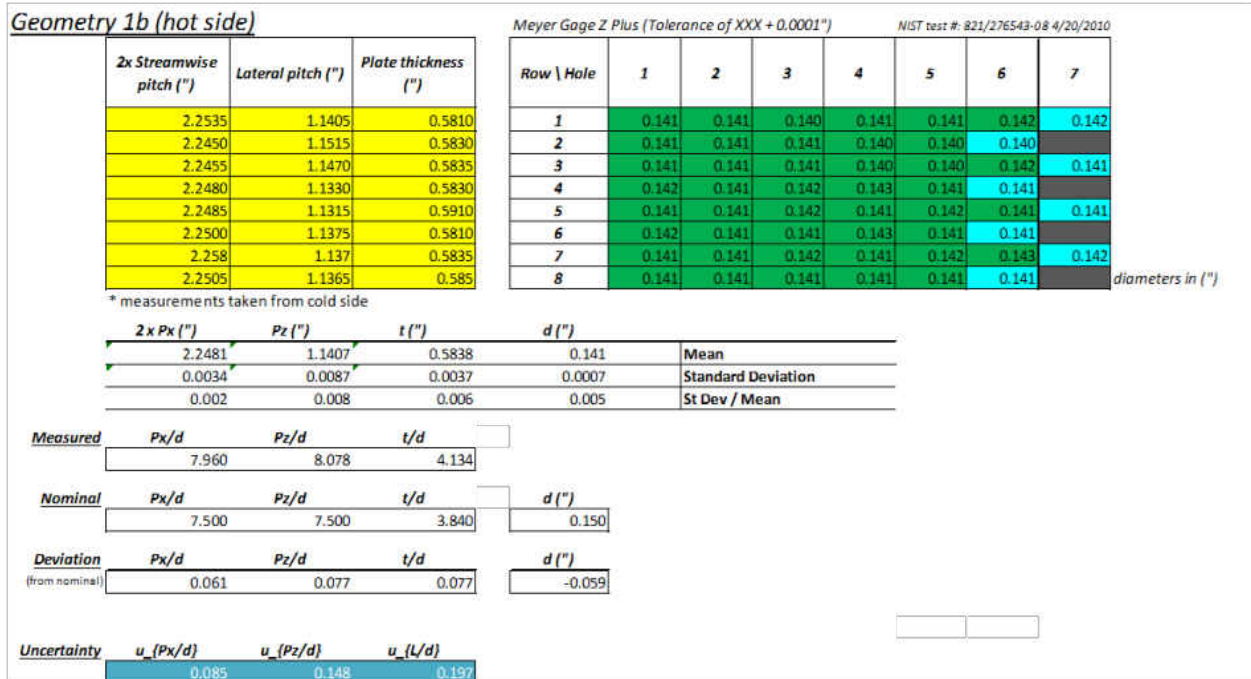


Figure B.2: Measurements of Geometry 1b, hot side

Geometry 1b (cold side)			Meyer Gage Z Plus (Tolerance of XXX + 0.0001")								NIST test #: 821/276543-08 4/20/2010
2x Streamwise pitch (")	Lateral pitch (")	Plate thickness (")	Row \ Hole	1	2	3	4	5	6	7	
2.2535	1.1405	0.5810	1	0.148	0.148	0.148	0.149	0.148	0.147	0.149	
2.2450	1.1515	0.5830	2	0.148	0.148	0.148	0.148	0.149	0.148	0.148	
2.2455	1.1470	0.5835	3	0.148	0.148	0.148	0.148	0.148	0.147	0.148	
2.2480	1.1330	0.5830	4	0.148	0.148	0.148	0.148	0.148	0.148	0.148	
2.2485	1.1315	0.5910	5	0.148	0.148	0.148	0.148	0.148	0.147	0.148	
2.2500	1.1375	0.5810	6	0.148	0.148	0.148	0.148	0.148	0.148	0.148	
2.258	1.137	0.5835	7	0.148	0.148	0.148	0.148	0.148	0.147	0.148	
2.2505	1.1365	0.585	8	0.148	0.148	0.148	0.148	0.148	0.148	0.148	diameters in (")

2x Px (")	Pz (")	t (")	d (")	
2.2481	1.1407	0.5838	0.148	Mean
0.0034	0.0087	0.0037	0.0004	Standard Deviation
0.002	0.008	0.006	0.003	St Dev / Mean

Measured	Px/d	Pz/d	t/d	
	7.596	7.708	3.945	

Nominal	Px/d	Pz/d	t/d	d (")
	7.500	7.500	3.840	0.150

Deviation (from nominal)	Px/d	Pz/d	t/d	d (")
	0.013	0.028	0.027	-0.013

Uncertainty	u_(Px/d)	u_(Pz/d)	u_(L/d)
	0.044	0.123	0.158

Figure B.3: Measurements of Geometry 1b, cold side

Meyer Gage Z Plus (Tolerance of XXX + 0.0001")								NIST test #: 821/276543-08 4/20/2010
Row \ Hole	1	2	3	4	5	6	7	
1	0.007	0.007	0.008	0.008	0.007	0.005	0.007	
2	0.007	0.007	0.007	0.008	0.009	0.008	0.008	
3	0.007	0.007	0.007	0.008	0.008	0.005	0.007	
4	0.006	0.007	0.006	0.005	0.007	0.007	0.007	
5	0.007	0.007	0.006	0.007	0.006	0.006	0.007	
6	0.006	0.007	0.007	0.005	0.007	0.007	0.007	
7	0.007	0.007	0.006	0.007	0.006	0.004	0.006	
8	0.007	0.007	0.007	0.007	0.007	0.007	0.007	diameters in (")

Figure B.4: Difference between measured hole diameters for Geometry 1b, hot vs cold side

Geometry 2			Meyer Gage Z Plus (Tolerance of XXX + 0.0001")							NIST test #: 821/276543-08 4/20/2010		
	2x Streamwise pitch (")	Lateral pitch (")	Plate thickness (")	Row \ Hole	1	2	3	4	5	6	7	
	3.0320	2.0940	0.5740	1	0.149	0.148	0.147	0.146	0.146	0.146	0.147	
	3.0005	2.0935	0.5720	2	0.146	0.146	0.146	0.147	0.146	0.146		
	3.0000	2.0960	0.5770	3	0.147	0.146	0.147	0.146	0.147	0.147	0.147	
	2.9940	2.0950	0.5700	4	0.146	0.146	0.146	0.146	0.147	0.146		
	2.9475	2.0950	0.5750	5	0.146	0.146	0.146	0.146	0.146	0.146	0.146	
			0.5670	6	0.146	0.146	0.146	0.146	0.145	0.146		
				7	0.145	0.145	0.145	0.145	0.145	0.145	0.145	
				8	0.145	0.146	0.145	0.145	0.146	0.146		diameters in (")
	2 x Px (")	Pz (")	t (")	d (")								
	2.9948	2.0947	0.5725	0.146	Mean							
	0.0303	0.0010	0.0036	0.0008	Standard Deviation							
	0.010	0.000	0.006	0.005	St Dev / Mean							
Measured	Px/d	Pz/d	t/d									
	10.251	14.340	3.919									
Nominal	Px/d	Pz/d	t/d	d (")								
	10.000	14.000	3.840	0.150								
Deviation (from nominal)	Px/d	Pz/d	t/d	d (")								
	0.025	0.024	0.021	-0.026								
Uncertainty	u_c(Px/d)	u_c(Pz/d)	u_c(L/d)									
	0.235	0.155	0.190									

Figure B.5: Measurements of Geometry 2

Geometry 5

Meyer Gage Z Plus (Tolerance of +0.0001")

NIST test #: 821/276543-08 4/20/2010

2x Streamwise pitch (")	Lateral pitch (")	Plate thickness (")
2.2400	1.1485	0.5845
2.2725	1.1300	0.5850
2.2345	1.1785	0.5855
2.2485	1.1625	0.5830
2.2820	1.1350	0.5840
2.2435	1.1545	0.5790
2.2265	1.1270	0.5835
2.2860	1.1470	0.5880
2.2430	1.1400	0.5855
2.6150	1.1370	0.5820

Row \ Hole	1	2	3	4	5	6	7
1	0.142	0.146	0.145	0.145	0.145	0.146	0.146
2	0.141	0.145	0.145	0.145	0.145	0.145	0.145
3	0.141	0.145	0.145	0.145	0.145	0.145	0.145
4	0.142	0.146	0.145	0.145	0.145	0.145	0.145
5	0.142	0.145	0.145	0.145	0.145	0.145	0.145
6	0.141	0.145	0.145	0.144	0.145	0.145	0.145
7	0.141	0.145	0.145	0.145	0.145	0.144	0.145
8	0.142	0.145	0.144	0.144	0.144	0.145	0.145

diameters in (")

2 x Px (")	Pz (")	t (")	d (")	
2.2555	1.1509	0.5835	0.144	Mean
0.0207	0.0199	0.0024	0.0013	Standard Deviation
0.009	0.017	0.004	0.009	St Dev / Mean

Measured	Px/d	Pz/d	t/d
	7.808	7.968	4.040

Nominal	Px/d	Pz/d	t/d	d (")
	10.000	14.000	3.840	0.150

Deviation (from nominal)	Px/d	Pz/d	t/d	d (%/100)
	-0.219	-0.431	0.052	-0.037

Uncertainty	u_{Px/d}	u_{Pz/d}	u_{L/d}
	0.205	0.314	0.241

Figure B.6: Measurements of Geometry 5

Geometry 6			Meyer Gage Z Plus (Tolerance of XXX + 0.0001")							NIST test #: 821/276543-08 4/20/2010
2x Streamwise pitch (")	Lateral pitch (")	Plate thickness (")	Row \ Hole	1	2	3	4	5	6	7
3.0035	2.1250	0.5900	1	0.145	0.145	0.146	0.146	0.146	0.146	0.146
2.9895	2.1090	0.5873	2	0.145	0.145	0.146	0.146	0.146	0.147	0.146
2.9925	2.1130	0.5855	3	0.145	0.144	0.145	0.145	0.145	0.145	0.145
3.0085	2.1110	0.5925	4	0.145	0.144	0.145	0.144	0.144	0.145	0.145
3.0160	2.1175	0.5845	5	0.145	0.145	0.144	0.144	0.143	0.145	0.144
3.0095	2.1140	0.5885	6	0.145	0.144	0.144	0.145	0.145	0.145	0.145
3.0065	2.118	0.586	7	0.145	0.145	0.143	0.143	0.143	0.144	0.144
3.0025	2.127	0.582	8	0.145	0.145	0.144	0.144	0.143	0.142	0.144

2 x Px (")	Pz (")	t (")	d (")	
3.0020	2.1151	0.5881	0.145	Mean
0.0110	0.0064	0.0029	0.0010	Standard Deviation
0.004	0.003	0.005	0.007	St Dev / Mean

Measured	Px/d	Pz/d	t/d	
	10.375	14.620	4.065	

Nominal	Px/d	Pz/d	t/d	d (")
	10.000	14.000	3.840	0.150

Deviation (from nominal)	Px/d	Pz/d	t/d	d (")
	0.038	0.044	0.059	-0.036

Uncertainty	u_{Px/d}	u_{Pz/d}	u_{L/d}
	0.163	0.221	0.203

Figure B.7: Measurements of Geometry 6

APPENDIX C
HOTWIRE MEAN PROCESSING ALGORITHM

```

1 close all; clear all; clc
2 %
3 y0 = 0.05; %inches
4
5 %%%%%%%%%%%%%%%%%%%%%%%%%%%%%%%%%%%%%%%%%%%%%%%%%%%%%%%%%%%%%%%%%%%%%%%%%
6
7 % load traverse data
8 traverse_filename = '\152pointtraverse.xlsx';
9 traverse_sheet = 'traverse';
10 traverse_range = 'A1:C152';
11 filename = '20141015_Diff_M090_L15_025kHz_10s';
12
13 % load traverse data
14 [numeric , text , raw] = xlsread(traverse_filename , traverse_sheet , ...
    traverse_range);
15 clear text raw
16
17 % define y vector
18 y_inches_uncorr = numeric(:,3);
19
20 n = length(y_inches_uncorr);
21
22 % load inst voltages
23
24 N = 0.25e6;
25
26 v_inst = zeros(n,N);
27
28 tic
29 for i = 1:n
30     g = sprintf('%s', 'v_dumb = textread('', num2str(i-1), '.txt');');
31     eval(g);
32     v_inst(i,:) = v_dumb';
33 end
34 toc
35
36 %% calibration v -> u
37
38 % Hot film from 10-14-2014
39 c0 = 28.1886786973504000;
40 c1 = 4.0562488732089200;
41 c2 = 0.1482233115652990;
42 c3 = -0.0005595366979101;
43
44 u_inst = c3*v_inst.^3 + c2*v_inst.^2 + c1*v_inst + c0;
45 clear v_inst c0 c1 c2 c3
46 clear g i numeric traverse_filename traverse_range traverse_sheet v_dumb
47
48 %% save
49 save(filename)

```

```

50
51 %%%%%%%%%%%%%%%%%%%%%%%%%%%%%%%%%%%%%%%%%%%%%%%%%%%%%%%%%%%%%%%%%%%%%%%%%
52 %%%%%%%%%%%%%%%%%%%%%%%%%%%%%%%%%%%%%%%%%%%%%%%%%%%%%%%%%%%%%%%%%%%%%%%%%
53 %%%%%%%%%%%%%%%%%%%%%%%%%%%%%%%%%%%%%%%%%%%%%%%%%%%%%%%%%%%%%%%%%%%%%%%%%
54
55 clc, close all
56
57 %% load data
58 % tic
59 % g = sprintf('%s', 'load ', filename);
60 % eval(g)
61 % toc
62
63 N      = size(u_inst,2);
64
65 %% mean
66
67 u_mean = mean(u_inst,2);
68
69
70 y = y0 + y_inches_uncorr;
71
72 %% fluc
73
74 for i = 1:length(u_mean)
75     u_fluc(i,:) = u_inst(i,:) - u_mean(i);
76 end
77
78 for i = 1:length(u_mean)
79     u_rms(i,1) = ( sum(u_fluc(i,:).*u_fluc(i,:)) / size(u_inst,2) ).^(1/2);
80 end
81
82 %% plot
83
84 % semilog
85 figure
86 subplot(1,3,1)
87 semilogx(y,u_mean,'k.-')
88 ylabel('U (m/s)')
89 xlabel('y_{uncorrected} (inches)')
90 axis([0.001 10 0 50])
91
92 subplot(1,3,2)
93 semilogx(y,u_rms,'k.-')
94 ylabel('u'_{rms} (m/s)')
95 xlabel('y_{uncorrected} (inches)')
96 axis([0.001 10 0 2.5])
97
98 subplot(1,3,3)
99 semilogx(y,u_rms./u_mean,'k.-')

```

```

100 ylabel('TI')
101 xlabel('y_{uncorrected} (inches)')
102 axis([0.001 10 0 0.06])
103
104 % physical
105 figure
106 subplot(1,3,1)
107 plot(u_mean,y,'k.-')
108 xlabel('U (m/s)')
109 ylabel('y_{uncorrected} (inches)')
110 axis([0 50 0 1])
111
112 subplot(1,3,2)
113 plot(u_rms,y,'k.-')
114 xlabel('u'-'_{rms} (m/s)')
115 ylabel('y_{uncorrected} (inches)')
116 axis([0 2.5 0 1])
117
118 subplot(1,3,3)
119 plot(u_rms./u_mean,y,'k.-')
120 xlabel('TI')
121 ylabel('y_{uncorrected} (inches)')
122 axis([0 0.06 0 3])
123
124
125 %% table
126
127 table(:,1) = y;
128 table(:,2) = u_mean;
129 table(:,3) = u_rms;
130 table(:,4) = u_rms./u_mean;
131
132
133
134 %% histogram time
135
136
137 hist_X = [0:0.1:50];
138
139
140 hist_u = zeros(n,length(hist_X));
141
142 tic
143 for i = 1:n
144     hist_u(i,:) = hist(u_inst(i,:),hist_X)/N;
145 end
146 toc
147
148
149 [hist_X_mesh hist_y_mesh] = meshgrid(hist_X,y);

```

```

150
151
152 figure
153 contourf(hist_X_mesh, hist_y_mesh, hist_u)
154 xlabel('u (m/s)')
155 ylabel('y (inches)')
156 title('Probability density of instantaneous streamwise velocity')
157 colorbar
158 axis([20 50 0 3])
159
160 x = [0 0.01:0.01:0.09];
161 clim = [min(x) max(x)];
162 dx = min(diff(x));
163 yplot = clim(1):dx:clim(2);
164 Nx = length(x);
165 cmap = colormap(jet(Nx));
166 cmap2 = [...
167 interp1(x(:), cmap(:,1), yplot(:)) ...
168 interp1(x(:), cmap(:,2), yplot(:)) ...
169 interp1(x(:), cmap(:,3), yplot(:)) ...
170 ];
171 cmap3 = cmap2;
172 cmap3(1,:) = [1, 1, 1];
173 colormap(cmap3)
174 caxis(clim)
175 colorbar

```

APPENDIX D
HOTWIRE CLAUSER FIT PROCESSING ALGORITHM


```

1 clc, clear all, close all;
2
3 dataset = 1;
4
5 % load traverse data
6 if dataset == 1
7     [numeric , text , raw] = xlsread('\GEfilm BL study - 20141021.xlsx' , ...
8         'Cyl M=0.9 analysis' , 'B4:T156');
9     test_descrip = 'Cylindrical, M=0.9';
10    filename      = 'CYLM090_weird';
11 elseif dataset == 2
12 %     [numeric , text , raw] = xlsread('\GEfilm BL study - 20141021.xlsx' ...
13 %     , 'Diff M=0.9 analysis' , 'A1:R153');
14 %     test_descrip = 'Diffuser, M=0.9';
15 %     filename      = 'DIF_M090';
16
17 [numeric , text , raw] = xlsread('\GEfilm BL study - 20141021.xlsx' , ...
18     'Cyl M=0.3 analysis' , 'A1:R153');
19 test_descrip = 'Cylindrical, M=0.3';
20 filename      = 'CYLM030';
21
22 end
23
24 y_in(:,1) = numeric(:,1);
25
26 if dataset == 1
27     y_in(:,2) = numeric(:,2);
28 elseif dataset == 2
29     y_in(:,2) = numeric(:,1);
30 end
31
32 L = [-1:1:15];
33 if dataset == 1
34     u = numeric(:,3:size(numeric,2));
35 elseif dataset == 2
36     u = numeric(:,2:size(numeric,2));
37 end
38
39 u_inf      = mean(u(size(u,1)-20:size(u,1),:),1);
40
41 u_inf(u_inf==999) = NaN;
42
43 if dataset == 1
44     u_inf(9) = mean(u(108:118,9),1);
45 end
46
47

```

```

48 plot(L,u_inf,'k.-',[-2,16],[40,40],'ro-.')
49 xlabel('Location')
50 ylabel('U (m/s)')
51
52 for i = 1:length(u_inf)
53     u_norm(:,i) = u(:,i) / u_inf(i);
54 end
55
56 %% Laws
57
58 % VSL
59 vsl_y = logspace(-2, 1.2, 500);
60 vsl_u = vsl_y;
61
62
63 % LOG
64 kappa = 0.41;
65 Clog = 5.2;
66
67 log_y = logspace(0, 5, 500);
68 log_u = 1/kappa*log(log_y)+Clog;
69
70
71 % van DRIEST
72
73 % van_y=logspace(-2,4,1e4);           %y+ vector
74 %
75 % tic
76 % j=0;
77 % for i = van_y;
78 %     j=j+1;
79 %     van_u(j) = quadl(@int_vandriest,0,i,10^-1);
80 % end
81 % toc
82
83
84 %%
85
86 kin_nu = 15.89e-6;
87
88 %% LS
89 yomin = -0.05;
90 yomax = 0.25;
91 utmin = 1;
92 utmax = 2.5;
93 yo = [yomin:0.001:yomax];
94 u_tau_array = [utmin:0.001:utmax];
95
96 % INDEX = 17;
97 for INDEX = 1:17

```

```

98 for iii = 1:length(yo)
99     for jjj = 1:length(u_tau_array)
100
101 % convert y_mils to meters and add yo
102
103     if INDEX == 9;
104         if dataset == 1
105             y = (y_in(:,2) + yo(iii))*0.0254; % wall normal position ...
106                 corrected for offset in m
107         else
108             y = (y_in(:,1) + yo(iii))*0.0254; % wall normal position ...
109                 corrected for offset in m
110         end
111     else
112         y = (y_in(:,1) + yo(iii))*0.0254; % wall normal position ...
113             corrected for offset in m
114     end
115
116     u_tau_LS = u_tau_array(jjj);
117
118 % setup u+ and y+ for exp data
119 if INDEX == 3;
120     log_start = 59 ;
121     log_stop = log_start + 4 ; % THIS CAN BE CHANGED EASILY TO SEE ...
122         IMPACT IN V2 OF CODE
123 elseif INDEX == 7
124     log_start = 69 ;
125     log_stop = log_start + 4 ; % THIS CAN BE CHANGED EASILY TO SEE ...
126         IMPACT IN V2 OF CODE
127 elseif INDEX == 11
128     log_start = 70 ;
129     log_stop = log_start + 4 ; % THIS CAN BE CHANGED EASILY TO SEE ...
130         IMPACT IN V2 OF CODE
131 elseif INDEX == 15
132     log_start = 68 ;
133     log_stop = log_start + 4 ; % THIS CAN BE CHANGED EASILY TO SEE ...
134         IMPACT IN V2 OF CODE
135 elseif INDEX == 4
136     log_start = 54 ;
137     log_stop = log_start + 4 ; % THIS CAN BE CHANGED EASILY TO SEE ...
138         IMPACT IN V2 OF CODE
139 elseif INDEX == 8
140     log_start = 61 ;
141     log_stop = log_start + 4 ; % THIS CAN BE CHANGED EASILY TO SEE ...
142         IMPACT IN V2 OF CODE
143 elseif INDEX == 12

```

```

139     log_start = 48     ;
140     log_stop  = log_start + 4     ; % THIS CAN BE CHANGED EASILY TO SEE ...
        IMPACT IN V2 OF CODE
141 elseif INDEX == 16
142     log_start = 55     ;
143     log_stop  = log_start + 4     ; % THIS CAN BE CHANGED EASILY TO SEE ...
        IMPACT IN V2 OF CODE
144
145
146 else
147     log_start = 1     ;
148     log_stop  = 40     ; % THIS CAN BE CHANGED EASILY TO SEE IMPACT IN V2 ...
        OF CODE
149 end
150
151     y_log_region = y(log_start:log_stop);
152     u_log_region = u(log_start:log_stop,INDEX);
153
154     y_plus = y_log_region * u_tau_LS / kin_nu ;
155     u_plus = u_log_region / u_tau_LS         ;
156
157
158 % Sum of squares
159     SSE(jjj,iii) = sum( (u_plus - lotw(y_plus)).^2 );
160
161     end
162 end
163
164 [u_tau_index, y0_index] = ind2sub(size(SSE), find(SSE==(min(min(SSE)))));
165
166
167 u_tau(INDEX) = u_tau_array(u_tau_index);
168 y0(INDEX)    = yo(y0_index);
169
170 end
171
172 % INDEX          = INDEX
173 % optimum_u_tau = u_tau(u_tau_index)
174 % optimum_y0    = yo(y0_index)
175 %
176 %
177 % figure
178 % contourf(yo,u_tau,SSE,[0:.05:.5]);
179 % xlabel('y_0 (")')
180 % ylabel('u_\tau (m/s)')
181 % title('SSE Minimization')
182 % colorbar
183
184
185 %% Inner scaling

```

```

186
187 for i = 1:1
188 % utn1 = 1.9970; % 1 LS
189 % ut0 = 1.6840; % 2 LS
190 % ut1 = 1.5930; % 3 LS
191 % ut2 = 1.3010; % 4 LS
192 % ut3 = 1.4220; % 5 LS
193 % ut4 = 1.4010; % 6 LS
194 % ut5 = 1.8110; % 7 LS
195 % ut6 = 1.5300; % 8 LS
196 % ut7 = 1.4360; % 9 LS
197 % ut8 = 1.7270; % 10 LS
198 % ut9 = 2.0410; % 11 LS
199 % ut10 = 1.6760; % 12 LS
200 % ut11 = 1.6870; % 13 LS
201 % ut12 = 1.7040; % 14 LS
202 % ut13 = 1.9010; % 15 LS
203 % ut14 = 1.5280; % 16 LS
204 % ut15 = 1.7100; % 17 LS
205 %
206 % y0n1 = -0.0274; % 1 LS
207 % y00 = 0.0108; % 2 LS
208 % y01 = 0.1000; % 3 LS
209 % y02 = 0.1000; % 4 LS
210 % y03 = -0.0209; % 5 LS
211 % y04 = -0.0288; % 6 LS
212 % y05 = -0.0351; % 7 LS
213 % y06 = -0.0253; % 8 LS
214 % y07 = -0.0018; % 9 LS
215 % y08 = -0.0318; % 10 LS
216 % y09 = 0.0378; % 11 LS
217 % y010 = 0.0553; % 12 LS
218 % y011 = 0.0296; % 13 LS
219 % y012 = 0.0241; % 14 LS
220 % y013 = 0.0996; % 15 LS
221 % y014 = 0.1000; % 16 LS
222 % y015 = 0.0067; % 17 LS
223 %
224 % u_tau = [utn1, ut0, ...
225 % ut1, ut2, ut3, ut4, ut5, ...
226 % ut6, ut7, ut8, ut9, ut10, ...
227 % ut11, ut12, ut13, ut14, ut15];
228 %
229 % y0 = [y0n1, y00, ...
230 % y01, y02, y03, y04, y05, ...
231 % y06, y07, y08, y09, y010, ...
232 % y011, y012, y013, y014, y015];
233 end
234
235

```

```

236 for i = 1:length(u_inf)
237     u_p(:,i) = u(:,i) / u_tau(i);
238
239     if i==9
240         y_p(:,i)      = ((y_in(:,2)+y0(i)) * 0.0254) / (kin_nu/u_tau(i));
241         y_mm_corr(:,i) = (y_in(:,2)+y0(i)) * 0.0254 * 1000;
242     else
243         y_p(:,i)      = ((y_in(:,1)+y0(i)) * 0.0254) / (kin_nu/u_tau(i));
244         y_mm_corr(:,i) = (y_in(:,1)+y0(i)) * 0.0254 * 1000;
245     end
246 end
247
248 u_p(u_p == 0) = NaN;
249
250 close all
251
252 figure
253 semilogx(vsl_y,vsl_u,'k:',log_y,log_u,'k:') %,van_y,van_u,'k-.')
254 hold on
255 xlabel('y^+')
256 ylabel('u^+')
257 axis([0.1 10000 0 35])
258 g = sprintf('%s', 'title('', test_descrip, ': L-1 and L0''));
259 eval(g)
260
261 semilogx(y_p(:,1),u_p(:,1),'k.-')
262 semilogx(y_p(:,2),u_p(:,2),'k.-')
263
264
265 %%%
266 figure
267 subplot(2,2,1)
268 semilogx(vsl_y,vsl_u,'k:',log_y,log_u,'k:') %,van_y,van_u,'k-.')
269 hold on
270 xlabel('y^+')
271 ylabel('u^+')
272 axis([0.1 10000 0 35])
273 %%%
274
275 semilogx(y_p(:,3),u_p(:,3),'r.-')
276 semilogx(y_p(:,4),u_p(:,4),'g.-')
277 semilogx(y_p(:,5),u_p(:,5),'b.-')
278 semilogx(y_p(:,6),u_p(:,6),'m.-')
279 g = sprintf('%s', 'title('', test_descrip, ': L1,2,3,4''));
280 eval(g)
281
282 %%%
283 subplot(2,2,2)
284 semilogx(vsl_y,vsl_u,'k:',log_y,log_u,'k:') %,van_y,van_u,'k-.')
285 hold on

```

```

286 xlabel('y^+')
287 ylabel('u^+')
288 axis([0.1 10000 0 35])
289 %%%
290
291 semilogx(y_p(:,7) , u_p(:,7) , 'r.-')
292 semilogx(y_p(:,8) , u_p(:,8) , 'g.-')
293 semilogx(y_p(:,9) , u_p(:,9) , 'b.-')
294 semilogx(y_p(:,10), u_p(:,10), 'm.-')
295 g = sprintf('%s', 'title('', test_descrip, ': L5,6,7,8''));
296 eval(g)
297
298 %%%
299 subplot(2,2,3)
300 semilogx(vsl_y, vsl_u, 'k:', log_y, log_u, 'k:') %, van_y, van_u, 'k-.')
301 hold on
302 xlabel('y^+')
303 ylabel('u^+')
304 axis([0.1 10000 0 35])
305 %%%
306
307 semilogx(y_p(:,11), u_p(:,11), 'r.-')
308 semilogx(y_p(:,12), u_p(:,12), 'g.-')
309 semilogx(y_p(:,13), u_p(:,13), 'b.-')
310 semilogx(y_p(:,14), u_p(:,14), 'm.-')
311 g = sprintf('%s', 'title('', test_descrip, ': L9,10,11,12''));
312 eval(g)
313 %%%
314 subplot(2,2,4)
315 semilogx(vsl_y, vsl_u, 'k:', log_y, log_u, 'k:') %, van_y, van_u, 'k-.')
316 hold on
317 xlabel('y^+')
318 ylabel('u^+')
319 axis([0.1 10000 0 35])
320 %%%
321
322 semilogx(y_p(:,15), u_p(:,15), 'r.-')
323 semilogx(y_p(:,16), u_p(:,16), 'g.-')
324 semilogx(y_p(:,17), u_p(:,17), 'b.-')
325 g = sprintf('%s', 'title('', test_descrip, ': L13,14,15''));
326 eval(g)
327
328
329
330
331 %% periodic together
332
333 skip1 = 3;
334 skip2 = skip1 + 1;
335 skip3 = skip1 + 2;

```

```

336 skip4 = skip1 + 3;
337
338
339 figure
340
341 %%%%%%%%%%%%%%%%%%%%%%%%%%%%%%%%%%%%%%%%%%
342 subplot(2,2,1)
343 semilogx(vsl-y,vsl-u,'k:',log-y,log-u,'k:') %,van-y,van-u,'k-.')
344 hold on
345 xlabel('y^+')
346 ylabel('u^+')
347 axis([0.1 10000 0 35])
348
349 semilogx(y_p(:, skip1) , u_p(:, skip1) , 'r.-')
350 semilogx(y_p(:, skip1+4) , u_p(:, skip1+4) , 'g.-')
351 semilogx(y_p(:, skip1+8) , u_p(:, skip1+8) , 'b.-')
352 semilogx(y_p(:, skip1+12), u_p(:, skip1+12), 'm.-')
353
354 g = sprintf('%s', 'title('', test_descrip, ': L1,5,9,13')');
355 eval(g)
356
357 %%%%%%%%%%%%%%%%%%%%%%%%%%%%%%%%%%%%%%%%%%
358 subplot(2,2,2)
359 semilogx(vsl-y,vsl-u,'k:',log-y,log-u,'k:') %,van-y,van-u,'k-.')
360 hold on
361 xlabel('y^+')
362 ylabel('u^+')
363 axis([0.1 10000 0 35])
364
365 semilogx(y_p(:, skip2) , u_p(:, skip2) , 'r.-')
366 semilogx(y_p(:, skip2+4) , u_p(:, skip2+4) , 'g.-')
367 semilogx(y_p(:, skip2+8) , u_p(:, skip2+8) , 'b.-')
368 semilogx(y_p(:, skip2+12), u_p(:, skip2+12), 'm.-')
369
370 g = sprintf('%s', 'title('', test_descrip, ': L2,6,10,14')');
371 eval(g)
372
373 %%%%%%%%%%%%%%%%%%%%%%%%%%%%%%%%%%%%%%%%%%
374 subplot(2,2,3)
375 semilogx(vsl-y,vsl-u,'k:',log-y,log-u,'k:') %,van-y,van-u,'k-.')
376 hold on
377 xlabel('y^+')
378 ylabel('u^+')
379 axis([0.1 10000 0 35])
380
381 semilogx(y_p(:, skip3) , u_p(:, skip3) , 'r.-')
382 semilogx(y_p(:, skip3+4) , u_p(:, skip3+4) , 'g.-')
383 semilogx(y_p(:, skip3+8) , u_p(:, skip3+8) , 'b.-')
384 semilogx(y_p(:, skip3+12), u_p(:, skip3+12), 'm.-')
385

```



```

386 g = sprintf('%s', 'title('', test_descrip, ': L3,7,11,15')');
387 eval(g)
388
389 %%%%%%%%%%%%%%%%%%%%%%%%%%%%%%%%%%%%%%%%%%
390 subplot(2,2,4)
391 semilogx(vsl_y,vsl_u,'k:',log_y,log_u,'k:') %,van_y,van_u,'k-.')
392 hold on
393 xlabel('y^+')
394 ylabel('u^+')
395 axis([0.1 10000 0 35])
396
397 semilogx(y_p(:,skip4),u_p(:,skip4) , 'r.-')
398 semilogx(y_p(:,skip4+4),u_p(:,skip4+4) , 'g.-')
399 semilogx(y_p(:,skip4+8),u_p(:,skip4+8) , 'b.-')
400
401 g = sprintf('%s', 'title('', test_descrip, ': L4,8,10,14')');
402 eval(g)
403
404
405
406 %% plot u_tau and y0
407 y0(y0 < -0.045) = NaN;
408 % y0(y0 > 0.099) = NaN;
409
410 u_tau(u_tau == utmin) = NaN;
411 u_tau(u_tau == utmax) = NaN;
412
413
414
415 figure
416 subplot(1,2,1)
417 plot(L,u_tau,'k.-')
418 xlabel('Location #')
419 ylabel('u_\tau (m/s)')
420 axis([-2 16 utmin utmax])
421
422 subplot(1,2,2)
423 plot(L,y0,'k.-')
424 xlabel('Location #')
425 ylabel('y_0 ("')')
426 axis([-2 16 yomin yomax])
427
428
429
430 %% Delta 99
431
432 % y_mm_corr
433
434 % NaN -> 1 for u_norm
435 u_norm(isnan(u_norm)==1) = 1;

```

```

436
437 d99 = ones(size(u_inf));
438 for i = 1:length(u_inf)
439     d99(i) = y_mm_corr(find(u_norm(:,i) - 0.99 > 0,1),i); %delta99 in mm, ...
        first location with u/U > 0.99
440 end
441
442
443 d99(d99 < 5) = NaN;
444 figure
445 plot(L,d99,'k.-')
446 xlabel('Location')
447 ylabel('\delta_{99} (mm)')
448 axis([-5 16 0 40])
449 title(test_descrip)
450
451
452
453 %%
454 u_norm(u_norm==1) = NaN;
455
456 figure
457 hold on
458 plot(u_norm(:,1),y_mm_corr(:,1),'k.-')
459 plot(u_norm(:,2),y_mm_corr(:,1),'k.-')
460 plot(u_norm(:,3),y_mm_corr(:,1),'r.-')
461 plot(u_norm(:,4),y_mm_corr(:,1),'g.-')
462 plot(u_norm(:,5),y_mm_corr(:,1),'b.-')
463 plot(u_norm(:,6),y_mm_corr(:,1),'m.-')
464 plot(u_norm(:,7),y_mm_corr(:,1),'r<.-')
465 plot(u_norm(:,8),y_mm_corr(:,1),'g<.-')
466 if dataset ==1
467 plot(u_norm(1:118,9),y_mm_corr(1:118,2),'b<.-')
468 else
469 plot(u_norm(:,9),y_mm_corr(:,2),'b<.-')
470 end
471 plot(u_norm(:,10),y_mm_corr(:,1),'m<.-')
472 plot(u_norm(:,11),y_mm_corr(:,1),'rv.-')
473 plot(u_norm(:,12),y_mm_corr(:,1),'gv.-')
474 plot(u_norm(:,13),y_mm_corr(:,1),'bv.-')
475 plot(u_norm(:,14),y_mm_corr(:,1),'mv.-')
476 plot(u_norm(:,15),y_mm_corr(:,1),'r^.-')
477 plot(u_norm(:,16),y_mm_corr(:,1),'g^.-')
478 plot(u_norm(:,17),y_mm_corr(:,1),'b^.-')
479 xlabel('u/U')
480 ylabel('y (mm)')
481 axis([0.5, 1.1, 0, 30])
482 title(test_descrip)
483
484 %% table

```

```
485
486 table(:,1) = u_tau';
487 table(:,2) = d99';
488
489 %% save
490
491 save(filename)
```

APPENDIX E
HOTWIRE LENGTH SCALE PROCESSING ALGORITHM

```

1 clc, clear all, close all
2
3 load 20140929_data_050kHz_10s.mat
4
5 % sampling frequency and number of samples
6 f_s = 50e3;
7
8 u_inst = u_inst_050kHz_10s;
9 % u_inst = u_inst(:,1:size(u_inst,2)*3/10);
10
11 clear N y0 u_inst_050kHz_10s
12
13 %%
14 N_s = size(u_inst,2);
15 dt = 1/f_s;
16
17
18 t = [0:dt:(N_s-1)*dt];
19 y = y_inches_uncorr;
20 u = u_inst;
21
22 clear y_inches_uncorr u_inst
23
24 u_convect = mean(u,2);
25
26 n_lag_tylr = 12;
27 % nlag = int16(0.04/dt); % lags for integral scale
28 nlag = 2000; % lags for integral scale
29
30
31 %% auto correlation
32
33 for i = 1:length(y)
34     [acorr(:,i), lag] = autocorr(u(i,:),n_lag_tylr);
35     lag = lag*dt;
36
37     acorr_fit = fit(lag', acorr(:,i), 'poly2' );
38     coeffvals = coeffvalues(acorr_fit);
39     r = roots(coeffvals);
40
41     for j = 1:2
42         if r(j) > 0
43             t_taylor(i) = r(j);
44         else
45             end
46     end
47
48     if i == 10
49         figure
50         plot(lag, acorr(:,i), 'k.')

```

```

51     hold on
52     plot(acorr_fit)
53     hold off
54     end
55 end
56 l_taylor = t_taylor' .* u_convect;
57
58 % figure
59 % plot(t_taylor,y)
60 %
61 % figure
62 % plot(l_taylor,y)
63
64 clear i j r coeffvals acorr_fit acorr
65 for i = 1:length(y)
66     [acorr(:,i), lag] = autocorr(u(i,:),nlag);
67     lag = lag'*d_t;
68
69     acorr_fit = fit(lag, acorr(:,i), 'poly9' );
70     coeffvals = coeffvalues(acorr_fit);
71     integral_coeffs = polyint(coeffvals);
72     r = roots(coeffvals);
73
74     for j = 1:length(r)
75         if isreal(r(j)) == 0
76             r(j) = 99;
77         elseif r(j) < 0
78             r(j) = 99;
79         end
80     end
81     r = sort(r);
82     limit = r(1);
83
84     t_integral(i) = polyval(integral_coeffs,limit) - ...
85         polyval(integral_coeffs,0);
86
87     %% to plot parabola too
88     [acorr2(:,i), lag2] = autocorr(u(i,:),n_lag_tylr);
89     lag2 = lag2'*d_t;
90
91     acorr_fit2 = fit(lag2, acorr2(:,i), 'poly2' );
92     %%
93
94     if i == 10
95         figure
96         plot(lag, acorr(:,i), 'k.')
97         hold on
98         plot(acorr_fit)
99         plot(acorr_fit2, 'g-')

```

```

100     plot(limit,0,'ro')
101     hold off
102     xlabel('\tau (s)')
103     ylabel('\rho_{uu}')
104     axis([0 nlag*t(2) 0 1])
105     end
106 end
107
108 l_integral = t_integral' .* u_convect;
109
110 figure
111 subplot(1,2,1)
112 plot(l_integral,y,'g.',l_taylor,y,'b.')
113 axis([0 .3 0 3])
114 xlabel('L (m)')
115 ylabel('y (")')
116 legend('\Lambda-I', '\Lambda-\mu')
117
118 subplot(1,2,2)
119 plot(t_integral*1000,y,'g.',t_taylor*1000,y,'b.')
120 axis([0 6 0 3])
121 xlabel('t (ms)')
122 ylabel('y (")')
123 legend('\tau-I', '\tau-\mu')
124
125
126 %% table
127
128 table(:,1) = t_taylor'*1000;
129 table(:,2) = t_integral'*1000;
130 table(:,3) = l_taylor*100;
131 table(:,4) = l_integral*100;
132
133
134 %% check vs prediction of the ratio
135
136 % Uinf = u_convect;
137 % nu = 15.89e-6;
138 % Aconst = 1;
139 % Re_I = Uinf*l_integral/nu;
140 % shouldbe = (15/Aconst)^(1/2)*Re_I.^(-1/2);
141 %
142 % mu_over_int = l_taylor ./ l_integral;
143 %
144 % figure
145 % plot(y,mu_over_int,y,shouldbe)
146 % xlabel('y (mils)')
147 % ylabel('\Lambda-\mu / \Lambda-I')
148 % legend('Calculated', 'Expected')

```

APPENDIX F
PSP PROCESSING ALGORITHM


```

50 % pixels per hole diameter
51 x_ppd = x_ppm * d_nom
52 z_ppd = z_ppm * d_nom
53
54
55 % number of pitches to lat avg over
56 n_latavg_shift = 1.5;
57 n_latavg_pitch = 3;      % must be an integer
58 n_areaavg_xdir = 8;
59
60 % % % % % % % % % % % % % % % % % % % % % % % % % % % % % % % % % % %
61
62
63 %%% SWITCHES
64 crop      = 0;    % 1: crop on / 0: crop off
65 highlight = 0;    % 1 for highlight, 0 for no mod, -1 for forcing eta = 0,1
66 % grid     = 1;    % 1: grid on / 0: grid off
67 switch_filter = 0;
68
69 fluid_1 = 'air'; % air
70 fluid_2 = 'co2'; % co2 or air
71
72
73 %%% Image numbers
74 n_bg      = 1;
75 n_ref     = 12; %r15:4  r_mid:8  r3:12
76 n_tst_start = 5;
77 n_tst_stop  = 12; %11
78 % n_tst_stop = 6; %11
79
80
81
82 %% CROP
83
84 if crop == 1
85     y_i_crop = 1:1200; %vertical direction
86     x_j_crop = 1:1600; %horizontal direction
87 elseif crop == 0
88     y_i_crop = 1:1200; %vertical direction
89     x_j_crop = 1:1600; %horizontal direction
90 end
91
92
93 %% Read excel
94
95 [numeric , text , raw] = xlsread(filename , 'Data' , data_range);
96 clear numeric text
97
98
99 % define all variables from excel sheet

```

```

100 for i = 1:size(raw,1)
101     g = sprintf('%s', raw{i,1}, ' = cell2mat(raw(' , num2str(i), ...
        ',3:size(raw,2)))');
102     eval(g)
103 end
104
105 for i = 1:size(raw,1)
106     if strcmp('test_image',raw(i,1)) == 1
107         test_image = raw(i,3:size(raw,2));
108     end
109 end
110
111
112 %% INTENSITY RATIO
113
114 g = sprintf('%s', 'load ', char(test_image(n.bg)), '_20.mat');
115 eval(g);
116 bg = average(y-i-crop,x-j-crop);
117
118 clear average sdev g
119
120 g = sprintf('%s', 'load ', char(test_image(n.ref)), '_20.mat');
121 eval(g);
122 ref_flo_on = average(y-i-crop,x-j-crop);
123 clear average sdev g
124
125 ref = ref_flo_on - bg;
126
127
128 %% eta bar bar initialize
129 eta_bar_bar = zeros(size(M));
130
131
132 %% xgrid and zgrid
133 gv_resolution = .1;
134
135 x_d_gv = -10 : gv_resolution : 92;
136
137 if geo_pzd == 14
138     z_d_gv = -2.4 : gv_resolution : 86.3;
139 elseif geo_pzd == 7.5
140     z_d_gv = -2.4 : gv_resolution : 47.5;
141 else
142     display('Check geo_pzd')
143 end
144
145 [x_d_grid z_d_grid] = meshgrid(x_d_gv, z_d_gv);
146
147 x_d = x_d_grid(1,:);
148 z_d = z_d_grid(:,1);

```

```

149
150
151 %% mask
152 filter = ones(size(x-d-grid));
153
154 if switch_filter == 1
155
156 tic
157 for ifilt = 1:length(z-d)
158     for jfilt = 1:length(x-d)
159
160         for kfilt = 1:8
161             for lfilt = 1:7
162
163                 if mod(kfilt,2) == 0
164                     %number is even
165                     if (x-d(jfilt) - ...
166                        (kfilt-1)*geo_pxd)^2/(1/2/sind(20))^2 + ...
167                        (z-d(ifilt) - ((lfilt-1)*geo_pzd + ...
168                        geo_pzd/2))^2/(1/2)^2 < 1
169                         filter(ifilt,jfilt) = 0;
170                     end
171                 else
172                     %number is odd
173                     if (x-d(jfilt) - ...
174                        (kfilt-1)*geo_pxd)^2/(1/2/sind(20))^2 + ...
175                        (z-d(ifilt) - (lfilt-1)*geo_pzd)^2/(1/2)^2 < 1
176                         filter(ifilt,jfilt) = 0;
177                     end
178                 end
179             end
180         end
181     end
182 end
183
184
185 %% x/d and z/d
186
187 x_pix = 1:size(bg,2);
188 z_pix = 1:size(bg,1);
189
190 x_m = (x_pix - x_j_pixel_origin) / x_ppm;
191 z_m = (z_pix - z_i_pixel_origin) / z_ppm;
192
193 x-d_pre = x_m / d_nom;

```

```

194 z_d_pre = z_m / d_nom;
195
196
197
198 %% Define fluid properties
199 if strcmp(fluid_1, 'air') == 1;
200     prop_R1 = 287; %J/kg/K
201     prop_gamma1 = 1.4;
202     prop_Cp1 = 1007; %J/kg/K
203     prop_mu1 = 184.6e-7; %N*s/m^2
204     prop_Pr1 = 0.707;
205     prop_MW1 = 28.97; % kg/mol
206     display('Fluid 1 set as AIR')
207 else
208     display('Check fluid1');
209 end
210
211 if strcmp(fluid_2, 'co2') == 1;
212     prop_R2 = 188.9; %J/kg/K
213     prop_gamma2 = 1.289;
214     prop_alpha2 = 11e-6; % m^2/s
215     prop_Pr2 = 0.766;
216     prop_mu2 = 149e-7; %dyn visc N*s/m^2
217     prop_Cp2 = 851; %J/kg/K
218     prop_MW2 = 44.01; % kg/mol
219     display('Fluid 2 set as CO2')
220 elseif strcmp(fluid_2, 'air') == 1;
221     prop_R2 = 287; %J/kg/K
222     prop_gamma2 = 1.4;
223     prop_Cp2 = 1007; %J/kg/K
224     prop_mu2 = 184.6e-7; %N*s/m^2
225     prop_Pr2 = 0.707;
226     prop_MW2 = 28.97; % kg/mol
227     display('Fluid 2 set as AIR')
228 else
229     display('Check fluid2');
230 end
231
232 counter = 0;
233 eta_tensor = ones(length(z_d_gv), length(x_d_gv), n_tst_stop - n_tst_start + 1);
234 %%
235 for n_tst = n_tst_start:n_tst_stop
236     counter = counter + 1;
237
238     g = sprintf('%s', 'load ', char(test_image(n_tst)), '_20.mat');
239     eval(g);
240     t1 = average(y_i_crop, x_j_crop);
241     clear average sdev g
242
243

```

```

244 % ref = ref_flo-on - bg;
245 flow = t1 - bg;
246
247 IR = ref ./ flow;
248
249
250 figure
251 imagesc(IR)
252 caxis([0 1])
253 axis image
254 colorbar
255 xlabel('x (pixels)')
256 ylabel('z (pixels)')
257 g = sprintf('%s', 'title(''IR - M = ', num2str(M(n_tst)), ', I = ', ...
    num2str(I(n_tst)), ', Re_2 = ', num2str(Re_d_hole(n_tst), '%.0f'), '');');
258 eval(g)
259
260
261 % grid IR
262 IR_pre_grid = IR;
263 IR          = griddata(x_d_pre, z_d_pre, IR_pre_grid, x_d_grid, z_d_grid);
264
265
266
267 %% x/Ms
268
269 eq_slot_p = geo_pzd * 150; % mils ... because p was low tolerance we use ...
    the nominal hole diameter (instead of measurement)
270 eq_slot_se = pi()*(geo_d_in(1)*1000)^2/(4*eq_slot_p); % mils
271
272 x_Ms(:, n_tst-n_tst_start+1) = x_d * 150 / M(n_tst) / eq_slot_se;
273
274 %% IR to PR
275
276 c3 = -0.260014451687312;
277 c2 =  0.718213123196350;
278 c1 =  0.615235522498393;
279 c0 = -0.076849949211372;
280
281 roots_check_eta0 = [c3; c2; c1; c0-1];
282 roots_calibration_eta0 = roots(roots_check_eta0);
283
284 roots_check_eta1 = [c3; c2; c1; c0];
285 roots_calibration_eta1 = roots(roots_check_eta1);
286
287 if highlight == 1
288 IR( IR > roots_calibration_eta0(3) ) = 99999999;
289 elseif highlight == -1
290 IR( IR > roots_calibration_eta0(3) ) = roots_calibration_eta0(3);
291 IR( IR < roots_calibration_eta1(3) ) = roots_calibration_eta1(3);

```

```

292 elseif highlight == 0
293 end
294
295
296 PR = c3*IR.^3 + c2*IR.^2 + c1*IR + c0;
297
298 figure
299 imagesc(x_d, z_d, PR)
300 caxis([0 1])
301 axis image
302 colorbar
303 xlabel('x/d')
304 ylabel('z/d')
305 g = sprintf('%s', 'title(''PR - M = ', num2str(M(n_tst)), ', I = ', ...
    num2str(I(n_tst)), ', Re_2 = ', num2str(Re_d_hole(n_tst), '%.0f'), '');');
306 eval(g)
307
308
309
310 %% PR to \eta
311
312 PRair = 1; % must experimentally verify =1, PR of air as coolant test
313 MW = prop_MW2 / prop_MW1;
314
315 eta = 1 - (1+MW*(PRair./PR-1)).^(-1);
316 eta = filter .* eta;
317
318 eta_tensor(:, :, counter) = eta;
319
320 figure
321 imagesc(x_d, z_d, eta)
322 caxis([0 1])
323 axis image
324 colorbar
325 xlabel('x/d')
326 ylabel('z/d')
327 g = sprintf('%s', 'title(''\eta - M = ', num2str(M(n_tst), '%.3f'), ', I = ...
    ', num2str(I(n_tst), '%.3f'), ', Re_2 = ', ...
    num2str(Re_d_hole(n_tst), '%.0f'), '');');
328 eval(g)
329
330 %# get current colormap
331 map = colormap;
332 %# adjust for number of colors you want
333 rows = uint16(linspace(1, size(map,1), 10)) ;
334 map = map(rows, :);
335 %# and apply the new colormap
336 colormap(map);
337
338 g = sprintf('%s', 'print -dtiff eta-M-' , num2str(M(n_tst), '%.3f'), '.tif;');

```

```

339 eval(g)
340
341
342
343 %% lat avg eta
344 z_average_range = find(z_d > n_latavg_shift*geo_pzd,1) :find(z_d > ...
      (n_latavg_pitch+n_latavg_shift)*geo_pzd,1) ;
345
346
347 eta_bar = mean(eta(z_average_range,:),1) ;
348
349 figure
350 plot(x_d,eta_bar,'g.')
351 xlabel('x/d')
352 ylabel('Lat avg \eta')
353 axis([-20 100 0 1])
354 g = sprintf('%s', 'title('M = ', num2str(M(n_tst),'%.3f'), ', I = ', ...
      num2str(I(n_tst),'%.3f'), ' ');');
355 eval(g)
356 g = sprintf('%s', 'print -dtiff eta_bar_M-' , num2str(M(n_tst),'%.3f'), ...
      '.tif;');
357 eval(g)
358
359
360 figure
361 loglog(x_Ms(:,counter),eta_bar,'g.')
362 xlabel('x/Ms')
363 ylabel('Lat avg \eta')
364 axis([0.001 10000 0.001 1])
365 g = sprintf('%s', 'title('M = ', num2str(M(n_tst),'%.3f'), ', I = ', ...
      num2str(I(n_tst),'%.3f'), ', Re_2 = ', ...
      num2str(Re_d_hole(n_tst),'%.0f'), ' ');');
366 eval(g)
367 g = sprintf('%s', 'print -dtiff eta_bar_xMs_M-' , ...
      num2str(M(n_tst),'%.3f'), '.tif;');
368 eval(g)
369
370 %% Area averaged eta
371
372 x_average_range = find(x_d > 1/sind(20)/2,1):find(x_d > ...
      n_areaavg_xdir*geo_pzd,1);
373
374 eta_bar_bar(n_tst) = mean(mean(eta(z_average_range,x_average_range)));
375
376
377
378
379 %% CL eta
380 slices_cl = [0; 1*geo_pzd; 2*geo_pzd; 3*geo_pzd; 4*geo_pzd; 5*geo_pzd; ...
      6*geo_pzd];

```



```

381
382 for i = 1:length(slices_cl)
383     eta_cl(:,i,counter) = eta(find(z_d - slices_cl(i) > 0,1),:);
384 end
385
386 figure
387 plot(x_d,eta_cl(:,1,counter),'r.-')
388 hold on
389 plot(x_d,eta_cl(:,2,counter),'g.-')
390 plot(x_d,eta_cl(:,3,counter),'b.-')
391 plot(x_d,eta_cl(:,4,counter),'k.-')
392 plot(x_d,eta_cl(:,5,counter),'m.-')
393 plot(x_d,eta_cl(:,6,counter),'c.-')
394 plot(x_d,eta_cl(:,7,counter),'y.-')
395 % axis([
396
397
398 xlabel('x/d')
399 ylabel('\eta_{CL}')
400 legend('z/d = 0', 'z/d = 1*p/d', 'z/d = 2*p/d', 'z/d = 3*p/d', 'z/d = ...
401         4*p/d', 'z/d = 5*p/d', 'z/d = 6*p/d')
402 g = sprintf('%s', 'title('M = ', num2str(M(n_tst),'%.3f'), ', I = ', ...
403         num2str(I(n_tst),'%.3f'), ', Re_2 = ', ...
404         num2str(Re_d_hole(n_tst),'%.0f'), '');');
405 eval(g)
406 g = sprintf('%s', 'print -dtiff eta_cl-M-' , num2str(M(n_tst),'%.3f'), ...
407         '.tif;');
408 eval(g)
409
410 %% CL eta (1/4 pitch)
411 % slices_qrtr = [0; 1*geo_pzd; 2*geo_pzd; 3*geo_pzd; 4*geo_pzd; 5*geo_pzd; ...
412         6*geo_pzd];
413
414 for i = 1:length(slices_cl)-1
415     eta_qrtr(:,i,counter) = eta(find(z_d - ((i-1)+1/4)*geo_pzd > 0,1),:);
416 end
417
418 figure
419 plot(x_d,eta_qrtr(:,1,counter),'r.-')
420 hold on
421 plot(x_d,eta_qrtr(:,2,counter),'g.-')
422 plot(x_d,eta_qrtr(:,3,counter),'b.-')
423 plot(x_d,eta_qrtr(:,4,counter),'k.-')
424 plot(x_d,eta_qrtr(:,5,counter),'m.-')
425 plot(x_d,eta_qrtr(:,6,counter),'c.-')
426 % plot(x_d,eta_qrtr(:,7,counter),'y.-')
427 % axis([
428
429
430 xlabel('x/d')

```

```

426 ylabel('\eta_{1/4}')
427 % legend('z/d = (0+1/4)p/d','z/d = (1+1/4)p/d','z/d = (2+1/4)p/d','z/d = ...
      (3+1/4)p/d','z/d = (4+1/4)p/d','z/d = (5+1/4)p/d','z/d = (6+1/4)p/d')
428 legend('z/d = (0+1/4)p/d','z/d = (1+1/4)p/d','z/d = (2+1/4)p/d','z/d = ...
      (3+1/4)p/d','z/d = (4+1/4)p/d','z/d = (5+1/4)p/d')
429 g = sprintf('%s', 'title('M = ', num2str(M(n_tst),'%.3f'), ', I = ', ...
      num2str(I(n_tst),'%.3f'), ', Re_2 = ', ...
      num2str(Re_d_hole(n_tst),'%.0f'), '');');
430 eval(g)
431 g = sprintf('%s', 'print -dtiff eta_qrtr_M_ ', num2str(M(n_tst),'%.3f'), ...
      '.tif;');
432 eval(g)
433
434
435
436 %% eta 1/4 pitch lateral gradient
437
438 latgrad_n = 21;
439
440 for i = 1:latgrad_n
441     eta_qrtr_latgrad(:,i,counter) = eta(find(z_d - 1/4*geo_pzd > 0,1) - ...
      (latgrad_n-1)/2 + (i-1),:);
442     eta_qrtr_latgrad_zd(i) = z_d(find(z_d - 1/4*geo_pzd > 0,1) - ...
      (latgrad_n-1)/2 + (i-1));
443 end
444
445 figure
446 plot(x_d,eta_qrtr_latgrad(:,1,counter),'r.-')
447 hold on
448 plot(x_d,eta_qrtr_latgrad(:,2,counter),'g.-')
449 plot(x_d,eta_qrtr_latgrad(:,3,counter),'b.-')
450 plot(x_d,eta_qrtr_latgrad(:,4,counter),'k.-')
451 plot(x_d,eta_qrtr_latgrad(:,5,counter),'m.-')
452 plot(x_d,eta_qrtr_latgrad(:,6,counter),'c.-')
453
454
455
456 xlabel('x/d')
457 ylabel('\eta')
458 % legend('z/d = (0+1/4)p/d','z/d = (1+1/4)p/d','z/d = (2+1/4)p/d','z/d = ...
      (3+1/4)p/d','z/d = (4+1/4)p/d','z/d = (5+1/4)p/d','z/d = (6+1/4)p/d')
459 % legend('z/d = (0+1/4)p/d','z/d = (1+1/4)p/d','z/d = (2+1/4)p/d','z/d = ...
      (3+1/4)p/d','z/d = (4+1/4)p/d','z/d = (5+1/4)p/d')
460 g = sprintf('%s', 'title('Lateral Gradient: M = ', ...
      num2str(M(n_tst),'%.3f'), ', I = ', num2str(I(n_tst),'%.3f'), ', Re_2 ...
      = ', num2str(Re_d_hole(n_tst),'%.0f'), '');');
461 eval(g)
462 % g = sprintf('%s', 'print -dtiff eta_qrtr_M_ ', num2str(M(n_tst),'%.3f'), ...
      '.tif;');
463 % eval(g)

```

```

464
465
466
467 %% CL eta (half pitch)
468 halveslices_cl = [0.5*geo_pzd; 1.5*geo_pzd; 2.5*geo_pzd; 3.5*geo_pzd; ...
    4.5*geo_pzd; 5.5*geo_pzd;];
469
470 for i = 1:length(halveslices_cl)
471     eta_cl2(:,i,counter) = eta(find(z_d - halveslices_cl(i) > 0,1),:);
472 end
473
474 figure
475 plot(x_d,eta_cl2(:,1,counter),'r.')
476 hold on
477 plot(x_d,eta_cl2(:,2,counter),'g.')
478 plot(x_d,eta_cl2(:,3,counter),'b.')
479 plot(x_d,eta_cl2(:,4,counter),'k.')
480 plot(x_d,eta_cl2(:,5,counter),'m.')
481 plot(x_d,eta_cl2(:,6,counter),'c.')
482
483
484 xlabel('x/d')
485 ylabel('\eta_{CL}')
486 legend('z/d = 0.5','z/d = 1.5*p/d','z/d = 2.5*p/d','z/d = 3.5*p/d','z/d = ...
    4.5*p/d','z/d = 5.5*p/d')
487 g = sprintf('%s', 'title('M = ', num2str(M(n_tst),'%.3f'), ', I = ', ...
    num2str(I(n_tst),'%.3f'), ', Re_2 = ', ...
    num2str(Re_d_hole(n_tst),'%.0f'), '');');
488 eval(g)
489 g = sprintf('%s', 'print -dtiff eta_cl_M-' , num2str(M(n_tst),'%.3f'), ...
    '.tif;');
490 eval(g)
491
492 %% Tap locations
493
494 tapavg(n_tst,1) = mean(mean(eta(find(z_d > 1.9 - 0.2, 1):find(z_d > 1.9 + ...
    0.2,1),find(x_d > 56.1 - 8*geo_pxd - 0.2, 1):find(x_d > 56.1 - ...
    8*geo_pxd + 0.2,1))));
495 tapavg(n_tst,2) = mean(mean(eta(find(z_d > 1.9 - 0.2, 1):find(z_d > 1.9 + ...
    0.2,1),find(x_d > 56.1 - 6*geo_pxd - 0.2, 1):find(x_d > 56.1 - ...
    6*geo_pxd + 0.2,1))));
496 tapavg(n_tst,3) = mean(mean(eta(find(z_d > 1.9 - 0.2, 1):find(z_d > 1.9 + ...
    0.2,1),find(x_d > 56.1 - 4*geo_pxd - 0.2, 1):find(x_d > 56.1 - ...
    4*geo_pxd + 0.2,1))));
497 tapavg(n_tst,4) = mean(mean(eta(find(z_d > 1.9 - 0.2, 1):find(z_d > 1.9 + ...
    0.2,1),find(x_d > 56.1 - 2*geo_pxd - 0.2, 1):find(x_d > 56.1 - ...
    2*geo_pxd + 0.2,1))));
498 tapavg(n_tst,5) = mean(mean(eta(find(z_d > 1.9 - 0.2, 1):find(z_d > 1.9 + ...
    0.2,1),find(x_d > 56.1 - 0.2, 1):find(x_d > 56.1 ...
    + 0.2,1))));

```

```

499
500
501 %% Lateral slices eta
502
503 slices_lat = [0; geo_pxd*1/4; geo_pxd*2/4; geo_pxd*3/4; geo_pxd*4/4; ...
               geo_pxd*2; geo_pxd*3; geo_pxd*4; geo_pxd*5; geo_pxd*6; geo_pxd*7];
504
505 for i = 1:length(slices_lat)
506     ii(i) = find(x_d - slices_lat(i) > 0,1);
507 end
508
509 figure
510 plot(z_d,eta(:,ii(1)), 'k.-', z_d,eta(:,ii(2)), 'r.-', z_d,eta(:,ii(3)), ...
511      'g.-', z_d,eta(:,ii(4)), 'b.-', z_d,eta(:,ii(5)), 'c.-', z_d,eta(:,ii(6)), ...
512      'm.-', z_d,eta(:,ii(7)), 'kx-', z_d,eta(:,ii(8)), 'rx-', z_d,eta(:,ii(9)), ...
513      'gx-', z_d,eta(:,ii(10)), 'bx-', z_d,eta(:,ii(11)), 'cx-')
514 xlabel('z/d')
515 ylabel('\eta')
516 legend('x/d = 0', 'x/d = px/d*1/4', 'x/d = px/d*2/4', 'x/d = px/d*3/4', ...
517        'x/d = px/d*4/4', 'x/d = px/d*2', 'x/d = px/d*3', 'x/d = px/d*4', ...
518        'x/d = px/d*5', 'x/d = px/d*6', 'x/d = px/d*7')
519 axis([-15 75 0 1.4])
520 g = sprintf('%s', 'title('M = ', num2str(M(n_tst), '%.3f'), ', I = ', ...
               num2str(I(n_tst), '%.3f'), ', Re_2 = ', ...
               num2str(Re_d_hole(n_tst), '%.0f'), '');');
521 eval(g)
522 g = sprintf('%s', 'print -dtiff eta_slice_M_ ', num2str(M(n_tst), '%.3f'), ...
               '.tif;');
523 eval(g)
524
525
526 %% High pass filter to effectiveness
527 hp_limit = 0.05;
528 hp_eta = eta;
529 hp_eta(hp_eta < hp_limit) = 0;
530 hp_eta_bar = mean(hp_eta(z_average_range,:),1);
531
532
533 %% Noise in between holes version
534
535 noise_width      = 6*geo_pzd;
536
537 noise_region_x = find(x_d > -8,1):find(x_d > -3,1)    ;
538 noise_region_z = find(z_d > geo_pzd*3-noise_width/2,1):find(z_d > ...
                    geo_pzd*3+noise_width/2,1)    ;
539
540 noise_n          = length(noise_region_x)*length(noise_region_z);
541
542
543 noise_data(:, :, n_tst-n_tst_start+1) = eta(noise_region_z, noise_region_x);

```

```

544
545
546 %% highlight region and plot
547
548 eta_noise.highlight_region(:, :, n_tst) = eta;
549
550 % noise part
551 % eta_noise.highlight_region(noise_region_z, noise_region_x, n_tst) = 9999;
552 eta_noise.highlight_region(noise_region_z(1), noise_region_x(1) : ...
    noise_region_x( length(noise_region_x)), n_tst) = 0.7;
553 eta_noise.highlight_region(noise_region_z( length( noise_region_z)), ...
    noise_region_x(1):noise_region_x( length(noise_region_x)), n_tst) = 0.7;
554 eta_noise.highlight_region(noise_region_z(1): noise_region_z( length( ...
    noise_region_z)), noise_region_x(1), n_tst) = 0.7;
555 eta_noise.highlight_region(noise_region_z(1): noise_region_z( length( ...
    noise_region_z)), noise_region_x( length(noise_region_x)), n_tst) = 0.7;
556
557 % lat avg part and area avg part
558 eta_noise.highlight_region(z_average_range(1), x_average_range(1): ...
    x_average_range( length( x_average_range)), n_tst) = 0.5;
559 eta_noise.highlight_region(z_average_range( length(z_average_range)), ...
    x_average_range(1): x_average_range( length( x_average_range)), n_tst) ...
    = 0.5;
560 eta_noise.highlight_region(z_average_range(1): z_average_range( ...
    length(z_average_range)), x_average_range(1), n_tst) = 0.5;
561 eta_noise.highlight_region(z_average_range(1): ...
    z_average_range( length(z_average_range)), ...
    x_average_range( length(x_average_range)), n_tst) = 0.5;
562
563 % eta_noise.highlight_region(find(z_d > -0.0001, 1), x_average_range) = 9999;
564
565 % eta cl part
566 for icl = 1:length(slices_cl)
567 eta_noise.highlight_region(find(z_d - slices_cl(icl) > 0, 1), :, n_tst)= 9999;
568 end
569
570 % eta lat part
571 for ilat = 1:length(slices_lat)
572 eta_noise.highlight_region(:, find(x_d - slices_lat(ilat) > 0, 1), n_tst)= 9999;
573 end
574
575 tap_width = 0.2;
576 % tap locations
577 eta_noise.highlight_region(find(z_d > 1.9 - tap_width, 1):find(z_d > 1.9 + ...
    tap_width, 1), find(x_d > 56.1 - 8*geo_pxd - tap_width, 1):find(x_d > ...
    56.1 - 8*geo_pxd + tap_width, 1), n_tst) = 0.8;
578 eta_noise.highlight_region(find(z_d > 1.9 - tap_width, 1):find(z_d > 1.9 + ...
    tap_width, 1), find(x_d > 56.1 - 6*geo_pxd - tap_width, 1):find(x_d > ...
    56.1 - 6*geo_pxd + tap_width, 1), n_tst) = 0.8;

```

```

579 eta_noise_highlight_region(find(z_d > 1.9 - tap_width, 1):find(z_d > 1.9 + ...
    tap_width,1),find(x_d > 56.1 - 4*geo_pxd - tap_width, 1):find(x_d > ...
    56.1 - 4*geo_pxd + tap_width,1),n_tst) = 0.8;
580 eta_noise_highlight_region(find(z_d > 1.9 - tap_width, 1):find(z_d > 1.9 + ...
    tap_width,1),find(x_d > 56.1 - 2*geo_pxd - tap_width, 1):find(x_d > ...
    56.1 - 2*geo_pxd + tap_width,1),n_tst) = 0.8;
581 eta_noise_highlight_region(find(z_d > 1.9 - tap_width, 1):find(z_d > 1.9 + ...
    tap_width,1),find(x_d > 56.1 - 0*geo_pxd - tap_width, 1):find(x_d > ...
    56.1 - 0*geo_pxd + tap_width,1),n_tst) = 0.8;
582
583
584
585 %%%%%%%%%%%%% copied from noise code
586 hist_x = [-0.1:0.002:0.1];
587 for noise_i = 1:size(noise_data,3)
588     % Reshape
589     noise_vectors(:,noise_i) = reshape(noise_data(:,:,noise_i), ...
        [size(noise_data,1) * size(noise_data,2), 1]);
590
591     % Create histograms
592     hist_N(:,noise_i) = hist(noise_vectors(:,noise_i),hist_x) / ...
        length(noise_vectors(:,noise_i));
593
594     noise_mean(noise_i) = mean(noise_vectors(:,noise_i))';
595     noise_sdev(noise_i) = std(noise_vectors(:,noise_i)); %%%%%%%%%%%%%
596 end
597 %%%%%%%%%%%%%
598
599
600 if n_tst == n_tst_start
601
602 figure
603 imagesc(x_d,z_d,eta_noise_highlight_region(:,:,n_tst))
604 caxis([0 1])
605 axis image
606 colorbar
607 xlabel('x/d')
608 ylabel('z/d')
609 g = sprintf('%s', 'title('\eta - M = ', num2str(M(n_tst),'%.3f'), ', I = ...
        ', num2str(I(n_tst),'%.3f'), ', Re_2 = ', ...
        num2str(Re_d_hole(n_tst),'%.0f'), '');');
610 eval(g)
611
612 end
613
614
615 %% gradients
616
617 [fx fz] = gradient(eta(:,:,));
618

```

```

619 dummy = 0.05;
620
621
622 cmapn = fix(0.5*10); % 10 is number of levels
623 cmapr = [(0:1:cmapn-1)/cmapn,ones(1,cmapn)];
624 cmapg = [(0:cmapn-1)/cmapn, (cmapn-1:-1:0)/cmapn];
625 cmapb = [ones(1,cmapn), (cmapn-1:-1:0)/cmapn];
626 cmapc = [flipud(cmapr(:)), cmapg(:), flipud(cmapb(:))];
627
628
629 figure
630 imagesc(x_d,z_d,fx)
631 axis image
632 xlabel('x/d')
633 ylabel('z/d')
634 colorbar
635 caxis([-dummy/5 dummy/5])
636 colormap(cmapc)
637 g = sprintf('%s', 'title('d\eta/d(x/d): M = ', num2str(M(n_tst),'%.3f'), ...
        ', I = ', num2str(I(n_tst),'%.3f'), ', Re_2 = ', ...
        num2str(Re_d_hole(n_tst),'%.0f'), '');');
638 eval(g)
639 g = sprintf('%s', 'print -dtiff eta_xgrad_M-' , num2str(M(n_tst),'%.3f'), ...
        '.tif;');
640 eval(g)
641
642 figure
643 imagesc(x_d,z_d,fz)
644 title('d\eta/d(z/d)')
645 axis image
646 xlabel('x/d')
647 ylabel('z/d')
648 colorbar
649 caxis([-dummy dummy])
650 colormap(cmapc)
651 g = sprintf('%s', 'title('d\eta/d(z/d): M = ', num2str(M(n_tst),'%.3f'), ...
        ', I = ', num2str(I(n_tst),'%.3f'), ', Re_2 = ', ...
        num2str(Re_d_hole(n_tst),'%.0f'), '');');
652 eval(g)
653 g = sprintf('%s', 'print -dtiff eta_zgrad_M-' , num2str(M(n_tst),'%.3f'), ...
        '.tif;');
654 eval(g)
655
656 %% Export to excel
657 eta_bar_table_datazz(:,n_tst - n_tst_start + 1) = eta_bar;
658 hp_eta_bar_datazz(:,n_tst - n_tst_start + 1) = hp_eta_bar;
659
660 end
661
662 %% Generate table for copy

```

```

663 eta_bar_table_xd      = [0; 0; x-d'];
664 eta_bar_table_headerM = M(n_tst_start:n_tst_stop);
665 eta_bar_table_headerI = I(n_tst_start:n_tst_stop);
666 eta_bar_table_header  = [eta_bar_table_headerM; eta_bar_table_headerI];
667
668 eta_bar_table_almost  = [eta_bar_table_header; eta_bar_table_datazz];
669
670 clear eta_bar_table_datazz eta_bar_table_headerM eta_bar_table_headerI ...
    eta_bar_table_header
671
672 %% Noise data
673
674 if highlight == 0
675     save(sprintf('%s', 'noise_data-', date, '.mat'), 'noise_data')
676 else
677     display('No noise saved, set highlight = 0 to enable')
678 end
679
680 %% Static pressure in tunnel
681 primary_Ps = [primary_Ps_1; primary_Ps_2; primary_Ps_3; primary_Ps_4; ...
    primary_Ps_5; primary_Ps_6; primary_Ps_7];
682
683 % axial locations of pressure measurements - 20140707
684 primary_Ps_x = [0.08255; 0.1397; 0.1778; 0.254; 0.3683; 0.46355; 0.635];
685
686
687 figure
688 hold on
689 plot(primary_Ps_x, primary_Ps(:,1), 'k.-')
690 plot(primary_Ps_x, primary_Ps(:,2), 'r.-')
691 plot(primary_Ps_x, primary_Ps(:,3), 'g.-')
692 plot(primary_Ps_x, primary_Ps(:,4), 'b.-')
693 plot(primary_Ps_x, primary_Ps(:,5), 'c.-')
694 plot(primary_Ps_x, primary_Ps(:,6), 'm.-')
695 plot(primary_Ps_x, primary_Ps(:,7), 'y.-')
696 plot(primary_Ps_x, primary_Ps(:,8), 'k.-.')
697 % plot(primary_Ps_x, primary_Ps(:,9), 'r.-.')
698 % plot(primary_Ps_x, primary_Ps(:,10), 'g.-.')
699 % plot(primary_Ps_x, primary_Ps(:,11), 'b.-.')
700 % plot(primary_Ps_x, primary_Ps(:,12), 'c.-.')
701 hold off
702 xlabel('Streamwise distance from tunnel leading edge (m)')
703 ylabel('Static gage pressure in tunnel (Pa)')
704 legend('Test 1', 'Test 2', 'Test 3', 'Test 4', 'Test 5', 'Test 6', 'Test ...
    7', 'Test 8', 'Test 9', 'Test 10', 'Test 11', 'Test 12')
705
706 %% dP/PR vs M
707
708 % generate average Pplenum vector
709 plenum_P_all = [plenum_P_1; plenum_P_2; plenum_P_3];

```



```

710 plenum_P      = mean(plenum_P_all,1);
711
712 % absolute source and sink pressures
713 plenum_P_abs  = plenum_P + test_Patm;
714 primary_Psink = primary_Ps(2,:) + test_Patm;
715
716 % calculate dP and PR
717 discharge_PR  = plenum_P_abs ./ primary_Psink;
718 discharge_dP  = plenum_P - primary_Ps_2; %dP in
719
720 % plot dP and PR vs M
721 figure
722 subplot(1,2,1)
723 plot(discharge_dP, M, 'k.')
724 xlabel('dP (Pa)')
725 ylabel('M')
726 subplot(1,2,2)
727 plot(discharge_PR, M, 'k.')
728 xlabel('PR = P_{source}/P_{sink}')
729 ylabel('M')
730
731
732 %% Discharge coefficient - Cd
733
734 % geometric area
735 discharge_A_total = geo_N .* pi() .* (geo_d_m).^2 /4; % total metering ...
       area in m^2
736
737 % dP calcs
738 discharge_ideal_V_dp = (2*discharge_dP ./ coolant_density).^ (1/2); % dP ...
       calc of ideal velocity
739 discharge_mdot_ideal_dP = coolant_density .* discharge_ideal_V_dp .* ...
       discharge_A_total; % ideal coolant mdot in kg/s
740
741 % PR calc
742 discharge_mdot_ideal_PR = primary_Psink.*discharge_A_total.* ...
       (2*prop_gamma2./ (prop_R2.*(plenum_T_1+273.15)*(prop_gamma2-1)).* ...
       (plenum_P_abs./primary_Psink).^ ((prop_gamma2-1)./prop_gamma2)-1)).^ (1/2);
743
744 % calculate Cd from both methods
745 discharge_Cd_dP = coolant_mdot ./ discharge_mdot_ideal_dP;
746 discharge_Cd_PR = real(coolant_mdot ./ discharge_mdot_ideal_PR);
747
748
749 % table
750 discharge_Cd_PR = real(discharge_Cd_PR);
751 a_COPY_ME_Cd = [discharge_dP', discharge_Cd_dP', discharge_PR', ...
       discharge_Cd_PR'];
752
753

```

```

754 figure
755 subplot(1,3,1)
756 plot(M,discharge_Cd_dP,'k.',M,discharge_Cd_PR,'rx')
757 xlabel('M')
758 ylabel('C_d')
759
760 subplot(1,3,2)
761 plot(discharge_dP,discharge_Cd_dP,'k.',discharge_dP,discharge_Cd_PR,'rx')
762 xlabel('dP (Pa)')
763
764 subplot(1,3,3)
765 plot(discharge_PR,discharge_Cd_dP,'k.',discharge_PR,discharge_Cd_PR,'rx')
766 xlabel('PR')
767
768 %% area avg eta
769 figure
770 plot(M, eta_bar_bar,'k.-')
771
772
773 %% NOISE plots
774
775 figure
776
777 if size(hist_N,2) == 1
778     plot(hist_x,hist_N(:,1),'k.-')
779
780     hold on
781     plot([noise_mean(1), noise_mean(1)], [0, 1], 'kx-')
782 elseif size(hist_N,2) == 2
783     plot(hist_x,hist_N(:,1),'k.-', ...
784         hist_x,hist_N(:,2),'y.-')
785
786     hold on
787     plot([noise_mean(1), noise_mean(1)], [0, 1], 'kx-', ...
788         [noise_mean(2), noise_mean(2)], [0, 1], 'yx-')
789
790 elseif size(hist_N,2) == 3
791     plot(hist_x,hist_N(:,1),'k.-', ...
792         hist_x,hist_N(:,2),'y.-', ...
793         hist_x,hist_N(:,3),'g.-')
794
795     hold on
796     plot([noise_mean(1), noise_mean(1)], [0, 1], 'kx-', ...
797         [noise_mean(2), noise_mean(2)], [0, 1], 'yx-', ...
798         [noise_mean(3), noise_mean(3)], [0, 1], 'gx-')
799
800 elseif size(hist_N,2) == 4
801     plot(hist_x,hist_N(:,1),'k.-', ...
802         hist_x,hist_N(:,2),'y.-', ...
803         hist_x,hist_N(:,3),'g.-', ...

```

```

804     hist_x,hist_N(:,4), 'b.-')
805
806     hold on
807     plot([noise_mean(1), noise_mean(1)], [0, 1], 'kx-', ...
808         [noise_mean(2), noise_mean(2)], [0, 1], 'yx-', ...
809         [noise_mean(3), noise_mean(3)], [0, 1], 'gx-', ...
810         [noise_mean(4), noise_mean(4)], [0, 1], 'bx-')
811
812 elseif size(hist_N,2) == 5
813     plot(hist_x,hist_N(:,1), 'k.-', ...
814         hist_x,hist_N(:,2), 'y.-', ...
815         hist_x,hist_N(:,3), 'g.-', ...
816         hist_x,hist_N(:,4), 'b.-', ...
817         hist_x,hist_N(:,5), 'm.-')
818
819     hold on
820     plot([noise_mean(1), noise_mean(1)], [0, 1], 'kx-', ...
821         [noise_mean(2), noise_mean(2)], [0, 1], 'yx-', ...
822         [noise_mean(3), noise_mean(3)], [0, 1], 'gx-', ...
823         [noise_mean(4), noise_mean(4)], [0, 1], 'bx-', ...
824         [noise_mean(5), noise_mean(5)], [0, 1], 'mx-')
825
826 elseif size(hist_N,2) == 6
827     plot(hist_x,hist_N(:,1), 'k.-', ...
828         hist_x,hist_N(:,2), 'y.-', ...
829         hist_x,hist_N(:,3), 'g.-', ...
830         hist_x,hist_N(:,4), 'b.-', ...
831         hist_x,hist_N(:,5), 'm.-', ...
832         hist_x,hist_N(:,6), 'c.-')
833
834     hold on
835     plot([noise_mean(1), noise_mean(1)], [0, 1], 'kx-', ...
836         [noise_mean(2), noise_mean(2)], [0, 1], 'yx-', ...
837         [noise_mean(3), noise_mean(3)], [0, 1], 'gx-', ...
838         [noise_mean(4), noise_mean(4)], [0, 1], 'bx-', ...
839         [noise_mean(5), noise_mean(5)], [0, 1], 'mx-', ...
840         [noise_mean(6), noise_mean(6)], [0, 1], 'cx-')
841
842 elseif size(hist_N,2) == 7
843     plot(hist_x,hist_N(:,1), 'k.-', ...
844         hist_x,hist_N(:,2), 'y.-', ...
845         hist_x,hist_N(:,3), 'g.-', ...
846         hist_x,hist_N(:,4), 'b.-', ...
847         hist_x,hist_N(:,5), 'm.-', ...
848         hist_x,hist_N(:,6), 'c.-', ...
849         hist_x,hist_N(:,7), 'r.-')
850
851     hold on
852     plot([noise_mean(1), noise_mean(1)], [0, 1], 'kx-', ...
853         [noise_mean(2), noise_mean(2)], [0, 1], 'yx-', ...

```

```

854     [noise_mean(3), noise_mean(3)], [0, 1], 'gx-', ...
855     [noise_mean(4), noise_mean(4)], [0, 1], 'bx-', ...
856     [noise_mean(5), noise_mean(5)], [0, 1], 'mx-', ...
857     [noise_mean(6), noise_mean(6)], [0, 1], 'cx-', ...
858     [noise_mean(7), noise_mean(7)], [0, 1], 'rx-'
859
860 elseif size(hist_N,2) == 8
861     plot(hist_x, hist_N(:,1), 'k.-', ...
862          hist_x, hist_N(:,2), 'y.-', ...
863          hist_x, hist_N(:,3), 'g.-', ...
864          hist_x, hist_N(:,4), 'b.-', ...
865          hist_x, hist_N(:,5), 'm.-', ...
866          hist_x, hist_N(:,6), 'c.-', ...
867          hist_x, hist_N(:,7), 'r.-', ...
868          hist_x, hist_N(:,8), 'k.-')
869
870     hold on
871     plot([noise_mean(1), noise_mean(1)], [0, 1], 'kx-', ...
872          [noise_mean(2), noise_mean(2)], [0, 1], 'yx-', ...
873          [noise_mean(3), noise_mean(3)], [0, 1], 'gx-', ...
874          [noise_mean(4), noise_mean(4)], [0, 1], 'bx-', ...
875          [noise_mean(5), noise_mean(5)], [0, 1], 'mx-', ...
876          [noise_mean(6), noise_mean(6)], [0, 1], 'cx-', ...
877          [noise_mean(7), noise_mean(7)], [0, 1], 'rx-', ...
878          [noise_mean(8), noise_mean(8)], [0, 1], 'kx-')
879
880 else
881     display('No noise plot generated, more than 8 runs')
882 end
883
884 xlabel('\eta')
885 ylabel('N samples')
886 title('Noise')
887 axis([-0.1 0.1 0 0.06])
888 % grid on
889
890
891 legend('Test 1', ...
892        'Test 2', ...
893        'Test 3', ...
894        'Test 4', ...
895        'Test 5', ...
896        'Test 6', ...
897        'Test 7')
898
899 g = sprintf('%s', 'print -dtiff eta_noise_', date, '.tif;');
900 eval(g)
901
902
903 noise_mean = noise_mean';

```

```

904 noise_sdev = noise_sdev';
905
906 noise_table = [noise_mean, noise_sdev]
907
908
909
910 %% Plot lat avgs
911
912 figure
913
914 if size(hist_N,2) == 1
915     plot(x_d', eta_bar_table_almost(3:size(eta_bar_table_almost,1),1),'k.-')
916     legend('Test 1')
917 elseif size(hist_N,2) == 2
918     plot(x_d', ...
919         eta_bar_table_almost(3:size(eta_bar_table_almost,1),1),'k.-', ...
920         x_d', eta_bar_table_almost(3:size(eta_bar_table_almost,1),2),'r.-')
921     legend('Test 1', ...
922         'Test 2')
923 elseif size(hist_N,2) == 3
924     plot(x_d', ...
925         eta_bar_table_almost(3:size(eta_bar_table_almost,1),1),'k.-', ...
926         x_d', eta_bar_table_almost(3:size(eta_bar_table_almost,1),2),'r.-', ...
927         x_d', eta_bar_table_almost(3:size(eta_bar_table_almost,1),3),'g.-')
928     legend('Test 1', ...
929         'Test 2', ...
930         'Test 3')
931 elseif size(hist_N,2) == 4
932     plot(x_d', ...
933         eta_bar_table_almost(3:size(eta_bar_table_almost,1),1),'k.-', ...
934         x_d', eta_bar_table_almost(3:size(eta_bar_table_almost,1),2),'r.-', ...
935         x_d', eta_bar_table_almost(3:size(eta_bar_table_almost,1),3),'g.-', ...
936         x_d', eta_bar_table_almost(3:size(eta_bar_table_almost,1),4),'b.-')
937     legend('Test 1', ...
938         'Test 2', ...
939         'Test 3', ...
940         'Test 4')
941 elseif size(hist_N,2) == 5
942     plot(x_d', ...
943         eta_bar_table_almost(3:size(eta_bar_table_almost,1),1),'k.-', ...
944         x_d', eta_bar_table_almost(3:size(eta_bar_table_almost,1),2),'r.-', ...
945         x_d', eta_bar_table_almost(3:size(eta_bar_table_almost,1),3),'g.-', ...
946         x_d', eta_bar_table_almost(3:size(eta_bar_table_almost,1),4),'b.-', ...
947         x_d', eta_bar_table_almost(3:size(eta_bar_table_almost,1),5),'m.-')
948     legend('Test 1', ...
949         'Test 2', ...
950         'Test 3', ...
951         'Test 4', ...
952         'Test 5')
953 elseif size(hist_N,2) == 6

```

```

950 plot(x_d', ...
      eta_bar_table_almost(3:size(eta_bar_table_almost,1),1),'k.-', ...
951 x_d', eta_bar_table_almost(3:size(eta_bar_table_almost,1),2),'r.-', ...
952 x_d', eta_bar_table_almost(3:size(eta_bar_table_almost,1),3),'g.-', ...
953 x_d', eta_bar_table_almost(3:size(eta_bar_table_almost,1),4),'b.-', ...
954 x_d', eta_bar_table_almost(3:size(eta_bar_table_almost,1),5),'m.-', ...
955 x_d', eta_bar_table_almost(3:size(eta_bar_table_almost,1),6),'c.-')
956 legend('Test 1', ...
957        'Test 2', ...
958        'Test 3', ...
959        'Test 4', ...
960        'Test 5', ...
961        'Test 6')
962 elseif size(hist_N,2) == 7
963 plot(x_d', ...
      eta_bar_table_almost(3:size(eta_bar_table_almost,1),1),'k.-', ...
964 x_d', eta_bar_table_almost(3:size(eta_bar_table_almost,1),2),'r.-', ...
965 x_d', eta_bar_table_almost(3:size(eta_bar_table_almost,1),3),'g.-', ...
966 x_d', eta_bar_table_almost(3:size(eta_bar_table_almost,1),4),'b.-', ...
967 x_d', eta_bar_table_almost(3:size(eta_bar_table_almost,1),5),'m.-', ...
968 x_d', eta_bar_table_almost(3:size(eta_bar_table_almost,1),6),'c.-', ...
969 x_d', eta_bar_table_almost(3:size(eta_bar_table_almost,1),7),'kx-')
970 legend('Test 1', ...
971        'Test 2', ...
972        'Test 3', ...
973        'Test 4', ...
974        'Test 5', ...
975        'Test 6', ...
976        'Test 7')
977 elseif size(hist_N,2) == 8
978 plot(x_d', ...
      eta_bar_table_almost(3:size(eta_bar_table_almost,1),1),'k.-', ...
979 x_d', eta_bar_table_almost(3:size(eta_bar_table_almost,1),2),'r.-', ...
980 x_d', eta_bar_table_almost(3:size(eta_bar_table_almost,1),3),'g.-', ...
981 x_d', eta_bar_table_almost(3:size(eta_bar_table_almost,1),4),'b.-', ...
982 x_d', eta_bar_table_almost(3:size(eta_bar_table_almost,1),5),'m.-', ...
983 x_d', eta_bar_table_almost(3:size(eta_bar_table_almost,1),6),'c.-', ...
984 x_d', eta_bar_table_almost(3:size(eta_bar_table_almost,1),7),'kx-', ...
985 x_d', eta_bar_table_almost(3:size(eta_bar_table_almost,1),8),'rx-')
986 legend('Test 1', ...
987        'Test 2', ...
988        'Test 3', ...
989        'Test 4', ...
990        'Test 5', ...
991        'Test 6', ...
992        'Test 7', ...
993        'Test 8')
994 else
995 display('No noise plot generated, more than 8 runs')
996 end

```

```

997
998 xlabel('x/d')
999 ylabel('Lat Avg \eta')
1000 axis([-20 100 0 1])
1001
1002 %% eta bar vs bias
1003
1004 figure
1005
1006 plot(eta_bar_bar(n_tst_start:n_tst_stop),noise_mean,'k.-')
1007
1008 xlabel('Area average \eta')
1009 ylabel('\eta = 0 bias')
1010 grid on
1011
1012
1013 %% Copy these tables
1014 a_COPY_ME_eta_bar_table      = [eta_bar_table_xd, eta_bar_table_almost];
1015 a_COPY_ME_xMs               = x_Ms;
1016 a_COPY_ME_dPvM              = [M', discharge_dP', discharge_PR', ...
    discharge_Cd_dP'];
1017 a_COPY_ME_eta_area          = [M', I', eta_bar_bar'];
1018
1019 % a_COPY_ME_names = ones(size(eta_bar_table_almost,2),1)
1020 for i = 1:size(eta_bar_table_almost,2)
1021     a_COPY_ME_names(i) = {sprintf('%s', 'M = ...
    ', num2str(M(i+n_tst_start-1),3), ', I = ', ...
    num2str(I(i+n_tst_start-1),3))};
1022 end
1023
1024
1025 %% GA table
1026
1027 tapavg_ga      = [coupon_C-1', coupon_C-2', coupon_C-3', coupon_C-4', ...
    coupon_C-5'] / 100;
1028
1029 tapavg_ga_eta = 1 - (1+MW*(PRair./(1-tapavg_ga)-1)).^(-1);
1030
1031 % eta = 1 - (1+MW*(PRair./PR-1)).^(-1);
1032
1033
1034 %% save workspace
1035 save(date)

```

APPENDIX G
PSP UNCERTAINTY PROCESSING ALGORITHM


```

49     Ir_sb = griddata(x-d_pre, z-d_pre, Ir_sb, x-d_grid, z-d_grid);
50     Ibg   = griddata(x-d_pre, z-d_pre, bg, x-d_grid, z-d_grid);
51     Ir    = griddata(x-d_pre, z-d_pre, ref_flo_on, x-d_grid, z-d_grid);
52 % elseif grid == 0
53 % end
54 toc
55
56
57
58 %%
59
60
61 % for n_tst = n_tst_start:n_tst_stop
62 for n_tst = n_tst_start:n_tst_start
63
64
65
66 g = sprintf('%s', 'load ', char(test_image(n_tst)), '_20.mat');
67 eval(g);
68 It_sb = sdev(y_i_crop, x_j_crop) / sqrt(n_samples);  %% sqrt20 makes this ...
        SxBAR!
69 It    = average(y_i_crop, x_j_crop);
70 clear average sdev g
71
72 % if grid == 1
73     It_sb = griddata(x-d_pre, z-d_pre, It_sb, x-d_grid, z-d_grid);
74     It    = griddata(x-d_pre, z-d_pre, It, x-d_grid, z-d_grid);
75 % elseif grid == 0
76 % end
77
78 IR = (Ir - Ibg) ./ (It - Ibg);
79
80 partial_IR_wrt_Ir =          1 ./ (It - Ibg);
81 partial_IR_wrt_It = -(Ir - Ibg) ./ (It - Ibg).^2;
82 partial_IR_wrt_Ibg = (Ir - It) ./ (It - Ibg).^2;
83
84
85 %% So far we have:
86 %     Ibg
87 %     sb_Ibg
88 %     Ir
89 %     sb_Ir
90 %     It
91 %     sb_It
92
93
94 %% IR uncertainty - only precision - currently the constituent ...
        uncertainties are all sdev, low CI - multiply by t/z-score
95

```

```

96 IR_sb = ( (partial_IR_wrt_Ir.*Ir_sb).^2 + (partial_IR_wrt_It.*It_sb).^2 ...
    + (partial_IR_wrt_Ibg.*Ibg_sb) .^ 2 ).^(1/2);
97 % IR_nu = ( Ir_sb.^2 + It_sb.^2 + Ibg_sb.^2 ).^2 ./ ( Ir_sb.^4/n_dof + ...
    It_sb.^4/n_dof + Ibg_sb .^4 / n_dof);
98
99
100
101 %% PR uncertainty from IR
102
103 PR = c3*IR.^3 + c2*IR.^2 + c1*IR + c0;
104 partial_PR_wrt_IR = 3*c3*IR.^2 + 2*c2*IR + c1;
105
106 Syx = 0.016;
107 syhat = 0.0017;
108
109 PR_sb = ((partial_PR_wrt_IR .* IR_sb).^2 + syhat^2).^(1/2) ;
110
111
112 %% eta from PR
113
114 eta = 1 - (1+MW*(PRair./PR-1)).^(-1);
115
116 partial_eta_wrt_PR = -MW * PRair ./ PR.^2 ./ ( 1 - MW + MW * (PRair ./ ...
    PR) ).^2;
117
118 eta_sb = t_sl_95 * abs( partial_eta_wrt_PR .* PR_sb ) ;
119
120
121 %% sensitivity coefficients
122 Ir_theta = partial_eta_wrt_PR .* partial_PR_wrt_IR .* partial_IR_wrt_Ir;
123 It_theta = partial_eta_wrt_PR .* partial_PR_wrt_IR .* partial_IR_wrt_It;
124 Ibg_theta = partial_eta_wrt_PR .* partial_PR_wrt_IR .* partial_IR_wrt_Ibg;
125
126 %% plot uIR and uPR and uETA
127 % figure
128 % subplot(2,3,1)
129 % imagesc(x_d,z_d,IR_mean)
130 % xlabel('x/d')
131 % ylabel('z/d')
132 % g = sprintf('%s', 'title(''IR - M = ', num2str(M(n_tst)), ', I = ', ...
    num2str(I(n_tst)), ' ');');
133 % eval(g)
134 % axis image
135 % colorbar
136 % caxis([0 1])
137 %
138 % subplot(2,3,2)
139 % imagesc(x_d,z_d,PR_mean)
140 % xlabel('x/d')
141 % ylabel('z/d')

```

```

142 % g = sprintf('%s', 'title(''PR - M = ', num2str(M(n_tst)), ', I = ', ...
    num2str(I(n_tst)), ' ');');
143 % eval(g)
144 % axis image
145 % colorbar
146 % caxis([0 1])
147 %
148 % subplot(2,3,3)
149 % imagesc(x_d,z_d,eta_mean)
150 % xlabel('x/d')
151 % ylabel('z/d')
152 % g = sprintf('%s', 'title('\eta - M = ', num2str(M(n_tst)), ', I = ', ...
    num2str(I(n_tst)), ' ');');
153 % eval(g)
154 % axis image
155 % colorbar
156 % caxis([0 1])
157 %
158 % subplot(2,3,4)
159 % imagesc(x_d,z_d,IR_u)
160 % xlabel('x/d')
161 % ylabel('z/d')
162 % g = sprintf('%s', 'title(''u_{IR} - M = ', num2str(M(n_tst)), ', I = ', ...
    num2str(I(n_tst)), ' ');');
163 % eval(g)
164 % axis image
165 % colorbar
166 % caxis([0 0.05])
167 %
168 % subplot(2,3,5)
169 % imagesc(x_d,z_d,PR_u)
170 % xlabel('x/d')
171 % ylabel('z/d')
172 % g = sprintf('%s', 'title(''u_{PR} - M = ', num2str(M(n_tst)), ', I = ', ...
    num2str(I(n_tst)), ' ');');
173 % eval(g)
174 % axis image
175 % colorbar
176 % caxis([0 0.05])
177 %
178 % subplot(2,3,6)
179 % imagesc(x_d,z_d,eta_u)
180 % xlabel('x/d')
181 % ylabel('z/d')
182 % g = sprintf('%s', 'title(''u_{\eta} - M = ', num2str(M(n_tst)), ', I = ...
    ', num2str(I(n_tst)), ' ');');
183 % eval(g)
184 % axis image
185 % colorbar
186 % caxis([0 0.05])

```

```

187
188 figure
189 subplot(2,1,1)
190 imagesc(x_d,z_d,eta)
191 xlabel('x/d')
192 ylabel('z/d')
193 g = sprintf('%s', 'title('\eta - M = ', num2str(M(n_tst),2), ', I = ', ...
    num2str(I(n_tst),2), ' ');');
194 eval(g)
195 axis image
196 colorbar
197 caxis([0 1])
198
199 %# get current colormap
200     map = colormap;
201     rows = uint16(linspace(1, size(map,1), 10)) ;
202     map = map(rows, :);
203     colormap(map);
204
205 subplot(2,1,2)
206 imagesc(x_d,z_d,eta_sb)
207 xlabel('x/d')
208 ylabel('z/d')
209 g = sprintf('%s', 'title('u_{\eta} - M = ', num2str(M(n_tst),2), ', I = ...
    ', num2str(I(n_tst),2), ' ');');
210 eval(g)
211 axis image
212 colorbar
213 caxis([0 0.05])
214
215 %# get current colormap
216     map = colormap;
217     rows = uint16(linspace(1, size(map,1), 10)) ;
218     map = map(rows, :);
219     colormap(map);
220
221
222 g = sprintf('%s', 'print -dtiff eta_plus_ueta_M-' , num2str(M(n_tst), ...
    '%.3f'), '.tif;');
223 eval(g)
224
225 figure
226 imagesc(x_d,z_d,eta_sb)
227 xlabel('x/d')
228 ylabel('z/d')
229 g = sprintf('%s', 'title('u_{\eta} - M = ', num2str(M(n_tst),2), ', I = ...
    ', num2str(I(n_tst),2), ' ');');
230 eval(g)
231 axis image
232 colorbar

```

```

233 caxis([0 0.05])
234
235 %# get current colormap
236     map = colormap;
237     rows = uint16(linspace(1, size(map,1), 10)) ;
238     map = map(rows, :);
239     colormap(map);
240
241
242 g = sprintf('%s', 'print -dtiff ueta_M_' , num2str(M(n_tst), '%.3f'), '.tif;');
243 eval(g)
244
245 %% lat avg eta
246
247 eta_bar = mean(eta(z_average_range,:),1) ;
248
249 eta_bar_sb = (sum(eta_sb(z_average_range, :) .* ...
    eta_sb(z_average_range,:))) .^ (1/2) / length(z_average_range);
250
251 eta_bar_pu = eta_bar + eta_bar_sb;
252 eta_bar_mu = eta_bar - eta_bar_sb;
253
254
255 figure
256 plot(x_d,eta_bar,'g.', x_d,eta_bar_pu,'r.', x_d,eta_bar_mu,'r.', ...
    x_d,eta_bar_sb,'b.')
257 xlabel('x/d')
258 ylabel('Lat avg \eta')
259 g = sprintf('%s', 'title('M = ', num2str(M(n_tst),2), ', I = ', ...
    num2str(I(n_tst),2), ' ');');
260 eval(g)
261
262 end
263
264 %% Plot mean, sdev of the mean (sdev / sqrt(N)) and normalized values ...
    individually
265 figure
266 imagesc(Ibg)
267 axis image
268 colorbar
269 title('Background Image')
270
271 figure
272 imagesc(Ir)
273 axis image
274 colorbar
275 title('Reference Image')
276
277 figure
278 imagesc(It)

```

```

279 axis image
280 colorbar
281 title('Test Image')
282
283 figure
284 imagesc(Ibg_sb)
285 axis image
286 colorbar
287 title('Background Image Standard Deviation / sqrt(N=20)')
288
289 figure
290 imagesc(Ir_sb)
291 axis image
292 colorbar
293 title('Reference Image Standard Deviation / sqrt(N=20)')
294
295 figure
296 imagesc(It_sb)
297 axis image
298 colorbar
299 title('Test Image Standard Deviation / sqrt(N=20)')
300
301
302 Ibg_norm = Ibg_sb ./ Ibg;
303 Ir_norm  = Ir_sb  ./ Ir;
304 It_norm  = It_sb  ./ It;
305
306
307 figure
308 imagesc(Ibg_norm)
309 axis image
310 colorbar
311 title('Background Image Standard Deviation / sqrt(N=20) / Mean')
312
313 figure
314 imagesc(Ir_norm)
315 axis image
316 colorbar
317 title('Reference Image Standard Deviation / sqrt(N=20) / Mean')
318
319 figure
320 imagesc(It_norm)
321 axis image
322 colorbar
323 title('Test Image Standard Deviation / sqrt(N=20) / Mean')

```

LIST OF REFERENCES

- [1] Goldstein, R. J., Shavit, G., and Chen, T. S., 1965. “Film-cooling effectiveness with injection through a porous section”. *Journal of Heat Transfer*, 87(3), pp. 353–361.
- [2] Gritsch, M., Schulz, A., and Wittig, S., 1998. “Adiabatic wall effectiveness measurements of film-cooling holes with expanded exits”. *J. Turbomach.*, 120(3), pp. 549–556.
- [3] Hutchins, N., Nickels, T., Marusic, I., and Chong, M., 2009. “Hot-wire spatial resolution issues in wall-bounded turbulence”. *J. Fluid Mech.*, 635, pp. 103–136.
- [4] Polezhaev, J., 1997. “The transpiration cooling for blades of high temperature gas turbine”. *Energy Convers. Mgmt.*, 38(10-13), pp. 1123–1133.
- [5] Bunker, R. S., 2006. “Cooling design analysis”. In *DOE Gas Turbine Handbook*. Department of Energy.
- [6] Goldstein, R. J., 1971. “Film cooling”. *Advances in Heat Transfer*, 7, pp. 321–379.
- [7] Bogard, D., and Thole, K., 2006. “Gas turbine film cooling”. *AIAA Journal of Propulsion and Power*, pp. 699–709.
- [8] Hartnett, J., Birkebak, R., and Eckert, E., 1961. “Velocity distributions, temperature distributions, effectiveness and heat transfer for air injected through a tangential slot into a turbulent boundary layer”. *Journal of Heat Transfer*, 83(3), pp. 293–306.
- [9] Pedersen, D. R., Eckert, E. R. G., and Goldstein, R. J., 1977. “Film cooling with large density differences between the mainstream and the secondary fluid measured by the heat-mass transfer analogy”. *Journal of Heat Transfer*, 99(4), November, pp. 620–627.
- [10] Sinha, A. K., Bogard, D. G., and Crawford, M. E., 1991. “Film-cooling effectiveness downstream of a single row of holes with variable density ratio”. *Journal of Turbomachinery*, 113(3), pp. 442–449.
- [11] Aga, V., 2009. “Experimental flow structure investigation of compound angled film cooling”. PhD thesis, ETH Zurich.
- [12] Goldstein, R. J., Eckert, E. R. G., Eriksen, V. L., and Ramsey, J. W., 1969. Film cooling following injection through inclined circular tubes. Tech. rep., NASA.

- [13] Baldauf, S., Scheurlen, M., Schulz, A., and Wittig, S., 2002. “Correlation of film-cooling effectiveness from thermographic measurements at enginelike conditions”. *Journal of Turbomachinery*, 124(4), pp. 686–698.
- [14] Baldauf, S., Scheurlen, M., Schulz, A., and Wittig, S., 2002. “Heat flux reduction from film cooling and correlation of heat transfer coefficients from thermographic measurements at enginelike conditions”. *Journal of Turbomachinery*, 124(4), pp. 699–709.
- [15] Natsui, G., Claretti, R., Wolski, C., Ricklick, M., and Kapat, J., 2013. “Feasibility study of a film source coupling transpiration and a row of cylindrical film holes”. *ASME Paper No. GT2012-70051*.
- [16] Papell, S. S., 1960. Effect on gaseous film cooling of coolant injection through angled slots and normal holes. Tech. Rep. TN-D299, NASA.
- [17] Sasaki, M., Takahara, K., Kumagai, T., and Hamano, M., 1979. “Film cooling effectiveness for injection from multirow holes”. *Journal of Engineering for Power*, 101(1), pp. 101–108.
- [18] Kasagi, N., Hirata, M., and Kumada, M., 1981. “Studies of full-coverage film cooling part1: Cooling effectiveness of thermally conductive wall”. In ASME Paper No. 81-GT-37.
- [19] Martiny, M., Schulz, A., and Wittig, S., 1995. “Full-coverage film cooling investigation: Adiabatic wall temperatures and flow visualization”. In ASME Paper No. 95-WA/HT-4.
- [20] Harrington, M. K., McWaters, M. A., Bogard, D. G., Lemmon, C. A., and Thole, K. A., 2001. “Full-coverage film cooling with short normal injection holes”. In ASME Paper No. GT2004-54043.
- [21] Mhetras, S., Han, J.-C., and Rudolph, R., 2007. “Effect of flow parameter variations on full coverage film-cooling effectiveness for a gas turbine blade”. In ASME Paper No. GT2007-27071.
- [22] Le Grives, E., Nicolas, J. J., and Genot, J., 1979. “Internal aerodynamics and heat transfer problems associated to film cooling of gas turbines”. In ASME Paper No. 79-GT-57.
- [23] Crawford, M. E., Kays, W. M., and Moffat, R. J., 1976. Heat transfer to a full-coverage film-cooled surface with 30degree slant-hole injection. Tech. rep., NASA.
- [24] Crawford, M. E., Kays, W. M., and Moffat, R. J., 1980. “Full-coverage film cooling part 1: Comparison of heat transfer data for three injection angles”. *Journal of Engineering for Power*, 102(4), pp. 1000–1005.

- [25] Crawford, M. E., Kays, W. M., and Moffat, R. J., 1980. “Full-coverage film cooling part ii: Heat transfer data and numerical simulation”. *Journal of Engineering for Power*, 102(4), pp. 1006–10012.
- [26] Kelly, G. B., and Bogard, D. G., 2003. “An investigation of the heat transfer for full coverage film cooling”. In ASME Paper No. GT2003-38716.
- [27] Metzger, D. E., Takeuchi, D. I., and Kuenstler, P. A., 1973. “Effectiveness and heat transfer with full-coverage film cooling”. *Journal of Engineering for Power*, 95(3), pp. 180–184.
- [28] Mayle, M. E., and Camarata, F. J., 1975. “Multihole cooling film effectiveness and heat transfer”. *ASME Journal of Heat Transfer*, 97(4), pp. 534–538.
- [29] Ling, J. P., Ireland, P. T., and Turner, L., 2002. “Full coverage film cooling for combustor transition sections”. In ASME Paper No. 2002-GT-30528.
- [30] Ligrani, P., Goodro, M., Fox, M., and Moon, H.-K., 2012. “Full-coverage film cooling: film effectiveness and heat transfer coefficients for dense and sparse hole arrays at different blowing ratios”. pp. 061039–1 to 061039–13.
- [31] Andrews, G. E., Khalifa, I. M., Asere, A. A., and Bazdidi-Tehrani, F., 1995. “Full coverage effusion cooling with inclined holes”. In ASME Paper No. ASME95-GT-274.
- [32] Andreini, A., Facchini, B., Picchi, A., Tarchi, L., and Turrini, F. “Experimental and theoretical investigation of thermal effectiveness in multiperforated plates for combustor liner effusion cooling”.
- [33] Yavuzkurt, S., Moffat, R. J., and Kays, W. M., 1980. “Full-coverage film cooling part 1. three-dimensional measurements of turbulence structure”. *Journal of Fluid Mechanics*, 101, pp. 129–158.
- [34] Yavuzkurt, S., Moffat, R. J., and Kays, W. M., 1980. “Full-coverage film cooling part 2. prediction of the recovery-region hydrodynamics”. *Journal of Fluid Mechanics*, 101, pp. 159–178.
- [35] Michel, B., Gajan, P., Strzelecki, A., Wagner, B., Savary, N., and Kourta, A. e. a., 2009. “Full coverage film cooling using compound angle”. *C. R. Mecanique*, 337(6), pp. 562–572.
- [36] Sellers, J. P., 1963. “Gaseous film cooling with multiple injection stations”. *AIAA Journal*, 1(9), pp. 2154–2156.
- [37] Kirollos, B., and Povey, T., 2013. “An energy-based method for predicting the additive effect of multiple film cooling rows”. In ASME Paper No. GT2013-94934.

- [38] Metzger, D. E., Kuenstler, P. A., and Takeuchi, D. I., 1976. “Heat transfer with film cooling within and downstream of one to four rows of normal injection holes”. In ASME Paper No. 76-GT-83.
- [39] Cho, H. H., and Goldstein, R. J., 1995. “Heat (mass) transfer and film cooling effectiveness with injection through discrete holes: Part 2 – on the eexposed surface”. *Journal of Turbomachinery*, 117(3), pp. 451–460.
- [40] Miller, M., 2011. “Heat transfer in a coupled impingement-effusion cooling system”. Ms thesis, University of Central Florida.
- [41] Natsui, G., Claretti, R., and Kapat, J., 2012. “Experimental evaluation of full coverage film cooling arrays: adiabatic film cooling effectiveness”. *ASME Paper No. HT2012-58131*.
- [42] Claretti, R., Natsui, G., Crawford, M., Brown, G., Landis, K., and Kapat, J., 2012. “Experimental evaluation of full coverage film cooling arrays: heat transfer augmentation”. *ASME Paper No. HT2012-58343*.
- [43] Hodges, J. A full coverage film cooling study: the effect of an alternating compound angle.
- [44] Natsui, G., 2012. “Surface measurements and predictions of full-coverage film cooling”. Ms thesis, University of Central Florida.
- [45] George, W. K. Does turbulence need god?
- [46] Abdullah, K., Hisato, O., Ken-ichi, F., and Takeomi, I., 2012. “Heat transfer and aerodynamics studies of multiple cooling holes”.
- [47] Incropera, F., Dewitt, D., Bergman, T., and Lavine, A., 2007. *Fundamentals of Heat and Mass Transfer*, 6th edition ed. John Wiley and Sons.
- [48] George, W. K. Lectures in turbulence for the 21st century.
- [49] van Driest, E. R. “On turbulent flow near a wall”. pp. 1007–1011.
- [50] Coles, D., 1956. “The law of the wake in the turbulent boundary layer”. *J. Fluid Mech.*, 1(2), pp. 1000–1005.
- [51] Guo, J., Julienn, P. Y., and Meroney, R. N., 2005. “A modified log-wake law for zero-pressure-gradient turbulent boundary layers”. *Journal of Hydraulic Research*, 43(4), pp. 421–430.
- [52] Holm, D., 2005. “Taylor’s hypothesis, hamilton’s principle, and the lans- α model for computing turbulence”. *Los Alamos Science*, 29(13).

- [53] Baret, M., and Hollingsworth, K., 2001. “On the calculation of length scales for turbulent heat transfer correlation”. *J. Heat Transfer*, 123(5), p. 878.
- [54] Ames, F., 1991. “Heat transfer with high intensity, large scale turbulence: the flat plate turbulent boundary layer and the cylindrical stagnation point”. Phd thesis, Stanford University.
- [55] Elsner, J., 1996. “On the measurement of turbulence energy dissipation”. *Measurement science and technology*, 7(10), pp. 1334–1348.
- [56] Lewalle, J., and Ashpis, D. Estimation of time scales in unsteady flows in a turbomachinery rig.
- [57] Tennekes, H., and Lumley, J. L. *A First Course in Turbulence*.
- [58] Pietrzyk, J., Bogard, D., and Crawford, M., 1989. “Hydrodynamic measurements of jets in crossflow for gas turbine film cooling application”. *ASME J. Turbomach.*, 111(2), pp. 139–145.
- [59] Kohli, A., and Bogard, D., 2005. “Turbulent transport in film cooling flows”. *J. Heat Transfer*, 127(5), pp. 513–520.
- [60] Burd, S., and Simon, T., 1999. “Turbulence spectra and length scales measured in film coolant flows emerging from discrete holes”. *ASME J. Turbomach.*, 121(3), pp. 551–557.
- [61] Kohli, A., and Bogard, D., 1998. “Fluctuating thermal field in the near-hole region for film cooling flows”. *ASME J. Turbomach.*, 120(1), pp. 86–91.
- [62] Aga, V., Rose, M., and Abhari, R., 2008. “Experimental flow structure investigation of compound angled film cooling”.
- [63] El-Gabry, L., Thurman, D., Poinsette, P., and Heidmann, J., 2011. “Turbulence and heat transfer measurements in an inclined large scale film cooling array: Part i, velocity and turbulence measurements”. In ASME Paper No. GT2011-46491.
- [64] Wright, L., McClain, S., and Clemenson, M., 2011. “Effect of density ratio on flat plate film cooling with shaped holes using psp”. *Journal of Turbomachinery*, 133(4), pp. 041011–1 to 041011–11.
- [65] Thielicke, W., and Stamhuis, E., 2014. *PIVlab - Time-Resolved Digital Particle Image Velocimetry Tool for MATLAB (version: 1.4)*.
- [66] Thielicke, W., and Stamhuis, E., 2014. “Pivlab - towards user-friendly, affordable and accurate digital particle image velocimetry in matlab”.
- [67] Thielicke, W. The flapping flight of birds - analysis and application.

- [68] Wieneke, B., and Pfeiffer, K., 2010. “Adaptive piv with variable interrogation window size and shape”. *15th International Symposium on Applications of Laser Techniques to Fluid Mechanics*.
- [69] Nogueira, J., Lecuona, A., and Rodriguez, P. A., 1997. “Data validation, false vectors correction and derived magnitudes calculation on piv data”. *Measurement Science and Technology*, 8(12), p. 1493.
- [70] Sciacchitano, A., Neal, D., Smith, B., Warner, S., Vlachos, P., Wieneke, B., and Scarano, F., 2014. “Collaborative framework for piv uncertainty quantification: comparative assessment of methods”. *17th International Symposium on Applications of Laser Techniques to Fluid Mechanics*.
- [71] Nicoll, W., and Whitelaw, J., 1967. “The effectiveness of the uniform density, two-dimensional wall jet”. *Int. J. Heat and Mass Transfer*, 10(5), pp. 041011–1 to 041011–11.
- [72] Goldstein, R. J., and Jin, P., 2001. “Film cooling downstream of a row of discrete holes with compound angle”. *Journal of Turbomachinery*, 123(2), pp. 222–229.
- [73] Kays, W., and Crawford, M. *Convective heat and mass transfer*.
- [74] Liu, T., and Sullivan, J., 2005. *Pressure and Temperature Sensitive Paints*.
- [75] Zhang, L., and Fox, M., 1999. “Flate plate film cooling measurement using psp and gas chromatograph techniques”. In ASME Paper No. AJTE99-6241.
- [76] Jones, T., 1999. “Theory for the use of foreign gas in simulating film cooling”. *Int. J. of Heat and Fluid Flow*, 20(3), pp. 349–354.
- [77] Charbonnier, D., Ott, P., Jonsson, M., Cottier, F., and Kobke, T., 2009. “Experimental and numerical study of the thermal performance of a film cooled turbine platform”. In ASME Paper No. GT2009-60306.
- [78] Han, J., and Rallabandi, A., 2010. “Turbine blade film cooling using psp technique”. *Frontiers in Heat and Mass Transfer*, 1.
- [79] Unifib pressure sensitive paint; www.psp-tsp.com.
- [80] Kameda, M., Yoshida, M., Sekiya, T., and Nakakita, K., 2015. “Humidity effects in the response of a porous pressure-sensitive paint”. *Sensors and Actuators B: Chemical*, 208.
- [81] Asme performance test codes 19.1 – test uncertainty.
- [82] Crites, R., and Benne, M., 1995. “Emerging technology for pressure measurements in wind tunnels - pressure sensitive paint”. In AIAA Paper No. AIAA 95-0106.

- [83] Egami, Y., and Asai, K., 1995. “Effects of antioxidants on photodegradation of porous pressure-sensitive paint”. In AIAA Paper No. 2002-2905.
- [84] Liu, Q., 2006. “Study of heat transfer characteristics of impinging air jet using pressure and temperature sensitive luminescent pain”. PhD thesis, University of Central Florida.
- [85] Ahn, J., Mhetras, S., and Han, J., 2005. “Film-cooling effectiveness on a gas turbine blade tip using pressure-sensitive paint”. *J. Heat Transfer*, 127(5), pp. 521–530.
- [86] Mhetras, S., Han, J., and Rudolph, R., 2012. “Effect of flow parameter variations on full coverage film-cooling effectiveness for a gas turbine blade”. *J. Turbomachinery*, 134.
- [87] Narzary, D., Liu, K., Rallabandi, A., and Han, J., 2012. “Influence of coolant density on turbine blade film-cooling using pressure sensitive paint technique”. *J. Turbomachinery*, 136.
- [88] Schmidt, D., Sen, B., and Bogard, D., 1996. “Film cooling with compound angle holes: adiabatic effectiveness”. *J. Turbomach*, 118(4), pp. 807–813.
- [89] Goldstein, R. J., Jin, P., and Olson, R., 1999. “Film cooling effectiveness and mass/heat transfer coefficient downstream of one row of discrete holes”. *J. Turbomach*, 121(2), pp. 225–232.
- [90] Jung, I., and Lee, J., 2000. “Effects of orientation angles on film cooling over a flat plate: Boundary layer temperature distributions and adiabatic film cooling effectiveness”. *J. Turbomach.*, 122(1), pp. 153–160.
- [91] Yu, Y., Yen, C.-H., Shih, T., Chyu, M., and Gogineni, S., 2002. “Film cooling effectiveness and heat transfer coefficient distributions around diffusion shaped holes”. *J. Heat Transfer*, 124(5), pp. 820–827.
- [92] Eberly, M., and Thole, K., 2014. “Time-resolved film-cooling flows at high and low density ratios”. *J. Turbomach*, 7(10), pp. 1334–1348.